



Czech
Technical
University
in Prague

F4

Faculty of Nuclear Sciences and Physical Engineering
Department of Physics

DOCTORAL THESIS

**Experimental Studies of Runaway Electrons
in Tokamaks**

Prague 2023

Ing. Ondřej Ficker

Bibliografický záznam

Autor Ing. Ondřej Ficker
České vysoké učení technické v Praze,
Fakulta jaderná a fyzikálně inženýrská
Katedra fyziky

Název práce Experimentální studium ubíhajících elektronů v tokamacích

Studijní program Aplikace přírodních věd

Studijní obor Jaderné inženýrství

Školitel prof. RNDr. Jan Mlynář, PhD.
České vysoké učení technické v Praze,
Fakulta jaderná a fyzikálně inženýrská,
Břehová 7,
114 19 Praha 1

Ústav fyziky plazmatu AV ČR
U Slovanky 2525/1a
182 00 Praha 8

Školitel–specialista -

Akademický rok 2023

Počet stran 313

Klíčová slova tokamak, plasma, disrupce, ubíhající elektrony, synchrotronní záření, diagnostika, equilibrium

Bibliographic Entry

Author Ing. Ondřej Ficker
Czech Technical University in Prague,
Faculty of Nuclear Sciences and Physical Engineering
Department of Physics

Title of Dissertation Experimental Studies of Runaway Electrons in Tokamaks

Degree Programme Applications of Natural Sciences

Field of Study Nuclear Engineering

Supervisor prof. RNDr. Jan Mlynář, PhD.
Czech Technical University in Prague,
Faculty of Nuclear Sciences and Physical Engineering,
Břehová 7, 114 19 Prague 1

Institute of Plasma Physics of the CAS
U Slovanky 2525/1a
182 00 Prague 8

Supervisor–specialist -
-

Academic Year 2023

Number of Pages 313

Keywords tokamak, plasma, runaway electrons , synchrotron radiation,
diagnostics, disruption, equilibrium

Abstrakt

Tato práce je zaměřena na analýzu experimentů s ubíhajícími elektrony (RE) na tokamaku COMPASS v kontextu evropského výzkumu termojaderné fúze a zahrnuje také analýzu relevantních dat z tokamaku JET. RE představují zásadní riziko pro provoz reaktorů typu tokamak. Disertační práce obsahuje studium vzniku ubíhajících elektronů v počáteční fázi výboje i při náhlé ztrátě proudu vysokoteplotním plazmatem způsobené vstřikem nečistot, ale také studium ztrát ubíhajících elektronů při různých mangetohydrodynamických nestabilitách. Mezi nejdůležitější výsledky patří pozorování a objasnění vztahu mezi magnetickou rovnováhou svazku ubíhajících elektronů a jejich kinetickou energií. Tento vztah je využit ke zlepšení řízení radiální polohy svazku. Tato metoda měření průměrné kinetické energie RE je také použita pro analýzu výbojů se vstřikem různých množství a typů plynů na tokamaku COMPASS i JET. Vstřik lehčích plynů na tokamaku COMPASS, především druhotný vstřik deuteria, vede k pomalému poklesu proudu, který nezpůsobuje nežádoucí nárůst průměrné kinetické energie RE a tak je vhodný k bezpečnému potlačení svazku. Analogická pozorování byla dosažena i na větších zařízeních. Záření RE je analyzováno také, zejména vznik HXR, fotoneutronů a synchrotronního záření. Práce také obsahuje technická shrnutí kampaní s RE provedených na tokamaku COMPASS.

Abstract

This thesis is focused on the analysis of runaway electron (RE) experiments in the COMPASS tokamak in the context of the European fusion research with some amount of JET tokamak data analysis included. The RE phenomenon presents an imminent threat for a tokamak fusion reactor. Within this thesis, the RE generated in the tokamak discharge start-up, during and after the Ohmic current termination by impurity injection are studied as well as the losses of RE due to various magnetohydrodynamic instabilities. One of the most important results of the thesis is the observation and description of the relation between the magnetic equilibrium in the RE beam phase and the kinetic energy of the RE. The relation is used to improve the radial position control of the beam. This method of kinetic energy measurement is applied to analysis of discharges with injection of various gas types and amounts on both COMPASS and JET. Lighter gas injection, namely the secondary injection of deuterium, are shown to lead to optimal current decay that does not induce an increase of average RE kinetic energy and therefore it is suitable for safe mitigation of the beam. Analogical observations were achieved at large devices. RE radiation is also analysed, namely HXR, photoneutron production and synchrotron radiation. Besides, the thesis contains technical summaries of the RE campaigns performed at COMPASS.

Contents

Aims of the thesis	1
1 Introduction	3
1.1 The need of fusion power	3
1.2 Fusion reactions and ITER	5
1.3 Runaway electrons in tokamaks	8
1.4 Work of the author and outline of this thesis	10
2 Runaway electron physics	13
2.1 Magnetic field configuration of the tokamak	13
2.2 Simple estimate of RE parameters	16
2.2.1 Plasma and runaway electron current	16
2.2.2 Magnetic energy of the runaway electrons	17
2.2.3 Loop voltage and kinetic energy	18
2.3 Discharge scenarios and phases prone to the RE generation	19
2.3.1 Plasma start-up	19
2.3.2 Low density discharges	20
2.3.3 Disruption	21

2.4 Description of runaway electrons in the plasma	23
2.4.1 Test particle description	23
Full orbit description	23
Gyro-averaged description	24
Trajectory of one poloidal transit - bounce averaging	25
2.4.2 Kinetic description	26
2.4.3 Fluid description	30
2.5 Generation mechanisms	31
2.5.1 Dreicer generation mechanism	32
Dreicer generation rates	32
2.5.2 Hot-tail mechanism	33
2.5.3 Secondary mechanism-avalanche	33
2.6 Background plasma and induced electric field	34
2.7 Radiation of runaway electrons and production of secondary particles	35
2.7.1 Bremsstrahlung	36
2.7.2 Synchrotron radiation	37
2.7.3 Generation of secondary particles	38
2.8 RE avoidance and mitigation	38

2.8.1 Massive material injection	39
2.8.2 De-confinement and energy dissipation by magnetic field and kinetic perturbations	40
2.8.3 Controlled impact	41
2.9 Detrimental effects of runaway electron impact	42
3 Overview of diagnostics, processing methods and models	43
3.1 Dedicated RE diagnostics and common diagnostics sensitive to RE presence . . .	43
3.1.1 Direct RE detection	43
3.1.2 RE Bremsstrahlung measurement	44
3.1.3 Photoneutron measurement	45
3.1.4 Synchrotron and cyclotron radiation measurement	46
3.1.5 Impact diagnostics	47
3.1.6 Background plasma diagnostics	48
3.1.7 Detrimental effects of RE on other diagnostics and their use in measurements	49
3.2 Signal processing and analysis methods	50
3.2.1 Pulse counting	50
3.2.2 Peak height and shape analysis	51
3.2.3 Pulse-shape discrimination	51

3.2.4 Frequency domain methods	52
3.2.5 Spectral analysis	52
3.2.6 Cross-spectrum, cross-correlation and coherence	52
3.2.7 Inverse problems	53
3.2.8 Spectra unfolding	54
3.2.9 Tomography	54
3.2.10 Control algorithms	55
3.3 Special diagnostics and processing methods implemented during COMPASS RE experiments	57
3.3.1 Measurements of HXR energies with the NaI(Tl) spectrometer and the REGARDS spectrometer	57
3.3.2 Evaluation of HXR fluxes over large range by synthesised measurements from multiple detectors	61
3.3.3 Distinguishing HXR and neutron peaks in the tokamak experiments	71
3.3.4 Modification of AXUV and SXR tomography algorithm for the runaway electron beam	75
3.3.5 Installation of REIS2 spectrometer for measurements of synchrotron radiation	75
3.3.6 Calibration of injection valves, pressure measurements and residual gas analysis	76
3.4 Simulation tools relevant to RE physics	84
3.4.1 Simulation tools relevant for secondary RE effects and other useful tools ...	85

4 RE experiments on COMPASS and other tokamaks - scenarios and main results 87

4.1 European tokamaks with extensive RE program	87
4.2 COMPASS	88
4.2.1 COMPASS diagnostics and gas injection setup	89
4.2.2 COMPASS RE campaigns	91
4.3 RE experiment scenarios on COMPASS	92
4.3.1 The ramp-up scenario	94
4.3.2 The flattop scenario with TQ and full current RE beam	95
4.3.3 Zero and controlled external loop voltage during the RE beam phase	97
4.4 Important COMPASS RE results complementing this thesis	99
4.4.1 Critical electric field at COMPASS	99
4.4.2 The effect of shaping and density on RE losses	99
4.4.3 Application of diagnostics principles from particle physics	100
4.4.4 RMPs	100
4.4.5 Injection of graphite pellets	101
4.4.6 Calorimetric measurements	101
4.4.7 Measurement of high frequency perturbations	102
4.5 RE experiments and scenarios at other EUROfusion tokamaks	102

4.5.1 RE experiments at TCV	102
4.5.2 RE experiments at ASDEX-U	103
4.5.3 JET	105
4.5.4 JET RE experiments	106
4.5.5 COMPASS-Upgrade and runaway electrons	107
5 RE in start-up and flattop in the COMPASS experiments	109
5.1 Start-up runaway electrons in COMPASS	109
5.1.1 The start-up sequence and conditions in COMPASS	110
5.1.2 Variety of start-up RE events	114
5.1.3 Dedicated start-up RE experiments	116
5.2 Statistical analysis of the COMPASS start-up RE	122
5.2.1 Selection of parameters and discharges	122
5.2.2 The effect of the density	124
5.2.3 The E/E_c of the RE and non-RE groups	126
5.2.4 The effect of the pre-fill and gas injection after the break-down	128
5.2.5 Deuterium line radiation and conclusion of the statistical analysis	129
5.2.6 Simple model of the start-up RE with acceleration	132
5.2.7 Basic use of STREAM for modelling of the COMPASS start-up RE	134

5.3 Runaway electrons in the flattop of COMPASS discharges.....	136
5.4 Periodic RE losses	138
5.4.1 Overview of periodic RE loss causes	138
5.4.2 RE confinement in the H-mode and ELM-related losses	141
5.4.3 Magnetic islands improving the RE confinement	144
5.4.4 More insight into the "1 kHz" loss	147
5.5 Synchrotron radiation measurement with the RE in the flattop discharges....	148
5.6 Conclusion of start-up and flattop studies	153
6 Equilibrium of the runaway electron beam	155
6.1 Equilibrium in high temperature tokamak discharges	155
6.1.1 High current betatrons	157
6.2 Possible modification of the magnetic equilibrium and Grad-Shafranov-like equation for RE beam	158
6.3 Understanding the position stability of the RE beam in COMPASS	160
6.3.1 COMPASS Poloidal field coil system	161
6.3.2 Improved position control for the RE beam on COMPASS	163
6.4 Simple energy estimate based on magnetic equilibrium in full RE beam	166
6.4.1 The estimate based on B_v and radial position	166

6.4.2	The estimate based on the pressure from EFIT	167
6.4.3	Energy estimate in the case of plasma discharge with RE population	170
6.5	Other effects of betatron/tokamak RE equilibrium	174
6.5.1	HFS X-point and possible self-compression	175
6.5.2	Orbits for different energies and impact locations	177
6.5.3	Diagnostics evidence for RE orbits limited at HFS and at LFS	180
6.6	Summary of RE equilibrium applications	183
7	Analysis of RE in COMPASS and JET discharges in support of RE beam mitigation techniques	185
7.1	The ramp-up scenario RE beam analysis	185
7.1.1	RE beam reproducibility	186
7.1.2	Detailed look on the ramp-up RE beam generation	188
7.2	RE beam generated from the flat-top scenario - brief overview of results	192
7.2.1	Conditions for RE generation using gas injection valve and MGI	192
7.2.2	Effect of different gas species and amounts on the RE current decay after the injection	193
7.2.3	Secondary injection of deuterium in COMPASS	196
7.2.4	Acceleration and deceleration of the RE beam	200
7.3	Analysis of the RE beams at JET	202

7.3.1 Application of tomography for analysis of RE beam properties on JET....	204
7.3.2 Secondary injection of deuterium and benign termination	205
7.3.3 Interpretation of synchrotron radiation at JET and analysis using SOFT synthetic diagnostics	208
7.3.4 Summary of the RE generation and mitigation results analysed in this thesis	211
8 Conclusions and outlook	213
Acknowledgments	216
Bibliography	219
A List of acronyms	237
B Plasma diagnostics setups and overviews of COMPASS RE campaigns	239
B.1 5 th -12 th RE campaign.....	239
B.1.1 5 th RE campaign	239
B.1.2 6 th RE campaign	241
B.1.3 7 th RE campaign	242
B.1.4 8 th RE campaign	243
B.1.5 9 th RE campaign	245
B.1.6 10 th RE campaign	245
B.1.7 11 th RE campaign	246

B.1.8 12 th RE campaign	248
C Biot-Savart solver for investigation of RE equilibrium	251
D The attached publications and declaration	255

■ Aims of the thesis

- Apply, modify or develop suitable diagnostics methods for RE beam parameter measurement or estimation, e.g. energy, radiated power, etc.
- Conduct and analyse runaway electron experiments on COMPASS aimed at understanding of runaway electron losses
- Analyse the start-up RE phenomenon in COMPASS
- Conduct and analyse experiments with generation of runaway electron beam using impurity gas injection of various gas species and amounts in COMPASS
- Participate in experiments at other tokamaks and apply similar analysis methods as in the case of COMPASS



Chapter 1

Introduction



1.1 The need of fusion power

Harnessing thermonuclear fusion in an effective and safe manner is quite a challenge. A challenge that has been in the focus of human civilisation for almost 70 years and despite the fact that the world has significantly changed over this period, the goal did not lose anything from its attractiveness and legendarity. However, it is good to remind ourselves how does fusion stand in the context of the year 2023. There are three main advantages that are usually cited in connection to fusion: no emissions of green-house gases or air pollutants, large world-wide available stock of primary resources and safe operation. The first advantage is of increasing importance as the human influence on the global climate change needs to be limited and fusion is definitely one of the best options how to replace the fossil fuels in coordination with "renewable sources of energy" (RSE). The necessary condition to make fusion useful in this effort is however its rapid evolution and implementation into massive energy production as soon as possible. It is hard to predict, however at the current path, the fusion research is heading rather towards the high duty cycle / base-load energy source than to a back-up electricity source for peak hour or small local source. This is given in particular by the development costs, relatively low flexibility of the discharge scenario and large size of the reactor, that currently seems to be unavoidable. Anyway, power plant of these properties is exactly the optimal type to become a complementary electricity source to the renewable resources and batteries/hydrogen economics. Indeed, despite the huge financial resources invested into the development, optimisation and construction of in particular solar and

wind power generation units, some principal obstacles prevent the renewable sources of energy from becoming the only source of electricity. Being dependent on the weather conditions and natural day and year condition variation, the renewable sources of energy are "intermittent" sources, having typically quite low duty cycle with peaks and valleys generally not synchronised with the peaks and valleys of the consumption. This variation can be partly compensated by the increased storage of electrical energy. This meets with the other trend pursued lately - the electromobility. In principle, car batteries can be charged using the over-production of RSE with large buffer battery plants to compensate for the phase shift of the charge demand and production. This can be optimised even better if hydrogen cycle and fuel cell powered cars are developed and spread. Despite the promising technologies mentioned above, the coexistence of RSE with a reliable source of energy is necessary to cover also the requirements of huge consumers, like industrial sites and also heat production in winter months that is necessary in large fraction of the most populated regions of the world. Hopefully, fusion can once overtake this job and until then, the road should be paved by safe designs of fission reactors and also high-tech, combined cycle, gas and coal power plants that should be as much environmentally friendly as possible in order to help with the transition. The second reason, i.e. the availability of fuel for fusion, is a strong argument as well, it is for sure that the fossil fuels will be consumed sooner or later within tens, hundreds or thousands of years and we must be ready for this. Currently, more than 90% of primary energy is still produced using fossil fuels and the need for energy will be growing as can be seen in figure 1.1 that is based on the data published in [1].

The two previous arguments indicate that this dominance will have to be changed on a time scale of several generations in parallel with feeding the increasing demand for energy.

Another argument regarding the fuel availability arises if we look further in the future - in the case that the humanity wants to ever attempt the manned interstellar journey or even routine space flights to planets or moons of planets beyond Mars, it will not be possible without harnessing the energy of the thermonuclear fusion. An appropriate source of energy for such journey and establishing bases on the surface or orbits on these space bodies will require isolated source of energy with very high power/mass ratio and option to extract fuel from the environment. At the current state of knowledge, controlled fusion is as optimal solution as we can get for this task.

The third main argument for fusion, inherent safety and stability, is related to the temperature dependence of the reaction probability that peaks or saturates above certain temperature range and the nature of the high temperature plasma confinement with significant energy losses generally increasing with

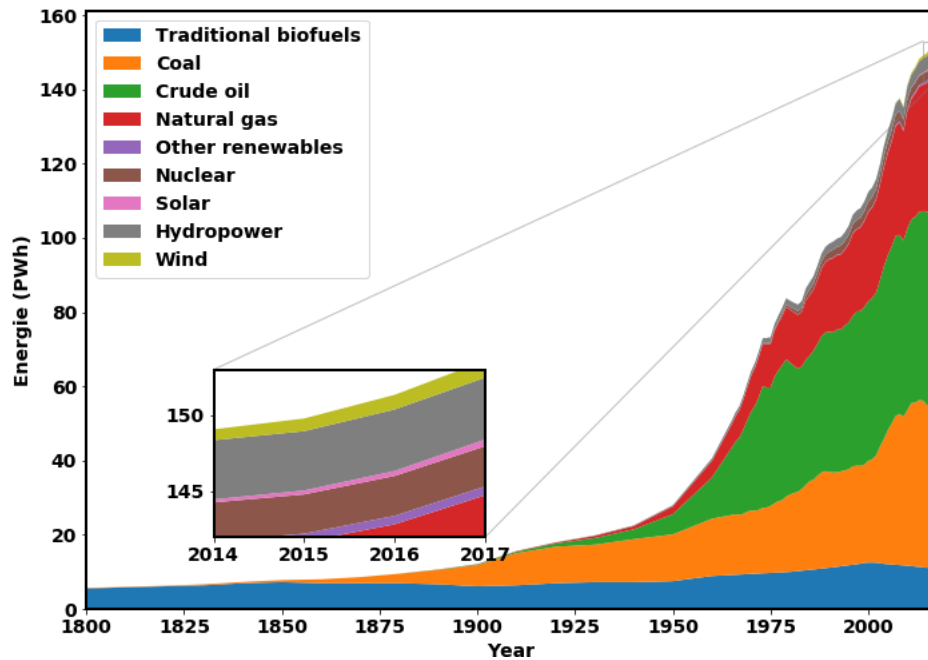


Figure 1.1: Time evolution of primary energy production sources, based on "Our world in data" dataset, primary source of data [1]

temperature. These facts lead to stability at high temperatures and remove the risk of uncontrolled reaction runaway, energy build-up and subsequent explosion. This remains a risk in some fission reactor designs. Moreover, the fuel is continuously supplied in a form of gas or strictly limited amount of solidified gas, so the amount of material that can fuse is very limited in the reactor at any time instance.

On top of the motivation mentioned above, it is clear that the resources for the research are available in the world economics more than ever before and the fusion research, although being multi-generation Odyssey, continuously gets closer to the final goal. For these reasons the projects pursuing the research of controlled thermonuclear fusion need to be supported.

1.2 Fusion reactions and ITER

Controlled thermonuclear fusion remains one of the major challenges of our age. Unlike our ancestors just 100 years ago, we are aware of the mechanism of inexhaustible (on the human time scale) source of power of the stars and thanks to the rapid progress in the physics research in 20th century we also

know that reproducing energy generation using fusion reactions on Earth is at the edge of our technological options but can be still reachable. It is not only an exciting and complex physics and engineering goal, but also a sensitive indicator of the stability of the global political environment as achieving electricity production based on fusion reactions can be barely a task for a single nation. Just now we are living in the decisive age - ITER (International Thermonuclear Experimental Reactor,[2]) is under construction in France, with components being manufactured all over the world. The main aim of ITER is to show the engineering feasibility of fusion-based energy production. Despite that many approaches to sustain fusion reactions emerged during the past 60 years, ITER is build as a tokamak [3], a magnetic confinement fusion (MCF) axisymmetric device, because these devices proved to have the best experimental results so far in the terms of energy confinement but also in terms of produced fusion power.

The general criterion that must be fulfilled in an energetic fusion reactor is the so called Lawson criterion [4]

$$n\tau_E \geq f(T), \quad (1.1)$$

where n is particle density (ion density) and τ_E is the energy confinement time, the function of the temperature on the left hand side is related to the type of the reaction through average reactivity $\langle\sigma v\rangle$, i.e. a product of the fusion reaction cross section and reactant velocity, which is equal to the number of reactions in cubic meter per second and per unit reactant densities. The cross section σ is then representing the probability of the reaction by an effective area of the particle interaction, commonly defined via relation $\sigma = \frac{R}{\Gamma N}$ to number of reactions R , particle flux Γ and target particle number N . The average reactivity can be approximated by a constant near its minimum. For the fusion fuel mix of deuterium and tritium which reaches high reactivity values still in the accessible range of temperatures (tens of keV) and ignited plasma (no auxiliary heating required, the fusion reaction sustains itself) the criterion can be written as

$$n\tau_E \geq \frac{12T}{\langle\sigma v\rangle \epsilon_\alpha}, \quad (1.2)$$

where T is the plasma (ion) temperature, $\langle\sigma v\rangle$ is the aforementioned reactivity and ϵ_α is the energy of the α particle that is one of the products of the DT fusion reaction, confined in the MCF device as it is a charged particle. Near the location of the minimum in temperature ($T = 10 - 20\text{keV}$), the function on the right hand side can be approximated by a constant

$$n\tau_E \geq 1.5 \cdot 10^{21} \text{ m}^{-3}\text{s}. \quad (1.3)$$

The best discharges in multiple tokamaks were characterised by achieving the values of the parameters n , T , τ_E in the region of interest - densities in the range 10^{19} to 10^{20} m^{-3} are just the typical tokamak values, temperatures well above 10 keV were achieved with auxiliary heating power in large machines like JET [5] or JT-60U [6], and confinement times approaching to 1 s (at

JET [7]). However, achieving and sustaining the optimal combination of parameters in order to achieve net fusion power still remains a challenge. The DT is clearly the most promising nuclear fusion fuel mixture and according to figure 1.2 it is obvious that we cannot even think of using any other reaction before completely mastering the controlled DT reaction as the cross-section for any other fusion reaction is about two orders of magnitude smaller. There are numerous research and development issues that did not allow us to build a tokamak-based power plant so far, the most important ones are listed below

- **Confinement time scaling leading to large volume reactors:** Even when considering the simplest model of diffusion (ignoring the magnetic field) - a random walk, it is obvious that the confinement time (particle confinement time in this case) scales with the characteristic linear dimension of the reactor squared. Indeed, larger machines are generally characterised by higher confinement time (both particle and energy) and therefore the plasma volume of ITER will be more than 800 m^3 . Such size is connected not only with high material costs, manufacturing and transport difficulties but also with large values of magnetic energy in the confining magnetic field.
- **Critical material requirements - heat and radiation fluxes:** The heat fluxes on the most exposed plasma facing components are comparable only to a few of other applications (return modules of spaceships entering the atmosphere, etc.). Furthermore, the temperature of the components will be changing in cycles in the range of many hundreds of Kelvins and the fluxes of the fast neutrons from the fusion reactions will cause the damage in the order of units of dpa (displacement per atom). In the future power-plants the structural stability of the materials affected by such irradiation doses remains a question. These facts together with the requirements on the plasma purity (low Z , low sputtering materials preferred) and low tritium retention (Carbon ruled out) make the selection of the optimal first wall material extremely challenging. Moreover the high neutron fluxes also discriminate some of the materials used in the diagnostic systems and support structure steel components. For example nickel that is transmuted by neutron radiation to ^{60}Co that is one of the most dangerous radionuclides, cannot be used. Many cutting-edge materials are currently considered and tested [8], including special alloys or liquid metals, however ITER will use beryllium first wall and tungsten divertor (part of the vessel exposed to largest heat fluxes due to the geometry of the magnetic field).
- **Pulsed operation:** As start-up and current drive in the traditional tokamak is governed by the transformer effect, the current in the central solenoid must be changing in order to sustain the magnetic configuration and to some degree, to heat the plasma. Although the research in the auxiliary heating and current drive methods (neutral beam injection -

NBI and wave heating - Electron Cyclotron Resonance Heating / Current Drive (ECRH/ECCD), Ion Cyclotron Resonance Heating (ICRH) and Lower Hybrid Current Drive (LHCD) [9]) secured a large improvement and the discharges with purely non-inductive phase were reported [10, 11], the fully continuous regime required by the grid from a base-load power plant has yet to be developed and proved if the tokamak concept is about to succeed. A necessary condition to achieve this goal is that all the tokamak coils are superconductive, which increases the cost of the machine.

- **Extreme complexity:** ITER will be composed of more than one million parts, with the main systems including large superconducting magnets, one of the largest vacuum vessels, one of the largest cryogenic systems, nuclear-safety-grade and tritium technologies, plasma diagnostics systems based on cutting edge physics principles and many other unique technologies and solutions. The components are manufactured all around the world. It is a tremendous social and technological challenge to manage the assembly of the machine and to maintain and run such an impressively complex system.
- **Sensitivity to critical instabilities:** Despite the good experimental energy confinement time values, tokamaks have a severe disadvantage - there is a large group of instabilities driven by or connected with the current flowing through the plasma ring. Some of them can be critical and may lead to a sudden loss of energy confinement and plasma current quench - an event called a disruption. The disruptions not only terminate the discharges, but what is worse, they are connected with large heat fluxes and extreme forces acting on the magnets, vacuum vessel and supporting structures [12]. Disruptions may also lead to generation of runaway electron (particles with relativistic energies of the order of tens of MeV) beams that can present a large danger to the wall and cooling systems.

This list of research and development issues is then of course complemented by the socioeconomic and political issues of high cost and lack of political will to invest into the long-term international fusion research programs.

■ 1.3 Runaway electrons in tokamaks

The true danger for tokamak operation are the rapid plasma current terminations, known as disruptions [14]. During disruptions, a significant part of the plasma magnetic and thermal energy may be converted to the kinetic energy

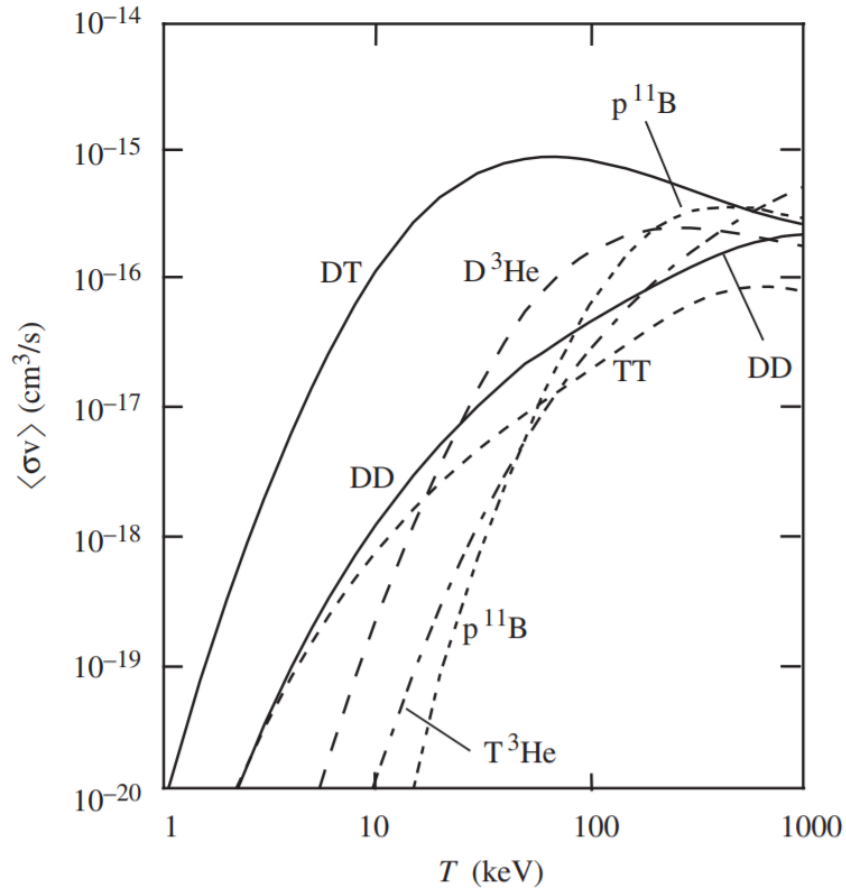


Figure 1.2: The reactivity for various thermonuclear reactions in the relevant range of temperatures. The resonant DT reaction clearly reaches the highest reactivity value in the region around $T_i = 10$ keV that is accessible in the present large tokamaks. The reactivity for DT reaction is approximately 100x larger than the reactivity of the DD reaction in this temperature region. Reproduced from [13]

of the beam of runaway electrons. The expected runaway beam current in ITER predicted to carry up to 70% of the pre-disruptive current and the energies of the electrons (already measured at many devices these days) are in the order of tens of MeV [15]. In recent experiments and modelling efforts even full conversion of plasma current into the runaway electron current was observed, although perhaps with lower energies in this case. The physics of the runaway electrons is not yet fully understood and the diagnostics development and experimental investigation are being intensified in the recent years due to the urgent need to secure safe operation of ITER either completely without runaway electron beams or with a reliable mitigation method in the case that the runaway beam generation cannot be avoided. Runaway electron experiments present also an important part of the experimental program at the COMPASS tokamak [16, 17, 18, 19, 20, 21, 22] as well as programs of

majority of the tokamaks in the world. To simplify the problem as much as possible, we can say that runaway electron beam presents a dangerous phenomenon that can take over some part of the plasma thermal, but namely magnetic energy during the rapid plasma discharge termination and focus the destructive power. Therefore it is needed to either reliably stop its creation or to be able to convert its energy to a less destructive form (IR-VIS-UV radiation) or at least spread the deposition to the wall in time and/or area. From a point of view of physics interest and diagnostics, it is important that such relativistic electrons produce hard X-ray photons due to interaction with plasma and wall nuclei and these photons can be easily detected. The presence of high HXR flux may also trigger a giant dipole resonance in the nuclei of some isotopes and cause generation of photo-neutrons. Moreover, it was calculated that a beam of runaway electrons together with a good confinement may turn the tokamak into a source of positrons (i.e. the beam electrons have sufficient energy for e^-e^+ pair creation) [23], however this interesting fact is not yet confirmed experimentally.

1.4 Work of the author and outline of this thesis

This thesis is a report of the work of the author in the field of runaway electron physics. It mostly contains an analysis of the selection of experimental results achieved during the 12 dedicated runaway electron campaigns conducted at the COMPASS tokamak where the author has been proponent and coordinator of the experiments. The COMPASS data analysis is complemented by a selection of experimental results and analysis of the JET tokamak data as the author actively participated as diagnostics coordinator of the runaway electron experiments at this European machine. Furthermore, the thesis briefly mentions the participation of the author in the runaway electron programs at TCV and AUG tokamaks where the author acted as a scientific coordinator in some sessions of the RE experiments. Within the work on this thesis, several numerical models and data analysis tools were developed and other advanced numerical models available in Europe were applied to relevant experimental data. The work on the thesis also included numerous hardware installations, calibrations and developments of diagnostic analysis methods, some of them described in the text. During the doctoral studies, the author was working on several other topics that are not included in this thesis but did bring important broader image and valuable experience to the author. These topics include namely - neutron diagnostics, plasma tomography for different scenarios like radiation of heavy impurities, plasma control and tokamak design including namely structural simulations and material properties of the coil support structure. Furthermore, the author has been teaching introductory student courses, giving popular fusion talks, leading excursions

to COMPASS facilities, co-organising international meetings, etc.

The thesis is organised as follows. In the second chapter which follows the introduction, the basic overview of the theoretical background of runaway electron physics as well as common experimental practices is given, starting with simple relations regarding runaway electron current and energy and continuing with different methods of runaway electron description, generation mechanisms and interaction with the environment including generation of radiation and secondary particles. In the third chapter, the diagnostics tools and methods are described including the work of the author in the HXR analysis, tomography or gas valve calibration and the chapter is concluded by brief list of applicable modelling tools as some of these were used within the scope of this thesis. The fourth chapter describes the diagnostics setup and the operation scenarios run at COMPASS within the runaway electron studies and common points with scenarios run at other European tokamaks, namely TCV, ASDEX Upgrade and JET. The chapter is complemented by the Appendix C which contains overviews of last 8 RE campaigns conducted on the COMPASS tokamak with diagnostics installation schemes, range of pulses and brief summary of results. The fifth chapter is focused on the analysis of the non-disruptive RE scenarios, namely the RE generated in the beginning of the discharge. The phenomena of start-up RE is studied by the means of dedicated experiments, statistical analysis and also modelling. The second part of the chapter is focused on periodic losses of RE due to various instabilities during the discharge, including oscillations provoked by coil power sources and natural plasma instabilities. The sixth chapter is entirely dedicated to the RE beam equilibrium. Specifically, it is compared to the standard high temperature plasma equilibrium and the applications on the COMPASS tokamak are shown. This includes the improvement of radial position control and simple estimates of total kinetic energy, the calculation of the magnetic fields from the RE beam and passive structure were possible using the Biot-Savart tool further described in Appendix D. The seventh, final chapter describes the most interesting results achieved during RE beams generation using massive gas injection on COMPASS. This includes namely the use of the equilibrium-based estimates and other diagnostics analysis relevant in the context of the thesis that allowed for comparison of the effects of various gas amounts and species. Similar analysis is performed on the RE beams generated and affected by massive gas injection and shattered pellet injection at JET. The results described in the final 3 chapters are complemented by the results published in the attached impact journal and conference papers and other listed publications with the contribution of the author. The thesis is finalised with the conclusions chapter.

Chapter 2

Runaway electron physics

Runaway electrons (REs) may appear in tokamak plasmas in the case that the electric force accelerating the electrons - that is present due to Ohmically driven current - is not sufficiently compensated by the Coulomb drag force. This is true for a part of electron distribution that is faster than a certain critical velocity (a parameter dependent on density and electric field). The situation that critical velocity is comparable to thermal velocity may occur in case of low density plasmas - which is not the case in reactor relevant plasma - or due to high electric field that is easily created during the sudden termination of a discharge and decay of the Ohmic plasma current (a disruption). Some important aspects of the RE physics are described in master thesis of the author [19] or in PhD thesis of Miloš Vlaineić that focuses namely on the experimental analysis of the COMPASS data [20]. In the following sections the most important RE description methods and RE physics features are reminded and the most recent developments in the theoretical approach to the field are briefly described.

2.1 Magnetic field configuration of the tokamak

Runaway electrons exist within the magnetic configuration of the tokamak and are strongly affected by its topology. Therefore, it is worth reminding the basic principles of this magnetic configuration at this stage. The tokamak plasma and vessel are characterised by a toroidal shape, with the minor radius a , major radius R_0 . The main directions are toroidal (along larger

circumference) and poloidal (along minor circumference). The main parts of the tokamak assembly are displayed in the left part of the figure 2.1.

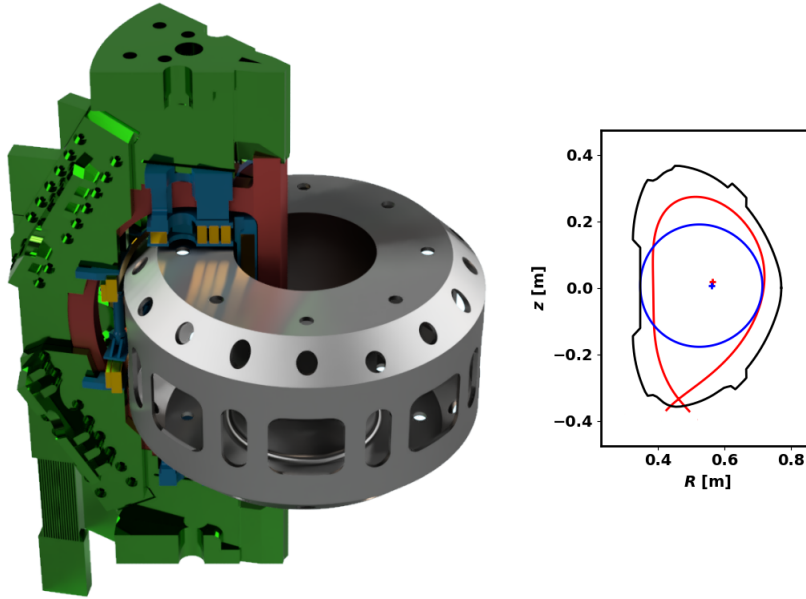


Figure 2.1: Left: The main parts of the tokamak - vacuum vessel in silver; toroidal sector of an early design of COMPASS-U: poloidal field coils in yellow, toroidal field coils in red, support structure of the poloidal field coils in blue and main support structure in green; rendered using Fusion 360, Right: Limiter (blue) and divertor (red) configurations of the plasma boundary in the COMPASS tokamak poloidal cross-section

Tokamaks are characterised by a strong toroidal magnetic field B_t of the order of units of Tesla. This field secures that the charged particles are revolving on a helical trajectory around a closed field line with a relatively small Larmor radius of the order of millimeters (fast electrons) or centimeters (fast ions). Due to the geometry of the toroidal field coils, that are closer to each other at the inboard side of the tokamak, the B_t decreases with major radius of the machine R as

$$B_t = \frac{B_0 R_0}{R}, \quad (2.1)$$

where B_0 is the toroidal magnetic field value on the vacuum vessel toroidal axis (or in case of definition using particular magnetic equilibrium, the value at the magnetic axis). Because of this dependence, B_t at the inboard side is stronger and this region is called the high field side (HFS), while the outboard side is called the low field side (LFS). The gradient caused by this dependence is also an important feature of the tokamak geometry and source of particle drifts together with the curvature of the closed field lines.

The configuration formed by the toroidal field only would result in a charge separation through the ∇B and curvature drifts [3] and subsequent radial loss of the plasma ring confinement. The additional poloidal field that allows for canceling the spacial charge by connecting the HFS and LFS is introduced namely by the induced current in the plasma ring. The current is induced by the transformer effect from the change of current in the primary winding. The configuration with combined toroidal and poloidal field has helical field lines that revolve both along the toroidal and poloidal directions. To stabilise the plasma ring against radial expansion that naturally arises with the toroidal current (hoop force) and thermal plasma pressure, external vertical field from a set of ring coils is introduced. The cross-section shape can be further modified by other ring coils with current direction parallel or anti-parallel to the plasma current. In this configuration, plasma is in force equilibrium with the field of external coils and contact with the plasma facing components can be optimised. The tokamak magnetic configuration of arbitrary cross-section shape, including the plasma boundary, is typically described using the poloidal magnetic flux function Ψ which is constant on toroidal (flux) tubes - i.e. concentric curves on the poloidal cross-section - and the plasma parameter profiles can be defined as a simple functions of Ψ , for more details of the concept see chapter 3 of[3].

Two main configurations with respect to the plasma-wall interaction can be distinguished: limiter and divertor configuration, see the right part of figure 2.1. In the limiter configuration, the separatrix or last closed flux surface (LCFS) of the plasma is defined by a flux contour that touches the plasma facing components (PFCs) in a narrow region on the poloidal cross-section, i.e. a circle in the full 3D geometry. This configuration is dominantly used for plasma start up, controlled termination of the discharge and also for most of the RE experiments at the current devices. The plasmas can be limited at the HFS or the LFS. The other configuration is called the divertor configuration and is characterised by a X-point in the flux contour map where poloidal field is zero. In this configuration the plasma from the confined volume has no direct contact with the wall, however there are still significant fluxes of the lost particles at the strike points where the last closed flux surface that contains the X-point intersects the wall. Much less RE experiments were done in this configuration worldwide, although it is the selected configuration for ITER and most probably disruptions will occur from this configuration. However, the tokamak plasma has always been initiated in a limiter configuration and therefore such configurations have to be studied as well. Various modifications of the divertor configuration were tested in order to spread the heat-loads from lost particles across larger area of the PFCs (sweeping of the strike points in time, increasing the number of strike points or increasing the footprint) or in order to increase the radiated energy before the lost particles hit the wall (prolonging the divertor leg or introducing a heavier gas like N or Ne into the divertor to increase the radiation cooling). The description of the general features of the tokamak physics can be found in book [3].

2.2 Simple estimate of RE parameters

In order to identify runaway electrons in the tokamak and roughly estimate their parameters, it is not necessary to dive too deep in the first principle physics while such estimates may be very important in designing control algorithms or taking decisions in the design of the tokamak systems.

2.2.1 Plasma and runaway electron current

The currents in the tokamak can exist due to multiple causes. The standard toroidal plasma current follows the Ohm's law with Spitzer resistivity that is a function of temperature T_e and effective charge Z_{eff}

$$Z_{\text{eff}} = \frac{\sum Z_i n_i}{n_e}, \quad (2.2)$$

where Z_i and n_i are charge numbers and density of all ion types present in plasma and n_e is the electron density. The resistivity is defined as

$$\eta_{\parallel}^{\text{Spitzer}} = \frac{\sqrt{2m_e} Z_{\text{eff}} e^2 \ln \Lambda}{12\pi^{3/2} \epsilon_0^2 T_e^{3/2}} \times F(Z_{\text{eff}}), \quad (2.3)$$

where m_e is the electron mass, ϵ_0 the permittivity of the vacuum, e the electron charge and $\ln \Lambda$ the Coulomb logarithm that depends on Debye shielding length and Coulomb collision properties and is defined e.g. in [24]. $F(Z_{\text{eff}})$ is defined as $F(Z) = \frac{1+1.198Z+0.222Z^2}{1+2.966Z+0.753Z^2}$ and describes the relation of the parallel and perpendicular resistivity $\eta_{\parallel} = \eta_{\perp} F(Z)$. [25] Other correction factors are also introduced for the toroidal geometry. The generalised Ohm's law in plasma without motion then reads

$$j = \sigma E = 1/\eta_{\parallel}^{\text{Spitzer}} E \quad (2.4)$$

where j is the current density, E is the electric field and $\sigma = 1/\eta$ is the plasma conductivity. The relation is valid also for the total Ohmic plasma current I_p and the loop voltage U_{loop} , $I_p = \frac{1}{R_{\Omega}} U_{\text{loop}}$ and can be obtained after multiplication of the (2.4) by the cross-section area of the plasma A . In reality, all the parameters included in (2.4), are strongly dependent on the position in the plasma, especially along the minor radius coordinate, the 0D representation described here presents significant simplification based on suitably averaged values that may require additional numerical corrections depending on the profile of the parameters. The Ohmic current component in

the tokamaks can be described using this simple model. However, in toroidal geometry a self-generated current - the bootstrap current - connected with the pressure gradient and particles trapped in the magnetic mirror naturally arising from the toroidal geometry may carry a significant percentage of the total current. Additional current density fraction may be also driven by the auxiliary current drive and heating methods (e.g. electron cyclotron current drive.) All these effects are desirable and help to spare the Voltseconds of the primary circuit. On the other hand, the runaway electrons can carry current without any external drive once they are generated. The amplitude of the current density of the runaway electrons is given by their number density n_{RE} and velocity v exclusively.

$$j_{RE} = en_{RE}v, \quad (2.5)$$

this further simplifies in the ultra-relativistic case with v approaching a constant speed of light c and RE current is then directly proportional to the RE density. The practical consequence of this fact is that in case of constant plasma current feedback control, RE presence can be registered by drop of the required loop voltage. When the Ohmic and runaway electron currents are considered together, total current density is represented by the simple sum

$$j_{tot} = \frac{1}{\eta}E + en_{RE} \langle v \rangle. \quad (2.6)$$

If all included quantities are measured with sufficient precision, the fraction of current carried by RE can be also calculated. The runaway electron beam is then a phase of the tokamak discharge in which the shear majority of the current is carried by the runaway electrons. During this phase the companion plasma temperature is several orders of magnitude lower than in a normal Ohmic tokamak discharge. Under these circumstances the runaway current is directly measured by the plasma current diagnostics. The runaway current can range from barely measurable values up to MA intensities.

■ 2.2.2 Magnetic energy of the runaway electrons

The runaway current directly determines the magnetic energy stored in the poloidal field of the current loop in the same way as in the case of Ohmic plasma current

$$W_{mag} = \frac{1}{2}LI_{RE}^2. \quad (2.7)$$

It is obvious that the magnetic energy rises quickly with the current. The inductance in the case of plasma or runaway electron beam has two components $L = L_i + L_e$. L_i is the internal inductance related to the plasma volume and the current profile shape, the complementary external inductance L_e represent inductance of the toroidal current loop. Typically, the magnetic

energy of the plasma or RE ring may reach multiple kJ at small machines up to 0.5 GJ for the ITER plasma. Via the mechanism of electromagnetic induction and runaway electron losses and generation the magnetic energy can be converted to the kinetic energy: by acceleration of fast electrons due to decreasing current inducing electric field - or vice versa -by loss of fast electrons and generation of new low energy runaway electrons or increasing Ohmic plasma current contribution.

2.2.3 Loop voltage and kinetic energy

The loop voltage is naturally present in the tokamaks as the plasma current is very important component of the magnetic equilibrium. The loop voltage is either driven by the change of current in the central solenoid or by fast change of current in the plasma and it is the primary source of accelerating force producing the runaway electrons. Loop voltage can be easily measured by a flux loop parallel to the plasma ring, however this measurement gives only a very rough estimate on what is happening inside the plasma. The integral of the loop voltage along the path of a test particle gives the upper margin and a very crude estimate of the energies that may be achieved. There are many mechanisms that counter-act this accelerating force, most of them will be discussed in the further text. In the ultra-relativistic case, we can consider the energy gain of the RE to be equal to

$$\Delta E_k = c \int \frac{U_{loop}}{2\pi R} dt. \quad (2.8)$$

This means that the maximum available energy is proportional to the flux swing (in the tokamak jargon also called "available Volt-seconds") of the machine. On COMPASS this gives roughly larger tens of MeV of RE energy provided that the electrons have been accelerated from the beginning of the discharge. The fast decay of a 15 MA plasma current in ITER can theoretically bring much larger energies, however other limiting factors will apply.

The total kinetic energy of RE beam or RE population within thermal plasma is then given by the integral of the single particle energy across the distribution function, or simply a product of an average energy per particle and the number of RE.

$$W_k = \int f(\mathbf{v}) m_{e,0} c^2 (\gamma - 1) d\mathbf{v} = \langle E_k \rangle N_{RE}. \quad (2.9)$$

Thanks to the relation of the runaway electron number and current, the total kinetic energy is also proportional to a product of the I_{RE} and the $\langle E_k \rangle$. Therefore, total kinetic energies of multi-MA RE beams with average energy in the order of tens of MeV reach the order of units to tens of MJ.

2.3 Discharge scenarios and phases prone to the RE generation

During the tokamak discharge, RE are most likely to be generated in three scenarios: plasma initiation - breakdown, low density discharge phases that may arise from an error of density control and a mitigated or unmitigated disruption.

2.3.1 Plasma start-up

The start-up of the tokamak discharge relies on an inductive plasma breakdown in most machines. The voltage allowing the breakdown does not have to be very large, as the connection length from the center of the vessel to the limiter can be very long thanks to the present B_t . An optimum of the pre-fill gas pressure p , stray poloidal field B_s in the vicinity of the magnetic axis and the toroidal electric field E_{tor} need to be achieved in order to initiate the plasma formation. Then a small amount of free electrons may multiply by the Townsend avalanche. The length of the open field line that the electrons follow is sufficient for securing multiple collisions leading to ionisation and continuous acceleration of the electron at the same time. The operational space within the three selected parameters for a model case of the COMPASS-U tokamak is displayed in figure 2.2. The effective connection length is calculated as

$$L_f = 0.25a \frac{B_t}{B_s}, \quad (2.10)$$

that means a quarter of the minor radius times ratio of main toroidal field over the poloidal stray magnetic field. Typically, the vertical component of the stray magnetic field is dominating across the plasma cross-section due to the geometry of the external poloidal field coils and namely the conductive structures. The required electric field \mathcal{E} can be calculated according to the formula [26] for pre-fill pressure p and open field line/effective connection length L_f :

$$\mathcal{E}_{\text{avalanche}} \left(\text{Vm}^{-1} \right) \geq \frac{93.8 \times p}{\ln(3.83 \times p \times L_f)}. \quad (2.11)$$

The electron and ion density is quickly increasing and the closed field lines and flux surfaces are soon formed, however this situation with elevated electric field and rapidly evolving density and temperature that cannot be precisely controlled is an obvious potential source of runaway electrons. It seems that

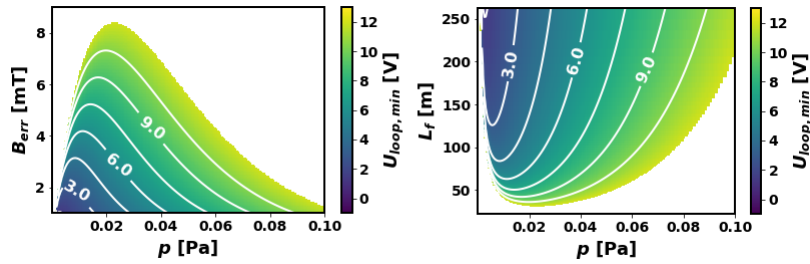


Figure 2.2: The diagram of parameter combination for a successful breakdown in a machine with $B_t = 5\text{T}$, $R = 0.9\text{m}$ and $a = 0.28\text{m}$. The necessary breakdown voltage is shown as a function of the pre-fill pressure - x-axis - and the stray magnetic field value (left) connection length (right) - y axis.

the density evolution in several tens of ms just after the breakdown is of importance and sufficient source of neutral gas needs to be present to avoid the RE generation. The situation might worsen due to presence of impurities which was one of the main reasons for the regular RE appearance in the early tokamaks. Details of the experimental analysis of breakdown RE are discussed in chapter 5. RE-free breakdown often requires some optimisation, however it can be relatively easily achieved by modifying the gas puff wave forms on most machines, see e.g. [18]. On the other hand this can be problematic in ITER as the technical constraints of the powerful superconducting coils and very thick conductive vessel with a long time constant do not allow significant toroidal electric field and thus the breakdown must be conducted under a very low pre-fill pressure. This is why the issue of the start up runaway electrons is still studied in present devices.

2.3.2 Low density discharges

Naturally, the condition for generation of the RE can be satisfied by lowering the density in a quiescent phase of a normal plasma discharge where constant electric field is applied for sustaining the plasma current. This can happen artificially to study the RE or to allow a transition of the plasma to a special confinement mode that may be achieved only with low density. However, at large machines controlled approach of critically low densities is avoided and this situation may arise only due to severe failure of the density control system. The probability of such failure is typically very small as the control system is often backed up both on the side of the diagnostics - e.g. multiple interferometer lines-of-sight and actuators - multiple gas injection valves or pellet launching systems. Furthermore, when a failure of a significant part of the density control systems is detected, the discharge can be terminated in a controlled way. For example, the RE generation due to the density control system failure has occurred in one discharge in the modern history of largest

operating tokamak - JET, this event is documented in [27].

■ 2.3.3 Disruption

The disruption is a sudden discharge termination that can have various causes and is always characterised by

- pre-disruption phase - a plasma discharge phase that is already affected by a critical instability or plasma parameter value outside the stable part of the operational space of the tokamak that leads to the collapse of the temperature profile or loss of macroscopic plasma stability
- thermal quench (TQ) - fast loss of thermal energy, temperature profile can collapse within 1 ms even at larger machines
- current quench (CQ) - loss of plasma current, slower than TQ with characteristic times given by the resistivity of the cooled plasma. This phase lasts typically units to hundreds of ms depending on the size of the machine. The fast decay of the current induces large toroidal electric field that is an important ingredient for RE generation.

In case that the runaway electrons are produced during this event, two other phases are typically distinguished

- Runaway electron plateau - a phase following the incomplete current quench when all the measured current may be carried by the runaway electrons, it may have constant current, however the term is used in a case of a gradually decreasing or increasing current as well.
- Runaway electron beam termination - the final stage when RE beam energy is dissipated. It can take either a very devastating form of a direct wall impact or decay via another mechanism may occur.

The sketch of the evolution of main parameters of interest for the cases of disruption with and without the RE beam generation with annotated phases of the phenomena is shown in figure 2.3, based on the parameter evolution in suitable JET discharges. The generation of the runaway electron beam during the disruption is considered to be the most dangerous phenomena, however not all disruptions are prone to RE beam formation. Density limit,

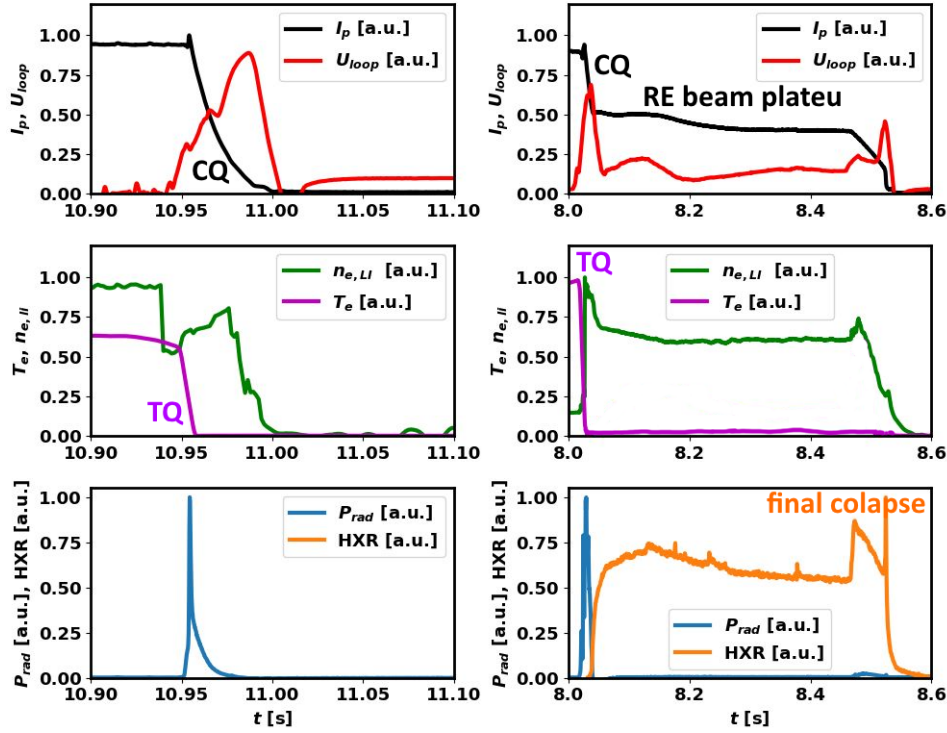


Figure 2.3: Evolution of plasma parameters of interest - plasma current I_p , loop voltage U_{loop} , line integrated electron density $n_{e,li}$ and electron temperature T_e , radiated power P_{rad} and hard X-rays (HXR) for a mitigated disruption without the RE generation (left column) and with the RE beam generation (right column). The increased HXR signal shows presence of the runaway electrons and the phases of the discharge termination are indicated. Example based on relative parameter evolution in JET discharges #96877 a #95132

critical MHD instability, e.g. large magnetic islands and sudden or gradual impurity influx are among the most usual disruption causes. The effects of the disruptions present a large risk to the tokamak even without the generation of the runaway electrons - the thermal loads from plasma particles and radiation are large, in case of position instability so called halo currents may be driven through the vessel and plasma facing components and impose extreme forces especially if these currents are perpendicular to the magnetic field. Due to the rapid loss of the plasma current also the forces acting on the coil system are subject to very fast changes. Therefore, the large machines are equipped with a disruption mitigation system that is primarily based on the injection of a large amount of gas mixture which includes higher Z noble gas to increase the radiated fraction of the lost plasma energy. Unfortunately, such mitigation strategy may push the conditions closer to the RE generation region. Therefore post-disruption RE are intensively studied at current experimental devices and extrapolation to large ITER plasmas is conducted using advanced models.

2.4 Description of runaway electrons in the plasma

The runaway electrons present a species with different properties compared to the thermal plasma particles. Most importantly relativistic approach becomes unavoidable for their description, while for the thermal tokamak plasma ions and electrons classical description is completely sufficient. Furthermore, the large absolute values of energy and possibly complicated shape of the distribution function of the runaway electrons require a more detailed description than simple fluid approach in order to correctly characterise the population. For detailed calculation of the trajectories of small part of particles, full orbit or gyro-averaged test particle description can be used, however close collisions are usually neglected in this approach or Monte Carlo approach needs to be implemented. In the case of a phenomena strongly related to the velocity distribution and involving many particles, the kinetic description is the best option. While very simple calculations that may help to interpret the tokamak experiments can be done using the fluid approach. In the following subsections, the main equations and methods of these approaches along with some of the latest developments are introduced.

2.4.1 Test particle description

The motion of the runaway electrons or other particles in magnetised plasma in the tokamak configuration can be simplified based on the ordering of the characteristic time scales, e.g. in [28]

$$\tau_{cy} \ll \tau_b \ll \tau_{coll}, \tau_{rad}, \tau_{acc} \quad (2.12)$$

which means that the characteristic collisional, acceleration and radiation times of a RE are much longer than poloidal transit (bounce) characteristic time τ_b and gyration time τ_{cy} - periods related to phenomena that are further described below. When these conditions are valid trajectory simplification can be achieved by averaging out these periodic motions.

Full orbit description

The full-orbit test particle description is given by the solution of the Lorentz equation for particle moving in external electric and magnetic fields, which in its relativistic form reads

$$\frac{d}{dt}(m_0\gamma\mathbf{v}) = Q\mathbf{E} + Q\mathbf{v} \times \mathbf{B} \quad (2.13)$$

and can be derived empirically or from the relativistic Lagrangian that includes both particle part and interaction with the magnetic field

$$L = L_P + L_{\text{int}} = -m_0 c^2 \sqrt{1 - \mathbf{v}^2/c^2} - Q\phi + Q\mathbf{A} \cdot \mathbf{v} \quad (2.14)$$

The full orbit motion is composed of the motion along the magnetic field line and revolution around it, which results in helical motion of the particle. As the electric but namely magnetic field structure in the tokamak can be very complicated, the trajectories of the electrons must be simulated numerically. The full orbit description of the particle trajectory is not suitable for simulations of phenomena on longer timescales as typical time step to follow the motion is of the order of 10^{-12} s.

■ Gyro-averaged description

However, the revolution of the electron around the field-line (gyration) can be averaged out under certain conditions. Then, the motion of the gyro-center is followed which still captures the drift motion or the trajectories of trapped particle in magnetic mirror configuration which may arise in the tokamak. The most important condition to apply this averaging is that magnetic field changes are negligible on the space scale of the Larmor radius and time scale of the gyration period. This is fulfilled for slow electrons, however it can be violated for very fast electrons and perturbed field which is the case of the disruption. The relativistic guiding center Lagrangian was derived by Wimmel in [29], and discussed in detailed e.g. in RE physics overview paper [30], where the following form is discussed

$$L = \frac{e}{c} \left[\mathbf{A} + \frac{mc}{e} u_{\parallel} \mathbf{b} \right] \dot{\mathbf{X}} + \frac{m^2 c}{2e} J_{\perp} \dot{\zeta} - e\Phi - mc^2 \sqrt{1 + \frac{u_{\parallel}^2}{c^2} + \frac{J_{\perp} B}{c^2}}, \quad (2.15)$$

with $\dot{\mathbf{X}}$ describing the guiding center motion, u_{\parallel} is velocity parallel to the magnetic field, ζ is the gyro-phase and J_{\perp} a relativistic form of the adiabatic invariant closely related to the magnetic moment of the particle with implicit definition

$$J_{\perp} = \mu \frac{2}{m} \sqrt{1 + \frac{u_{\parallel}^2}{c^2} + \frac{J_{\perp} B}{c^2}}. \quad (2.16)$$

The exact relation of the u_{\parallel} to parallel component of the guiding center velocity $\dot{\mathbf{X}}$ is then given by:

$$(\mathbf{b} \cdot \dot{\mathbf{X}}) = \frac{u_{\parallel}}{\sqrt{1 + \frac{u_{\parallel}^2}{c^2} + \frac{J_{\perp} B}{c^2}}}. \quad (2.17)$$

This formulation follows the Liouville theorem and allows introduction of guiding-center kinetic description. Furthermore, formulation using canonical coordinates can be achieved using the magnetic field geometry of the tokamak [30]

$$B_\varphi = B_0 R_0 / R; B_\theta = B_0 \frac{r^2}{R_0 q(r)} \left(1 - \frac{r}{R_0} \cos \theta + \Delta' \cos \theta - \int_0^r \frac{\Delta'_1}{r_1} dr_1 \cos \theta \right), \quad (2.18)$$

where r is the minor radius coordinate, $q(r)$ is the safety factor indicating the helicity of the field lines and $\Delta(r)$ is the Shafranov shift and quantities with index 1 are denoting the integration variable r_1 and functions of this variable. Using this description, the toroidal angle ϕ , poloidal angle θ and gyro phase ζ can be used as Canonical variables and

$$\begin{aligned} P_\varphi &\equiv \frac{e}{c} \left[A_\varphi + \frac{mc}{e} u_\parallel \frac{B_\varphi}{B} \right], \\ P_\theta &\equiv \frac{e}{c} \left[A_\theta + \frac{mc}{e} u_\parallel \frac{B_\theta}{B} \right] \\ P_\zeta &\equiv \frac{m^2 c}{2e} J_\perp \end{aligned} \quad (2.19)$$

as the canonical momenta. In these variables the Lagrangian and Hamiltonian of the guiding center orbit take a simple form of

$$\begin{aligned} L &= P_\varphi \dot{\phi} + P_\theta \dot{\theta} + P_\zeta \dot{\zeta} - H, \\ H &= e\Phi + \sqrt{m^2 c^4 + c^2 \left(P_\varphi - \frac{e}{c} A_\varphi \right)^2 \left(\frac{B}{B_\varphi} \right)^2 + m^2 c^2 J_\perp B} \end{aligned} \quad (2.20)$$

The toroidal canonical momentum P_ϕ , perpendicular adiabatic invariant J_\perp and the energy given by the Hamiltonian H are relativistic invariants. The guiding center orbits of RE are roughly copying the shape of the flux surfaces but are shifted to the LFS with respect to the flux surfaces. More specifically the passing electrons move along the surfaces of constant P_ϕ . The guiding center description can be used to track the particles in weakly perturbed fields, in certain synthetic diagnostics tools and similar applications.

■ Trajectory of one poloidal transit - bounce averaging

The gyration around the magnetic field line is not the only periodic motion that may be averaged out in certain situations. The two types of particle orbits

with respect to poloidal cross-section of the tokamak are both characterised by a specific frequency. The passing orbits which complete the motion along the poloidal circumference of the plasma are characterised by frequency of this poloidal revolution $\omega_{pol} = v_t \pi R_0 q$, where v_t is the toroidal component of parallel velocity. The trapped particle (banana) orbits are characterised by a turning point in the region of increased B_t and can be described by frequency of oscillations between these turning points. $\omega_b = \sqrt{\frac{\epsilon}{2}} \frac{v_\perp}{qR}$, where r and R are minor radius of the particle gyro-center position and major radius of the magnetic axis, respectively, $\epsilon = r/R$, q is the safety factor or inverse helicity of the magnetic field lines and v_\perp perpendicular velocity of the particle. Averaging over the poloidal angle is of course possible only in case that the observed phenomena has smaller characteristic frequencies than these two frequencies ω_{pol} and ω_b . This approach is especially needed in simplified kinetic simulations. When the poloidal angle is averaged out, the only remaining spacial variable is the radial position of the particle r which is related to drifts and other transport phenomena.

2.4.2 Kinetic description

To describe a process where significant population of RE is involved, even the guiding center or bounce averaged particle modelling approach does not present sufficient simplified description. Runaway electrons as well as other plasma particles can be described by probability distribution in the (\mathbf{x}, \mathbf{v}) -space or (\mathbf{x}, \mathbf{p}) -space. The Boltzman equation describes the evolution of the distribution function

$$\begin{aligned} \frac{\partial f}{\partial t} + (\mathbf{v} \cdot \nabla_{\mathbf{x}}) f + \left(\frac{\mathbf{F}}{m} \cdot \nabla_{\mathbf{v}} \right) f &= C + S \\ \int f(t, \mathbf{x}, \mathbf{v}) d^3 \mathbf{v} &= n(t, \mathbf{x}) \end{aligned} \quad (2.21)$$

where S is the source term which can be related to particle injection or losses and C is the collisional operator. In the Fokker-Planck equation, the collisional operator describing small angle collisions is implemented. This description is suitable for the Coulomb collisions in plasma as the electrostatic force acts over long distances and the probability of the close collisions is relatively low. Using the general formulation of Fokker-Planck equation and the specific properties of the Coulomb interaction in plasma [24] the non-relativistic Fokker-Planck equation for distribution of the particle species

α reads

$$\begin{aligned} \frac{\partial f_\alpha}{\partial t} + (\mathbf{v}_\alpha \cdot \nabla_{\mathbf{x}}) f_\alpha + \left(\frac{\mathbf{F}_\alpha}{m_\alpha} \cdot \nabla_{\mathbf{v}} \right) f_\alpha &= \sum_{\beta} S_{\alpha\beta} \\ S_{\alpha\beta} &\equiv K \ln \Lambda_{\alpha\beta} \left[-\nabla_{\mathbf{v}} \cdot (f_\alpha \nabla_{\mathbf{v}} H_{\alpha\beta}) + \frac{1}{2} \frac{m_\beta}{m_\alpha + m_\beta} (\nabla_{\mathbf{v}} \nabla_{\mathbf{v}}) : (f_\alpha \nabla_{\mathbf{v}} \nabla_{\mathbf{v}} G_{\alpha\beta}) \right] \\ H_{\alpha\beta}(\mathbf{v}_\alpha) &\equiv \int \frac{1}{g} f_\beta d^3 \mathbf{v}_\beta, \\ G_{\alpha\beta}(\mathbf{v}_\alpha) &\equiv \int g f_\beta d^3 \mathbf{v}_\beta. \end{aligned} \tag{2.22}$$

$g \equiv |\mathbf{v}_\alpha - \mathbf{v}_\beta|$ is the mutual velocity of colliding particles, m_α and m_β their masses. $H_{\alpha\beta}$ and $G_{\alpha\beta}$ are the Rosenbluth potentials describing the influence of the target particle population on the impacting particle distribution function - the first one is related to the collisional friction and the second one to the collisional diffusion. K is a constant calculated as $K \equiv \frac{1}{4\pi} \left(\frac{Q_\alpha Q_\beta}{\epsilon_0 m_\alpha} \right)^2 \frac{m_\alpha + m_\beta}{m_\beta}$ and $\Lambda_{\alpha\beta}$ is the Coulomb logarithm, i.e. logarithm of ratio of the Debye length as maximum interaction distance considered in the derivation and impact collision parameter leading to the deflection by 90° as the minimum considered distance, detailed definitions can be found e.g. in [24]. Both forms of the equation in velocity v and momentum p are used in the literature, the transformation is straightforward. The non-relativistic form of the equation can be still used for derivation of some characteristic properties of the non-relativistic part of the distribution that are relevant to RE as e.g. the Dreicer field and critical velocity under given circumstances. Using the equation 2.22, Maxwellian distribution of the target species f_β and mono-energetic test particle distribution as f_α , we can derive the Coulomb friction (drag) force from the first Rosenbluth potential, see e.g. [19] that is essential for the RE fluid description.

$$F_d = \frac{n_e e^4 \ln \Lambda}{4\pi \epsilon_0 m_e} \left[\frac{Z_{\text{eff}}}{v_{Ti}^2} \psi \left(\frac{v}{v_{Ti}} \right) + \frac{2}{v_{Te}^2} \psi \left(\frac{v}{v_{Te}} \right) \right]. \tag{2.23}$$

Where ψ is a Chandrasekhar function defined as

$$\psi(x) \equiv \frac{2}{\sqrt{\pi} x^2} \int_0^x \xi^2 e^{-\xi^2} d\xi, \tag{2.24}$$

that behaves as $1/x^2$ at large values of x . The two terms in (2.23) are corresponding to electron and ion terms. In the region of supra-thermal velocities of electrons, the contribution is comparable. [19] Using this drag force we can construct a simple equation of motion for the RE fluid represented by a single velocity v

$$\frac{\partial v}{\partial t} = \frac{eE}{m_e} - \frac{2e}{m_e} E_D \psi(v/v_{Te}), \tag{2.25}$$

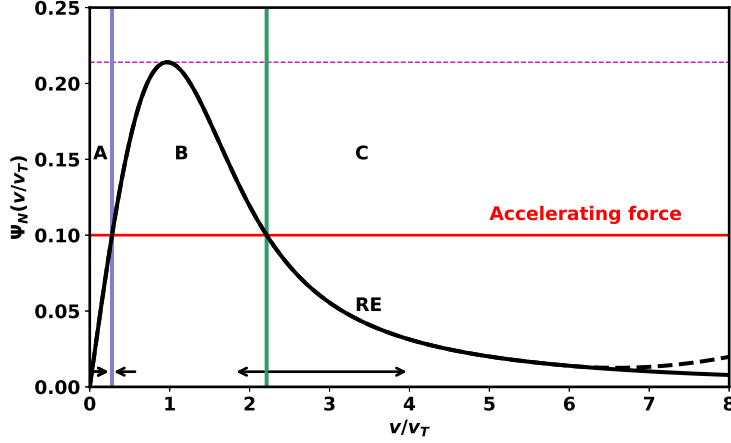


Figure 2.4: Scheme of the coulomb collision drag force and accelerating electric force acting on an electron in the tokamak, the Chandrasekhar function in black gives the collisional drag force and the dashed part is representing contribution of relativistic radiation to the drag, region C is the RE region where particles are accelerated to relativistic energies [19]

where $v_{T\beta}$ is the thermal velocity of target particles, E_D is Dreicer field, called critical field in the original paper [31] and that is defined as

$$E_D = \frac{n_e e^3}{4\pi\epsilon_0^2 k T_e} \ln \Lambda \quad \ln \Lambda = \ln \left(\frac{\lambda_D}{b_0} \right). \quad (2.26)$$

If the electric field reaches the value of $E_D \psi_D(1) \sim 0.43 E_D$ [32] where $\psi_D = 2\psi$ for the definition of ψ in eq. (2.24) accounting for different normalisation, all electrons are accelerated towards relativistic velocities as the electric force independent on the velocity overcomes the maximum of the friction force. On the other hand, from the relativistic point of view there is a minimum electric field for given density for which at least some electrons are accelerated, this limit is called the critical field, derived in [33] with introduction of the relativistic corrections

$$E_c = \frac{n_e e^3}{4\pi\epsilon_0^2 m_e c^2} \ln \Lambda. \quad (2.27)$$

The value of the critical field appeared to be higher in experiments which was explained by the energy dependence of the Coulomb logarithm, the radiation losses and namely the fact that for various pitch angles only the electric force component projected to the momentum vector direction is accelerating the relativistic electron and compensating for the energy losses [34, 35]. The electric acceleration and friction forces are plotted as a function of normalised velocity in fig. 2.4 for the non-relativistic case.

Derivation of the relativistic collisional operators is a challenging task, but has been achieved in a full non-linear form by Beliaev and Budker [36] and further developed in [37, 38]. The collisional operators for the specific

application were further exploited and implemented in a numerical code in [34]. This approach is working with equation for f in the form

$$\frac{\partial f}{\partial t} - \frac{e\mathbf{E}}{m_e c} \cdot \frac{\partial f}{\partial \mathbf{p}} + \frac{\partial}{\partial \mathbf{p}} \cdot (\mathbf{F}_s f) = C_{ee}\{f\} + C_{ei}\{f\} + S. \quad (2.28)$$

As can be seen compared to (2.22), the advection term is not considered, the second term on the right hand side is corresponding to the acceleration by electric field and the third term to other forces acting on the particle that are different from the collisional friction, e.g. relativistic radiation reaction force. The collisional operator C is divided to electron-ion and electron-electron parts. Electron-ion part is typically simplified based on the mass difference of the particles and thus no momentum transport from electrons to ions is considered. The approach used in [39] leads to five potentials that are analogous to two Rosenbluth potentials in (2.22) and that can be evaluated numerically. The non-linear approach is especially important in cases with highly distorted distribution function and high electric field.

In other cases, linearised variants of the collisional operators can be used. The derivation of linearised Fokker-Planck collisional operators is described in the thesis [35]. It results in using four specific collisional frequencies describing the processes that the distribution function may undergo: electron-electron slowing down frequency ν_S^{ee} describing collisional friction, electron-electron and electron-ion deflection frequencies ν_D^{ee} , ν_D^{ei} that lead to isotropisation of the distribution function and parallel momentum diffusion frequency ν_{\parallel}^{ee} that reduces any sharp gradients that may arise in the distribution function. Again, the fact that ions are much heavier than electrons leads to neglecting electron-ion slowing down frequency ν_S^{ei} and momentum diffusion frequency ν_{\parallel}^{ei} . The frequencies are defined in normalised relativistic momentum \bar{p} and normalised temperature $\Theta = \frac{T_e}{m_e c^2}$. For example the ν_S^{ee} reads

$$\nu_S^{ee} = \frac{1}{\tau_c} \frac{1}{\bar{p}} \frac{\ln \Lambda^{ee}}{\ln \Lambda_0} \Psi_S(\bar{p}, \Theta), \quad (2.29)$$

where $\tau_c = \frac{4\pi\epsilon_0^2 m_e^2}{c} n_e e^4 \ln \Lambda_0$ is the relativistic collision time, $\ln \Lambda^{ee}$ modification of the Coulomb logarithm based electron-electron collision properties and $\Psi_S(\bar{p}, \Theta)$ a special function [35] that can be simplified to a form shown below (2.30). These collision frequencies are apparently much more complicated than their non-relativistic counter-parts of course, however they naturally approach the non-relativistic limit that was described above and that acts in the equation of motion (2.25). This limit corresponds to Chandrasekhar function of variable $x = \bar{p}/\sqrt{2\Theta}$ that is also approaching the previously used variable $x = v/v_{Te}$ for non-relativistic speeds in figure 2.4. On the other hand in case that the γ factor of the studied RE population is much larger than the normalised temperature, the collision frequencies are simplified significantly

as well. In this way, the $\Psi_S(\bar{p}, \Theta)$ is reduced from its full linearised form as

$$\begin{aligned} \Psi_S(\bar{p}, \Theta) &\approx \frac{\gamma^2}{\bar{p}^2} \phi(x) - \frac{1}{\bar{p}^2} \sqrt{\frac{2}{\pi\Theta}} \bar{p} e^{-(\gamma-1)/\Theta} \\ &\rightarrow \begin{cases} \frac{\gamma^2}{\bar{p}^2}, & \gamma - 1 \gg \Theta, \text{ superthermal limit} \\ \psi(x)/\Theta, & \bar{p} \ll 1, \text{ non - relat. limit} \end{cases} \end{aligned} \quad (2.30)$$

The $\phi(x)$ is the error function that is closely related to the Chandrasekhar function as shown in [35] or [24]. The description using linearised collision operators is currently used in the state-of-the-art numerical codes, e.g. DREAM[40]. In this section, only the basic principles of the kinetic description of RE were briefly shown, for details see [35] and references therein.

2.4.3 Fluid description

The most simplified and the most practical approach especially for applications in interpretation of the tokamak RE experiments is the fluid description of runaway electrons. The method is describing the RE population as a fluid with specific properties, different than the thermal plasma. Total current can be then considered as a sum of plasma current and runaway current as in equation (2.6). This approach needs to be based on several results of the kinetic approach, especially growth rates of runaway electron population under given conditions and related to different generation mechanisms. These growth rates then increase the density of the RE fluid. The decay of the RE density is primarily related to different particle losses, caused e.g. by the magnetic field perturbations. The time derivative of the RE density can be then described as

$$\frac{\partial n_{RE}}{\partial t} = S_{dr} + S_{a_{h-t}} + S_{av} + S_{Comp} + S_{nucl} - S_{loss} \quad (2.31)$$

Where the S_x are the growth rates of different generation mechanisms that are described further and sinks related to RE losses. The equation of motion derived from the kinetic approach and described earlier (2.25) can be used to analyse the evolution of the RE fluid velocity or energy together with the density evolution. The electric force is responsible for the acceleration and collisional and radiation losses are responsible for the energy/velocity decay. The thermal plasma density and temperature can be also changed by different particle and heat sources and sinks related to the specific situation - e.g. various material injection methods. The thermal plasma equation of motion and heat equation together with e.g. a state equation would then complete the thermal plasma fluid continuum equations [24]. The two fluids - or three in case thermal plasma ions and electrons are treated separately - are coupled by the generation mechanisms, collisions and other less important energy and density transfer channels.

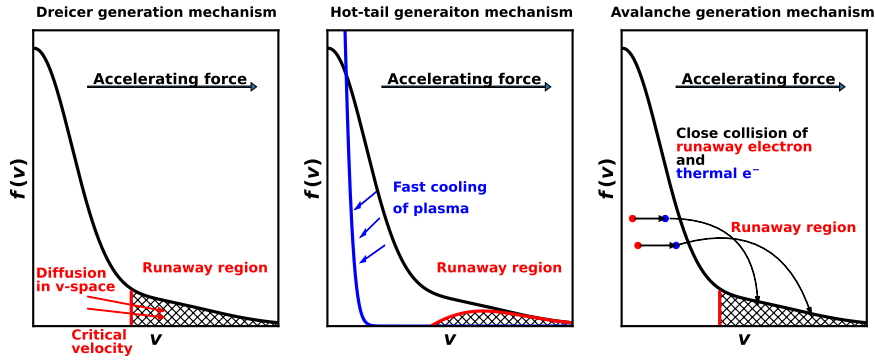


Figure 2.5: The three major generation mechanisms of RE (from left): Dreicer mechanism - the part of the distribution of electrons which is above the critical velocity is accelerated and new electrons are pushed to the runaway region; hot-tail mechanism - due to a rapid cooling, e.g. during a disruption, some electrons with too large collision time appear in the RE region; and the secondary-avalanche mechanism - an existing RE can knock-on a thermal electron to the runaway region

2.5 Generation mechanisms

The understanding of the different mechanisms of the RE generation is the key element in the runaway avoidance but also in the mitigation of already existing RE beam as generation of high energy electrons must be suppressed during the mitigation process which tend to create increased electric field in general. The generation mechanisms were also described in the master thesis of the author [19], the description here is more focused on the review of the recent developments in the field.

The three important mechanisms of runaway electron generation - the Dreicer mechanism S_{dr} , the hot-tail mechanism S_{h-t} and the avalanche mechanism S_{av} are briefly described in the further text and illustrated in a sketch 2.5, where the effect they have on the distribution function is shown. In a fusion reactor, these mechanisms might be accompanied by Compton scattering of HXR/gamma photons from neutron activation of surrounding solid elements S_{Comp} on plasma electrons and also by various nuclear sources of fast beta particles most importantly the Tritium decay, S_{nucl} . Although these two additional mechanism have low cross-sections, they may produce a seed for further amplification by the avalanche mechanism.

2.5.1 Dreicer generation mechanism

The Dreicer mechanism is related to the diffusion of the electrons in the velocity space if the collisional drag force is competing with an accelerating electric force. The generation rate of RE via the Dreicer mechanism is an extremely strong function of the electric field normalised by the Dreicer field. Furthermore, it is especially important to find the boundary of the runaway electron region from where the acceleration dominates. In order to do this, cross-section of electric acceleration and friction force curves from fig. 2.4 is found with the use of non-relativistic approach and super-thermal velocity approximation of Chandrasekhar function $\sim 1/x^2$. This approach is valid in case the electric field reaches a couple of percents of the Dreicer field and leads to the relation for the critical velocity

$$v_c = \sqrt{\frac{ne^3(1 + Z_{\text{eff}}/2)}{4\pi\epsilon_0^2 m_e E}} \ln \Lambda. \quad (2.32)$$

Every particle that is moving with the velocity higher than this function of density, electric field and impurities in the plasma is accelerated to relativistic velocities. The shape of the distribution function and number of particles above or in vicinity of this threshold decides about the number of runaway electrons generated by the Dreicer mechanism.

Dreicer generation rates

The formulas for the Dreicer generation rates were gradually improved in the past. The formula from Connor and Hastie [33] that is considering a relativistic correction to the original Kruskal-Bernstein generation rate

$$S_{\text{KB/NR}} = C\nu_{ee} \left(\frac{m_e c^2}{2T_e}\right)^{\frac{3}{2}} \left(\frac{E_D}{E_{\parallel}}\right)^{\frac{3}{16}(Z_{\text{eff}}+1)} e^{-\frac{E_D}{4E_{\parallel}} - \sqrt{\frac{(Z_{\text{eff}}+1)E_D}{E_{\parallel}}}}. \quad (2.33)$$

Where C is a scaling factor of a unit order. The relativistic correction has a form

$$S_{\text{R}} = S_{\text{NR}} e^{-\frac{kT_e}{m_e c^2} \left[\frac{1}{8} \left(\frac{E_D}{E_{\parallel}}\right)^2 + \frac{2}{3} \left(\frac{E_D}{E_{\parallel}}\right)^{3/2} \sqrt{1+Z_{\text{eff}}}\right]}. \quad (2.34)$$

It can be seen that these rates are exponentially sensitive to the electric field magnitude and depend on the temperature as well as the effective charge. In the recent years, these formulas have been modified especially with the treatment of partially screened impurities. Heavier impurity ions that do not completely ionise under given plasma conditions are partially screened by bound electrons during the interaction with the fast electrons and the degree

of the screening is dependent on the velocity of the impacting particle. In case of the Dreicer mechanism this effect is hard to describe analytically, however evaluation using runs of kinetic simulations and neural network has been performed in [41] and can be used in numerical tools like [40]. The Dreicer mechanism as a primary mechanism is important especially during start-up RE generation, during low density plasma discharges with the RE generation and in disruption RE generation with relatively colder pre-disruptive plasmas but higher electric field, e.g. during ramp-up phase without auxiliary electron heating at present machines.

2.5.2 Hot-tail mechanism

The hot-tail RE generation mechanism on the other hand is connected with the disruptions of high temperature plasmas. As mentioned in the previous sections, the thermal quench can be very fast reaching sub-ms time scales and if the tail of electron velocity distribution is energetic enough, the thermal quench time τ_{TQ} can be shorter than the average collision time τ_{coll} for these fast electrons. The situation is sketched in the central part of the fig. 2.5. We can assume the fast temperature change following the exponential decay

$$T_f = T_f + (T_0 - T_f)e^{-\frac{t}{\tau_{TQ}}}, \quad (2.35)$$

where T_f is the temperature after the thermal quench and T_0 is temperature of plasma before disruption. The RE source created in this way can be estimated based on the derivation done by Smith [42]. The temperature evolution 2.35 is applied together with v_c as the lower integration limit.

$$\frac{n_{ht}}{n_e} = \frac{4}{\sqrt{\pi}} \int_{v_c}^{\infty} \left(1 - \frac{(u_c^3 - 3\tau)^{2/3}}{(u_c^3 - 3\tau)^{2/3}} \right) e^{-u^2} u^2 du. \quad (2.36)$$

Here, $u = v/v_{T0} + 3\tau$, $u_c = v_c/v_{T0} + 3\tau$ and collisional time τ is obtained as a solution of differential equation in form $\tau(t) = (t - t_0)/\nu c^3 v_{T0}^3$, ν is the collisional frequency. Note that a different function for the temperature decay would result in a different formula. A more consistent approach combining the plasma energy density evolution based on radiation cooling and kinetic description for the supra-thermal electrons has been evolved recently in [43].

2.5.3 Secondary mechanism-avalanche

The secondary mechanism of runaway electron generation, also called the avalanche, causes amplification of the RE population from various primary

sources. Described by Rosentbluth and Putvinski in [44], the avalanche is a cumulative effect of so called knock-on collisions. These are collisions with small impact parameter and with large transfer of parallel momentum to a slow electron from the runaway electron. Obviously, this can result also in considerable pitch angle scattering of the impacting runaway electrons. However, in situation with considerable E/E_c , avalanche leads to exponential growth of the RE current, although average energy can be decreased [44]. The runaway electron generation in disruptions at large machines is dominated by this generation mechanism. The avalanche multiplication can be simply described as

$$\frac{\partial n_{\text{RE}}}{\partial t} = \Gamma n_{\text{RE}} \quad (2.37)$$

with Γ being the avalanche growth rate that can be related to electric field E and effective charge of the plasma Z_{eff} via [44]

$$\Gamma = \frac{e}{\ln \Lambda m_e c \sqrt{5 + Z_{\text{eff}}}}. \quad (2.38)$$

The effect of partially ionised impurity screening was added to the avalanche growth rates recently as described in [45] which modifies the avalanche growth rate in form

$$\Gamma = \frac{e}{m_e c \ln \Lambda_c} \frac{n_e^{\text{tot}}}{n_e} \frac{E_{\parallel} - E_c^{\text{eff}}}{\sqrt{4 + \bar{\nu}_s(p_{\star}) \bar{\nu}_D(p_{\star})}}, \quad (2.39)$$

where $\bar{\nu}_s(p_{\star}) \bar{\nu}_D(p_{\star})$ are normalised slowing-down and deflection collisional frequencies with correct implementation of partial screening, n_e^{tot} is the total (free + bound) electron density and formula for the electric field ($E_{\parallel} - E_c^{\text{eff}}$) secures that the growth rate vanishes at the effective critical field value which is a modification of (2.27). This formula converges to (2.38) in case of total ionisation. The modification causes a significant increase of the growth rate at higher electric fields and suggests that very high deuterium densities are necessary for suppression of the avalanche and the impurity injection can amplify the avalanche. As it delivers more potential targets for knock-on collisions and avalanche amplification in the form of bound electrons while the slowing down effect is limited due to the partial screening. The avalanche amplification factor of a RE seed during ITER disruption may reach up to 10^{20} or even more [41], which is one of the main reasons why REs are considered a very serious threat for ITER.

2.6 Background plasma and induced electric field

The background plasma co-existing with the runaway electrons needs to be taken into account not just as the medium that collisionally slows down the

runaway electrons but also as a current conducting medium with which the RE exchange energy through various channels. The main effect is that plasma with significant level of dust or impurities makes the background plasma resistivity large which can further increase the electric field/preference of the runaway current channel. This is important in both high temperature plasma with RE population (surviving start-up RE, high density) as in the post-disruptive plasma after impurity-mitigated disruptions. The post-disruptive background plasma is much colder than a typical tokamak plasma, typically just in the order of units of eV which makes it a very bad conductor as well as a hard-to-diagnose medium for the common tokamak temperature measuring apparatus. On the other hand, it is not excluded that the cold plasma may be reheated from the collisions with RE or that the low energy RE may eventually overtake majority of the current from the high energy ones. The power balance including different channels of energy transfer from the RE to background plasma and surrounding structures with the background plasma temperature estimated using the VUV measurement of argon radiation lines was presented in [46].

During the disruptions or decay of the RE beam current, electric field is induced, that can be described in a simple way, not taking into account possible profile variations, by

$$E_{\parallel}(r=0) = -\frac{1}{2\pi R} \frac{\partial LI_p}{\partial t} \approx -\frac{L}{2\pi R} \frac{\partial I_p}{\partial t}, \quad (2.40)$$

where R is major radius, L is flux inductance - ratio of poloidal flux at magnetic axis over total plasma current, special definition of inductance for this particular application used in [47],[35] and several other papers. It can be seen that fast current quench of a disruption can produce large electric fields but also too fast decay of current of an existing RE beam can cause additional acceleration of the high energy runaway electrons which is a drawback of certain RE mitigation methods.

2.7 Radiation of runaway electrons and production of secondary particles

The relativistic charged particles moving in external fields radiate as they are subject to acceleration. This radiation leads to a loss of RE energy and at the same time it presents a potential diagnostics method. The two most important sources of radiation and energy loss of runaway electrons are in-elastic collisions with ions, namely impurity ions, e.i. bremsstrahlung; and radiation due to curved trajectories of the electrons in the magnetic field, which is called synchrotron radiation. Synchrotron radiation is a continuous spectrum relativistic limit of the discrete spectrum cyclotron radiation. Due

to the relativistic velocities of the runaway electrons, both of these types of radiation are dominantly launched within along the immediate direction of motion of the electron, or within a small space angle around this direction. This creates a so called a headlight effect and the strong anisotropy is one of the most distinct features of the relativistic electron radiation, compared to the other sources of radiation in the tokamak plasma.

■ 2.7.1 Bremsstrahlung

The bremsstrahlung or braking radiation does occur in plasma also in case of thermal electrons and is responsible for radiation with continuous spectrum. The full derivation of the cross-section was done by Bethe, Heitler and Dirac in [48] and extended especially for the case of relativistic particles in [49], including the role of partial screening of ions. The spectral power density in case of thermal plasma bremsstrahlung is defined by formula

$$dP = 6.01 \cdot 10^{-30} \frac{gn_e^2 Z_{\text{eff}}}{\sqrt{T_e \lambda^2}} \exp\left(-\frac{12.40}{T_e \lambda}\right) dV d\lambda \left[\frac{W}{\text{cm}^3 \text{\AA}}\right] \quad (2.41)$$

where g is the quantum correction - the Gaunt factor and λ the wavelength. Through the Z_{eff} this formula shows a quadratic dependence on impurity charge. A beam of relativistic electrons is a subject to similar dependencies with relativistic corrections however the exact spectra and loss power are typically calculated by Monte-Carlo methods with suitable codes. The bremsstrahlung photons from the interaction of typical RE and ion or atom reach energies in the hard-X ray or gamma region of electromagnetic spectrum. Hard X-ray is a more suitable designation as the photons have very high energies but do not originate inside nucleus. The probability spectrum of the bremsstrahlung photon energy quickly decreases when approaching the energy of the relativistic electron. The additional drag force that this process adds to RE transport equations can be represented by additional collisional term as derived in [50]. The impurities play the most significant role in the loss effect via this channel. Despite the relatively low plasma densities the good confinement and significant number of RE can cause relatively high intensities of produced HXR radiation in the RE-plasma interaction. The other source of bremsstrahlung radiation in RE experiments is of course the RE interaction with solid materials, that have roughly 10 orders of magnitude larger density than the plasma and the relativistic electrons can reach very small depths in them. This interaction is a very intensive source of HXR radiation, typically more important than the interaction with plasma ions, especially during the periods with significant loss of RE to the wall.

2.7.2 Synchrotron radiation

A thermal electron in magnetic field of tokamak radiates cyclotron radiation uniformly to all directions on the main harmonics of cyclotron frequency $\omega_{CE} = \frac{qB}{m}$ typically in the micro-wave region. In case of relativistic electrons, these harmonics shift as $\omega_{CE} = \frac{qB}{\gamma m}$, then overlap and extend to continuous synchrotron radiation, which depending on the energy of the electron, may peak in IR or visible regions depending on the tokamak magnetic field. The synchrotron radiation in the tokamak is typically related to the perpendicular component of velocity v_{\perp} as the revolving around the field line, the large intensity of the field causes very small curvature radius of the motion - the Larmor radius r_L and this leads to large radiation intensities. However, as majority of the RE have high v_{\parallel} component, the relativistic beaming effect is dominantly in the toroidal counter-current direction. As observed in experiment, see e.g. [51]. The variation of the beaming in the poloidal direction with v_{\perp} has to be taken into account during the interpretation of the experimental images of synchrotron radiation. The synchrotron radiation was also analytically explored in [49]. The approximations for power spectrum in the cylindrical and toroidal geometry were summarised in [52] and can be calculated by a code SYRUP presented in this reference. A more recent code that takes into account the particle orbits and calculates a synthetic image or spectra based on the realistic tokamak magnetic field geometry is called SOFT (Synchrotron-detecting Orbit Following Toolkit) [53] and is utilised in following chapters of this thesis for interpretation of experimental data, the details on the SR calculation can be found in [28]. The dragging effect of the synchrotron radiation on the electron distribution can be described using relativistic radiation reaction force [54] that can be described by simplified formula [28]

$$\mathbf{F}_{\text{synch}} = -\frac{1}{\gamma\tau_{\text{synch}}} (\mathbf{p}_{\perp} + p_{\perp}^2 \mathbf{p}) \quad (2.42)$$

with the characteristic time scale being

$$\frac{1}{\tau_{\text{synch}}} = \frac{e^4 B^2}{6\pi\epsilon_0 m_e^3 c^3}. \quad (2.43)$$

It is obvious that the radiation reaction force is dominantly increased with perpendicular momentum and magnetic field magnitude, therefore high energy electrons with large pitch angle that may arise due to increased collision rate, are strongly radiating the synchrotron radiation and may lose energy via this channel.

■ 2.7.3 Generation of secondary particles

The main photon production channels due to existence of RE were covered in the previous sections. RE can be also responsible for generation of positrons and neutrons. The first case, generation of positrons through pair creation triggered by RE interaction with plasma ions should be in general possible inside the plasma. The acceleration and confinement of these positrons is theoretically considered in [55]. The acceleration of positrons would naturally happen in the direction opposite to the direction of acceleration of the electrons. However, the detection of the positrons is hardly possible due to huge HXR/gamma radiation background present in the RE experiments. The pair production as well as Compton effect and photoelectric effect naturally occur during the electron stopping in solid materials, however the detailed nature of this interaction is not studied here. Surprisingly, the RE in the tokamak may also cause generation of neutrons, through photo-neutronic reactions. In this process, first described in [56] high energy bremsstrahlung photons, with energy in the order of units or tens of MeV can destabilise neutron-rich isotopes of certain elements present in the tokamak which then release a neutron. The neutron energy is typically equal to the part of the photon energy exceeding the reaction threshold in case of endothermic reactions. Large fluxes of photon neutrons were detected at JET [57] and photon neutron detection has also become a thrustworthy RE diagnostics method at COMPASS [58].

■ 2.8 RE avoidance and mitigation

As was mentioned before, the most dangerous situation connected with RE is the generation of a RE beam during a sudden plasma termination, the disruption. The understanding of this scenario is the main focus of the international RE research. The aims of the disruption mitigation itself are namely [59]: minimising fast localised deposition of plasma thermal energy on the plasma facing components, minimising electromagnetic loads from induced eddy currents and halo currents - transient currents loops through plasma and plasma facing components. The electromagnetic loads are typically increased with the duration of the CQ [60]. Thus the disruption mitigation techniques typically aim on radiating away the plasma energy and shortening of the CQ. Unfortunately conditions that satisfy these requirements are also suitable for the RE generation. Therefore, the disruption mitigation techniques must be complemented or modified to prevent the other threat in the form of RE beam. In general there are two ways how to deal with this issue:

- **RE avoidance** - to prevent RE generation during the disruptions by decreasing the generation rate through the free parameters - electric field evolution, density evolution, impurity content or decreasing confinement of RE
- **RE mitigation** - in case that the RE avoidance fails, minimise the detrimental effect of already existing RE beam, i.e. decrease the number and/or energy of high energy electrons without causing focused impacts on the plasma facing components. This can be achieved through various methods theoretically, but requires deep experimental understanding and testing to be scaled to ITER and other large machines.

■ 2.8.1 Massive material injection

The dominant tool for mitigating the disruption thermal and electromagnetic effects as well as for RE avoidance and mitigation is the fast injection of large amount of impurity and/or hydrogen isotope atoms. This technique namely leads to increase of electron density and increase of energy losses via line radiation of the ionised and excited impurities. The contents of impurities also increases the resistivity of the plasma and speeds up the current quench. The problem is that the increased resistivity leads to increased electric field and RE generation and the spatiotemporal deposition of the injected material is absolutely crucial for the determination of RE generation and loss rates. Therefore several different injection methods have been developed.

■ Massive gas injection - MGI

The simple solution for the massive material injection can take a form of a fast high pressure valve [61] that can deliver quantities of gas an order of magnitude larger than the amount present during the plasma discharge in a tokamak vacuum vessel within a couple of ms. This technique might be too slow for large machines and furthermore the deposition is peaking at the edge, the MGI impurities are ionised and just slowly propagate via diffusion to the core of the plasma despite the huge initial pressure difference, possibly creating central regions where density remains low, but electric field becomes highly increased.

■ Shattered pellet injection - SPI

The shattered pellet injector is a much more complicated device than the massive gas injector, on the other hand it is designed to optimise the fast deposition of the injected material into as large area of the plasma cross-section as possible. The SPI hardware is typically formed by a device to prepare cryogenic solidified cylindrical pellets of selected gas or gas mixture, a propellant gas system possibly equipped by a punch to separate the pellet from the cold walls of the tube, barrel and bent shatter head that secures braking of the single pellet into spray of shards and gas that target as large part of the poloidal cross-section as possible. The details about SPI can be found e.g. in [62] and associated references. The SPI devices are currently installed on many important tokamak devices and studied in detail.

■ 2.8.2 De-confinement and energy dissipation by magnetic field and kinetic perturbations

The other technique that may at least partially mitigate the RE population is the increase of the RE transport via imperfections of the magnetic field or electromagnetic instabilities that enhance pitch angle scattering or have other decaying effects on the RE energy a density. RE orbits seem to be significantly sensitive to the fluctuations of various frequencies as shown further in this thesis and MHD instabilities may present suitable means for the RE population mitigation in all the discharge phases. During the disruptions, the flux surfaces of the magnetic configuration are typically destroyed and the magnetic field is stochastic after the TQ, however they can be reformed relatively quickly. This reformation may accelerate the RE generation and vice versa the reformation may be enhanced by the onset of the RE beam current. Deep understanding of the flux surface decay and reformation and adjustment of the disruption parameters based on this knowledge may improve the RE avoidance strategies.

■ Resonant magnetic perturbations (RMPs)

One of the most promising options for the controlled RE confinement is the use of the external error field generating coils, also called resonant magnetic perturbation coils. These sets of coils are usually shaped as saddle coils, rectangular patterns on the surface of the tokamak vacuum vessel and can produce radial component of magnetic field B_r that is not desirable under

normal circumstances and can enhance resistive magnetohydrodynamic mode activity and magnetic field stochastisation. These experiments were conducted at COMPASS extensively [63] and related simulations have shown strong effect on RE of some energies [64]. However as the RMPs are powered with external power sources and the forces acting on them are not negligible, they are limited in both reaction time and magnetic field amplitude and thus not able to create perturbation strong enough to affect core of a plasma/RE beam in large machines.

■ Inductively driven non-axisymmetric coils

Another way how to enhance the error field during the disruption using the electric field arising from the current decay itself is to place a helical, non-axisymmetric coil as close to plasma as possible and secure that the loop is formed during the disruption. This was studied so far as a theoretical concept in [65] and can present a viable concept for the mitigation.

■ Kinetic instabilities and wave interaction

At several tokamak experiments it was observed that RE population was mutually interacting with high frequency whistler waves that have frequencies 100-200 MHz in the tokamak plasmas, see e.g. [66]. The pitch angle scattering, caused by the presence of the instability, is believed to mitigate the initial RE populations during disruption under some circumstances as theoretically predicted in [67]. This is an actively studied field of processes that possibly enhance the RE mitigation and avoidance.

■ 2.8.3 Controlled impact

The last layer of defence against uncontrolled damage caused by RE is, not surprisingly, a controlled beam impact. If the RE beam can be controlled in position to sufficient degree, special dedicated targets or limiters can be prepared in the vacuum vessel. These may absorb the impact energy of runaway electrons. This is however a very risky strategy, not only relying on position control that might be difficult in case of runaway electrons, but also due to the nature of the impact that may still release large material quantities into the vacuum, worsening the conditions in the machine or cause

other negative effects. Should this option be seriously considered, the heat fluxes have to be spread to as large area as possible and the material carefully selected. In fact, if the RE impacts are spread in both time and space, ordinary limiters may survive them without troubles and this is the principle behind some of the mitigation techniques based on the enhanced RE losses due to suitable instabilities. In some design considerations for the future fusion power plant design, so called sacrificial limiters are considered for other plasma transient events in [68]. On the small scale, in the TJ-2 heliac - a machine operating without the plasma current, where some RE can be created during the plasma initiation - a mechanical paddle is used to sweep across the poloidal plasma cross-section to remove the runaway electrons.

2.9 Detrimental effects of runaway electron impact

The effects of the RE impact can be both local and remote. The local effects are connected namely with local hot spots that may be several cm deep and several cm in diameter resulting in plasma facing material melting (metallic wall) or sputtering (carbon). The damage caused by uncontrolled RE impact is shown e.g. in [69] and [63]. A simple tile can be replaced in case of current machines, however in ITER all the plasma facing components (PFCs) need to be actively cooled which poses the risk of a leak of the cooling medium into the vacuum vessel when the impact of RE burns through the material layers up to the cooling tubes. This would be a critical incident in any future power plant.

The remote effects may be surprising, however especially in the case of PFCs made of heavy materials, like tungsten, significant amount of impact RE energy is converted into HXR bremsstrahlung radiation which is forming tangential beam. This beam of high energy photons is able to bring havoc to more remote sensitive regions of tokamak construction. For example at WEST it appeared that such a beam is able to quench the superconducting toroidal field coil in its path [70] which is a very dangerous situation leading to quick boiling of the liquid helium coolant. Although the inter-lying material shielding the coil at ITER is much thicker these remote effects must be seriously considered. In case of a beam of HXR photons hitting a suitable structure, generation of a beam of neutrons is also not excluded.

Chapter 3

Overview of diagnostics, processing methods and models

3.1 Dedicated RE diagnostics and common diagnostics sensitive to RE presence

The dedicated RE diagnostics measures namely radiation effects of runaway electrons and secondary particles. The direct detection of the runaway electrons by suitable in-vessel probe is possible, however it requires very specialised vacuum compatible hardware, it is difficult to interpret as the environment is harsh and other effects may disturb the useful signal and furthermore, the magnetic field makes the particle trajectories complicated and the suitable position of the detector is absolutely essential for the the measurement.

3.1.1 Direct RE detection

The methods which can be used for the direct detection of the runaway electrons include

- electric probes, designed in a way to avoid signals from thermal plasma electrons or ions by geometry means or using bias voltage

using $\omega_{C,e} \sim B_t \sim \frac{1}{R}$. However, as the relativistically shifted frequency $\omega_{C,e} = \frac{qB}{\gamma m}$ violates the simple frequency-radius mapping, the best options in case of the RE presence in the plasma is to measure along vertical line of sight at constant B_t . In this configuration, the radiation of the supra-thermal population in the range of small hundreds of keV can be investigated [79] at second and third harmonics.

The continuous synchrotron radiation from multi-MeV RE can then measured by IR and visible cameras in tangential configuration looking along the direction of current thus observing the counter-current beamed synchrotron radiation from the relativistic electron population. Any other radiation detector or even spectrometer oriented in the same direction may be also used for the detection of the synchrotron radiation and measurements of its parameters. The most suitable are systems of cameras covering several different wavelength ranges and the same or similar field of view, e.g. spectroscopic imaging system used at TCV [80]. At COMPASS, bolometric camera sensitive in long-IR range ($\lambda = 7 - 13 \mu\text{m}$) and a fast mid-IR camera ($\lambda = 3 - 5 \mu\text{m}$) based on InGaAs sensor were recording the RE beam on different occasions, both capable of detecting synchrotron radiation despite the low magnetic field. At JET, three different cameras with a very similar field of view and visible, near IR and filtered ($\lambda = 3 - 3.5 \mu\text{m}$) mid-IR sensitivity range are utilised. The spectrometric system for synchrotron radiation observation REIS (Runaway Electron Imaging and Spectrometry) [81] using 3 different spectrometers covering the total spectral range from 400 nm to mid-IR range in latest version was applied on several European tokamaks including COMPASS. Alternatively, polarised synchrotron radiation can be measured by a suitable tangentially oriented collection system of a diagnostics with different purpose - e.g. Motional Stark Effect detection optics as was done in reference [82].

3.1.5 Impact diagnostics

The RE diagnostics most relevant to the prevention of the detrimental effects that RE may bring, is the diagnostics of the RE impacts, which could mean measurements of instantaneous heat-fluxes and surface temperatures or diagnostics of the total deposited energy. The heat fluxes may be measured by a calibrated IR camera observing the surface as done e.g. in [83],[18],[69]. The total deposited energy can be measured by observing the temperature equilibrium being reached in certain bulk material element that is hit by the RE beam and well thermally insulated from other structural elements as done in COMPASS in the framework of thesis [84].

detection in the stored data. The detector time characteristics versus the count rate needs to stay in the optimal region in order to be able to detect the peaks properly. However, using a suitable algorithm, even partially piled-up peaks may be resolved. On the other hand, the pulse height analysis may not be directly implemented, in these cases.

■ 3.2.2 Peak height and shape analysis

In case of a proportional response of the detector, the peak height is related to the energy of the incident particle (e.g. a HXR photon) and energy spectra can be obtained under the condition that absolute calibration is carried out. The relation between the electronic peak signal height and energy of the particle can be straightforward (e.g. NaI(Tl) scintillation detector of γ rays with practically linear response in the region of hundreds of keV and units of MeV), while in some other cases (e.g. proton-recoil neutron detectors), the relation is rather complicated and regularisation techniques must be applied. The time resolution of the spectral measurement is typically quite low as at least thousands or rather tens of thousands of pulses need to be collected to have a reasonable pulse height statistics. On large machines like JET, the energy-resolved measurement of neutrons or HXR is typically available on 10 ms time-scale, thanks to the ability to detect millions of peaks per second [90]. This is a sufficient time resolution given the JET discharge time scales. On smaller machines, these measurements are very difficult due to shorter duration of the experiment that may reach similar time-scale as the time window necessary for collection of sufficient number of pulses. The height of the peak may be distorted, by e.g. insufficient time resolution, noise or shift of the amplification gain, thus the most efficient, although computationally demanding is to fit each peak in the sequence by a known function of time. In case the data quality is good, a simple measure of peak height is usually sufficient for quick analysis of the spectra.

■ 3.2.3 Pulse-shape discrimination

Most of the detectors of neutrons are sensitive also to high-energy HXR or γ radiation due to inclusion of a stage sensitive to secondary ionising radiation. For this reason, pulse shape discrimination that allows to resolve the type of the incident particle can or must be implemented. This procedure is more complicated and dedicated electronics must be often developed. The neutron peaks are typically longer in duration or they have a slower leading edge, longer tail or multiple decay components. Again time-over-threshold algorithm may

can be found e.g. in [94] or [95]. For example, in the case of the magnetic probes situated at different toroidal positions at the tokamak vacuum vessel, the cross-spectrum and phase evolution diagram resolve the toroidal mode number of an observed magnetic island or other in-homogeneous rotating structure. An example of cross-coherence and its application to analysis of runaway electron interaction with magnetic islands can be found in paper A [18] that is attached to this thesis.

■ 3.2.7 Inverse problems

Inverse problems represent a common class of tasks in plasma diagnostics and anywhere else where scientists need to back-track a natural phenomena from a measurement. The typical properties of such problems are:

- The calculation goes in the opposite direction of time with respect to the detection process, e.g. we want to reconstruct a source of light from intensity detected by set of detectors.
- The problems are undetermined, i.e. the linear systems that (approximately) describe the physical measurement system are characterised by having more variables than equations.
- The problems are ill-posed, i.e the solution is not unique and a small change in the detected data may lead to a large changes in the calculated results - i.e. the system is ill-conditioned.

The second point above (in case of linear/linearised problems) leads to a need of an inversion of a rectangular matrix. Generally the linear inverse problem can be represented by the following equation

$$f_i = \sum_j^N T_{ij}g_j + \xi_i, \quad i \in 1, \dots, L, \quad (3.1)$$

where f_i are the measured signals, T_{ij} is the discrete representation of the instrument (response) function, transfer function or geometry matrix and g_j are the original values of the physics quantity, ξ_i are the errors of the measurement. The matrix T_{ij} cannot be inverted directly, however suitable regularisation methods are available. The most common method is an addition of a square matrix based on some property that we expected from the solution as was first proposed by Tikhnov (translated in [96]). In plasma physics, we almost exclusively work with continuous functions, thus we may expect

3.1, while rectangular pixel grid over plasma cross-section for two different diagnostics systems at the JET tokamak is shown in the bottom part of figure 3.1. This technique can be then used for reconstruction of emissivity profiles in SXR spectral region [99], total radiated power emissivity (as measured by bolometers), visible light emissivity, HXR/ γ radiation emissivity or neutron emissivity. The regularisation matrix, based on the assumption of the radiation intensity being a smooth function of the spacial coordinates, represents the 2D smoothing. It can be anisotropic depending on the problem symmetry, e.g. with a stronger smoothing along magnetic flux contours for SXR, representing bremsstrahlung and impurity radiation as intensities of this radiation are functions of T_e and n_e that are almost constant along the contours. The neural networks are often applied in this area of signal processing methods as they can significantly decrease the computation time and costs, the overview of the recent upgrades of the methods is included in [63].

3.2.10 Control algorithms

Feedback control is an important part of tokamak physics, without active control of numerous parameters, it would be rather impossible to conduct a physically relevant plasma discharge and aim for long pulse operation that is necessary in future fusion power plant. The tokamak control is summarised e.g. in a recent conference paper [100]. If we take an example of the plasma position control, the role of sensor in the loop can be covered by diagnostics coils measuring either local magnetic field or magnetic flux and the role of the actuator is covered by high power poloidal field coils. The control of plasma parameters is typically based on a simple and reliable principles and methods, namely linearisation of the process equations and PID (proportional-integral-differential) controllers. These controllers were run on analogue computers in past, while digital variants are used in a broad range of applications today. PID controller is commonly defined as

$$u(t) = K_p e(t) + K_i \int e(t) dt + K_d \frac{de}{dt}, \quad (3.2)$$

where $u(t)$ is the control variable (actuator effect), $e(t)$ is the error of the controlled parameter with respect to the reference value and K_p , K_i and K_d are proportional, integral and differential gains (constants). The constants can be derived based on analytical calculation, numerical model of the process or by training of the PID on existing data and dedicated control algorithm commissioning experiments. Most often a combination of all the mentioned methods is used. The control scheme can have single or multiple inputs and outputs (SISO, MIMO). Fusion research is now gradually shifting to more complicated control approach with fast advanced models of plasma physics

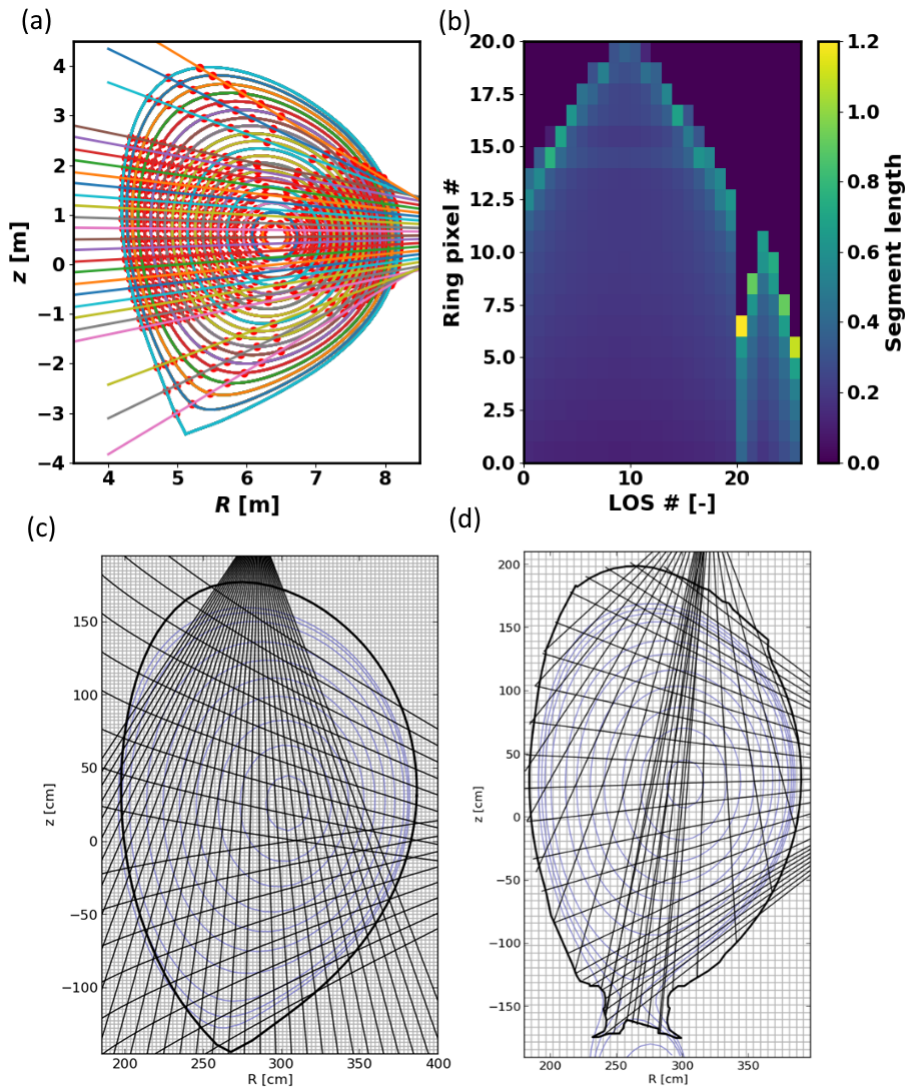


Figure 3.1: The layout of a tomographic diagnostics: (a) example of concentric pixels based on the Ψ contours and LOS crossing them, (b) the resulting contribution (response) matrix, (c) square pixel layout with plasma separatrix and LOS of JET SXR cameras, (d) square pixel layout, limiter contour and the LOS of the JET overview bolometers.

processes and transport running along with the discharge and interacting with the control schemes to provide complex approach to the control, see e.g. [101].

■ 3.3 Special diagnostics and processing methods implemented during COMPASS RE experiments

In this section, the special implementation of the methods and diagnostics means for the scope of this thesis is detailed, namely for the case of COMPASS experiments.

■ 3.3.1 Measurements of HXR energies with the NaI(Tl) spectrometer and the REGARDs spectrometer

In the following lines, the tests and results of HXR peak resolved measurements with the rather slow NaI(Tl) scintillation crystal are briefly summarised. The NaI(Tl) detector with a photo-multiplier tube and a voltage divider has been connected to a PXI computer with the fast oscilloscope card NI 5114 (125 MHz, 250 MS/s, 8bit, 64 MB memory, input impedance 50Ω or $1\text{ M}\Omega$). In the case of short peaks and optimal acquisition duration, such ADC card can be used for full signal acquisition and peak detection in the signal after the discharge at small devices with relatively short discharge duration (post-processing). The set-up was tested with the high input impedance and two γ radiation sources at the Golem tokamak, the resulting spectrum after several tens of seconds of acquisition is displayed in figure 3.2. The full absorption peaks for both isotopes are visible in the data.

After the calibration for the low impedance set-up which leads to peaks of much shorter duration, the same diagnostics was run during the dedicated RE campaign at the COMPASS tokamak. To decrease the number of low energy HXR the detector was placed to a lead bunker with 5 cm thick walls, doubled at the tokamak side. The time evolution of the collected signal for a discharge with only trace RE population (standard shot # 16594) is displayed in the left part of the figure 3.3. It is obvious that the envelope of the peak maxima is rising almost linearly in time in this case, the peaks from individual photons are well resolved if zoomed. If peak counting in time bins of suitable length is applied, it is possible to obtain the time evolution of the count rate/HXR flux that is apparently very different from the apparent raw signal evolution as shown in the right part of the 3.3. The coloured vertical lines are dividing the time evolution to four sections with same number of peaks, the spectra of these blocks are evaluated in the right section of 3.5. This method is suitable for studies of the energy evolution as the spectra are normalised to the same value. The observed maximum count rate is about 250 kHz. Based on the calibration, the 662 keV full absorption peak of Cs corresponds

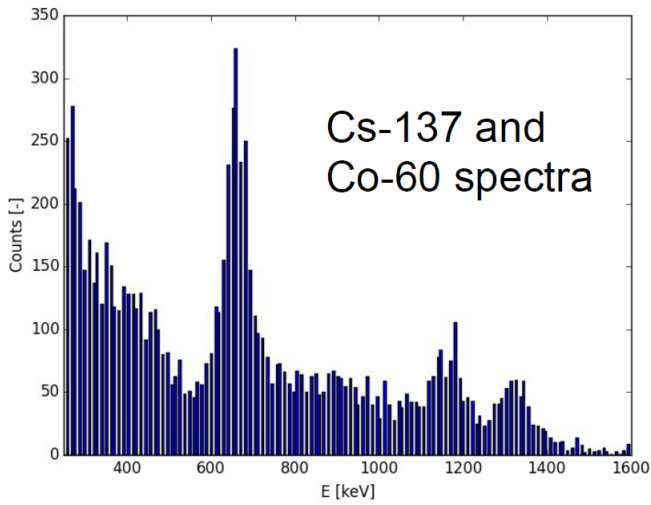


Figure 3.2: The ⁶⁰Co and ¹³⁷Cs γ spectra as measured by NaI(Tl) detector used for RE-generated HXR measurement at COMPASS, the full absorption peaks at 662 keV, 1173 keV and 1332 keV are visible in the data.

to 0.07 V. The largest peaks approach the maximum energy to be reliably detected by the standard 2 inch scintillator, roughly 7 MeV (at this energy only half of the particles with optimal trajectory are fully stopped in the medium).

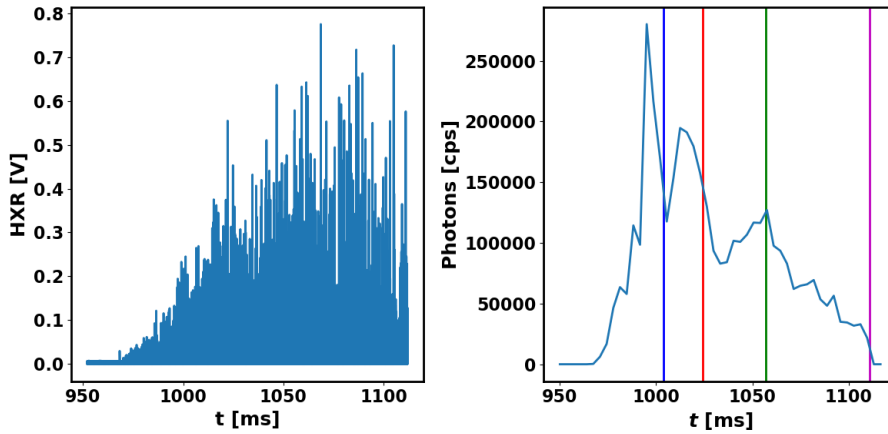


Figure 3.3: Left: Time evolution of the HXR detector signal in the "standard shot" discharge (starting at 960 ms) with trace RE population. Right: Time evolution of number of counts in the same discharge.

Unfortunately, in case of large HXR fluxes that may occur in dedicated RE discharges, the peaks are piled up and furthermore - in case of even larger fluxes - the PMT saturation leads to a drop of the signal and the data are not useful as can be seen in the figure 3.4. In this case it would be necessary to increase shielding thickness up to 15 cm or even more and use a suitable

collimator or much faster scintillator.

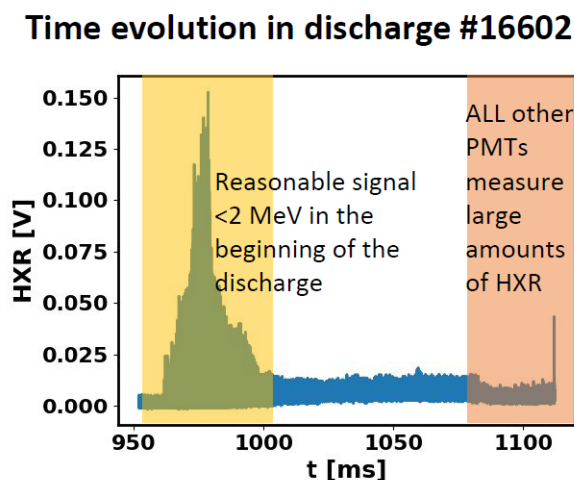


Figure 3.4: Time evolution of the HXR signal in case of low density discharges with dominant RE population, the diagnostics set-up fails to collect the events due to too high HXR flux.

Anyway, for the cases with an optimal number of HXR counts we can use the pulse height analysis (and calibration) to obtain the energy spectra of the HXR photons that are related by a non-trivial way to the distribution function of the incident RE. The inversion of the spectra can be in principle carried out [102]. The spectra from four time segments are displayed in the left part of figure 3.5. The results correspond to the expected fact that the RE are created almost exclusively during the plasma start-up phase and only well confined during the flattop phase with high density - the ratio of applied electric field to critical field is small in the plasma current flattop phase. The higher energy counts grow in number over the time, while there is a certain drop in the number of counts in the low density part of the spectra. This is even more visible if we use four time segments with same number of peaks rather than same duration. The corresponding regions were marked in fig. 3.3. Apparently, the first spectrum is composed of HXRs with much less energy than the subsequent spectra. The acceleration effect is visible despite the stochastic processes involved both in the HXR generation and detection. The error bars are based on Poisson statistics. Notice that the maximum energy reaches 7 MeV after just 100 ms of acceleration. The acceleration takes place in the current ramp-up phase at elevated electric field. The maximum energy of the incident photons must be even higher as the statistics of the measurement and the energy range of the detector is restricted by the detector size and of course distance from the source.

These measurements were the first ones confirming that the energy of RE in the COMPASS tokamak can reach larger units or even tens of MeV.

The HXR spectra measurement was significantly improved during the last

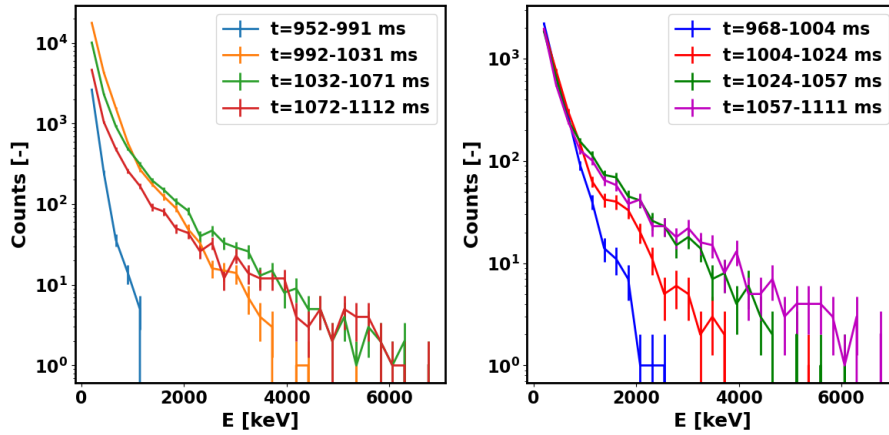


Figure 3.5: Left: HXR spectra from four time segments of same duration in shot # 16594. Right: HXR spectra based on four time segments with the same number of peaks.

two RE campaigns on COMPASS. During the 11th campaign, a group of experts from ISTP, CNR Milan and Milan University that have designed gamma spectrometers on multiple tokamaks around the world were invited to apply their HXR spectrometer called REGARDS to COMPASS RE discharges. The support - HW for positioning and shielding, triggering, etc. - was provided by the COMPASS team. The REGARDS is based on $\text{LaBr}_3(\text{Ce})$ scintillation crystal which has approximately 10x faster decay time than the $\text{NaI}(\text{Tl})$ crystal, PMT with gain control based on observation of signal caused by periodic blue LED light pulses and data acquisition system with FPGA module based on the NI Flex-Rio architecture. The detector was placed outside the main shielding of COMPASS, behind the north wall and equipped with simple lead shielding with several standard lead blocks.

This setup allowed measurement in the full RE beam scenario in most cases, characterised by very high HXR fluxes, where count rates well over 1 MHz were reached. The shielding wall on the other hand did not allow for efficient use of the detector during low HXR flux period, which means that before or without the injection of the noble gas and full RE beam generation this detector did not reach sufficient statistics. An example spectra from the whole discharge #19991 is shown in fig. 3.6. It is apparent, that the measured energies are larger than in the case of previous measurements - reaching up to 18 MeV. Although there are just units of peaks in several bins with energies larger than 14 MeV, given the duration of the measurement a majority of these peaks are clearly caused by the RE as cosmic radiation or other potential sources cannot reach such count rates. The number of peaks in the most populated bin reaches up to 10000. In another example from a discharge #19996 in fig. 3.7 the spectra is evaluated in several time bins with the same number of peaks (left) in each and evolution of the average energy is displayed with better time resolution. The acceleration of the RE is obviously seen from the data using both methods of visualisation.

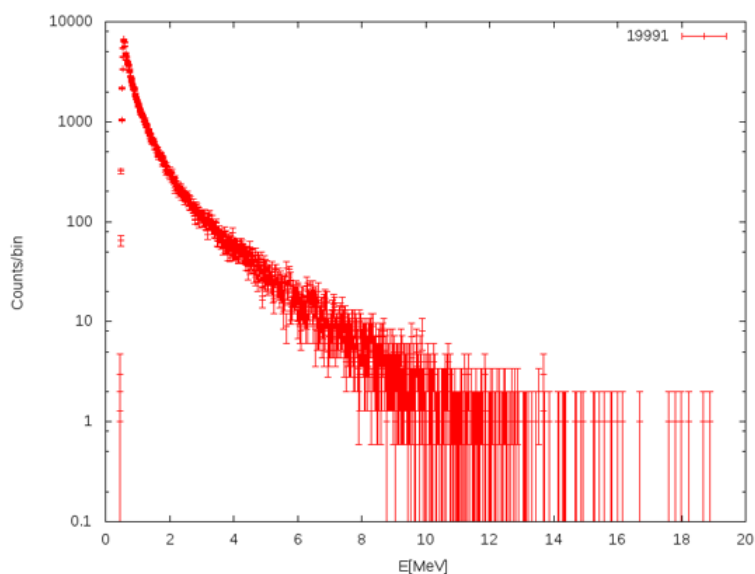


Figure 3.6: The spectra obtained by the REGARDS HXR spectrometer during COMPASS discharge #19991. Courtesy: Andrea dal Molin

During the last (12th) RE campaign a similar setup with CeBr₃ scintillation crystal was utilised as documented in [74]. This detector that is normally installed at the Golem tokamak achieved similar performance as REGARDS. The results of this setup are used for comparison in following chapters, however the technical details of these measurements are not subject of this thesis and will be included in the thesis of Jaroslav Čerovský.

3.3.2 Evaluation of HXR fluxes over large range by synthesised measurements from multiple detectors

The detectors presented in the previous chapter do offer energy resolution under suitable conditions. However, during most of the RE campaigns only detectors operating in the current mode were available. These detectors are essential for evaluation of all the discharges from the point of time evolution of HXR fluxes, related to RE generation and losses, including fast changes due to various periodic instabilities. The difference of the sensitivity of different detectors is limiting their use in different discharge phases and scenarios - e.g. a detector that is able to detect small population of RE is completely saturated in a full RE beam. Therefore a synthesis of different detector signals must be attempted in order to reliably compare discharges with different populations and derive absolute HXR fluxes. The idea was proposed by the author of this thesis and prove of principle of the method was achieved by a SUMTRAIC summer school student Johan Buermans

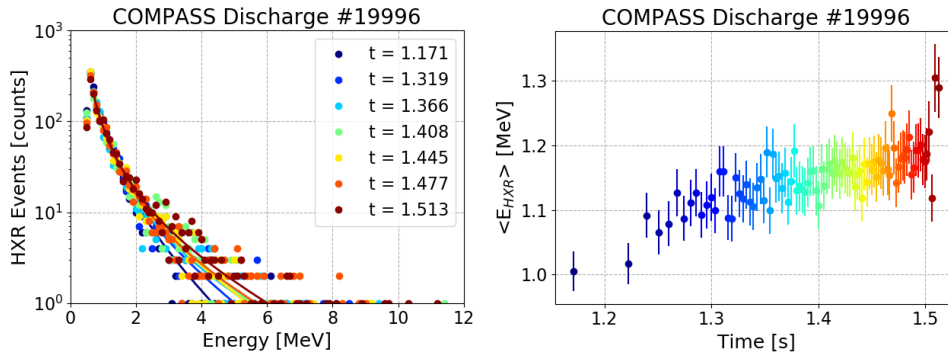


Figure 3.7: The spectra and average energy evolution obtained by the REGARDS spectrometer during the COMPASS discharge #19996. Courtesy: Andrea dal Molin

[103] under the supervision of the author of this thesis. Below, the detailed derivation, consideration of assumptions and applications of the method made by the author of this theses are reported. Several different measurements using dedicated an non-dedicated HXR detectors are taken into account:

- NaI(Tl) HXR spectrometer used in a limited number of discharges and described above and placed in a lead shielding
- Standard NaI(Tl) used in the current regime as the main HXR detector
- Standard neutron detector placed in lead shielding, that is sensitive to high HXR flux effects in the scintillator and secondary to high fluxes of high-energy HXR photons through photo-neutron generation
- The PMTs without scintillating crystals placed outside the main concrete shielding walls
- The HXR effects on the fast visible cameras - observation of dots and in general intensity measured in the blind regions of the chip

Out of these detectors only the first one is providing the number of counts, related directly and reliably to the flux. To perform the connections in this chain of detectors, we have to impose some strong assumptions, first let us list those important only for the "calibration" of the HXR flux at detector position:

- The spatial structure of the HXR radiation field does not change significantly discharge to discharge, or within a discharge, which would affect the comparison of the detector signals. This assumption can be expected

as valid - in case of toroidal source based on the interaction of the RE with the background gas the radiation field should be fairly stable and in case of wall interaction, the RE usually impact onto the most protruded component which can differ campaign to campaign, but rarely shot to shot.

- The range of fluxes in the experiments is much larger than the range or variation of the energies, thus the mixed effect on the current mode signal of the detectors is dominated by the fluxes. This can be justified as the measured range of energies typically spans over just 3 orders of magnitude - tens of keV - small tens of MeV, in fact rather 80 keV - 20 MeV as shown in the spectra in previous section and by the means of radiation transport simulation below. The span in the HXR fluxes can be much larger than that: The HXR source rate is ranging from 0 to $\sim N_{RE}/\tau_{\text{loss,min}}$ than is the fastest possible loss rate of all the RE. The number of RE can be roughly determined from the current $I_{RE} = 2\pi R_0 e N_{RE} \langle v \rangle$ In the case that we consider the average velocity to be close to speed of light, then e.g. 100 kA of current at COMPASS corresponds to $\sim 10^{15}$ runaway electrons. This means that the source rate can be approximately $\sim 10^{19}$ HXR/s in case of very fast impact of RE beam to the wall on the sub-ms timescale. To translate this to the flux levels at the detector position very roughly, we can use the isotropic/point source approach, i.e. the fraction of a space angle that is covered by the detector surface. For a detector positioned 8 m from the tokamak main axis, which is the case of detectors placed near the shielding wall, this gives a factor of $\sim 10^{-7}$ to relate the source rate and flux at the detector position, i.e. flux at the detector position may reach values in the range of 12 orders of magnitude, from 0 to $\sim 10^{12}$.
- Even if we neglect the differences in the shielding and sensitivity of the different detectors, the signals can be related to each other provided that suitable discharges are found.
- The detector response is linear across several orders of magnitude for each of the detectors and saturation can be recognised easily, This is valid for all the used detectors.
- The high voltage on the detector was not changed over the time. This requirement was fulfilled in the observed period.

In the case that we intend to relate the observed count rates to the absolute source of the HXR - as the measure of interaction of the RE with companion plasmas and the wall, we need to add other assumptions and calculations.

- One RE is typically responsible for generation of no more than small

Based on the listed assumptions we can state that

$$f_n = \frac{\bar{f}_{1,s_1}}{\bar{V}_{2,s_1}} \cdot \dots \cdot \frac{\bar{V}_{n-1,s_{n-1}}}{\bar{V}_{n,s_{n-1}}} \cdot V_{n,s}, \quad (3.3)$$

where f_n is the flux at the n -th detector in the series calculated using ratios of average voltages \bar{V}_{i,s_j} that correspond to detector signal of i -th detector in the given time period of the "calibration" shot s_j . By this chain the signals are related to the absolute value of count rate at the primary detector \bar{f}_1 . The result of this comparison is displayed in figure 3.8. Each pair of detectors seem to follow the same trends in the time evolution of the selected discharge and time window. In the left part of the figure, set of plots of absolute values of the detector signal pairs is shown in logarithmic scale while in the right part, the corresponding count rate of the less sensitive detector from each pair is plotted in linear scale using derived calibration ratios and equation (3.3). From the result it is obvious, that equivalent count rate corresponding to the peaks in the time evolution of the last compared discharge #16655 is larger than 10^9 cps, which by far cannot be resolved even with the fastest scintillators in the counting mode. In the next section we will try to relate the count rate to the actual source strength. Using this information we can compile a single signal out of the 3 current mode detector signals and calibrate it to equivalent fluxes of the NaI(Tl) spectrometer. The signal is based on the **HX** signal in the first part of the discharge until it reaches saturation, then **SHX** is used until it is not significantly surpassed by the **PMT**, then **PMT** is used to cover the part of the discharge with the largest fluxes. The results are summarised in figure 3.9 for two different discharges, the generation of the full RE beam is clearly visible by the steep rise from 1115 ms. This approach allows for consistent measurement of count rates over more than 6 orders of magnitude.

■ Influence of the vacuum vessel on the HXR fluxes and energies

The attenuation of the HXR signal can be in general estimated using tabulated values for different materials and simple analytical formulas. However, recently the Monte-Carlo particle transport models became available in several user-friendly computing environments, e.g. openMC [104] with the recently improved Python interface specifically designed for fusion neutronics calculations [105]. Complex CAD models can be introduced to the program geometry interface, however at the cost of large computing times. Simplified models can be used for valid estimates. To estimate the minimum energy of the primary HXR photons and overall drop in flux, a simulation with COMPASS Inconel vacuum vessel without ports was performed. The vacuum vessel corresponds to the minimum material thickness that is shielding the internal sources of the HXRs, in arbitrary direction, excluding the ports openings

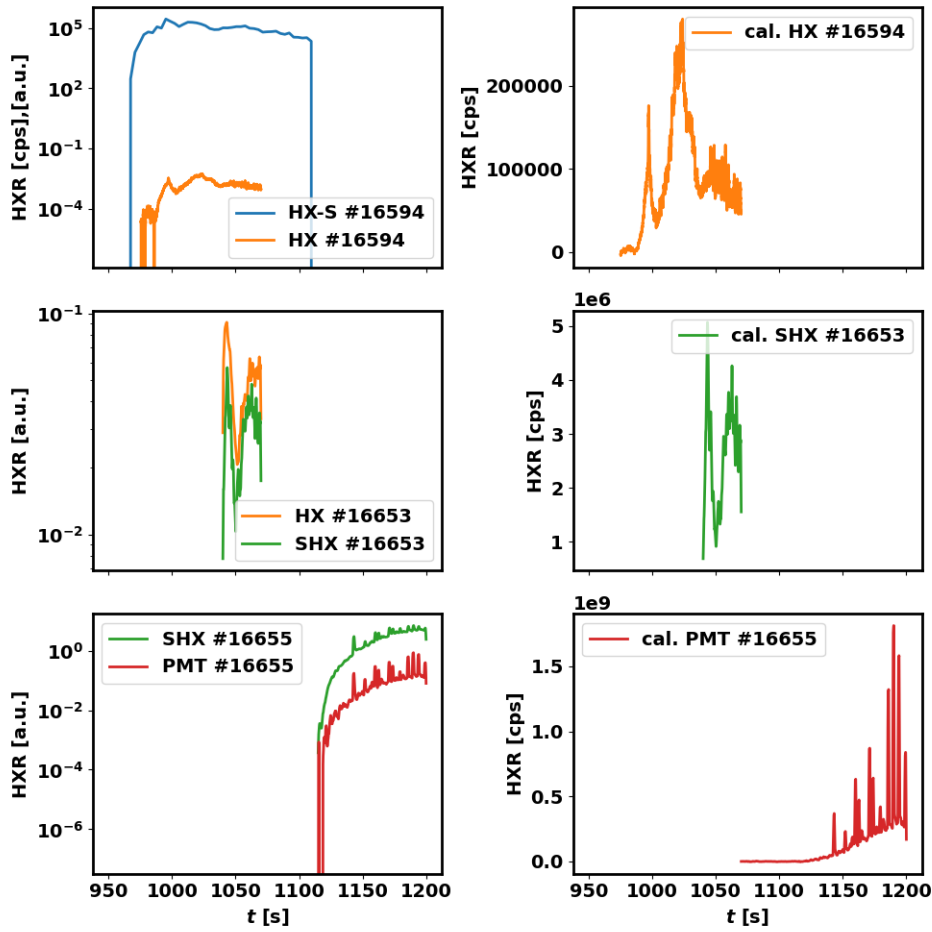


Figure 3.8: Left: In each frame a pair of signals of two detectors sensitive to HXR is coupled using a suitable shot, the y axis shows the amplitude of the raw detector signal, i.e. voltage, except for the **HX-S** which is in counts per second. Right: The detector signal recalculated to the equivalent count rate of the NaI(Tl) spectrometer **HX-S** using the signal ratios.

which are relatively small at COMPASS. The real shielding thickness will be larger in most directions (coils, support structure elements, etc.). The model geometry is shown in fig. 3.10 - the small sphere at the source and large sphere surrounding the vacuum vessel model serve for evaluation of the HXR fluxes. The material of the Vessel is corresponding to the Inconel 625 composition with the mass ratios of all the alloying elements in the center of the allowed range, balanced by the Ni amount and neglecting the trace elements below 1%. The resulting effect on the flat photon distribution from 10 keV to 500 keV and 10 keV to 5 MeV is shown in fig. 3.12. The orange and the green curve in each of the two figures are directly comparable and show the influence of the vacuum vessel body. The results are significantly different for the two energy ranges, it is apparent that HXR/ γ photons below approx. 80 keV from the source are significantly attenuated, thus we cannot

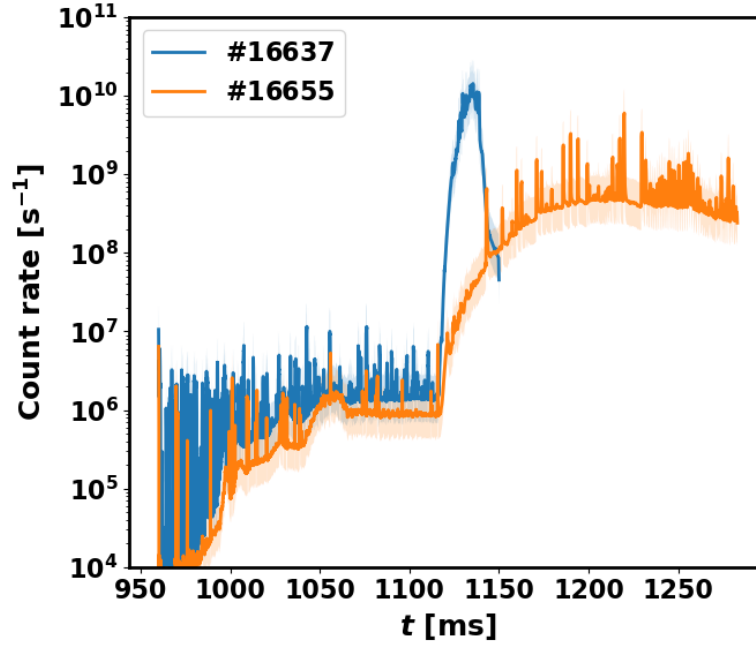


Figure 3.9: The unified signal based on the different detectors recalculated to count rate of the HXR spectrometer for two different discharges with different gas injection scenarios.

detect RE with energies below this limit. In fact, running the same simulation with an initial distribution spanning only from 10 to 100 keV, results in no particles detected outside at all, thus the attenuation factor at least equal to the number of particles used in this simulation, i.e. 10^5 , thus we cannot reliably detect RE of lower energy and all HXR of these energies are secondaries. Below the pair creation limit of 1022 keV, the photons of all energies are significantly attenuated by the vessel, the minimum attenuation in this energy range is roughly factor 8, on the other hand, in the right part of figure 3.12 it is obvious that pair creation leads to increase of photon flux in the hundreds-of-keV range with distinct peak at 511 keV corresponding to positron annihilation. In terms of average flux, the reduction caused by the presence of the Inconel vessel is 2 times in case of high energy range source case and 12 times in case of low energy case. In most of the studied scenarios the HXR source is containing energies well over the pair creation value, thus, the smaller attenuation factor is more valid, although the large range of attenuation and realistic distribution has to be taken into account in case of more detailed calculation. The spacial distribution of the fluxes can be observed in the figure 3.11. The bottom region is apparently shielded by the central column of the torus and gives rough estimate about the possible spacial inhomogenities.

This attenuation factor shifts the source strength corresponding to flux

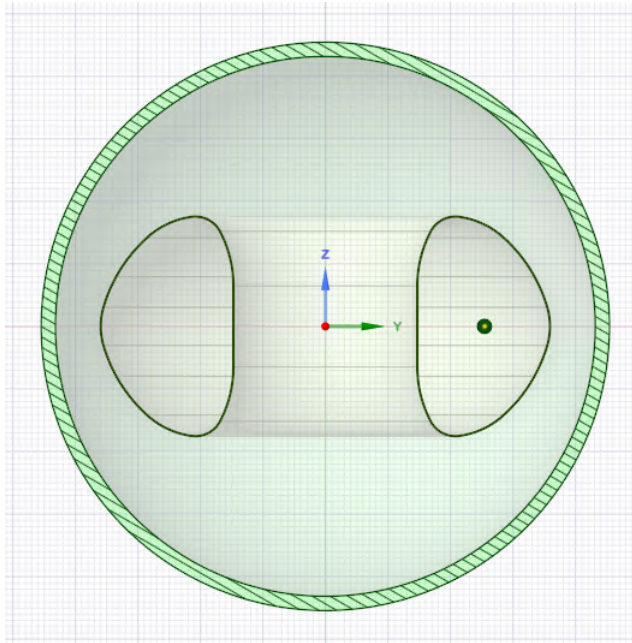


Figure 3.10: The geometry of the openMC HXR transport model with point source inside the realistic COMPASS vacuum vessel

measured by the HXR spectrometer and thus also by each of the detectors in the chain upward by a given multiplication factor and increases the uncertainty of this measurement.

■ Attenuation caused by the lead shielding bunkers

The primary detector of this detector chain was placed in a lead shielding bunker as previously mentioned. The lead blocks have width of 50 mm, thus the common shielding thicknesses are 50 and 100 mm. The simulation of such thick shielding is relatively demanding however for homogeneous material we can use estimates based on the photon corrections and attenuation, see [106], more specifically the web-based calculator [107], while for slits and other improvised collimating structures we can use MCNP or geometric approximations. It appears, as shown in the figure 3.13, that the minimum attenuation occurs near 5 MeV and the transmission for 50 mm of lead and energies of units of MeV ranges from 5% to 9% While in case of 100 mm it is approximately and order of magnitude lower. This is the fraction of photons reaching behind a homogeneous lead wall. In the case of a detector placed inside the bunker with side walls, some scattered photons that would get behind a homogeneous wall cannot reach the interior of the bunker, thus we can consider the attenuation factor at the upper boundary, i.e. 20 in the case of 50 mm and 200 in the case of 100 mm of lead shielding, the

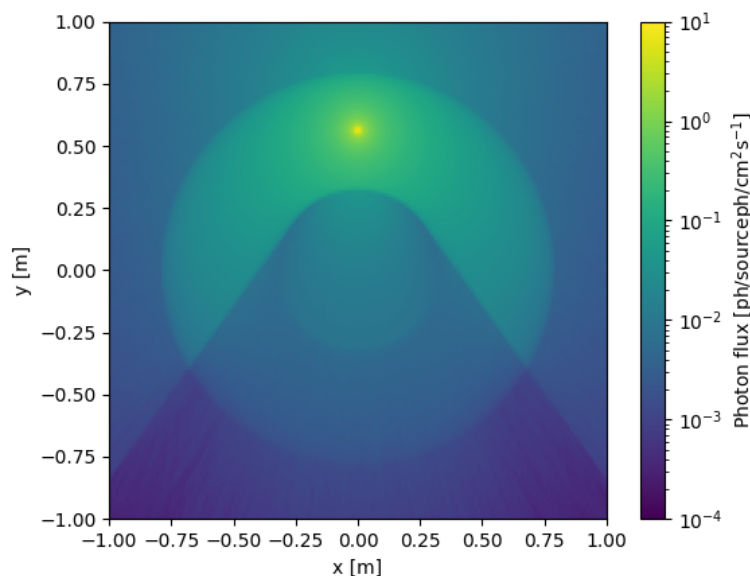


Figure 3.11: The spacial distribution of fluxes in the simulation with HXR isotropic source inside the COMPASS vacuum vessel

range is propagated to the resulting confidence interval. In the case of a simulation with a point source and a scintillation crystal cylinder placed inside a bunker with a front wall thickness 10 cm and a slit of a couple of mm. The fraction of radiation that reaches the detector inside the shielding compared to the radiation reaching the detector without any shielding is directly proportional to the dimension of the slit as expected. More specifically, the results are in table 3.2. Based on these calculations and assumptions,

Slit width [mm]	Detected fraction
20 mm	0.6
10 mm	0.3
5 mm	0.15
1 mm	0.03

Table 3.2: Fraction of gamma radiation of flat distribution from 100 keV to 5 MeV reaching a detector inside shielding with an entrance slit.

the overall attenuation factor estimated for the given shielding is 20 with the confidence interval from 7 to 100. This adds to the attenuation caused by the vacuum vessel. As one of the detectors of the chain is placed outside of the main concrete shielding wall (**PMT**) is already connected to the others based on a suitable discharge and time interval, we do not have to consider the effect of the shielding. However, based on the simulations the 60 cm of concrete corresponds to the attenuation factor of 50-70 in the given range of energies. This factor is naturally included in the detector ratios. The same applies to the shielding bunker of the third detector of the chain **SHX**.

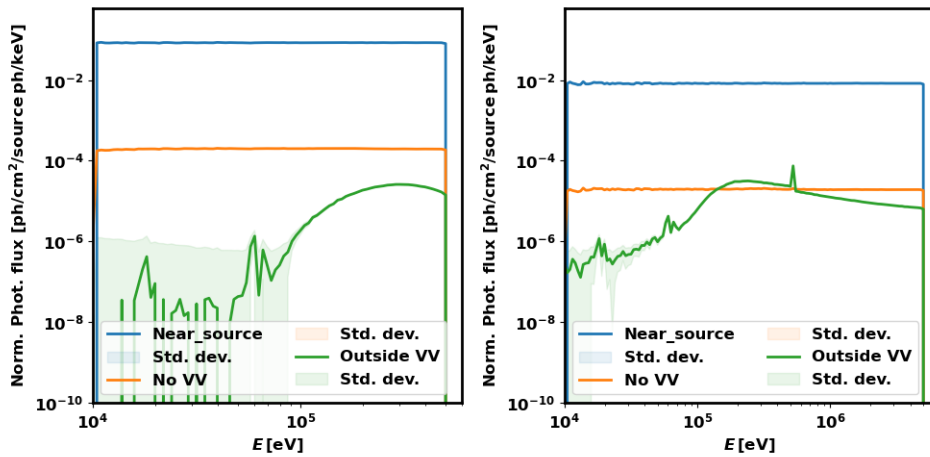


Figure 3.12: The attenuation of the HXR spectra due to the Inconel vacuum vessel of the COMPASS tokamak

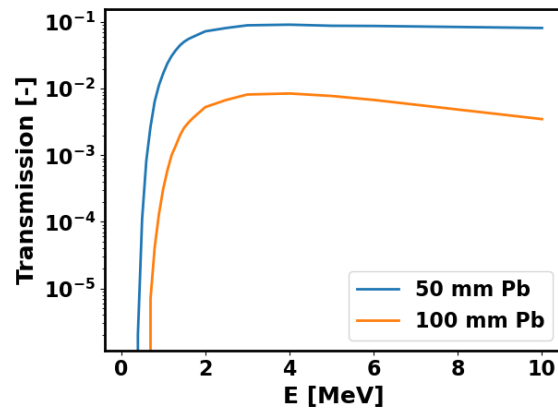


Figure 3.13: The transmission fraction of photons through lead shielding wall for two different thickness as a function of energy.

■ The connected signal with confidence intervals

Summing up this effort, the multiplication factors that need to be applied to recalculate the source rate are

- The spatial correction i.e. detector surface exposed to radiation vs size of the sphere at the detector position: the count rate needs to be multiplied by $2.3 \cdot 10^5$, the simulation with realistic crystal suggests that this factor must be 2-3 times larger due to escaping photons and other effects, this will be added to the confidence interval.
- Attenuation by the vessel - multiplication factor 2, confidence inter-

val depending on the energy or distribution function shape leads to multiplication factor up to 5.

- Attenuation by the lead bunker - multiplication factor 20, confidence interval, depending on the distribution function shape is 7 to 100.
- Other geometrical factors - non-homogeneity, anisotropy - confidence interval of multiplication factor 0.5 up to 2.

The anisotropy in terms of the flux variation in and outside the tokamak hall can be significantly higher in some cases. However as all the used detectors are placed at different locations outside of expected maxima or minima of a possible highly anisotropic pattern, i.e. forward beams on mid-plane with tangent cones from electrons impacting the protruding limiters, we assume that they measure close to average value of HXR flux within the unit sphere which is optimal for our purpose. This sums up to multiplication factor roughly $2 \cdot 10^7$ with confidence interval from $1.6 \cdot 10^6$ to $6 \cdot 10^8$. The result of the signal evaluations from figure 3.9 after application of these factors is shown in figure 3.14. The integral of the source of the HXR over the discharge duration reaches values close to number of runaway electrons that must be present to carry the maximum measured current or slightly lower than this value which is in the order of 10^{15} electrons for 100 kA of RE current. We would expect slightly larger number from the HXR counts compared to the number of RE calculated from the current as RE can be generated, lost and replaced by new RE and one electron can produce multiple HXR photons. Thus it seems that the actual multiplication factor should be slightly higher, but the HXR source rate is almost certainly within our confidence interval. This means that this method seems to be quite successful despite all the assumptions and uncertainties involved.

■ 3.3.3 Distinguishing HXR and neutron peaks in the tokamak experiments

The photoneutrons accompanying high energy runaway electron beams can be detected by scintillation detectors, however in order to correctly evaluate the fluxes of neutrons as compared to the HXR photons, it is necessary to separate the events caused by the two different particle species. The general description of the method and hardware used for this purpose is included in the section 3.2.3 of this chapter. One of the methods that can be used to distinguish the peaks caused by neutrons from the peaks caused by high energy photons is to plot a two-dimensional histogram of the peaks as a function of peak height and peak width (duration). With a suitable detector, two distinct lobes or structures should appear in the image of the mixed neutron and HXR field.

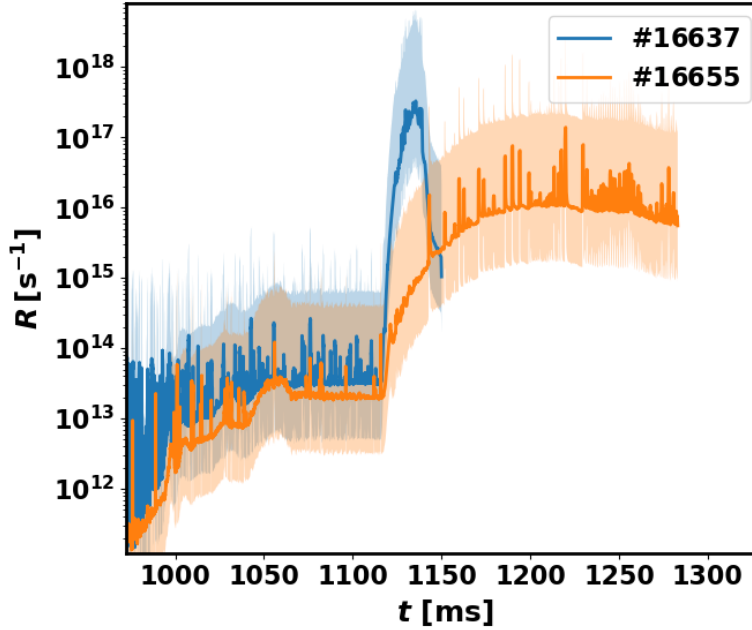


Figure 3.14: The compiled signal from 3 different detectors calibrated to absolute HXR source using the spacial corrections and attenuation factors.

The HXR peaks would form one of them and the neutrons the other one. The NuDET NEUTRON detector [77] proved to be suitable as it can detect the thermal neutrons but also the HXR photons with very different peak time characteristics. The 2D histogram of the peaks provides better control over the performance of the discrimination method. Moreover the 2D histograms allow also identification of pile-ups, gain drop or various significant noise phenomena in the signal. In the last campaigns of the COMPASS tokamak, the fast data acquisition was used with the NuDET NEUTRON detectors of different scintillator dimensions, i.e. different sensitivities, that were designed for the experiments and manufactured on request. The resulting peak histogram for a typical NBI discharge (almost exclusively neutrons) and typical RE discharge (large amount of HXR and some photoneutrons, detector outside the hall) measured by a sensitive detector (standard 40x4 mm disc scintillator [77]) is shown in figure 3.15. Same high voltage and data acquisition setup is used. With the 100 MSps (MegaSamples per second) acquisition rate, the HXR peaks lasting several tens of ns are detected but their width is just a couple of points. In the left part of figure 3.15, in the neutron dominant discharge, multiple blobs of similar height but different duration are apparent which do not have any reasonable justification and after close look on the signal, these features correspond to pile-ups of neutron peaks and a very significant loss of gain. In the right part of the same figure, the performance in the RE discharge is better with narrow peaks over large range of heights, however the highlighted lines parallel with the x-axis point to large number of pile-up

events again. The number of detected peaks is more than four millions within 200 ms in this case, therefore the pile-ups are expected based on the statistics. In the figure 3.16, the less sensitive detector (diameter of the scintillator 40

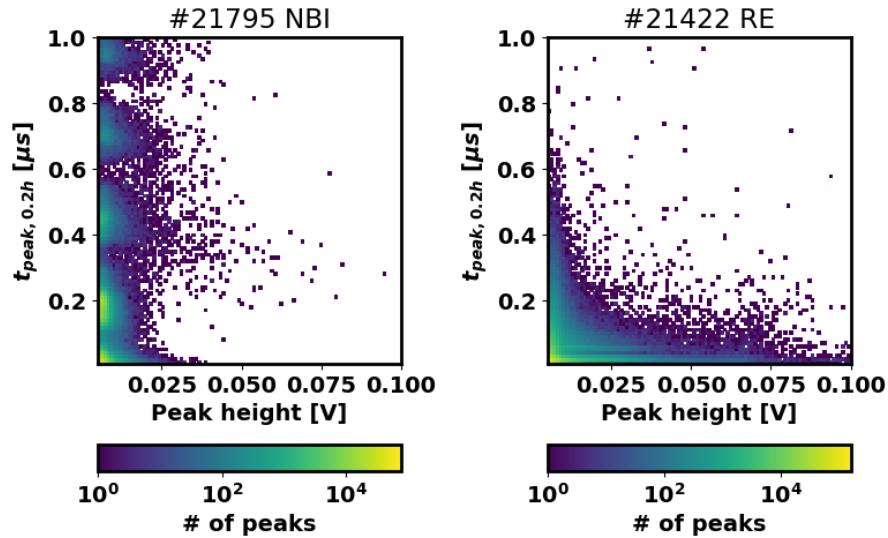


Figure 3.15: 2d histograms of peaks detected by a sensitive NuDET NEUTRON detector in the two selected discharges, x-axis represents the peak height and y-axis the peak duration at the 20% of the height.

mm and thickness just 0.4 mm) is detecting the peaks optimally. On the left, a continuous lobe of neutron peaks centered around width of 280 ns is identified. A signature of another lobe is at the lower margin of the time duration, corresponding to the HXR peaks. The 2D space can be thus divided into three segments as shown by the red lines - HXR peaks with height above noise and duration less than 100 ns, neutron peaks with height above noise and duration more than 100 ns and noise region with amplitudes below 10 mV. Note that the 1 MW NBI introduced significant noise in the PMT, thus larger noise margin is considered. The right part of the figure 3.16 shows the runway discharge, the noise is significantly lower and the neutron/HXR margin stays the same as it is the same detector. Apparently, the HXR peaks are very short, thus most of them are below the time resolution of the data acquisition and a couple of tens of neutron peaks can be identified. [h!] For a comparison, the same pair of histograms is show in figure 3.17 for a different scintillation detector that has a very good energy resolution for HXR photons and negligible sensitivity to neutrons. The well-defined linear structure that has peak width proportional to the peak height is visible in the right part of the figure. These 2D peak histograms allow for automated and reliable detection of photoneutrons in the signal and high dynamic range measurement of the HXR flux.

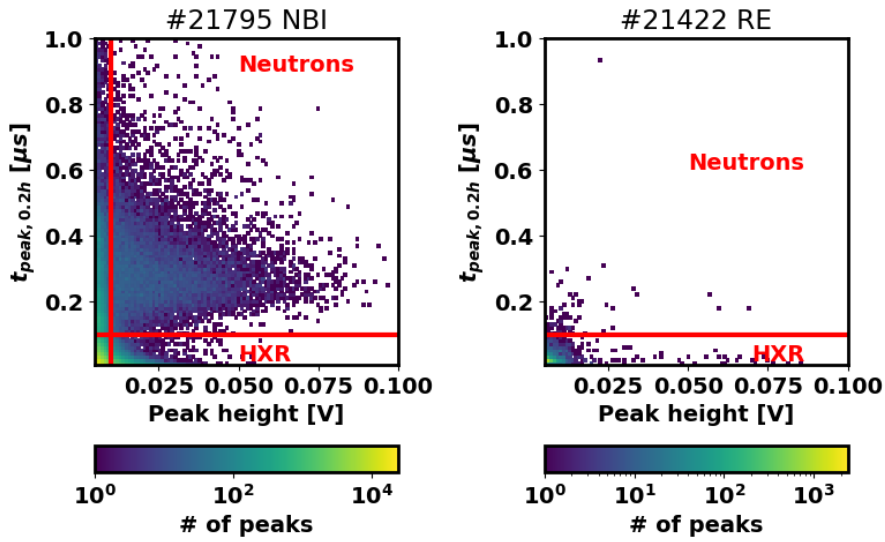


Figure 3.16: 2d histograms of peaks detected by a low-sensitivity NuDET NEUTRON detector in the two selected discharges, x-axis represents the peak height and y-axis the peak duration at the 20% of the height.

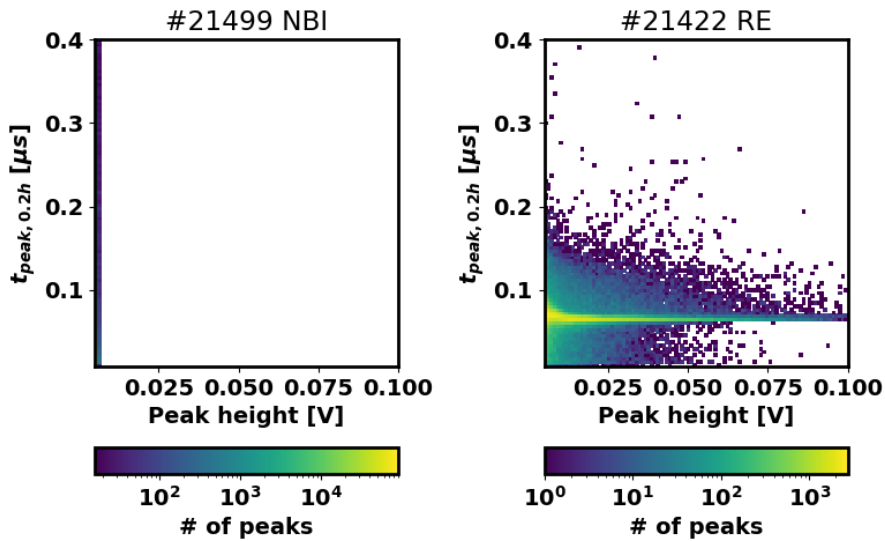


Figure 3.17: 2d histograms of peaks detected by a gamma detector $CeBr_3$ that is insensitive to neutrons, x-axis represents the peak height and y-axis the peak duration at the 20% of the height.

■ 3.3.4 Modification of AXUV and SXR tomography algorithm for the runaway electron beam

As mentioned previously the AXUV and SXR avalanche photodiodes are subjects to malfunctions during the RE experiments. The algorithm used for the tomographic reconstructions [63], recently restructured, optimised in Python and released as an open source code [108], was modified for the purpose of the reconstructions of the RE beam radiation on COMPASS. The modifications are described in the attached Paper B, page 3. Apart from the significant simplification of the smoothing matrix generation that is a general improvement of the code, reported in the [63] as well, the number of cameras used in the reconstruction had to be decreased on COMPASS. The only camera that was not irradiated by anisotropic and scattered hard radiation that was not possible to subtract in a straightforward manner was the bottom divertor camera looking up to the vacuum vessel and offering resolution along the radial direction. Moreover the boundary conditions had to be modified as well. The standard D-shaped limiter contour cannot be used without information about the vertical position of the radiation, the algorithm tends to put the center of mass of the radiation far below the midplane, where lines-of-sight are close to each other, creating non-physical artefacts. Unfortunately, the separatrix from the magnetic reconstruction cannot be used either due to special effects of the RE beam energy that are described further in this thesis. The problem was solved by using a circular boundary containing the separatrix with some additional space around it and without any prescribed derivative value of the reconstructed emissivity function at the reconstruction area boundary, especially at the plasma facing components. This configuration allowed for converging and realistic solutions, including identification of sharp radiation hot spots from LFS and HFS limiters in some cases.

■ 3.3.5 Installation of REIS2 spectrometer for measurements of synchrotron radiation

One of the tools that are currently used on several European machines for the detection of the synchrotron radiation is the REIS (Runaway Electron Imaging and Spectroscopy) diagnostics. The measurement with this diagnostics was also realised at the COMPASS tokamak. The hardware setup which was prepared by colleagues from ENEA, Italy, includes 4 spectrometers and 1 camera, optical cabling, objective and relevant electronics equipment. For the description of the previous version of REIS, see [81]. For the case of RE, the most important components are as follows:

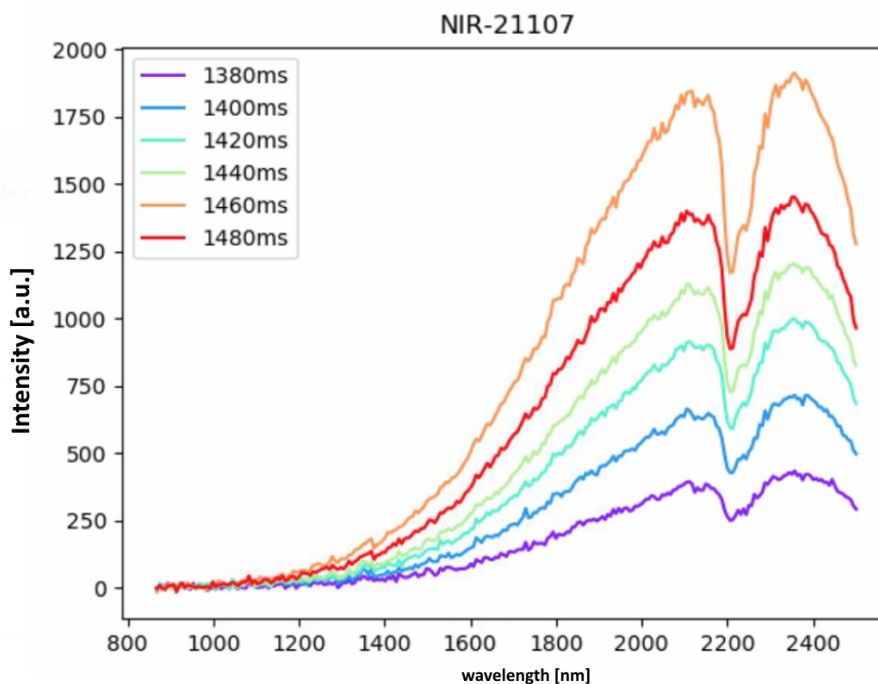


Figure 3.18: The NIR synchrotron radiation spectra from the RE beam in the COMPASS discharge #21107 for different time intervals, Courtesy of G. Ghillardi

valves placed at 3 different toroidal locations on port extensions at the LFS mid-plane of the vacuum vessel were used during the COMPASS operation. This type of valve has only two states - closed or fully opened for a given period of time when the voltage is supplied. During the calibration and before 9th RE campaign these valves were operated using waveform generator. During the experimental discharges the generators were effectively used to delay the universal diagnostics trigger coming right before the discharge. From the 9th campaign, the operation of the valve is controlled from the central controller unit based on the MARTE platform, this solution also directly saves the opening waveform data.

The valve that is used for injections of smaller amounts of gas (gas puff, impurity seeding) is based on the piezo-electric principle, it is the same valve type as the standard D2 fuelling valve. The piezo-electric valve used for the impurity injection is located in the bottom open divertor on the HFS of the vacuum vessel. The piezo-electric valve opening is controlled by the applied voltage, the response of the valve conductance C_v to applied voltage is approximately linear, although some threshold voltage needs to be applied for noticeable opening and there might be some hysteresis on the open-close path. This valve is directly controlled from the tokamak control system.

The flow rates of both valves can be measured using in-vessel pressure gauges after controlled injection of selected gas with the torus pumping stopped. The flow rate is affected by the valve properties, but also by the pressure

in the reservoir, technically the pressure difference between the two regions connected by the valve. However as we have high vacuum on the tokamak side and pressure in the order of atmospheric pressure on the reservoir side, the reservoir pressure is equal to the difference. The valve particle injection rate can be then calculated as

$$\frac{dN}{dt} = Q/V = C_v p_b / V = \frac{p_{vv}}{t_o} \frac{V}{k_B T}, \quad (3.4)$$

where $\frac{dN}{dt}$ is the particle flow rate, Q is the volumetric flow rate Δp is the pressure in the reservoir and V is the volume of the vacuum vessel. On the right hand side this is related to pressure increase in the vacuum vessel p_{vv} that can be measured, the time of the opening of the valve t_o and to the temperature T that is known and considered to be approximately 300 K. C_v is the conductance of the injection system, that should be independent of the other variables in the ideal case. A detailed calibration of the fuelling piezo-electric valve with different voltages was done with deuterium and reported in [109]. The calibration described here is focused on the parameters used during the injections - i.e. range of pressures and opening times used for the injections with the MGI system and piezo-electric valve to evaluate the number of injected particles directly. For better statistics and optimal pressure measurement range, bursts of multiple openings with the same parameters were used in the calibration valve opening waveforms. The pressure was measured by the broad range Pirani and Cold cathode combined vacuum gauge [110]. The number of openings in the waveforms are selected to be in the Pirani-only mode range. Both the Pirani and the Cold cathode measurements are sensitive to the vacuum pressure gauge. Pirani gauges, calibrated to nitrogen, typically indicate lower pressure for Ne, Ar and Kr than is the real value of the pressure in the given range around 1 Pa. Correction factors are fairly stable in this range being 1.39, 1.62 and 2.22 for Ne, Ar and Kr respectively. [111],[110]. Correction factors in the Cold cathode regime, that are applicable during some of the small amount injection measurements in the discharge are quite different [110].

■ Calibration of the MGI valve with Ar

The calibration of the MGI was done using argon and the North valve that was the primary MGI injection valve since the the east valve was moved closer to the toroidal field coil to make space for a new diagnostics and therefore not working reliably due to its magnetic principle of operation. In [20], the calibration is done for all three valves and variations of the opening time of the valve - minimum time of the voltage application for the valve to react, both between different valves and with the pressure in the reservoir were found. In the measurement described here, the variation seemed to be negligible,

furthermore the measurement here is done in more optimal pressure range in term of the gas sensitivity. However, the actual absolute value of injected particles with the common are similar calibration described here and in [20]. The results of the calibration with different pressures and valve openings are displayed in figures 3.19, 3.20 and 3.21. There is an apparent linear dependence of the number of injected particles on the opening time, which is defined as the time of application of the increased voltage with the reaction time of the valve electronic subtracted, in figure 3.19. The number of particles injected during a discharge is therefore typically in the order of 10^{20} which is an order of magnitude larger than the number of particles present in the vessel before the injection. Figure 3.20 shows also apparent linear dependence of the particle injection rate on the reservoir pressure. These values lead to the conductance C_v values near $10^{17} m^3 Pa^{-1} s^{-1}$, which is slightly higher compared to the values derived in [20], The conductance values differ for different opening times and pressures by variation of up to 20%.

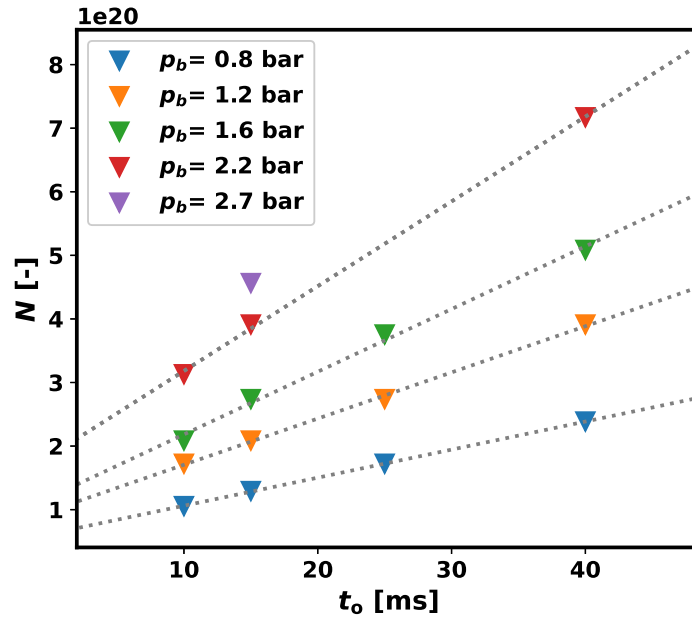


Figure 3.19: The number of particles injected by the MGI valve N as a function of the opening time t_o for different reservoir pressures.

The valve is connected to the larger volume of the reservoir through a couple of meters of thin connection tubes. Therefore it is expected, that the pressure would drop during longer openings of the valve. The particle injection rate drops as well as shown in figure 3.21, where the injection rate evolution with time was obtained by differentiating the data of measurements with different opening times. Despite the sparse data set, exponential decrease of the injection rate can be observed. This finding offers a rough correction

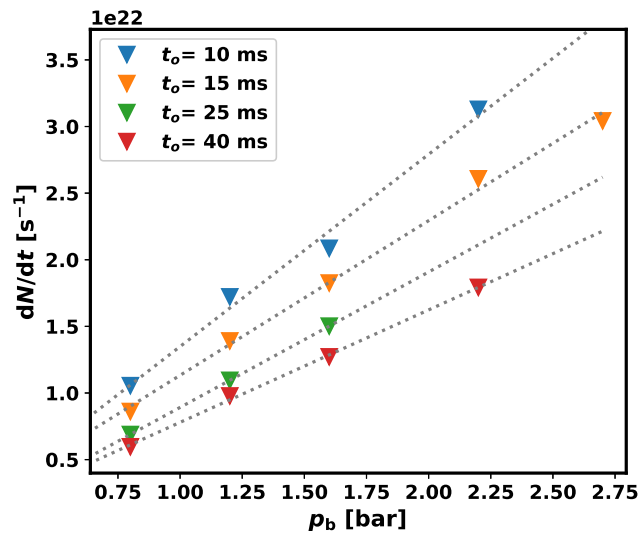


Figure 3.20: The particle injection rate dN/dt of the MGI valve as a function of the reservoir pressure p_b for the different opening times.

of the number of particles reaching the vessel during the experiments where evolution on the short time-scale is important.

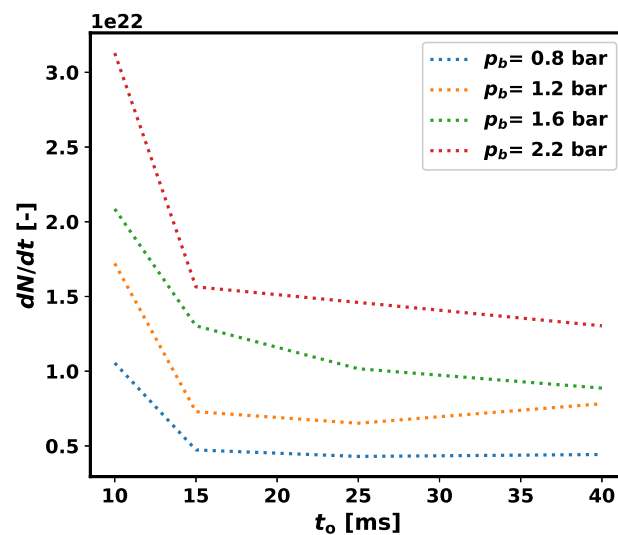


Figure 3.21: The evolution of the particle injection rate dN/dt of the MGI valve as a function time, based on differences between measurements with varying opening time.

■ Calibration of the piezo-electric valve with Ar, Ne and Kr

The piezo-electric valve was calibrated for the first time with impurity gases, in a similar manner as the MGI valve, however, due to the smaller conductance many more puffs had to be used to achieve the optimal Pirani gauge range. As we used the maximum voltage for the opening during most of the RE experiments, the calibration is done with the same setup and only the opening time is varied. The results are shown in figure 3.22, the typical gas injection puff of 20 ms duration leads to injection of $9 \cdot 10^{18}$ particles for the case of $p_b = 1.1$ bar. The C_v is reaching values approximately 25-30 times lower than in the case of the MGI, i.e. $4 \cdot 10^{15} m^3 Pa^{-1} s^{-1}$ and it shows much less pronounced dependence on the pressure and opening duration, perhaps due to shorter connection to the reservoir, and thus negligible drop in the real back pressure at the valve.

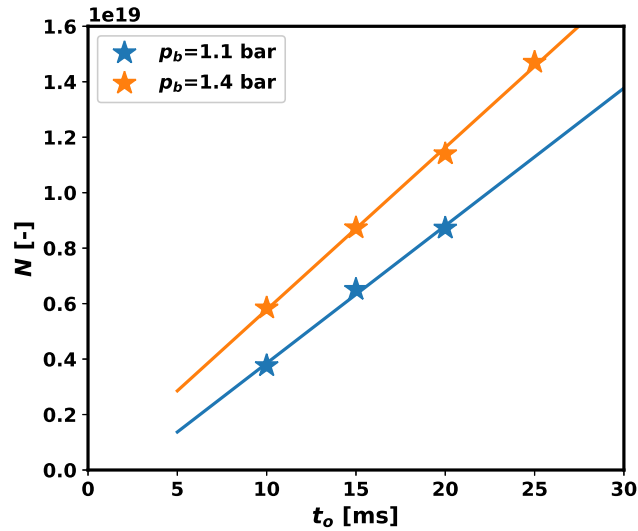


Figure 3.22: The number of injected particles via the piezo-electric valve for Ar and two different reservoir pressures as a function of the opening time.

The calibration was extended to cover three impurity gases (Ne, Ar, Kr) and the main injection parameters used. The results for 20 ms injection at 1.3 bar are listed in table 3.3. It seems that the lighter the gas is, the more particles are delivered to the tokamak vacuum vessel by the puff of the same parameters, which is expected. The decrease seem to be almost linear with Z or atomic mass. The expected gas propagation speed (speed of sound) is $\propto 1/\sqrt{m_A}$, however there can be other parameters and processes involved that affect the variation of the number of particles with the gas species. During this calibration, also 50% voltage amplitude was applied to the valve, however this results to injection of negligible amounts of impurity particles - 3 orders of magnitude lower than during 100% opening voltage

amplitude. Such puffs were indeed used in experiments with polluted gas pre-fill in the discharge start-up without any noticeable effect.

Element	Z	$N_{inj.} [-]$
Ne	10	8.8
Ar	18	7.6
Kr	36	5.6

Table 3.3: The different number of particles N injected by the gas puff of the same setup, varying with the gas species

■ Real time pressure measurement

The pressure measurement is conducted also in real-time during the COMPASS discharge by the same instrument, which can be used to confirm the estimate of injected gas amount based on the calibration. The pressure measurement is however subject to delays due to the gas propagation, so gas amount injected can be related to the peak of the measurement which may come even shortly after the discharge termination and the information about the time evolution of pressure rise usually cannot be traced to the actual injection evolution.

■ Residual gas analysis (RGA)

A more sophisticated measurement that is providing partial pressures of the different gases in the vacuum vessel is based on the residual gas analysis (RGA), that is using a mass spectrometer able to detect atoms of gas with atomic mass up to 50, in case of the model used on COMPASS. The scans with RGA were occasionally run during the COMPASS, RE campaigns especially in case of more complicated injections with gas mixtures. The examples of the results of the measurements are shown below. In figure 3.23, the elements contained in the pumped vessel after the discharge with Ar and Ne injection are shown, except these two elements, traces of deuterised methane or ammonia can be found, however at very low pressures.

The figure 3.24 shows time evolution of selected mass/elements in the discharge sequence of #18890, the actual discharge and injection that takes place on a time scale much shorter than the measurement time resolution are clearly visible in the data, the partial pressures of Ne and Ar can be roughly read. The subsequent pressure drop is not only caused by the active vacuum

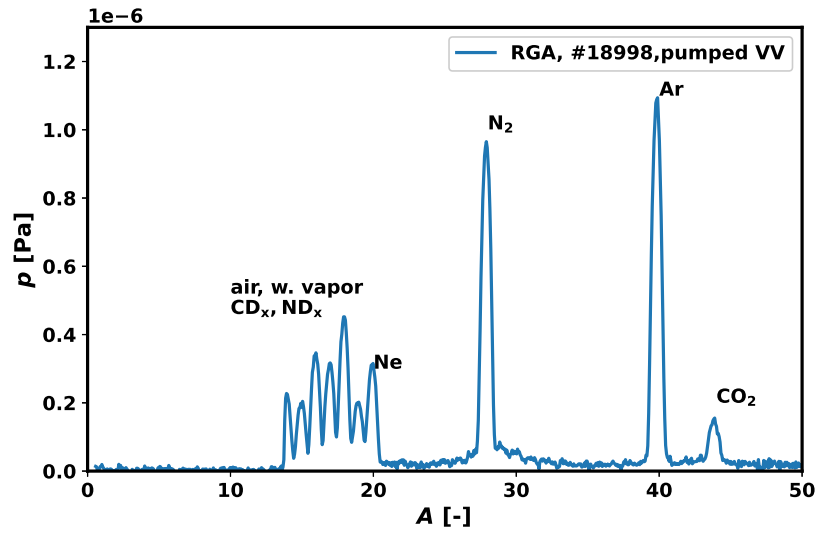


Figure 3.23: RGA scan performed after discharge #18998, Ar and Ne residuals and common impurities contribute to the pre-discharge residual gas pressure p in the ultra-high vacuum environment of the tokamak.

pumps but also by the adsorption on the carbon tiles (namely in the case of the deuterium) and other phenomena.

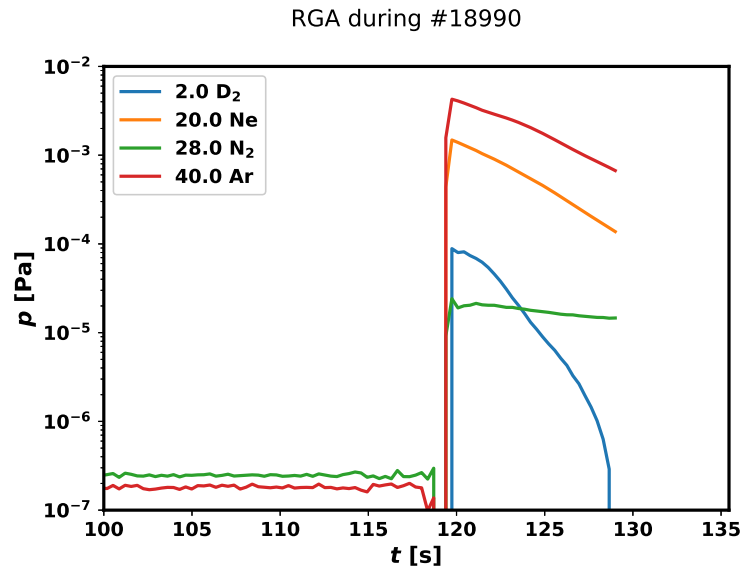


Figure 3.24: RGA time evolution of the main gas species partial pressures p before and after the COMPASS discharge #18890, the legend show the atomic mass. The injection of the Ar+Ne mixture along with the deuterium fueling and nitrogen pollution is obvious.

■ 3.4.1 Simulation tools relevant for secondary RE effects and other useful tools

On top of the dedicated codes for RE physics, some of the standard tokamak plasma physics codes, nuclear transport codes and other relevant tools that are useful for the evaluation of secondary RE effects, diagnostics modelling or evaluation the background plasma parameters for the input of the RE codes and experimental analysis are listed in this section.

- Nuclear transport simulators - MCNP6[116]/openMC[104], GEANT4[117], FLUKA [118] - HXR, photoneutron production, RE energy deposition in solid materials, damage caused by HXR beams, etc.
- DeGaSum [119] - HXR spectrometer toolkit allowing also inversion of the HXR spectra to RE distribution function
- Plasma Equilibrium tools - EFIT [120], JFIT, etc. and equilibrium post-processors e.g. Pleque
- Perturbed Plasma Magnetic Field - MARS-F [121], etc. - background for RE transport in perturbed plasmas, e.g. due to effects of RMPs
- Background plasma radiation tool/synthetic diagnostics environment, e.g. Cherab [122].
- FEM physics environments - ANSYS, COMSOL, etc. - simulation of relevant physics effects outside plasma and nuclear physics in tokamak - heat transport in solid materials, EM fields of tokamak coils or currents induced in the passive structures, etc.

Chapter 4

RE experiments on COMPASS and other tokamaks - scenarios and main results

After the importance of RE mitigation for safe ITER operation was realised as a crucial topic, almost all important European tokamaks were requested to study this phenomena. The research of runaway electrons needs discharge scenarios outside of the typical tokamak discharge conditions. The experiments focused on Runaway Electron generation in disruptions have a long tradition at JET, currently the largest operating tokamak. COMPASS has joined the Italian tokamak FTU in conducting RE experiments in 2014 within the framework of Medium Size tokamak workpackage of the Eurofusion Consortium, while main "Medium size tomamak" machines, Swiss TCV and German ASDEX-Upgrade have been conducting dedicated experiments since 2015. In the following paragraphs, brief review of the experiments conducted at different machines is given, to provide the reader with an improved picture of the common aims of the facilities in relation to the results section of this thesis.

4.1 European tokamaks with extensive RE program

First, let us introduce the basic differences between the machines and their important features. The most important parameters of COMPASS, the currently designed COMPASS-Upgrade tokamak, TCV, ASDEX-Upgrade and JET and their plasma discharges are shown in tab. 4.1. The the meaning of the abbreviations included in the table is as follows: single null divertor

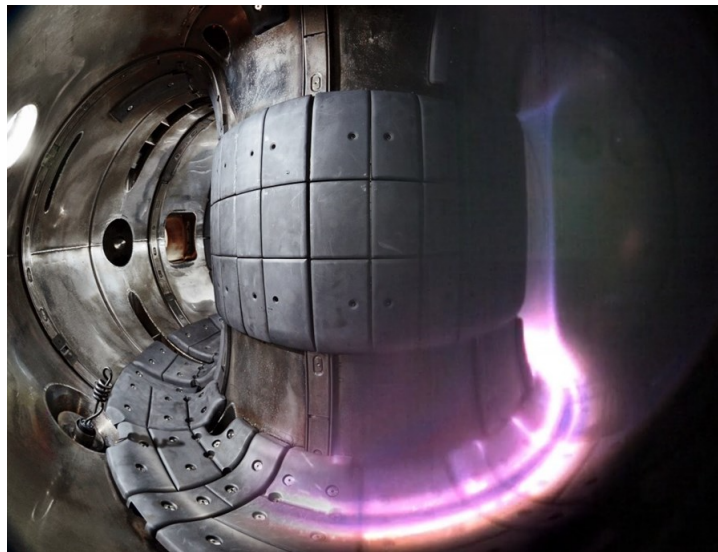


Figure 4.1: View of the vessel interior of the COMPASS tokamak combined with the view of the diverted plasma discharge. Courtesy of IPP Prague

were the quick deployment of new diagnostics, excellent coverage of magnetic diagnostics (more than 400 diagnostics coils), the most variable set of saddle coils for generating controlled error fields among European tokamaks and low risk of damage even during extreme scenarios. A combined view of the interior of the COMPASS plasma vessel and the plasma discharge is shown in the figure 4.1. The plasma facing components were made of graphite, which is able to confine significant amount of deuterium atoms via adsorption. This uncontrolled source of the deuterium atoms then affects the density control, crucial for the RE physics. The overview of the recent results of COMPASS, including some of the disruption and RE physics, is given in [125].

■ 4.2.1 COMPASS diagnostics and gas injection setup

Before its shutdown in 2021, twelve RE experiment campaigns have been conducted on COMPASS since 2014. The first campaigns were mostly focused on exploration of the RE behaviour in the machine and testing possible scenarios and basic RE diagnostics, while the most recent campaigns conducted with more experienced team, produced very useful dedicated scans and unique experimental details. The description and the details of namely the first 4 RE campaigns are summarised in the PhD thesis of Milos Vlainić [20]. The general scheme of the plasma diagnostic systems that were running throughout most of the lifetime of the COMPASS tokamak at IPP is shown in fig. 4.2 in a top view of the machine. The scheme shows most of the diagnostics listed in chapter 3 as the background plasma diagnostics, the extended gray

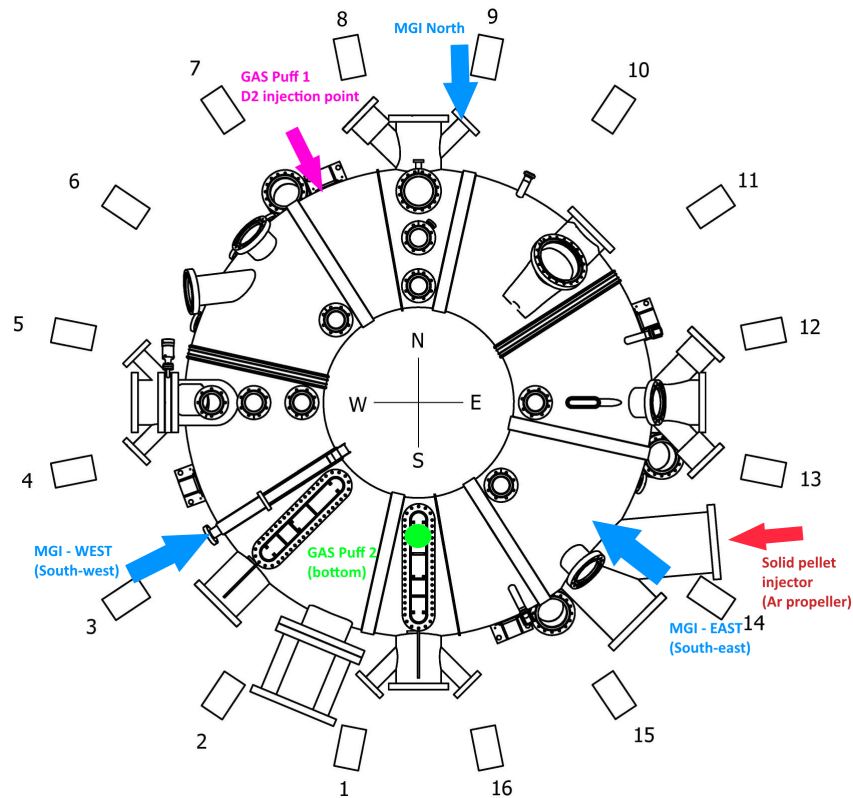


Figure 4.3: Gas injection valve locations at the COMPASS tokamak

4.2.2 COMPASS RE campaigns

The periods of the RE campaigns in the COMPASS life-time can be clearly identified via the radiation effects in the plot with long term statistics of average radiation measured by the HXR (**HX**) and the neutron detectors (**SHX**) during the discharges. This analysis is summarised in figure 4.4, the twelve RE campaigns can be easily recognised in the data of HXR NaI(Tl) detector in the top frame and Pb-shielded scintillator sensitive to both neutrons and HXRs in the bottom frame. For better orientation, these campaigns are highlighted in red and orange colours in the two plot frames, respectively. Beyond the RE dedicated campaigns, it is apparent that the increase of experience during the operation lead to suppression of the undesired RE events during the discharges, especially during polluted plasma start-ups.

The overviews of 5th to 12th COMPASS RE campaigns are included in the appendix B, which contains basic data about the campaign, diagnostics placement scheme, list of special diagnostics and summary of main aims and results for each of the campaigns. The most important results are detailed in the following chapters.

diagnostics (Cherenkov detector, HXR spectrometers), model validation of the basic generation mechanisms, but especially for the start-up RE physics and detailed investigation of the runaway electron transport in the discharges where activity of magneto-hydrodynamic instabilities is significant. Some of these effects are described in [18] and further in chapter 5, other results of RE generation in the low density discharges are presented in [16]. These discharges can be circular but also shaped and diverted. A similar discharge regime with respect to the RE [74] can be also studied in the Golem tokamak which is the oldest and one of the smallest tokamaks in operation, currently placed at the Czech Technical University.

3. **RE-dominated/slide away discharges:** If the density of a plasma discharge is low enough and the discharge is sufficiently long, the previous scenario can transfer to the slide-away discharge where majority of the current is carried by the electrons that are not a part of the Maxwell distribution, but gradually accelerated to relativistic energies at high E/E_c . Such discharges can then reach much longer duration than standard COMPASS discharges as very little loop voltage is needed for the current drive once the current is overtaken by the RE. It is important to note that in order to achieve low enough densities for this scenario on COMPASS, the wall had to be extremely clean and campaigns just after fresh boronisation were preferred. The worst terminations in terms of fast camera observation of PFC destruction were observed in this scenario.
4. **Pure RE beam produced by massive gas injection induced disruption in the ramp-up phase:** This scenario is the most relevant one for the large machines (AUG, JET, etc.) - most of the runaway electrons are generated at the moment of disruption due to the increased electric field induced by the quickly decaying plasma current and due to the fast cooling of the plasma (Dreicer mechanism is most probably much more important than hot-tail mechanism on COMPASS due to the small temperature) and subsequent avalanche multiplication. On COMPASS, it is however difficult to reach this scenario and it suffers from poor reproducibility. A disruption with distinct current quench and RE plateau was achieved almost exclusively in the current ramp-up phase of the discharge and with low electron densities.
5. **RE beam generated by gradual destruction of thermal plasma using injection of smaller amount of impurities** is a scenario that has proven to be the most useful and sufficiently reproducible to study various RE mitigation methods and improve understanding of the RE behaviour. Other small machines, like the Swiss tokamak TCV, implement a very similar type of scenario as well [126]. The most important difference with respect to the previous case or to the disruption generated RE beams at larger devices is that sufficiently large RE seed is built up before the injection and typically a smaller amount

of impurity gas is injected via a valve with smaller throughput, typically a piezoelectrically controlled valve or MGI with lower back pressures.

In the following lines, we will add some details to the description of the last two scenarios in the list as they have special control setup and options.

■ 4.3.1 The ramp-up scenario

At COMPASS, this scenario is particularly difficult to be achieved with sufficient reproducibility. It appeared that disruption with partial current quench and subsequent RE beam generation can be achieved in the plasma current ramp-up phase by injecting relatively large amount of Ar using fast solenoid valve (MGI). Typically, the injection triggering the beam generation is imposed 10-30 ms after the plasma current breakdown. The important limitation of this scenario is the fact that the plasma current is not controlled in the feedback regime in this phase of the discharge. The central solenoid (CS) is pre-magnetised to a certain negative current before the discharge to allow maximum flux swing and then discharged up to zero. Only after it crosses zero, the CS current is controlled in the positive value phase, which is typically in the flattop and ramp-down of the discharge. The electric field during the breakdown and ramp-up can be thus controlled only by changing three parameters - the maximum pre-magnetising current amplitude and switch-on times of two thyristors that cause drop of loop voltage, slower discharge of the CS [127]. By the means of these parameters, the electric field current ramp-up phase is pre-programmed within a relatively small range of options of three amplitude levels. The thyristor switch-on times were typically decreased during the dedicated RE experiments with this scenario to achieve higher probability of the RE beam generation. This is counter-intuitive as this causes lower electric field, however lower loop voltage may cause worse burn through of the plasma impurities which may enhance the RE generation in effect. This interpretation is further discussed in the subsequent chapters. An example of the evolution of plasma current, density, loop voltage and the direct in-vessel measurement of runaway electrons of energies higher than the given threshold, as measured by the Cherenkov detector, is shown in figure 4.5, together with the compiled HXR signal from multiple detectors as derived in section 3.3.2. The RE beam current has reached about 40 kA in this case, the injection comes very early in the discharge and the Cherenkov detector shows exceptionally interesting evolution, where low energy RE reach the detector head very early, while large energies come later. Also, the shielded HXR detector shows larger fluxes in the point where the standard HXR detector already saturates. A similar figure with other signals important for this scenario is shown also in the attached Paper B, figure 2. It has been

observed that this scenario may develop in 3 ways in general

- normal disruption with some REs being generated but lost immediately and no noticeable RE current plateau achieved
- partial current quench and generation of the RE beam - the beam can either have a negligible current of several kA, or significant of a couple of tens of kA - these categories are considered as separate ones in [17].
- complete conversion of the current to RE with subsequent rather slow decay

These 3 (4) cases were already identified in [17], however not all properties of this scenario were understood after the first campaigns and especially the "slow radiative decay" has not been correctly identified as full RE beam which is now confirmed by the Thomson scattering measurement of negligible values of temperature after the Ar injection. The boundaries of the preset parameter regions that lead to different cases may vary in time. The reasons for this and also for the fact that the scenario with partial current quench is almost exclusively achieved in the plasma current ramp-up may be several - the ramp-up is naturally accompanied by increased loop voltage U_{loop} and non-monotonic profiles both in terms of the radial density, current and temperature distributions but also in terms of the distribution of the supra-thermal electrons. Furthermore, the carbon wall may release uncontrolled amounts of deuterium that was adsorbed on the tiles and the generation in the early ramp-up phase is probably strongly linked with the start-up RE physics that is described in the next chapter. The discharges from the first couple of RE campaigns at COMPASS were analysed in [17] and [20]. Especially correlations of resulting runaway electron beam current and the type of the disruption with the pre-disruption plasma parameters were investigated in the thesis [20]. Later, numerous interesting details were reported based on the more focused sets of COMPASS experiments, e.g. clear magnetic field dependence [21] (Paper C) of the achieved RE beam current and the first observation of the short living filaments most probably formed of newly accelerated RE [18] (Paper A), some of these results will be further discussed in the following chapters.

■ 4.3.2 The flattop scenario with TQ and full current RE beam

At COMPASS, an additional valve of the very same type as the standard fuelling valve is typically used for impurity injection in this scenario, located

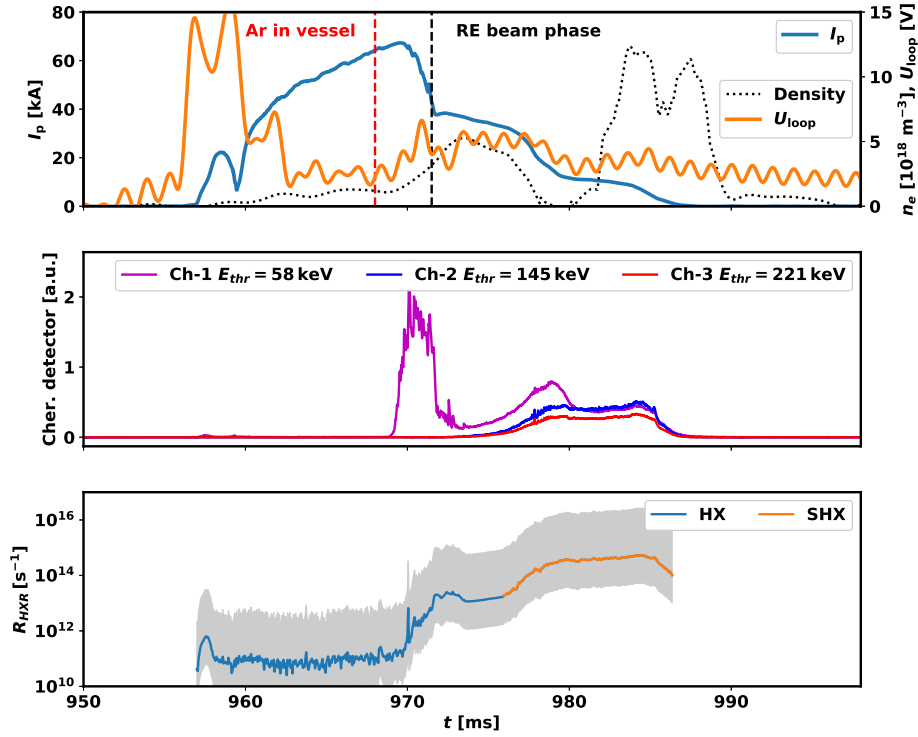


Figure 4.5: Time evolution of the most important plasma parameters and radiation diagnostics in the ramp-up scenario, discharge #13123

in the divertor area at the south of the machine. This injection scheme leads to a much slower thermal quench and even with small pre-injection (seeding) RE populations it secures generation of RE beam in the majority of the cases with current reaching full pre-injection current. The current of the beam decays after this type of injection by a much slower rate than in case of the massive gas injection, proportionally to the amount of the injected gas and other conditions [22]-Paper B. The most important advantage of this scenario is that the RE beams can be generated in the phase of the discharge where the current and current centroid position is fully controlled in the feed-forward or feed-back regime and thus special requirements on the beam acceleration, deceleration or position control can be imposed unlike in the ramp-up scenario. The MGI can be also used for the generation of quickly decaying full current RE beam in this scenario as well, as reported in [22], however for better control and longer duration, the smaller injected amount via the piezo-electric valve is preferred in order to study effects of other actuators like the resonant magnetic perturbations, secondary injections etc. This scenario is apparently less relevant to the reactor conditions in terms of RE generation as it relies on densities and RE seeds which should be well outside of the operation space, however it is a very relevant tool for understanding the RE beam behaviour and applying the mitigation techniques. At the same time, the existence of this scenario brings the very interesting conclusion that a full pre-disruption

current RE beam can be generated under suitable circumstances - in contrary to the usually achieved maximum current fractions of 60% [128] or 70% [15] of the pre-disruption currents during RE beam generation in a classic disruption. This fact highlights the need of the RE seed suppression in big machines, otherwise a series of failures can lead to this scenario e.g. via slightly failed burn through with start-up RE generation, followed by inability to restore the density control and activation of disruption mitigation system with a large impurity fraction that enhances the RE generation. A series of events that is very unlikely to happen but still not impossible and important to consider.

4.3.3 Zero and controlled external loop voltage during the RE beam phase

The external loop voltage, generated by the change of the current in the central solenoid, is typically governed by the feedback control of the requested plasma current on COMPASS. The control algorithm is adjusting the rate of the change of the current in the central solenoid to keep the plasma current constant. While the resistivity of the plasma may change with temperature and presence of impurities, the control is straightforward as the dependence of the plasma current on the voltage is still linear. This is not suitable for the RE beam in the high Z impurity background plasma as the relation between loop voltage and current can be non-linear (various RE generation mechanisms, acceleration, etc.) and depends on many other parameters. Therefore, it was desirable to design a control approach that would allow to fix the values of the dI_{OH}/dt from given time either at zero or at selected constant value. Several approaches were gradually tested to achieve this aim:

1. Reference and feed-forward: in a reference discharge with the current feedback, the evolution of the I_{OH} is recorded with special attention to find out the value reached during the injection, in the next discharge the I_{OH} is approximately programmed in feed-forward regime up to the injection, then fixed I_{OH} value is kept further. This approach is sensitive to changes of the plasma behaviour before the injection and requires another reference after a couple of discharges.
2. Automatised "catch value": special function that gets the value of I_{OH} from the standard controller at a given time and keeps constant I_{OH} from this point further.
3. Catch value + fixed $\frac{dI_{OH}}{dt}$: similar as previous point however instead of keeping zero derivative of the I_{OH} , this approach keeps selected non-zero value - both positive values - corresponding to controlled acceleration - and negative values, corresponding to braking of RE, can be requested.

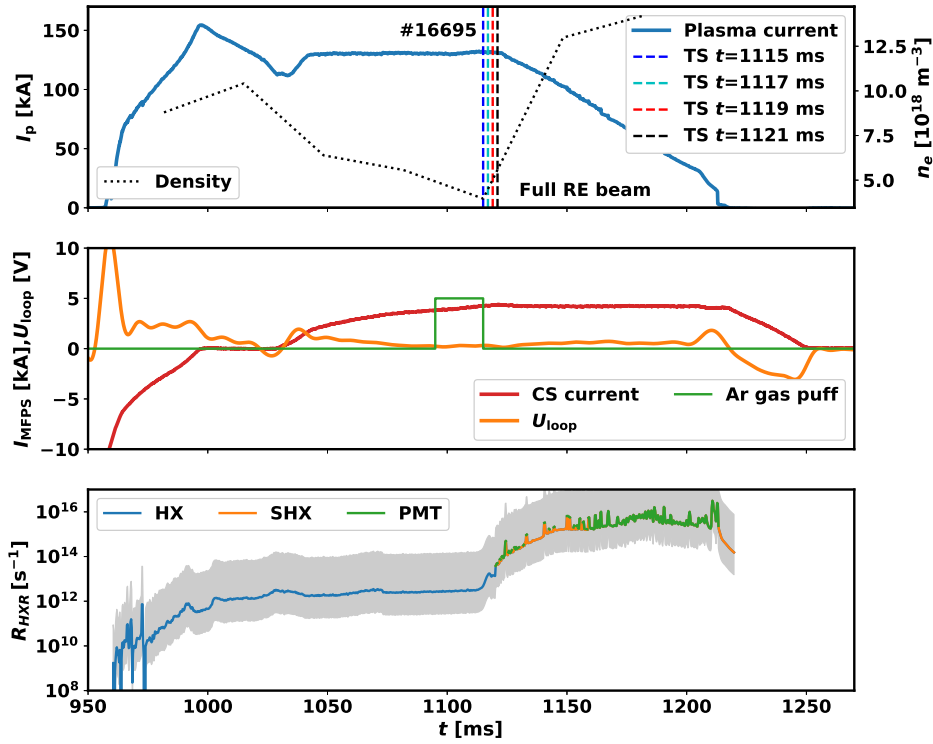


Figure 4.6: Time evolution of the most important plasma discharge parameters and HXR radiation diagnostics during the RE beam generation scenario triggered by small impurity injection amount in the flattop

The catch value was applied in the latest campaigns routinely, typically 5 ms after the closing of the impurity injection valve in case of the flattop scenario, i.e. shortly after the beam was generated. The evolution of the main plasma parameters - the plasma current, the electron density, the loop voltage, the current in the central solenoid, the Ar injection and the synthesised HXR signal (as derived in section 3.3.2) is shown in figure 4.6. It is apparent that the span of the HXR fluxes is 10 orders of magnitude and all the detectors from the detector chain come into play. The vertical lines in the top frame show timestamps of the temperature measurement by the TS. The corresponding profiles showing gradual decay of the temperature are included in figure 4 of the attached paper B [22].

4.4 Important COMPASS RE results complementing this thesis

The very extensive analysis of the low density scenario in the early COMPASS campaigns, MGI RE beam generation experiments, synchrotron radiation measurements and other important topics were summarised in the thesis of Miloš Vlainić [20], mentioned already multiple times in the previous text. Some of the results in the further chapters of this submitted thesis will be put into context of the analysis done by Vlainić. In the following paragraphs, the work lead by other colleagues and students at COMPASS in the field of RE diagnostics, RE experimental analysis is acknowledged and briefly described to give the reader a broader picture of the COMPASS RE activities and context of this thesis. The author of the submitted thesis has also provided help with experiment execution and analysis in some of these topics.

4.4.1 Critical electric field at COMPASS

One of the simplest but also most important validations of the theoretical formulas describing RE generation is the measurement of the critical electric field. Experimentally measured value is especially important as it draws the safety boundary for each device. The critical value boundary above which the RE appear should be $E/E_c = 1$, however in the experiments this value appears to be higher, some of the theoretical reasons for this were mentioned in chapter 2 and experimental analysis on multiple machines was done in [129]. Using a similar experimental scenario, i.e. avoiding the start-up RE and decreasing the density in the flattop it was shown that the $E/E_c = 14 - 20$ is needed for significant RE generation as reported in [20] and [130]. This result may be also affected by the threshold of the HXR measurement which is given by the spatial conditions and detector sensitivity as approximately 10^8 s^{-1} of minimum lost RE to be detected by the detectors and uncertainties of the measurements of other quantities, however the fact that the ratio is multiple times higher than the theoretical prediction is beyond any doubt.

4.4.2 The effect of shaping and density on RE losses

In COMPASS, elongated or diverted plasma scenarii seems to confine the RE much better than simple circular cross-section plasma even at high densities. While at $n_e = 3 \cdot 10^{19} \text{ m}^{-3}$ all RE generated during the start-up are lost from

phase or in the RE beam phase should increase the transport of the RE and possibly help to terminate the discharge with negligible damage. The COMPASS RMP coils which can achieve quite strong relative amplitudes much larger than $\delta B/B = 10^{-3}$ do affect the RE population significantly, as shown in [63] - Paper C, figure 6. Indeed, without the impurity gas injection, the current decay is accelerated significantly during the RMP application due to increased magnetic field stochastisation and RE transport. If RMP is applied before or after impurity gas injection, it results in significantly faster and wilder decays of the RE current or, in some cases, to complete prevention of the RE beam generation. More results, including supporting simulations were part of invited talk of E. Macúšová [137]. Simulations of the RE losses for COMPASS and DIII-D using the REORBIT and MARS-F codes are summarised in [64].

4.4.5 Injection of graphite pellets

In the view of the SPI program at other European tokamaks, the options for massive material injection of other type than massive gas injection were considered and to this end the Room Temperature Solid Pellet (RTSP) injector was borrowed from the ASDEX-U and used for injection of small carbon or boron-nitride pellets for triggering the disruption but also to attempt the mitigation of existing RE beam and to complement the RE beam diagnostics. The effects of the pellet on the plasma/or RE beam are very different compared to the gas injection and have been studied among other means, by the very fast cameras. The technical work on the adaptation of the system in the COMPASS environment and the physics results are very briefly mentioned in [125], while dedicated publication is in preparation by J. Čerovský.

4.4.6 Calorimetric measurements

In order to measure the total energy of the RE beam after its impact, a special graphite limiter was equipped with several temperature sensors at different positions and placed on the reciprocating manipulator. Using thermal dynamics simulation, the deposited energy could be estimated from the measured temperature evolution for many of the discharges in the last RE campaigns and the measured values are significantly higher than 10 kJ in some cases. A detailed description is given in the master thesis of Jakub Čaloud [84] and recent conference contribution [138]. Lately, the impact of the fast particles and generation of heat in the limiter has been modelled using FLUKA.

normally applied. The comparison of the measured current, electron density and HXR signal evolution for a typical COMPASS and typical TCV discharge with full conversion is shown in figure 4.7. The TCV can apparently reach much longer discharges, however otherwise the scenario is quite similar, the injection in this TCV discharge is more intensive but significantly shorter than in the COMPASS discharge (4 ms vs 20 ms) with the resulting RE current decay being slower in TCV, which may be attributed partially to lighter gas species but most probably to smaller injection amount if normalised by vessel volume. The negligible temperature of the plasma is confirmed in both cases by the Thomson scattering (not shown here). Both discharges rely on gradual build up of the pre-injection RE seed which is visible in the logarithmic display of the HXR signal. The HXR chain is used in the COMPASS case, while in the TCV case a single signal from the "PMTX", a detector that is characterised by sensitivity somewhere between the second and third detector in the COMPASS detector chain, is used. In both cases, the RE beam current decay is accompanied by small steps in the current and HXR spikes occurring at the same time, this corresponds to abrupt losses of a significant fraction of RE.

Lately, the experiments with secondary injection of light gas species (deuterium or helium) to achieve benign termination (discussed in further chapters for JET) have been also successfully performed and make important contribution to the international effort.

■ 4.5.2 RE experiments at ASDEX-U

The ASDEX-Upgrade is the second largest European tokamak and importantly the one with tungsten plasma facing components which is very relevant to ITER and potentially to DEMO as well. The magnetic field and currents achieve significantly larger values than in COMPASS and the machine is equipped by the auxiliary heating of all three major types - the NBI, ECRH and ICRH with quite large heating power. The RE experiments there have also been conducted since 2015, focused almost exclusively on RE beams generated during a disruption triggered by Ar or Ne MGI at the end of plasma current ramp-up, which means that the loop voltage is slightly larger than in the flattop case, similarly to the COMPASS RE beam generation scenario but with much larger currents and plasma temperature. The first results were reported in [142], RMPs using top and bottom rows with various mutual phasing were applied during the disruption with results confirming a specific phase as causing significant decrease in post-disruption RE current [143]. Other experiments include RE beam generation at different parameters, e.g. edge safety factor value or very different temperature profiles with core temperature reaching up to 14 keV achieved by ECRH/ECCD and comparison of different

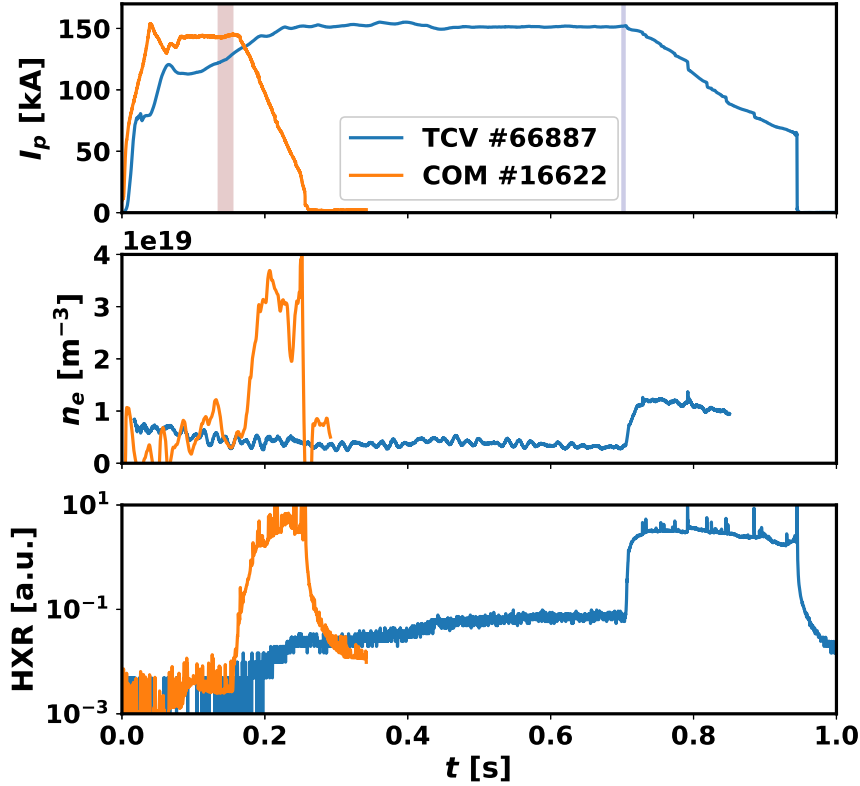


Figure 4.7: Comparison of flattop RE beam generation scenario of TCV (blue) and COMPASS (orange): first frame shows the plasma current and the opening of the injection valve that initiates the RE beam for each machine, second and third frame show the electron density evolution and the HXR signal, respectively.

gas species, namely Ar and Ne. In general, the effect of ECRH heating on the resulting RE current was recognised as important and the dependence of the RE generation on the ECRH power seems to be non-monotonic. Most probably high resistivity - lower temperature - plasma disruption is dominated by Dreicer RE generation while very high temperature plasma disruption RE generation can be dominated by the hot-tail mechanism. Very low probability of production of RE beam was observed with some intermediate values of central ECRH heating but this observation is yet to be properly analysed. Correlations of pre-disruption parameters with the RE generation were investigated also in [144]. Lately, the benign termination inspired by the results from JET [145] and DIII-D [146] was successfully attempted and the results will be published in near future. ASDEX-U RE beam generation results were also compared to ASTRA [115], GO and CODE simulations [147].

Some of the features of the RE beam generation experiments in COMPASS, TCV, ASDEX-U and JET were also compared in the paper by Vladislav Plyusnin [148].

A comparison of the disruption-generated RE beam in COMPASS, ASDEX-U and JET is shown in figure 4.8. Qualitatively the scenarios are comparable in all machines, all phases of the typical disruption and RE beam generation can be identified - the current spike, the CQ, the RE beam plateau and termination. However, the scale in both time and current magnitude is very different with COMPASS RE beams having small tens of kA and 10 ms, while AUG and JET RE beams are reaching several hundreds kA or even over 1 MA, respectively. The duration of the beams shown in this figure is just small hundreds of ms, while with improved position control and different mitigation strategies multiple-second beams were achieved in both machines. AUG is often using controlled ramp-down of the beam, while JET RE beams used to typically be vertically unstable and terminated more abruptly in some cases. The HXR signal is enhanced in case of larger current decay rates which is expected and further confirms that current is carried by RE. The figure suggests that the scaling and comparison of the RE beam experiments between the experiments is desirable and extrapolation towards ITER can be possibly conducted.

■ 4.5.3 JET

Joint European Torus (JET) is currently a largest operating tokamak in the world (soon to be joined by slightly larger Japanese machine JT60-SA) and the only one able to operate with the high fusion gain deuterium-tritium fuel mix. As the main test bed for ITER, it is equipped by the PFCs of the same material - i.e. main chamber limiters made of beryllium and divertor made of tungsten (ITER-Like-Wall, ILW). It is able to operate with large currents up to 4 MA and high toroidal magnetic field intensities up to 3.5 T. The auxiliary heating systems include NBI and ICRH with large heating power (nearly 40 MW in total). The interior with the ILW and overlay of the discharge radiation is shown in figure 4.9. The recent JET results are reported e.g. in [149]. The recently installed SPI further enhanced the disruption and RE physics capabilities of the device [150].

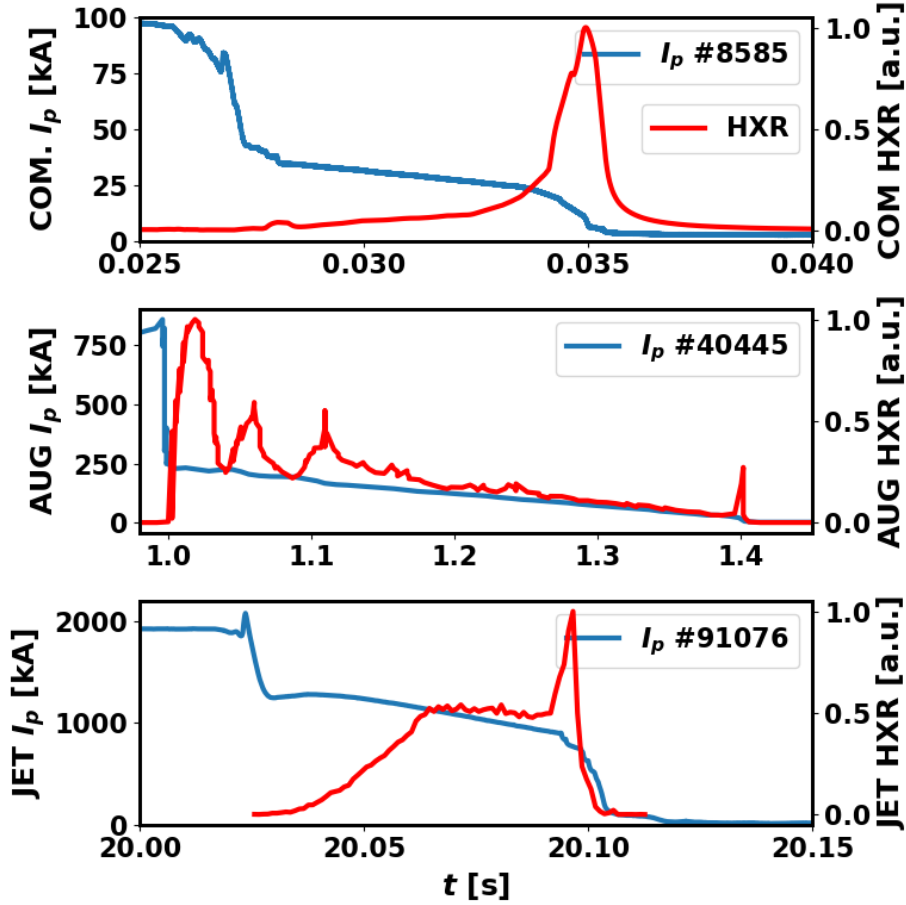


Figure 4.8: Comparison of the disruption generated RE beams in COMPASS, AUG and JET, in the order from the top frame to bottom one: the time evolution of the plasma current with noticeable CQ and RE beam phases together with the HXR signal is shown for each machine in the respective frame, time axis in each frame is related to the start of the discharge. Notice the different time scales of both axis for each machine/frame.

4.5.4 JET RE experiments

The JET RE experiments have long tradition and are very relevant to ITER and reactor conditions. A short overview of the JET RE experiment results is given here while some of the latest results are analysed in next chapters of this thesis. The dedicated JET RE program is mostly focused on generation of RE during mitigated disruptions, however start-up RE were also systematically analysed [151] as these events were observed during a significant fraction of the discharges. The failure of the density feedback control produced a couple of discharges suitable for studies of RE generation in quiescent low density discharges, see e.g. [27] and present a precedent of a possible similar issue in

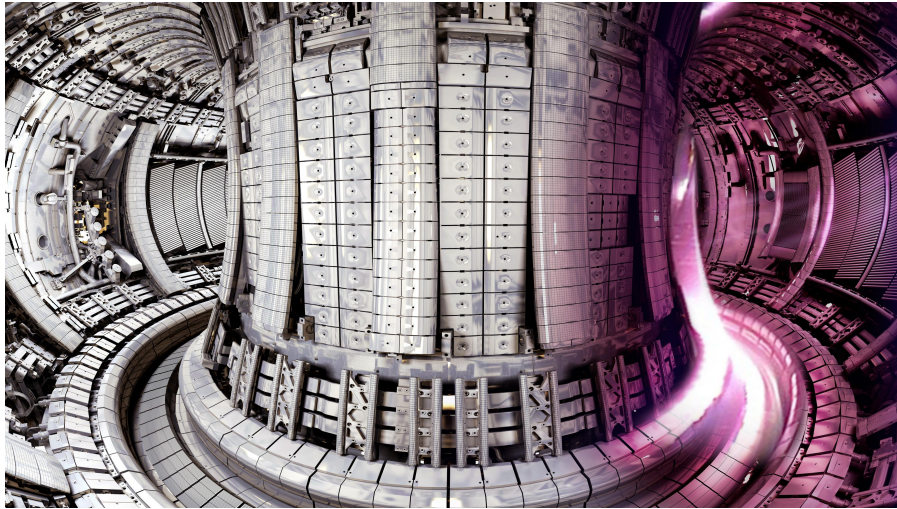


Figure 4.9: Combined view of the JET vacuum vessel interior and plasma discharge view. Figure courtesy of JET, EUROfusion

ITER which definitely must be avoided. The RE beams have been observed during mitigated and unmitigated disruptions in past with the carbon wall [152],[128]. In [153], the electron bremsstrahlung measurement using the SXR detectors were analysed with respect to the analytical calculation of the bremsstrahlung losses. In the ILW environment with disruption mitigated by the injection of mixture of Ar and deuterium, it has been shown that the RE are more likely to be generated in discharges with larger B_t and larger fraction of Ar in the mitigation mixture [69]. Moreover, the generation of the RE beam in the ILW was also simulated using the GO code in [154]. The recent efforts were focused on comparison on the effects of the SPI on generation and mitigation of RE and namely the newly developed benign termination technique [155],[70], [156] [157]. Some of the properties of the benign termination discharges performed at JET are also analysed in this thesis. The JET RE experiments will continue in 2022 and 2023 to provide maximum support in RE avoidance and mitigation understanding to ITER.

■ 4.5.5 COMPASS-Upgrade and runaway electrons

The tokamak COMPASS-Upgrade is currently in the final phase of the design stage, it will be placed in the same experimental hall as the COMPASS tokamak, however all the parameters will reach significantly higher values and the tokamak coils will work at the temperature of liquid nitrogen to allow higher currents and longer pulses. The design features of the COMPASS-U tokamak are summarised in [158]. Dedicated experiments focused on runaway electrons are currently not planned in the device, however RE phenomena

Chapter 5

RE in start-up and flattop in the COMPASS experiments

In the section 2.3.1 the tokamak discharge start-up was listed as one of the most dangerous situations allowing the runaway electron generation which cannot be completely excluded, especially in the case of a new device with no empirical knowledge of the discharge behaviour. On the other hand, the low density discharges with significant RE generation during the plasma current flattop are considered an error state with relatively low probability, however they are the simplest tool to study the RE physics under controlled conditions. In the following chapter, the analysis of the start-up RE generation on COMPASS is conducted via the methods of dedicated experiments, statistical analysis and simple modelling. In the second part of the thesis, the studies of the RE in the flattop case are focused on the periodic RE losses, which seem to be particularly rich in different mechanisms on COMPASS. The RE losses can be studied even in very high density scenarios in case the RE seed from the start-up is sufficient.

5.1 Start-up runaway electrons in COMPASS

The start-up RE are perhaps the most numerous RE event in COMPASS and due to the nature of the tokamak discharge initiation, these events are hard to be avoided completely even in the case of well optimised start-up sequence and large amount of empirical data from the previous experiments. As shown in figure 4.4 in previous chapter, many RE events have been observed in the

Plasma initiation in a tokamak (COMPASS time scales)

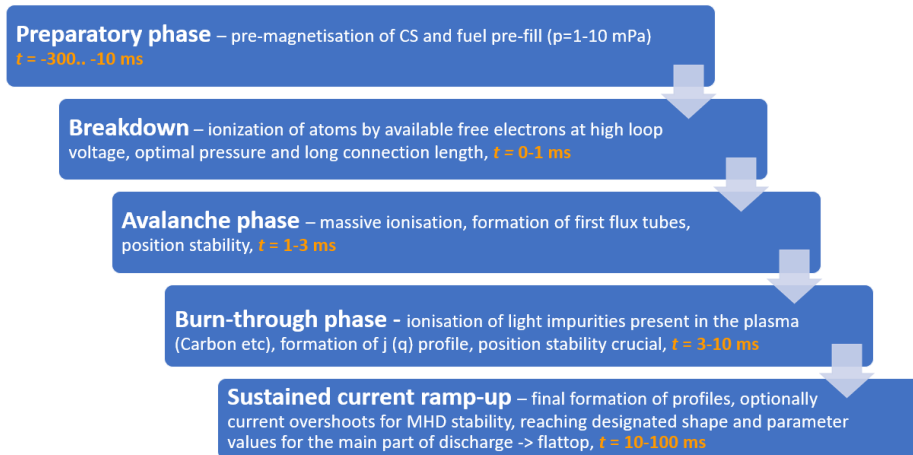


Figure 5.1: The phases of tokamak plasma start-up, their characterisation and typical approximate time scales of these phases in the case of COMPASS

non-RE related program of the COMPASS tokamak. These discharges were statistically analysed and furthermore several dedicated experiments have been conducted to explore the dependencies of the RE generation in more detail. First, let us remind the main features and phases of the tokamak start-up physics.

5.1.1 The start-up sequence and conditions in COMPASS

The tokamak start-up (with inductive drive) is a sequence of steps and phases that are shown in the evolution diagram in fig.5.1. The crucial parameters are the neutral gas pressure, stray magnetic field and loop voltage/electric field at the moment of breakdown. The diagrams of optimal conditions for plasma breakdown have been included in chapter 2 in figure 2.2. Later in the discharge start-up sufficient Ohmic heating input and limited content of low Z impurities that need to be ionised (burn-through) must be secured. In parallel the position stability, namely radial, must be attained. The generation of RE is typically considered to occur in the later stages of the tokamak start-up, namely during the plasma burn-through, however the electrons may reach significant energies even along the very long, yet open field lines.

The most important signals from a typical plasma start-up are shown in figure 5.2, i.e. the plasma and vessel currents in the first frame, the gas puff opening percentage (directly related to gas influx) and density in the second frame, the current evolution in the central solenoid and the induced loop

voltage in the third frame. Then, in the last frame the vertical magnetic field compensating at first the magnetic stray field arising from the currents induced in the vacuum vessel and then the hoop force acting on the plasma ring is shown together. Note that in case of COMPASS, the magnetic field of central solenoid is compensated by analogue function in the vacuum vessel volume, i.e. LFS, top and bottom coil turns connected to the same power supply as the CS are creating proportional magnetic field of opposite direction that cancels out the magnetic field from the CS at all current values and thus the B_v component from independently powered sets of coils only has to compensate for other sources of poloidal fields at the moment of the breakdown. In the last frame of the figure, the radiation from the H_α Balmer series line is also shown which indicates the amount of excited deuterium atoms during the process of the ionisation. The evolution can be compared to the phases described in figure 5.1. The external vertical field apparently follows the I_p evolution as they are connected via feedback loop and the loop voltage is characterised by the two steps connected to the thyristor switch-on times as described in description of scenarios in chapter 4. The oscillating phase of the gas-puff is corresponding to active density feedback phase. The breakdown of the plasma current occurs at the point of saturation of the vessel currents. Let us also remind that the standard COMPASS time axis starts at the discharge sequence initiation which is precisely defined, unlike the breakdown time itself which can vary depending on several conditions, but typically occurs in the range $t = 957 - 959$ ms on the standard COMPASS time axis.

In the detail of the breakdown time vicinity, as shown in figure 5.3 which includes the plasma current on a logarithmic scale, it can be clearly seen that initial current rise occurs without any external vertical field at relatively small voltage, however significant current increase is achieved only at high voltage and namely suitable B_v value, that compensates the stray field from the vessel currents and prolongs the field line connection length to the necessary value for full breakdown at a given voltage and gas pressure. The two time stamps of initial breakdown and sustained breakdown are shown by the black dashed vertical lines.

The typical breakdown has been also observed using fast camera with frame rate 100 kfps with wide angle view. Unfortunately, such recording were taken only during a couple of discharges. In figure 5.4, the sequence of images from this camera from a discharge #14650 is shown. This is a less typical breakdown than the one in #19952 shown in previous figures due to the RE ramp-up setup, however the nature of the plasma current increase is very similar. It is obvious that the initial current filament is created at the HFS, surprisingly slightly above the mid-plane, then it seems to expand radially and only after that a full sustained breakdown occurs with the typical radiating belt resembling the rotated check-sign on the cross-section which gradually

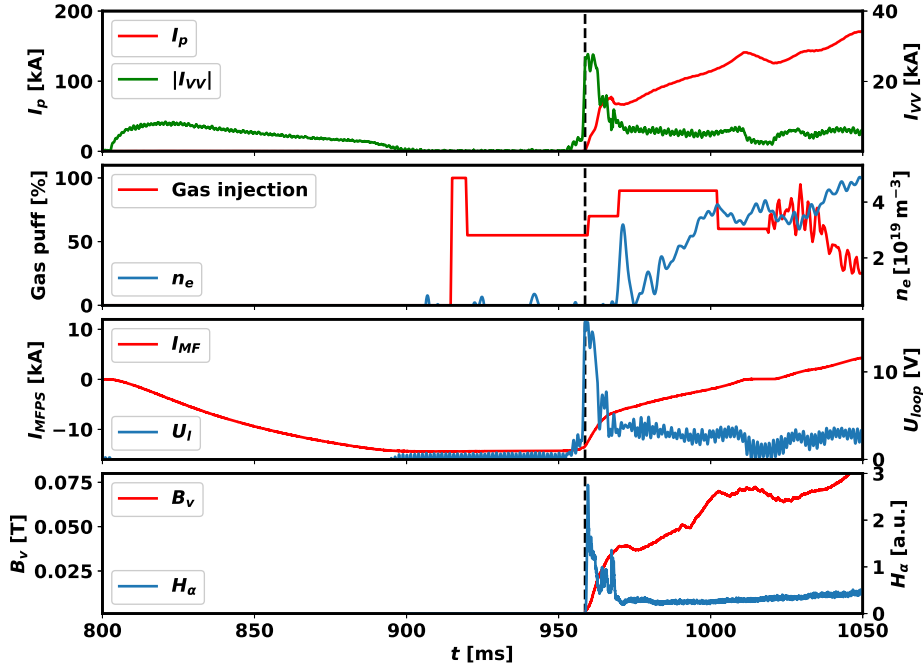


Figure 5.2: Time evolution of the most important plasma parameters during the COMPASS discharge start-up, from top: plasma current (red) and the vacuum vessel current (green), gas puff opening (red) and the electron density n_e (blue), the current in the central solenoid I_{CS} (red) and the induced loop voltage U_{loop} (blue), and in the last frame: vertical magnetic field B_v in red and H_α line radiation in blue. Based on data of discharge #19952

evolves to circular radiating belt at the HFS of the circular plasma. The occurrence of the first filament above the mid-plane is observed in majority of the recorded discharges and it seems to be related to the small plateau in the plasma current evolution. Typically, the RE are not considered to be generated before the formation of the first flux surfaces, however this multiple stage breakdown could create conditions such that significantly supra-thermal electrons are generated very early within a very small filament of closed flux surfaces and some of these particles may survive into the sustained plasma breakdown.

Before we shift to the investigation of the start-up RE under these conditions, let us consider the magnetic configuration at the point of breakdown. In figure 5.5, a poloidal cross-section map of the magnetic field caused by the currents induced in the vacuum vessel at the point of initial breakdown is calculated using a Biot-Savart tool in Python, that is further described in appendix C. We consider the stray magnetic field from the magnetising circuit (CS), i.e. the one generating loop voltage, to be compensated which is the case at COMPASS by design thanks to the hard-wired connections of the coils. The only important source of the non-toroidal stray field before ramp-up

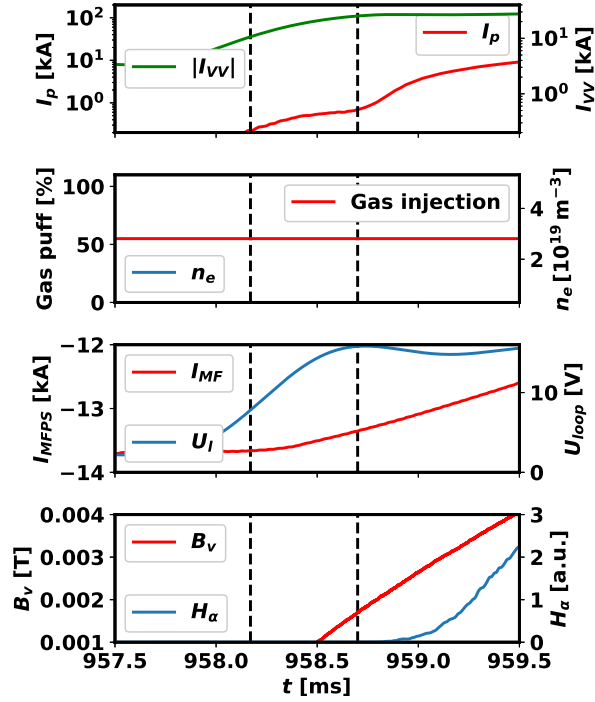


Figure 5.3: A detailed look on the moment of breakdown - enlarged period 957.5-959.5 ms from figure 5.2 with the same quantities displayed.

of the external B_v then should be the vessel currents as other continuous conductive structures are far away and relatively unimportant on COMPASS. The resulting magnetic field shows several minima at the HFS which are caused by the smooth D-shape of the vessel. The vacuum vessel should be top-down symmetric and the cross-section is taken from the CAD files, so the fact that the magnetic field minimum at the top of HFS is stronger than the rest of them might be just a matter of a small error of the vessel geometry import or asymmetry caused by some features of the program like the pixel resolution and weighting. The connection length is the longest in the minimum while both the pressure and the electric field should be very similar across the vessel, thus it is expected that the breakdown will occur in the minimum and indeed this is in a good agreement with the observation using the fast camera. The agreement on the HFS location is understandable, while the top-down asymmetry may have different causes in the model and in the experiment.

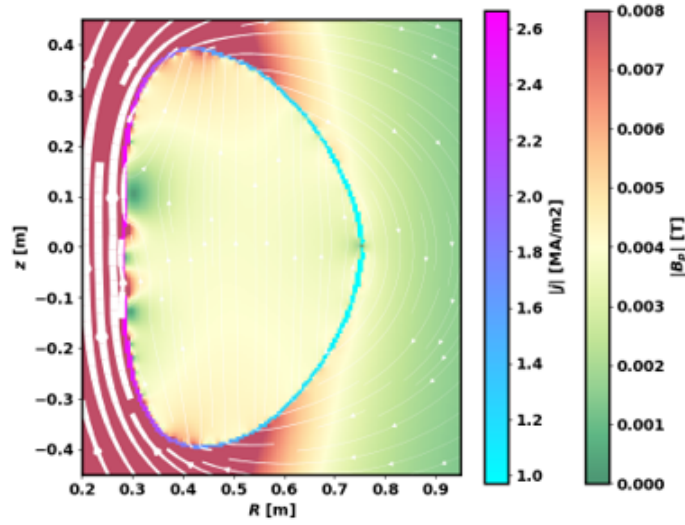


Figure 5.5: The currents induced in the vessel during the breakdown in the COMPASS tokamak and magnetic field created by them

up, due to too low density after formation of sustained flux surfaces, this generation is quite typical in case of the common discharges and often can be avoided by optimised fuelling as shown further in this chapter. The green case is characterised by a very fast buildup of the RE population as shown by the immediate increase of the ECE signal following a drop on the plasma current at the level of 10 kA. It cannot be concluded whether the RE are generated before or just at this event as the RE population may just reach the diagnostics LOS at this point, however it is certain that the RE have gained at least several hundreds of keV within the first couple of ms and they can be lost very early as they are detected by the HXR in a series of loss events shortly after that the ECE signal buildup. No HXRs are observed in the cyan case for several tens of ms as the confinement of RE is very good. Thus, it seems that the green case is plagued with the RE generation from the very beginning, maybe with seeds originating even before formation of the closed flux surfaces. The last, red case shown in the figure 5.6 is a discharge with significant neon pollution, that will be discussed later in detail. In brief, this scenario is characterised by the impurity burn-through failure that results in radiative decay of the plasma current. The density might be higher in this case, thus the ECE in some regions can be over-critical for the measurements and the signal is dominated by short spikes a pattern that repeats itself in the HXR signal with very small delay. Anyway, the discharge fails due to RE generation despite the high overall pre-fill pressure and plasma density.

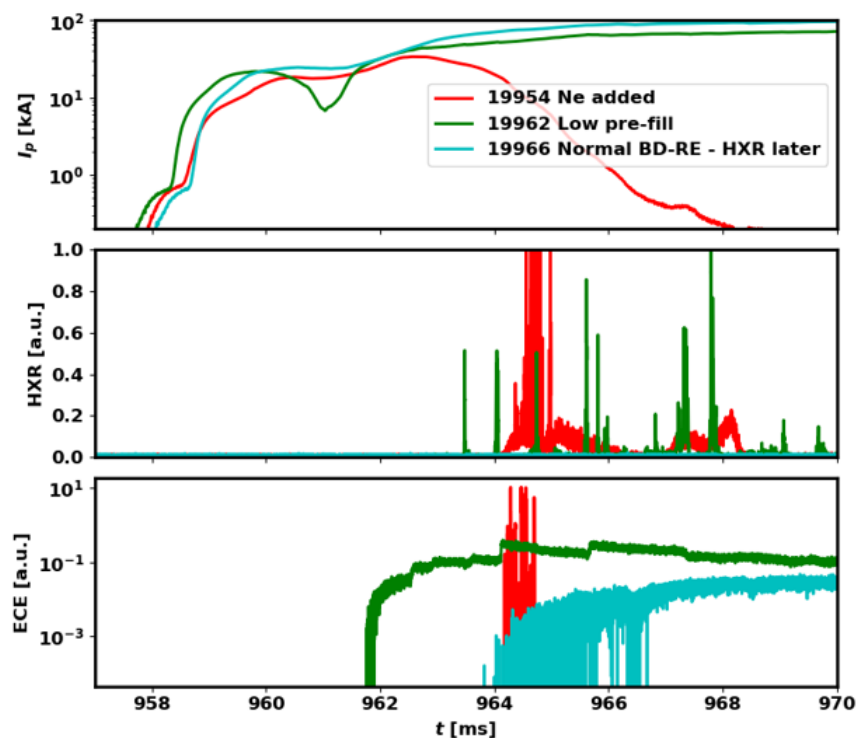


Figure 5.6: Plasma current, HXR intensity proportional to the number of lost RE and ECE intensity proportional to the amount of confined RE (with limited reliability in higher densities due to the cut-off) for three different "types" of breakdown RE events.

5.1.3 Dedicated start-up RE experiments

Several subtopics and parameter dependencies of the start-up RE generation were investigated in detailed experiments during the runaway electron campaigns and are briefly described in the following text.

Initial fuelling

The initial fuelling tuned ad-hoc during subsequent discharges is the main empirical tool to avoid the start-up RE. The fuelling waveform in the beginning of the discharge is characterised by three phases seen in figure 5.2. The first is full opening for up to 10 ms that initiates the valve operation and puffs in the main amount of the pre-fill gas, this is followed by a plateau of 20-50% opening for roughly 30 ms with additional pre-fill gas supply. At the end of the plateau, the breakdown occurs and after that the gas supply is usually increased for 10

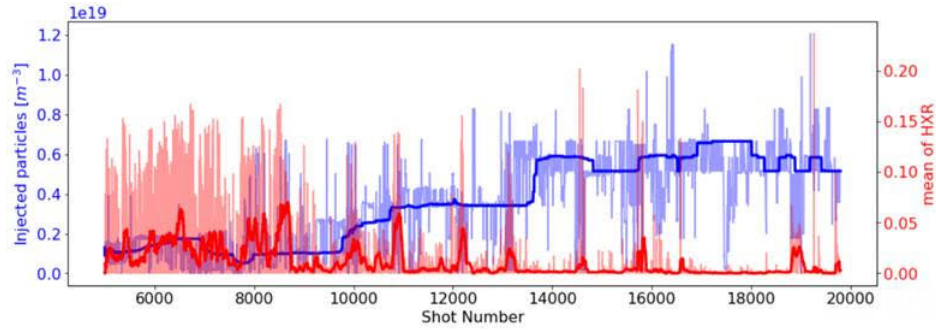


Figure 5.7: Evolution of two parameters with expected causal relation - gas puff opening before the breakdown and in the early phase of the discharge and HXR amplitude in a short window after the beginning of the discharge - as a function of COMPASS discharge number during its history, presented in [159]

ms ($t = 960 - 970$ ms) before switching to the density feedback control of the valve opening. It appeared in the dedicated experiments, that the value of the plateau and the value of the post-breakdown fuelling increase are decisive for the early density and thus the start-up RE generation. During the studies of the breakdown generation and saw-tooth instability induced losses reported in [19] and [18] (Paper A), this tool of RE control was studied and actively used. Based on a very simple calculation for COMPASS signals included in [19] using the Connor-Hastie Dreicer generation rates, the generation of the RE can vary over 10 orders of magnitude just based on the small fuelling and subsequent density variation after the breakdown.

This fact was empirically used for the COMPASS operation without deeper understanding of the phenomena. Indeed, on COMPASS, many of the discharges in the early years were accompanied by RE generation during the start up and only with operational experience this effect was completely controlled and avoided. The detection of early HXR that indicates RE generation during the start of the discharge is shown as a function of the COMPASS discharge number in the operation history of the tokamak in fig. 5.7. The other parameter evolution shown in the figure is the average gas puff opening before the breakdown (i.e. fuel pre-fill) and in the early phase of the discharge. There is an apparent relation between the two observed parameters: while in the early phase of the COMPASS operation, gas injection was typically lower and the unwanted HXR generation was significant, later the discharge startups were optimised with increased gas injection and significant startup RE generation occurred almost exclusively in dedicated experiments.

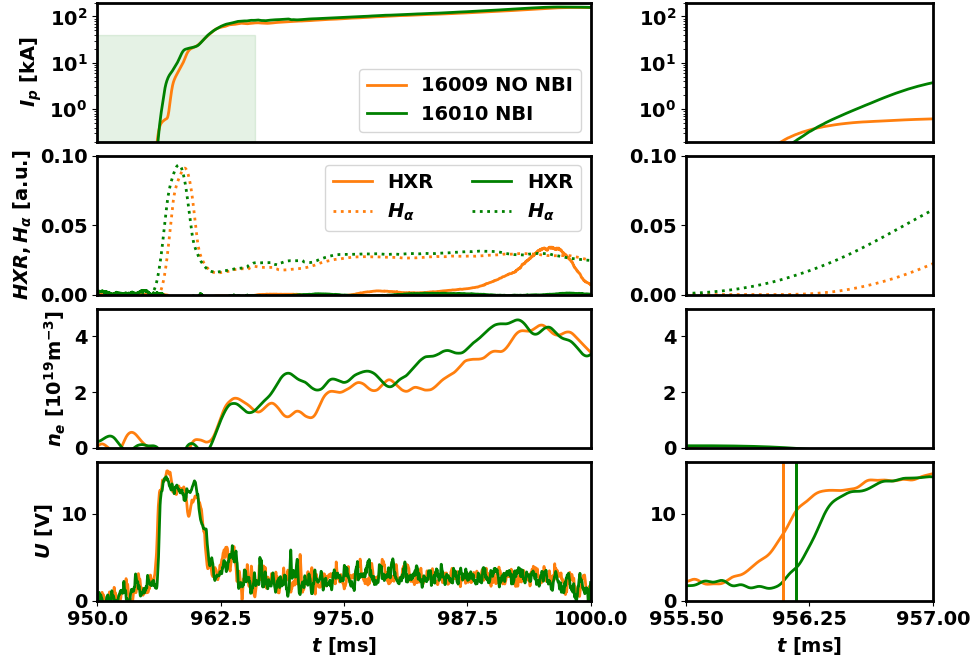


Figure 5.8: Comparison of the initial part of discharges with (green) and without (orange) the NBI injection applied to increase support the Ohmic breakdown. From top: plasma current with indicated NBI-on time (transparent green rectangle), the H-alpha signal and HXR signal, the line averaged density and the loop voltage, The right part of the figure shows the vicinity of the breakdown moment, with the breakdown voltage marked by the vertical lines of respective colours in the last frame.

significant fraction of the heating power and prevent the complete plasma ionisation, i.e. cause a fail of the burn-through. The typical impurities that may cause this failure are light impurities contained in air (N_2 or O_2) - due to various out-gassing events or small leaks - or light wall material, i.e. carbon. These are impurities that are typically highly ionised at the fusion plasma temperatures, however ionisation of significant amounts of them requires large amount of energy that may not be available during the Ohmic start-up. Potentially this can lead to a decay of the temperature and increased electric field and RE generation. To investigate this phenomena, controlled amounts of Ne were introduced in the pre-fill using the impurity bottom piezoelectric valve before the breakdown attempts on top of optimal deuterium pre-fill. This means that the density of neutrals is further increased, which based on the simple approach should further lower the probability of the RE generation. However, the situation is more complicated as seen in the figure 5.9. The reference with no neon content is RE-free reliable breakdown (in orange in 5.9), addition of small amounts of Ne in the order of small units of percent or less does not affect the breakdown. The case in the cyan colour is characterised by significant addition of neon - well above 10% - this results in increase of the radiation during the breakdown as measured by H_α . Note that the increase

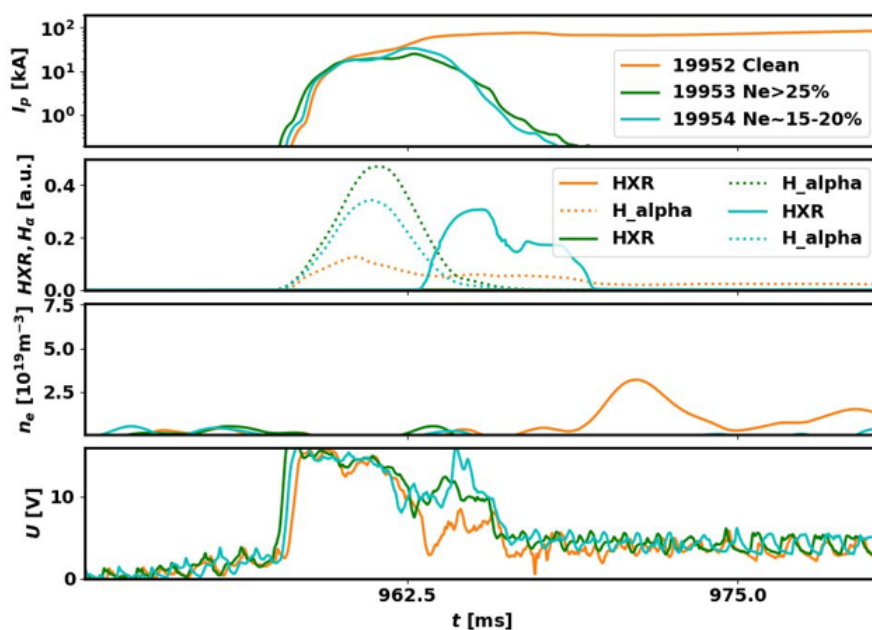


Figure 5.9: The start-up phase of discharges with controlled amount of Ne impurity atoms - plasma current on the logarithmic scale, the H_α showing the line radiation, that may be also polluted by some Ne I line radiation, HXR radiation, the electron density and the loop voltage for 3 discharges with different impurity content

in this signal can mean slower and less effective ionisation of the deuterium atoms in the environment with increased amount of impurities, however it can also be related to Ne I radiation as some of the strong persistent lines like 659.8 nm or 650.6 can contribute to the filtered signal due to relatively broad FWHM of the filter. In either case it means that the radiation losses are larger. The discharge with medium amount of Ne is able to reach only several tens of kA and then collapses with significant amount of HXR, thus the RE generation induced by the burn-through failure is obvious. In the case that the neon pollution is further increased to several tens of percent (green case), the radiation is also further increased, the plasma current evolution looks very similar, however no RE are generated and it seems that the breakdown simply fails due to inability of the Ohmic heating to cope with the radiation cooling.

The neon fraction estimate is based on the valve calibration and injection parameters. To further check the Neon presence and what is the exact meaning of the H_α signal a spectrum measured in the range 630-680 nm is shown in figure 5.10. A discharge #19951 had to be used instead of #19952 due to missing signal, however they are identical from the studied point of view. Apart from the H_α at 656 nm, all the prominent lines are of Ne I. Consistently with the injected amount the Ne lines are strongest in #19953,

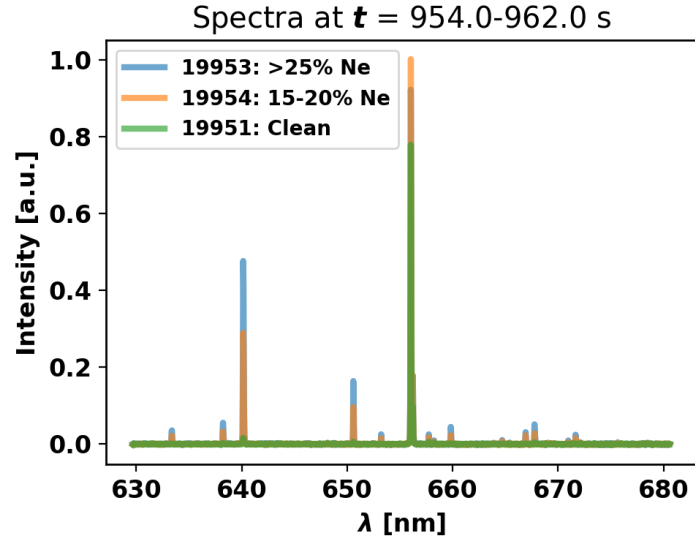


Figure 5.10: The spectra of the three discharges with different neon pollution of the deuterium pre-fill. H_{α} line at 656 nm is dominant, however Ne I lines are well pronounced in the polluted discharges.

slightly less pronounced in #19954 and not present in the discharge without the Ne injection. The H_{α} line is strongest in #19954, which is not consistent with the previous plot, however the 650 nm line of Ne I can significantly contribute to the filtered measurements as the filter width is more than 10 nm with H_{α} being at the upper edge of the range. The higher signal of the H_{α} filtered measurement for #19953 can be explained by this fact. In any case, the measured line radiation is much larger in the polluted cases compared to the clean case and this is a clear signature of the burn-through difficulties. This result is in qualitative agreement with the recent modeling [112] and also issues with start-up of discharges in WEST where significant amount of RE was observed during the high density breakdown [70] and linked to the presence of the impurities. The discharges in the restart periods can be characterised by increased amount of impurities and the results presented here can help to explain some of the RE events observed during these periods.

■ Ramp-up RE beam by the optics of the start-up RE

In the view of the role of impurities in the start-up RE generation, the scenario with very early massive gas injection used to generate the RE beam can be affected by the burn-through physics. The discharge prior to the injection is sustained, however, the margin of the available Ohmic heating power above the value needed for the impurity burn-through is rather small, which supports

Parameter	time range [ms]	Values	Avail.	Reliab.
HXR mean	20 - 50	$10^{-9} - 10^{-1}$ a.u.	+++	++
HXR max	20 - 50	$10^{-4} - 1$ a.u.	+++	++
U_l mean	10-20	1 - 10 V	+++	+++
n_e mean	10-20	$0.3 - 3 \cdot 10^{19} \text{ m}^{-3}$	++	+
E/E_c	10-20	1-1000	++	+
mean p	9-34	0.001-0.03 Pa	+	-
Gas inj. pre	-40 - 0	10^{18} - 10^{19} part.	++	+
Gas inj. post	0 - 10	10^{17} - 10^{19} part.	++	+
H_α max	-5 - +5	0.1 - 10 V	+++	+

Table 5.1: Signals and their parameters included in the statistical analysis of the start-up RE, the time range of interest, expected amplitude range and availability and reliability of the signal in the database

presented here, the buffer was found to be obsolete. Various parameters that should affect the RE presence were investigated. The parameters of interest, selected time range of interest with respect to the break-down time and typical ranges are listed in table 5.1 together with approximate evaluation of the availability of the signal, i.e. how often the signal is not missing and reliability, i.e. influence of possible changes and outages of the diagnostics setup on the results. The set of parameters is not exhaustive and will be expanded in future, however it will be demonstrated that even in the present form this data set can bring important conclusions.

The HXR mean parameter is an average value of the voltage output of the standard HXR NaI(Tl) detector in the observed time range for each discharge that is not further normalised, but relying on the fact that the detector setup was not changed in the observed period of COMPASS operation. The value of this parameter that is selected as the boundary of the RE subset is shown in figure 5.11 using a vertical line, together with the histogram of the parameter. There is a high concentration of discharges with HXR mean near the level of 10^{-3} and a close check on the representative discharges in this peak shows that they are mostly RE free or with single small RE loss event which is not dangerous, while larger values in the same decade like $5 \cdot 10^{-3}$ already show significant continuous RE losses, thus the boundary is set to $2 \cdot 10^{-3}$. The spread of the RE-free discharges from 10^{-6} to 10^{-3} a.u. in the HXR mean parameter is effectively caused by the change of noise from campaign to campaign and occasional very small cross-talks at the board of the data acquisition system. The RE discharges then reach values of the mean HXR of up to 10^{-1} which corresponds to critical RE events or on-purpose RE generation discharges. The selected threshold leaves relatively similar number of discharges in the two groups: over 3000 in RE group and over 4900 in the non-RE group. This is in accordance with the fact that start up RE were quite frequent in COMPASS compared to other machines. The HXR maximum shown in the same figure points out smaller span than the HXR

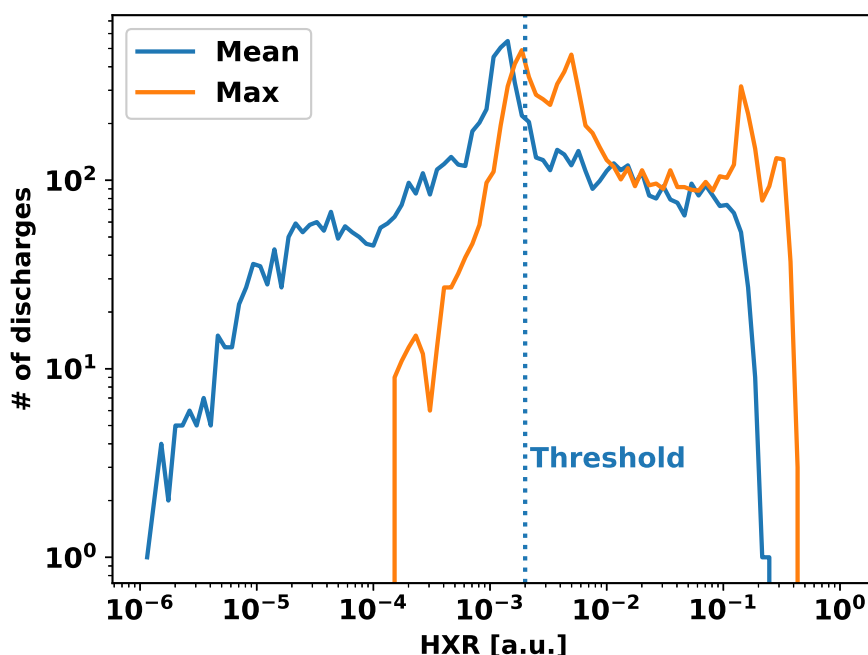


Figure 5.11: Histogram of the HXR mean and maxima in the period after the breakdown for the suitable COMPASS database discharges and the selected threshold to separate the two groups of interest.

mean histogram, however it has a more complicated pattern, therefore the mean is generally more suitable for the group division.

5.2.2 The effect of the density

With the threshold set we can explore the role of the different parameters. The following figures will always have the same form with different parameters displayed. These are 2D histograms of the data set in the HXR mean parameter and another specific parameter, where the discharge density is displayed in the shades of red for the RE group and in shades of blue in the non-RE group. The medians and median average deviation (MAD) in the positive and negative directions for the parameter of interest are displayed for each group in the corresponding colour. These statistics are better choice for the given data as mean and standard deviation are hampered by outliers given the fact that the span of some parameters is several orders of magnitude. Correlation coefficients of the selected parameters are also given in further text, however in some cases the standard correlation methods, like e.g. the Pearson correlation coefficient calculated over the whole data set can miss

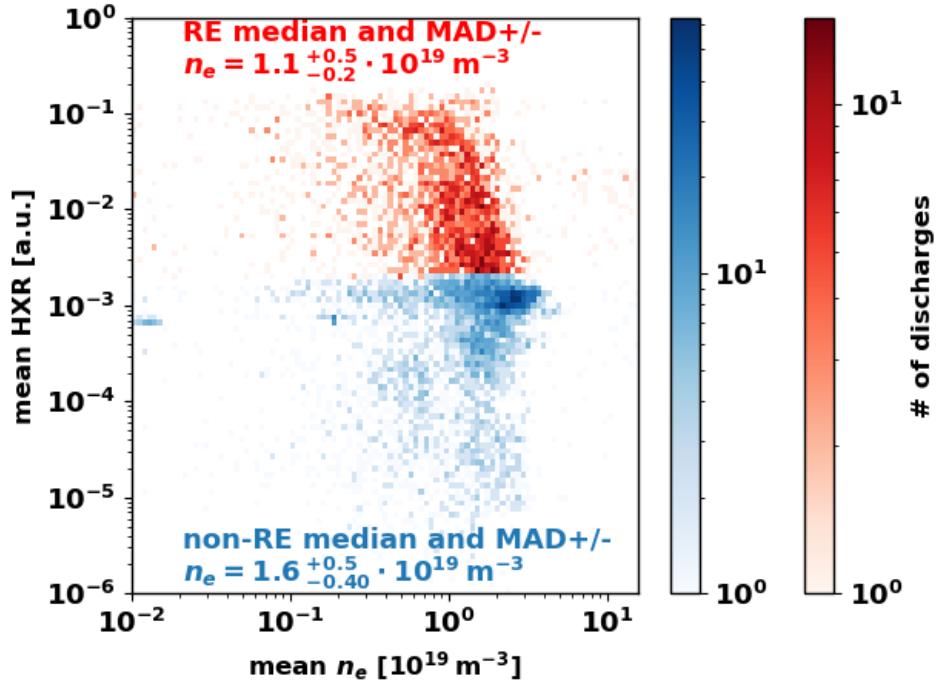


Figure 5.12: Histogram of the mean early n_e and mean HXR for RE and non-RE groups in the COMPASS database together with median and median average deviation

some of the differences between the two groups, that are visible using the histogram and group median method. As first, let us explore the density as it should be the parameter directly affecting the RE generation through critical field in the generation formulae. The issue with the density parameter lies in the fact that the interferometer measuring the density has been changed after the discharge #9250 and the new interferometer is unfortunately affected by increased noise in low densities which can, together with the geometric restrictions of the line-of-sight, cause large span in the averaged density values. In principle, discharges with densities more than order of magnitude below median could be removed as the values cannot be physical, however we prefer to use the full data set and comment on the consequences. Based on figure 5.12, we can see that the non-RE group is characterised by significantly higher densities than the RE group but the MAD-defined intervals are not separated. This is a strong confirmation of the theoretical expectation given the possible issues caused by the hardware can becloud the dependencies. On the other hand, if we calculate the correlation coefficient over the whole data set it is as low as $r = -0.01$ which would suggest that the quantities are only very weakly correlated.

Naturally, it is of interest to check the correlation of the density with the total injected particles as these parameters should be directly proportional

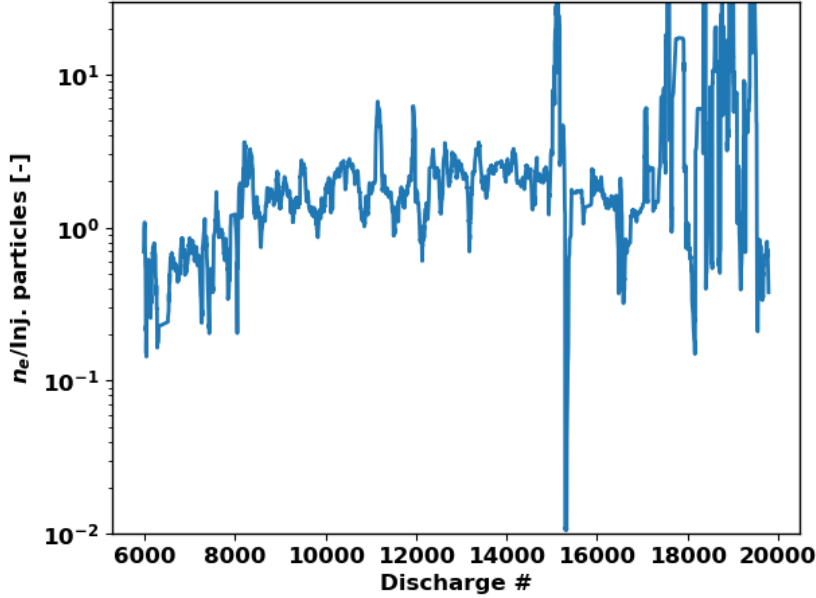


Figure 5.13: The evolution of the ratio of early electron density and the injected particles - pre-fill and early discharge injection in the history of COMPASS discharges

in case the ionisation is successful. The correlation coefficients are positive, but very small in the range $r = 0.01 - 0.06$ depending on the subset. This can be partially caused by the diagnostics issues, but importantly also by the wall recycling which can be significant in the carbon wall environment. In this way, the discharge history and tokamak wall conditioning history is significantly affecting the neutral gas pressure and thus the evolution of the density itself. The evolution of the ratio of early plasma density and number of injected particles discharge to discharge in the COMPASS history is shown in fig. 5.13. We would expect the value of this ratio at the level of 2-3 as the plasma volume is smaller than the vessel volume by approximately this factor. Indeed, it can be seen that the value is most often in the vicinity of factor 2, however significant outliers are present. Most of these very significant outliers can be tracked to issues with the density signal, however some smaller amplitude patterns in the data can be tracked to the campaign and wall conditioning schedule. This issue requires deeper analysis in future.

■ 5.2.3 The E/E_c of the RE and non-RE groups

In the case that we look to the statistics of the E/E_c which appears directly in some of the generation mechanism formulae, the situation is slightly less clear. This parameter is inversely proportional to the density, therefore we

expect it to be smaller for the non-RE case. However, E/E_c is also directly proportional to the other directly measured parameter, the loop voltage. The distribution of the average loop voltage - controlled using the tree parameters of the CS circuit discharging described in chapter 4 - is characterised by two different groups corresponding to different setup of these parameters. However, this rather technical property of the distribution could further mask the relation of the E/E_c to the runaway presence in the experiments. In figure 5.14, some effect of the U_l grouping can be observed however, the most dense clusters are clearly determined by $1/n_e$ if we compared this plot with figure 5.12. The median E/E_c of the RE group is by 50% larger than the median of the non-RE group, however the average deviations are huge and and the confidence intervals are strongly overlapping. The reasons are given by the large spread of the data points in density. The correlation coefficient of E/E_c and the HXR mean for the whole data set is even smaller then for density $r = -0.008$ which is in this case corresponding even to a very weak opposite trend then the expected one. For just the RE group $r = 0.02$ which is very weak correlation, but at least in the right sense. The grouping median method is again more reliable than the correlation. The critical role of E/E_c can be still confirmed and optimising this parameter can be considered as one of the necessary conditions for RE-free breakdown.

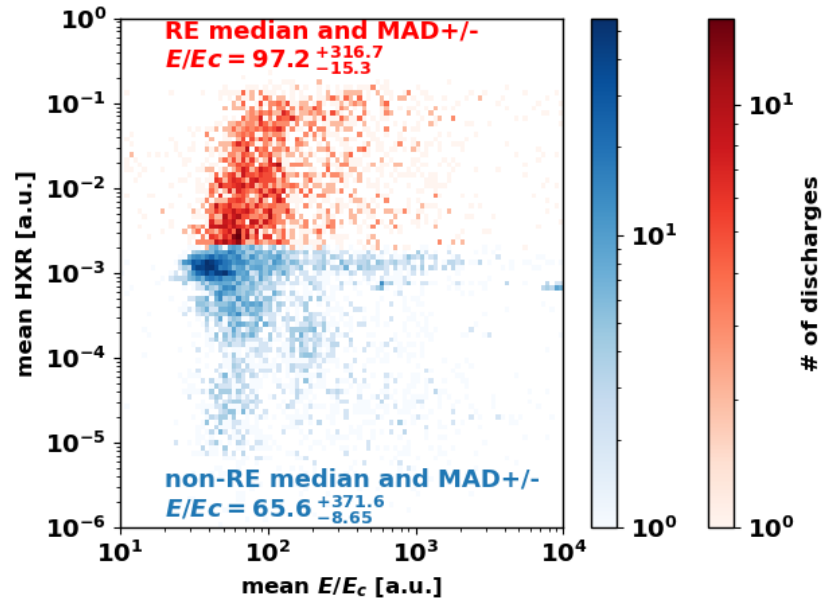


Figure 5.14: Histogram of the mean E/E_c and mean HXR for RE and non-RE groups in the COMPASS database together with median and median average deviation

5.2.4 The effect of the pre-fill and gas injection after the break-down

Now we can test the hypothesis that the pre-fill gas injection, but namely the gas injection after the break-down is crucial for the RE generation avoidance or suppression. Unfortunately, the neutral pressure measurement is not suitable for this statistical analysis as it has been often missing and the pressure peak related to the pre-fill is significantly delayed due to the location of the gauge and thus the time range of interest is rather ambiguous. Luckily, we can use the controlled parameter that directly affects the neutral pressure as well as the density, i.e. the gas valve opening evolution. The average number of injected particles is based on the gas puff opening waveform, which is typically a step function as seen in 5.2. Using the calibration of the valve presented in [109] and average reservoir pressure of 0.9 bar, this is translated to the number of injected particles. Note that the reservoir pressure can vary a bit and this value was not recorded. There are two observed periods for the gas injection - the pre-fill injection which is injection from 920 ms up to the breakdown (960 ms) and the early post-breakdown injection, i.e. 960-970 ms. The histogram for the pre-fill injection is shown in fig. 5.15. Apparently, the mean is significantly smaller for the RE case than for the non-RE case and the confidence intervals are completely disjoint, the correlation coefficient reaches significant value $r = -0.25$. The standard correlation measures are more reliable here as the number of significant outliers is small. Thus apparently, the higher pre-fill gas injection is beneficial for the RE suppression.

The histogram and medians for the injected particle number in the period after the breakdown can be seen in figure 5.16. It is visible that the waveform average naturally reaches just a couple of discrete levels taking the form of the vertical bands. A clear trend can be seen, the bands with the higher injected particle number seem to be shifted downwards, i.e. have less RE/HXR. The median of the non-RE group is double the median of the RE group and furthermore, the intervals of the deviation are disjoint and the correlation coefficient with the measured HXR is even higher in the absolute value $r = -0.35$ than in the previous case. This shows very strong dependence compared to the other studied parameters - the more gas is injected in this period, the lower is the probability of the RE generation. The correlation of the sum of the injected particles in both periods reaches $r = -0.3$ with the HXR mean. This means that by the selected statistical measures, the gas injection after the breakdown seems to be more important for the RE avoidance/suppression than the pre-fill injection on COMPASS. This is potentially good news for the new machines that have to operate with low pre-fill breakdown as the superconducting coils, very conductive vessels and big major radius allow only limited electric field to be achieved. The density can be quickly increased after the sustained low density breakdown and the

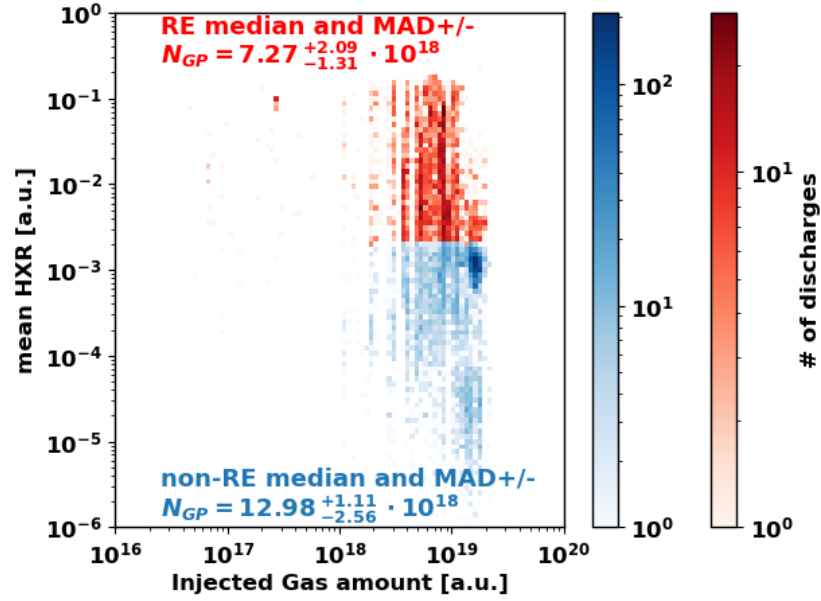


Figure 5.15: Histogram of injected particle number during period before the breakdown, i.e. the pre-fill, for RE and non-RE groups in the COMPASS database together with median and median average deviation

RE generation seems to be still prevented.

5.2.5 Deuterium line radiation and conclusion of the statistical analysis

The last investigated parameter, with a possible relation to the RE generation that was consistently measured during the observed period of COMPASS operation is the H_α peak amplitude as shown in figure 5.17. Apparently, it reaches just slightly higher values for the non-RE subset. However, the correlation coefficient is relatively large, $r = -0.17$ suggesting that with increasing HXR, the H_α radiation decreases. This could be explained by the higher plasma density of the discharges in this group which can result in more line radiation and at the same time, lower RE generation probability. This would be another confirmation of the trends reported in the previous sections. The competing mechanism going in the other direction would be valid for highly polluted discharges where RE generation would be possible at high densities. Higher H_α signal intensities - as shown in the previous section describing the dedicated experiments with neon pollution of the pre-fill - can accompany discharges with burn-through difficulties and significant RE generation. The correlation coefficient suggest that the first mechanism is more dominant and so the H_α dependence represents the role of the density

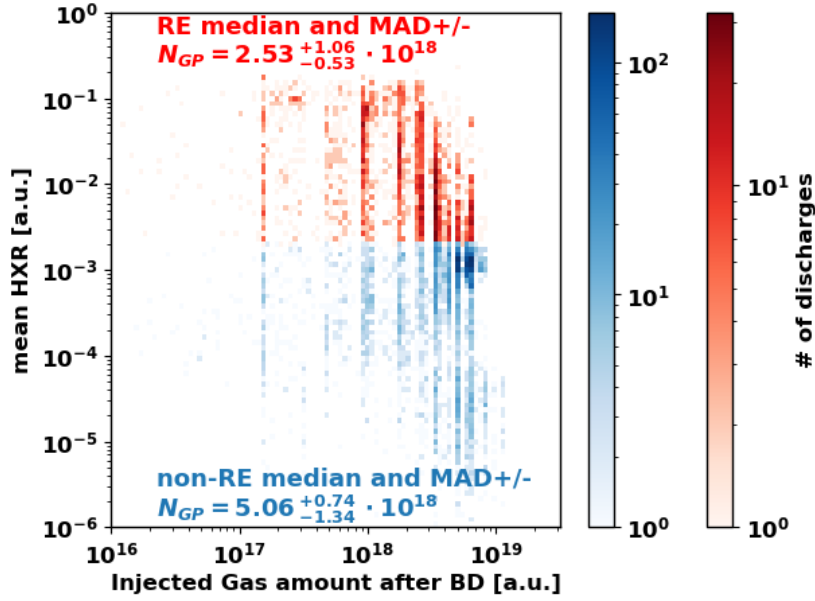


Figure 5.16: Histogram of injected particle number during period just after the breakdown and mean HXR for RE and non-RE groups in the COMPASS database together with median and median average deviation

to some extent.

To conclude, the conducted statistical analysis shows clear evidence that increased early plasma density caused by increased gas injection after the moment of breakdown can suppress the RE generation. This is related namely to the "normal" (cyan) start-up RE event type in the figure 5.6 with later RE generation but also to the green case with very early RE generation. Of course the pre-fill gas injection must be in the reasonable range to prevent complete breakdown failures. The impurity type of the RE generation (red in figure 5.6) is probably much less frequent in COMPASS as it should appear in the density dependence with the opposite trend, but this claim needs to be confirmed using suitable signal to represent the amount of impurities in the plasma, which can be either based on filtered PMTs for specific impurity emission line or detection of lines in the spectrometer data. These parameters, which may be reliable only in small subset of the discharges will be added to the analysis in near future as their are available in the COMPASS database. Moreover, suitable measures representing the early temperature and plasma area to calculate the other important quantities - the Dreicer field and the streaming parameter, will be also evaluated and included in planned publication of these results. The streaming parameter is the ratio of the drift velocity, i.e. velocity corresponding to the current density, and thermal velocity of electrons. The diagnostics necessary for the calculation of these parameters are unfortunately available only in the phase with sufficient plasma current and plasma size.

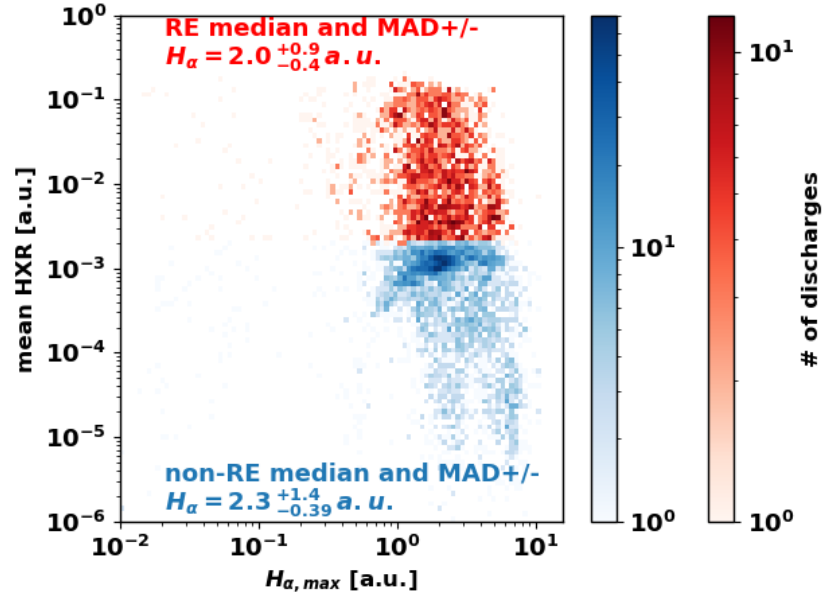


Figure 5.17: Histogram of H_α peak magnitude during the breakdown and mean HXR for RE and non-RE groups in the COMPASS database together with median and median average deviation

The electron temperature is measured by the Thomson scattering which has a vertical LOS that passes plasma only after it is large enough and that has relatively small temporal resolution, with the first measurement coming typically after 970 ms. The plasma area is then calculated by the EFIT reconstruction, which might be less reliable at very low currents at the beginning of the discharge. Therefore, these parameters are not included in the present study before their reliability is carefully considered. The ECE can also be used as a measure of RE presence, similarly as the HXR mean in this study with the ability to detect the RE presence much earlier within a studied discharge. However, in the early, low density part of the discharge, the ECE in the radial configuration can measure thermal plasma contribution and therefore just the campaigns with ECE placed on the vertical port outside of the thermal resonance LOS are eligible. The reason for not using ECE for temperature evaluation, the common purpose of this diagnostics, is the same - the thermal signal can be polluted by the supra-thermal electrons which is an especially unfortunate bias in the case of this study. The last parameter that should be considered in future work is the level of magnetic perturbation, which can also degrade the start-up plasma performance.

the two step thyristor switching used at COMPASS, the smoothing by the conductive vessel and drop caused by the plasma resistivity decrease, very roughly.

- The density is modelled as a simple power function with arbitrary exponent to affect the speed of the density increase consistently in the beginning of the discharge. Alternatively, any analytical modification can be added or it can be represented by a suitable ionisation model or supplied from the experiment.
- The temperature T_e is considered to follow linear increase, but as in the case of the density, arbitrary time series can be used.

The results of the model for the case with the RE generation and continuous acceleration are shown fig. 5.18. The figure shows the evolution of the electron density, the electric field, $E/E_{c,eff}$ and namely the critical velocity and velocities and energies of 3 accelerated particles that turn into RE at different time instance after the breakdown. The initial velocity of these particles is considered to be the critical velocity at the given time instance. In this case of linear density increase, very high electric field for initial phase and increased electric field for further 10 ms, it is apparent that once the particles overcome the critical velocity, they can be accelerated until they are lost as the critical velocity is being increased very slowly and never comes anywhere close to the velocity of the accelerated particles.

On the other hand in fig. 5.19 two cases with different density evolution are presented. The first one (dotted lines) with persistent, although slower RE acceleration as the critical velocity gets very close to the speed of light with time, corresponding to the density increase that is faster than in the previous figure. The RE generated in this case still survive and can form a dangerous seed in a later disruption. The second case - with density increase later after the breakdown that may prevent further acceleration - is drawn with continuous line. The increase of the density comes several ms after the breakdown when the external electric field is already significantly smaller than at the breakdown and some electrons are already accelerated to significant velocities. However it may still prevent the supra-thermal electrons from further acceleration as it moves the critical velocity/energy to much higher values gradually and in this way the runaway particles are captured by the non-runaway region. The density evolution in this case represents the later increase of gas injection that was found to be statistically important for the non-RE cases in the previous sections of this text.

The aim of this model was to show that the thermalisation by increase of plasma density after the sustained breakdown can contribute to the RE suppression. However, other loss mechanism, e.g. due to low RE particle

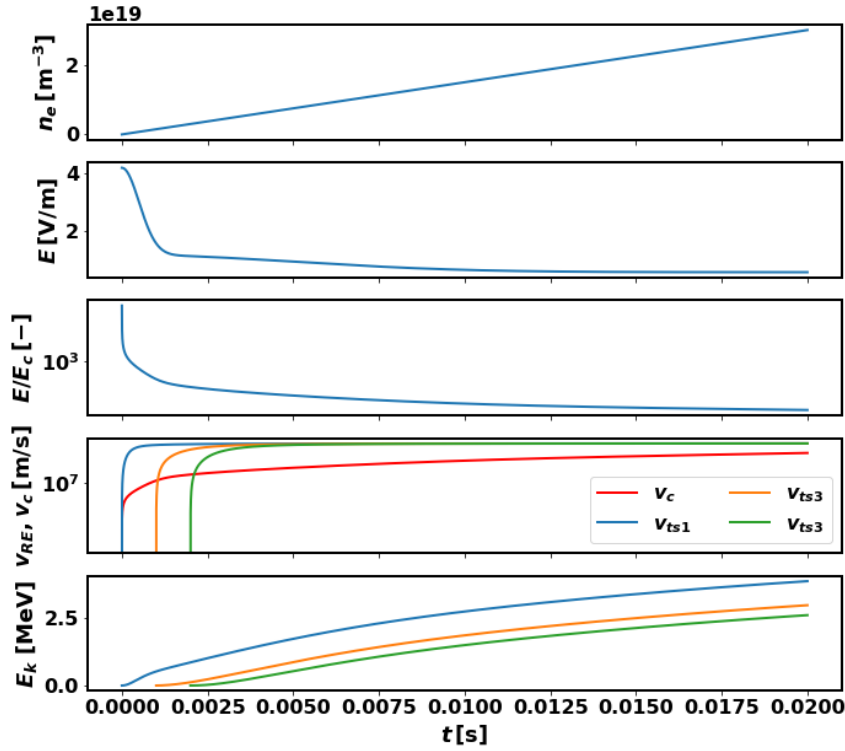


Figure 5.18: The break-down RE acceleration model for the E and n_e evolution allowing the RE generation and acceleration up to relativistic velocities.

confinement time or high pitch angle scattering, can be equally or more important in suppressing the RE population. The conclusion is that kinetic approach in the vicinity of the runaway boundary is crucial for correct description and must be used in more complex models of the whole physical situation of start-up RE generation and/or suppression.

■ 5.2.7 Basic use of STREAM for modelling of the COMPASS start-up RE

One of the models that include complicated physics of the gas ionisation together with an advance RE fluid model is the STREAM code developed by M. Hoppe et al. [112]. The runaway part of the model is based on the well proven multi-approach (fluid/kinetic) RE code DREAM [40], while the breakdown physics part of the code including plasma ionisation and simple circuit model with the conductive wall is modelled in similar way as in the

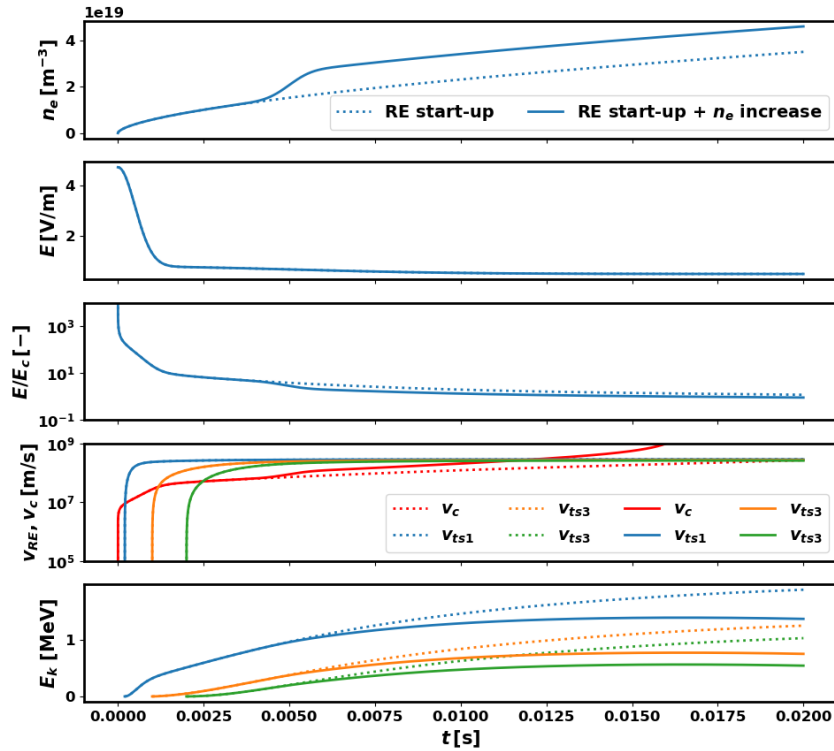


Figure 5.19: The break-down RE acceleration model for the E and n_e that allows RE acceleration - dashed lines and the case with later increase of density may slow down most of the RE

DY0N code used e.g. for the breakdown modelling at JET [26]. The model was run with the COMPASS vessel parameters - the resistance, inductance and dimensions - and approximate initial conditions. The output of the simulation using pure deuterium plasma with pre-fill injection only and self-consistent evolution of the loop voltage is shown in figure 5.20. The STREAM code follows time evolution of many parameters, many of them are shown in the figure with brief description in the figure caption. This particular simulation run resulted in negligible RE population being generated and lost. The short plateau on the plasma current is often observed in COMPASS experimental discharges as mentioned in the previous sections. However, some features and time scales of the COMPASS breakdown phase seem not to be reproduced by STREAM and require deeper validation and tuning of the model to the discharge parameters, yet it is a valuable tool for start-up RE interpretation and therefore the illustration of its ongoing application is included here.

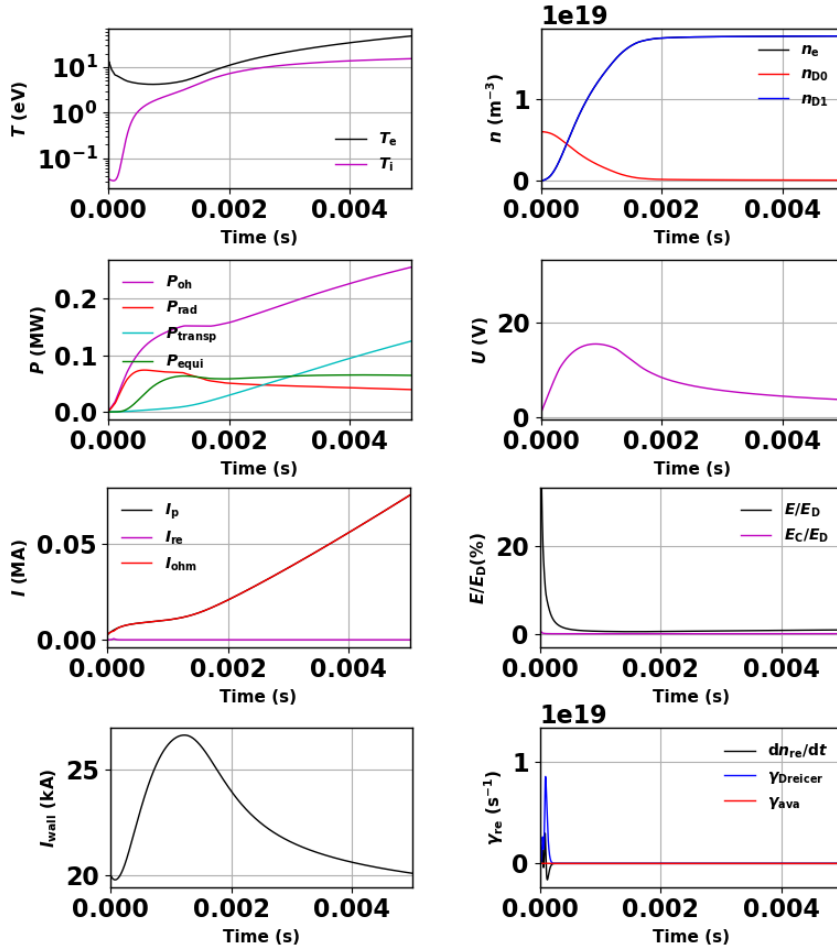


Figure 5.20: The output of the STREAM model (row, column): (1,1) the electron T_e and ion temperatures T_i , (1,2) electron density n_e and density of ions and neutrals, (2,1) the various power channels involved including the ohmic heating P_{OH} and radiated power P_{rad} , (2,2) the loop voltage U , (3,1) the plasma current including the Ohmic I_{OH} and RE I_{RE} fractions, (3,2) the electric field to Dreicer field fraction and the critical to Dreicer field fraction, (4,1) the conductive wall current, (4,2) the RE source term dn_{RE}/dt and the Dreicer γ_{Dr} and avalanche γ_{ava} growth rates; figure produced using STREAM

5.3 Runaway electrons in the flattop of COMPASS discharges

The runaway electrons were studied in low density discharges at the COMPASS tokamak especially in the early stage of the COMPASS RE program. These experiments included the evaluation of the critical electric field mentioned earlier, several scans motivated by model validation (e.g. [162]), parameter scans (density, plasma current, etc.) and the ultra low density

discharges. Besides the evaluation of these discharges containing slide-away electron population in the thesis [20], the long discharges were analysed in the poster [163] of the author of this submitted thesis. For completeness, the brief summary of the results included in the poster is listed below.

- To achieve this regime with densities below $5 \cdot 10^{18}$ it is necessary to conduct experiments within a couple of operation days after a fresh boronisation
- The decreased electric field in the flattop and consumption of CS volt-seconds allowed for reaching discharge lengths up to 1.3 s, limited only by technical constraints of data acquisition and TF coil heating/power supply performance
- The continuous component of the HXR signal during these discharges is significantly lower than during RE-rich discharges with higher density, which can be attributed to lower source from plasma but also to much better RE confinement probably due to the absence of transport caused by collisions and the background plasma instabilities
- The losses are mostly modulated by small oscillations of position introduced due to remaining oscillating component from the 12-pulse AC-DC current converters of the PF coil power sources. Thanks to the slow ramps superposed on the radial position requests, it was proved that these losses can occur on both LFS and HFS limiters.
- The termination of this discharge occurs due to the radial position instability either on the LFS - slow, gradual movement, insufficiently compensated by feedback control, or at the HFS - basically an overreaction of the feedback control to prompt position instability, with the fastest current quench rates ever recorded in a tokamak to our knowledge. Indeed 100 kA of plasma/RE current can be lost within 10 μ s. Some of these extremely fast terminations were included in the statistical analysis of the COMPASS disruptions [164] and briefly mentioned in paper C [21].
- The HFS termination also caused the worst impacts ever recorded on COMPASS with sublimation of the protruding edge of the carbon roof-shaped HFS limiter, see photo in [21] attached to this thesis as paper C, and very brief, but extremely intensive HXR burst, saturating even a majority of blind pixels in the camera images in the affected frame. These impacts and heat loads are typically not observed when Ar is injected to such discharge before its termination. This makes the long slide-away discharges without any gas injection the most dangerous RE scenario on COMPASS.

1. Magnetic island (NTM) rotation (green)
 - f typically 6-12 kHz or harmonics depending on the magnetic island rotation frequency and mode number
 - conditions to occur: $1 < n_e < 4 \cdot 10^{19} \text{ m}^{-3}$ i.e. low enough density for the magnetic island development, but high enough not to enter RE dominant discharge - details of the phasing of magnetic signal with respect to the position of the LFS limiter where RE loss is expected are included in Paper A
 - The mode number can be $m/n=3/1$, i.e. at $q = 3$ which is near the edge in these discharges
 - Regarding the relative amplitude, assuming the standard HXR detector is in the linear regime, the HXR signal in the maximum of the period can reach 2x the value in the minimum
 - In terms of absolute amplitude the magnetic islands can in general strongly suppress but also enhance the losses, further discussed below
 - In the thesis [165], it is shown that same frequency pattern can be also observed in the heat flux on the HFS limiter observed by the fast IR camera, further confirming the HXR signal represents periodic losses of RE at limiters
 - Example discharges: #10004, #13084
2. Periodic losses directly related to converter oscillations (position oscillations, magenta)
 - f typically 400 - 500 Hz, depending on flywheel rotation frequency
 - conditions to occur: $n_e < 1 \cdot 10^{19} \text{ m}^{-3}$, i.e. this regime occurs in RE dominated plasma, free from other MHD instabilities
 - based on analysis in [163], it is expected the modulation is caused by small oscillations in the radial position
 - in Paper A and in [83] it is shown that the same oscillations are visible in the heat loads on the outer midplane protection limiter observed by the very fast IR camera - Amplitude ratio can reach up to $(\text{max}/\text{min})=5$ or even more
 - Example discharges #12084, #8682
3. Losses due to sawtooth instability crashes (blue)
 - f of peaks typically 100 to 500 Hz depending on sawtooth crash frequency
 - conditions to occur: $n_e > 4 \cdot 10^{19} \text{ m}^{-3}$, peaking temperature profile and $q_0 < 1$, not necessarily detected by EFIT
 - Observation reported in Paper A and previously in [166]
 - Clearly related to losses, possible RE generation in Sawtooth magnetic reconnection region excluded on COMPASS [19]
 - Amplitude ratio peak/base can reach units or even an order of magnitude
 - Example discharges: #8632, #8636, #8632
4. Losses with ELM (edge localised mode) instability and L-H transition oscillations (brown)
 - f the same as f_{ELM} which can be larger tens or hundreds of Hz at

RE generation by primary mechanisms in COMPASS is excluded and thus the sawteeth and ELM instability losses in this density range are causing the decay of the RE population, while the other types of losses may or may not be compensated by the RE generation at low density. The knowledge of the instabilities that lead to faster decay of RE population might be used to save a discharge with a critical RE event risk, e.g. due to seed coming from the start-up RE. If the loss mechanisms are well understood or even can be controlled, the seed could be expelled before the discharge is allowed to advance to a stage with a risk of major disruption and RE beam generation. In the following paragraphs, we will just briefly discuss some of the most important loss phenomena in more detail before concluding the chapter.

Periodic losses of RE on COMPASS

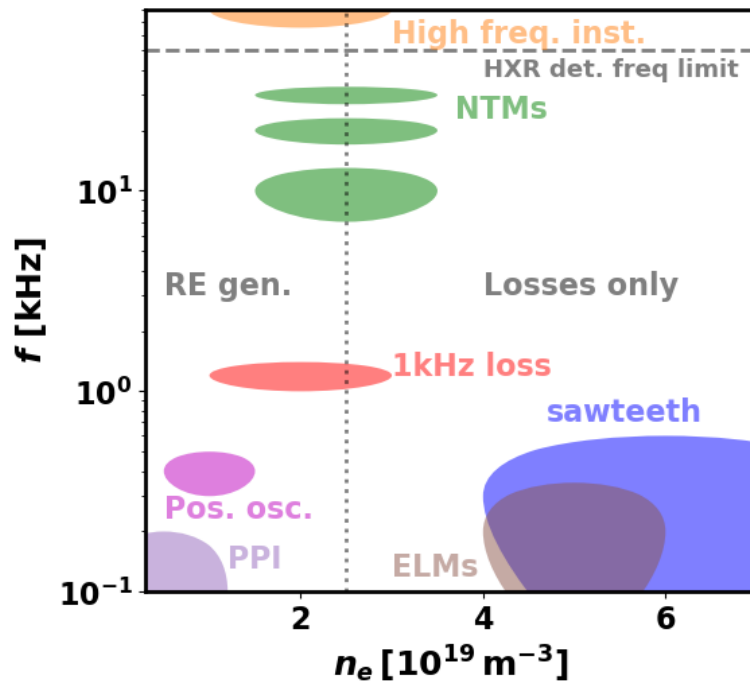


Figure 5.21: Different periodic loss mechanisms in the frequency and plasma density parameter space

■ 5.4.2 RE confinement in the H-mode and ELM-related losses

One of the most interesting loss mechanism are the RE losses in high power discharges. Any RE population present in such a phase poses a risk as a disruption of plasma with a high thermal energy and a high current can - in a large machine - secure good conditions for the avalanche multiplication and therefore potentially very intense RE beams. In, COMPASS, the RE

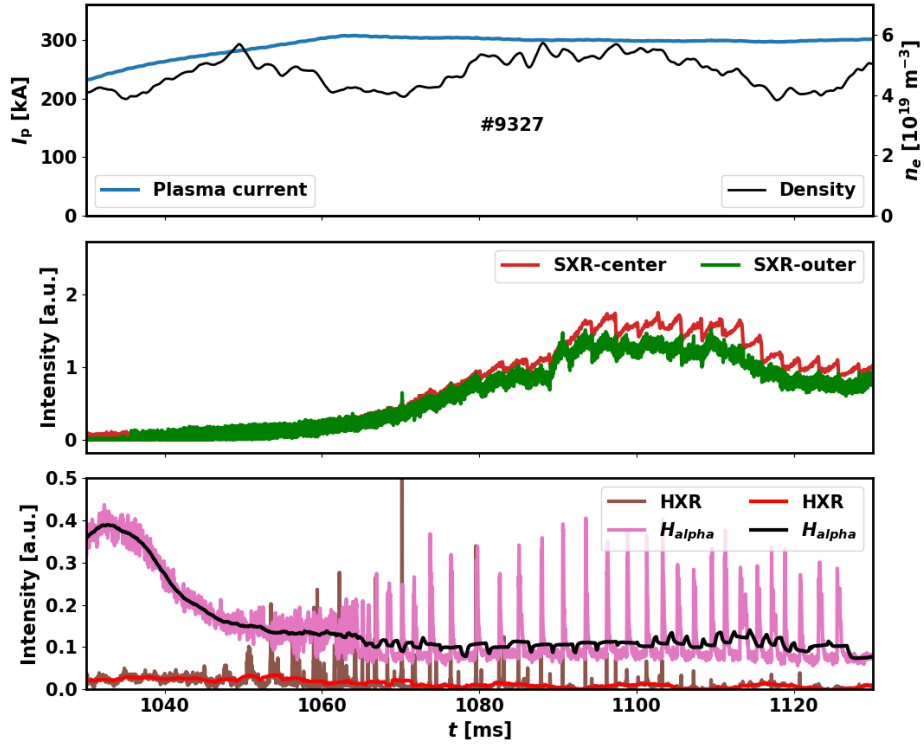


Figure 5.22: The RE losses during L-H transition and ELMs, plasma current I_p , plasma density n_e , core and edge SXR channels and high resolution + smoothed signals of H_α and HXR radiation. Discharge #9327.

small hidden sawtooth crashes, however they cannot be easily matched with any features in the magnetics or other radiation signals that would support this. However, the observation may also suggest that the transport barrier is still evolving in cycles in the ELM-free regime, but this is invisible in the H_α signal. In that case, the trace RE population would become a very interesting diagnostics method for analysis of the confinement in these regimes as the orbits of RE seem to be perturbed easily which leads to these periodic losses. The HXR signal amplitude increases again after the H-L transition in #7876, which is outside of the range of figure 5.23, and decays quickly during the final L-mode and early ramp-down stage, suggesting that the RE confinement was improved in the H-mode. Anyway, the confinement of the RE in the ELM-free regime seem to be fundamentally different to thermal confinement represented by the H_α signal, while RE are lost namely with ELMs during the ELMy H-mode and in general better confined in the inter-ELM period.

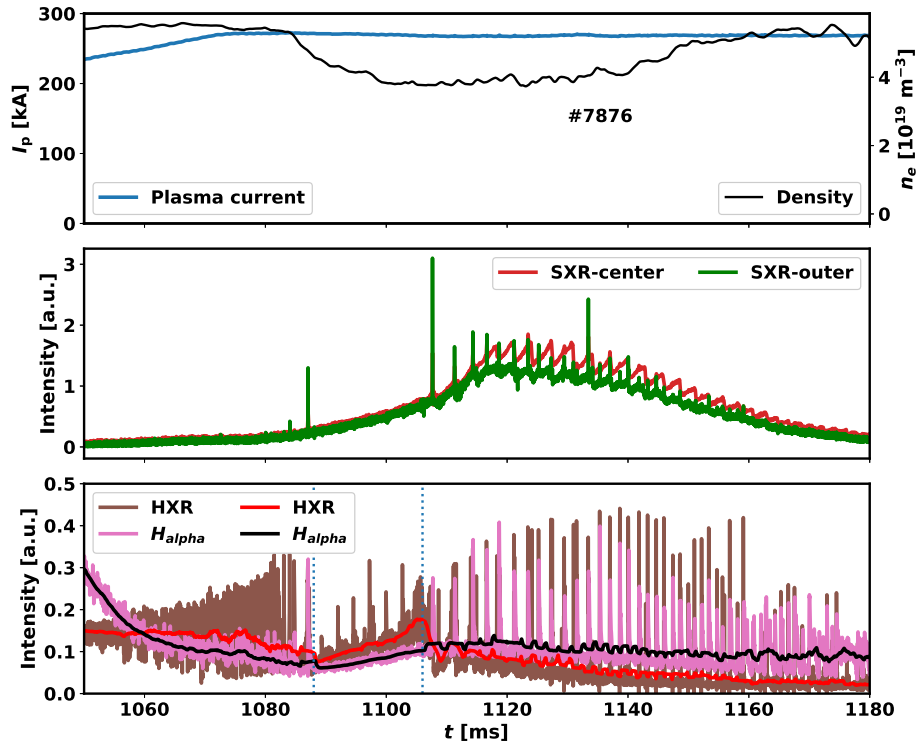


Figure 5.23: The RE losses during L-H transition and, ELM-free regime and ELMs, plasma current I_p , plasma density n_e , core and edge SXR channels and high resolution + smoothed signals of H_{α} and HXR radiation. Discharge #7876.

5.4.3 Magnetic islands improving the RE confinement

Another issue of large interest that was intensively studied at COMPASS is the role of magnetic islands/tearing modes (TMs) on the RE transport. The magnetic islands are in general isolated areas where the magnetic field lines that are otherwise situated at nested flux surfaces reconnect and form local closed magnetic configurations of various mode numbers, they typically cause a degradation of energy confinement, overview of physics of these instabilities can be found e.g. in [168]. In Paper A [18], it is shown that the HXR signal and magnetic perturbation signal related to the island rotation are strongly correlated, i.e. the HXR losses are modulated on the island rotation frequency that is typically 6-12 kHz for the $n = 1$ toroidal mode number. Coherent structures with double and triple the frequency can be also observed in the HXR signal in some cases. Moreover, using several arrays for the magnetic perturbation measurements at different toroidal positions and assuming that the HXR are created by the impact of the RE at the LFS protection limiter that has a specific toroidal position, it may be concluded that losses come from the O-point of the magnetic island. Moreover, it was observed that

the magnetic island can both enhance and suppress the losses of RE. This behaviour is shown in the two following examples. First, in figure 5.24, two discharges with identical pre-set parameters are compared using the plasma current, density, loop voltage, ECE - as a measure of confined RE population - and shielded HXR detector signals with the last frame showing spectrogram of Mirnov coil ($A_{\theta 02}$, i.e. outer mid plane B_{θ} component) signal measuring the poloidal component of the fluctuating magnetic field, situated on the LFS midplane, for discharges #13084 and #13085. The discharges differ in the evolution of the plasma current ramp up, which can point to a slightly different start-up RE population and different plasma current profile evolution. However, the difference intensifies after $t = 1050\text{ ms}$ when the number of the confined RE rapidly grows based on the ECE signal, but also based on the drop of the U_{loop} applied to sustain the requested plasma current. A coherent magnetic signal of frequency near 10 kHz, corresponding to magnetic island with toroidal mode number $n = 1$, then appears in the discharge #13084 and not in #13085. Given the subsequent behaviour of the lost and confined RE signals, namely the fact that the confined RE signal is significantly larger and losses are significantly smaller in #13084 with massive spike of released RE/HXRs just at the disruptive end of the discharge, it is apparent that the magnetic island works as an extremely efficient transport barrier for the RE in this case. Most probably, the magnetic island is 3/1 positioned at the edge of the plasma, but well inside the separatrix in this case - based on the q_{edge} from EFIT. The position might be crucial for the nature of the magnetic island effect.

On the other hand, in figure 5.25, capturing the end of plasma current flattop, and unsuccessful ramp-down followed by disruption of discharge #16650, both enhanced losses and suppressed losses due to the presence of the magnetic islands are seen. In the first frame the safety factor q evolution near the separatrix which affects the existence of the magnetic island is shown with reference value of 3 shown in red, the second and third frame show ECE and HXR signals and the magnetic perturbation spectrogram as described in the previous figure. The losses of RE detected by the shielded HXR detector are negligible in the beginning of the observed period, while the amount of confined RE is significant based on the supra-thermal ECE signal. However, during the first appearance of the magnetic island at $t = 1175\text{ ms}$ huge loss event is observed in HXR and confirmed by the drop of the ECE and drop of current. The island disappears which could be related to the change of edge q and the losses stop. The situation repeats in a couple of ms, this time, however, the losses decrease while the island still exists and just slightly later it actually seems that the island starts to help the confinement as the losses are very low and confined population starts to increase, perhaps due to beneficial density conditions. Later, the current ramp-down is initiated which leads to increase of q_{95} above 3. The magnetic island rotation frequency gradually drops and eventually the island is either locked or ceases to exist which leads to abrupt losses again. Then the island reappears and enhances

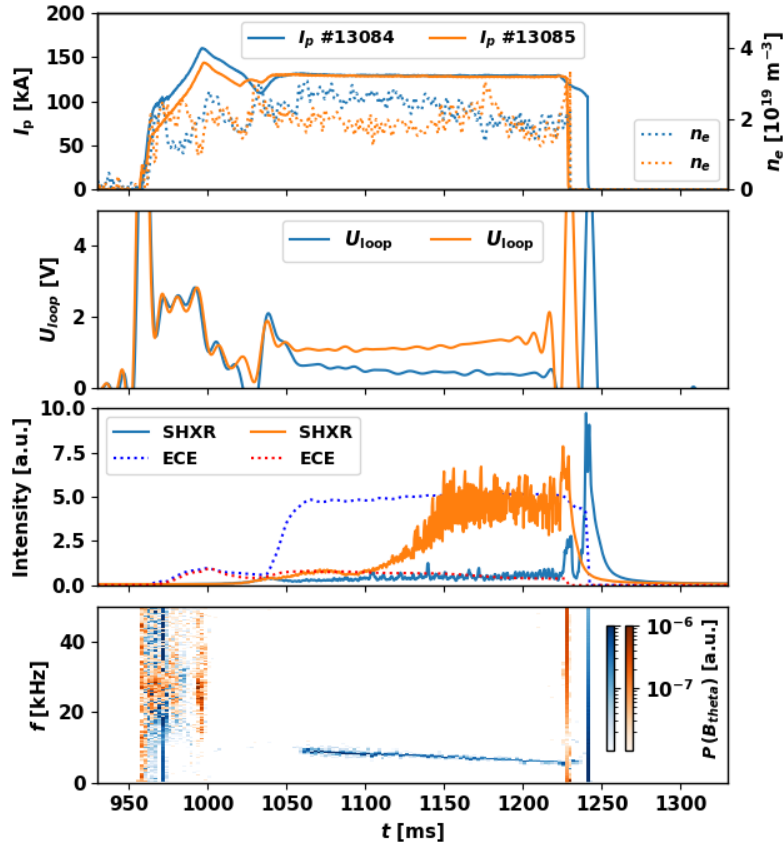


Figure 5.24: Plasma current I_p , electron density n_e , loop voltage U_{loop} , ECE (dotted) and HXR signals and power spectrum evolution for poloidal magnetic field perturbations for two discharges that differ by the presence of a magnetic island.

the RE confinement up to the disruption, where rest of the RE population is released. This evolution suggests that the island position - safety factor profile - is indeed crucial in determination of its role in the RE confinement. Perhaps, in the case when rational surface and then the resistive perturbation is formed at or even across the separatrix, it leads to enhancement of losses while in the case that that it is formed slightly away from the separatrix, surprisingly both inside and outside of it, it leads to the confinement enhancement - suppression of losses. This could explain the observation in the case that the magnetic island has the mode numbers $m/n = 3/1$ at all stages in the presented examples #13084 and #16650. However, the q profile calculation is probably affected by the RE presence as the RE drift orbits are significantly displaced in COMPASS (see the next chapter 6). Therefore, the situation can be even more complicated and deserves detailed studies with non-linear

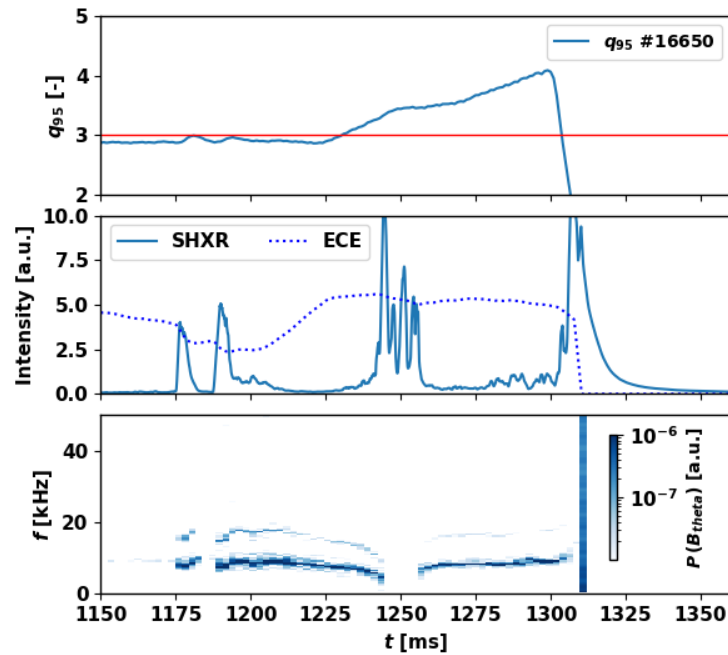


Figure 5.25: q_{95} value, ECE (dotted) and HXR signals and spectral power spectrum evolution for poloidal magnetic field perturbations for discharge #16650, where both sudden losses but also increase of RE confinement due to presence of magnetic island is observed.

MHD modelling using e.g. JOREK with test particle module [113] to be able to develop strategies for RE confinement control based on magnetic island control by ECRH in future devices.

■ 5.4.4 More insight into the "1 kHz" loss

The losses with frequencies between 1-2 kHz observed in quite large number of COMPASS low density discharges are by far the most enigmatic. In the Paper A [18], it was shown that the frequency of the loss peaks scales with the flywheel rotation frequency setup that directly affects the noise frequency in all PF and central solenoid circuits and that has a direct effect on the losses in the very low density regimes via the small position oscillations. However, despite the frequency of the 1 kHz losses is changed by the same factor as the noise in the PF circuits, it has in general value affected by several other parameters. One of these parameters that we have identified is the q_{95} , which would suggest that these losses are somehow related to magnetic configuration. There are also hints that plasma density can affect the frequency as well,

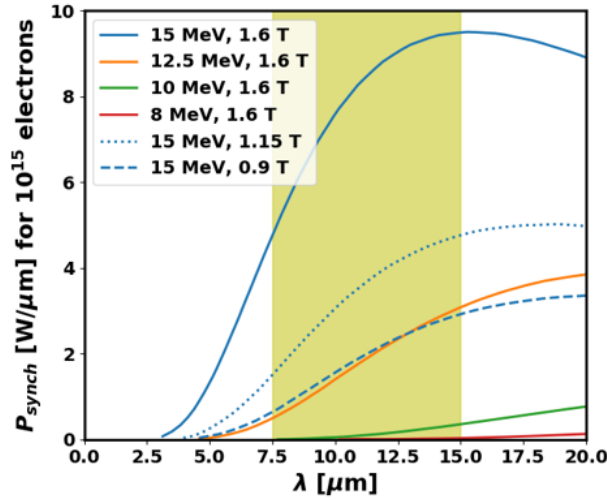


Figure 5.26: Spectra of synchrotron radiation for mono-energetic population of runaway electrons of given energy in given magnetic field of the COMPASS tokamak, the yellow band shows the wavelength range of the COMPASS bolometric IR camera. Calculated using SYRUP.

significant synchrotron radiation power and higher magnetic field is beneficial to increase the power of radiation in the range of the camera. Higher field is naturally present at the HFS of the vacuum vessel - for $B_t = 1.5$ T on the magnetic axis, the field near the HFS limiter can be well over 2 T.

The experiments were focused on the synchrotron radiation (SR) measurement namely in the first COMPASS RE campaigns [20]. SR was clearly observed and its nature proved by lack of observation of the radiation pattern when reversing the direction of the current and so the flight direction of the electrons. Moreover, the movement of the pattern was matched to the requested changes of position, leaving no doubt that SR was observed. However, the radiation pattern of the source is accompanied by a reflection pattern that peaks on the midplane due to the parabolic shape of the LFS vacuum vessel surface. In the more recent campaigns, a scan in the magnetic field intensity was proposed by the author of this thesis and the related IR data were analysed in the thesis [165], the resulting synchrotron radiation intensity evolution is shown in figure 5.27. The time traces seem to be ordered in amplitude in accordance with the magnetic field magnitude, however the RE populations may slightly differ. It is also quite apparent, that a steep rise in intensity starts only later in the discharges, perhaps when the RE population generated continuously from the start-up reaches sufficient energy to be detected by the camera. After this, the intensity rise initially seems to have exponential character, however later on, it is slower, rather linear. In the inserted image of the SR pattern from an older discharge #9814 the HFS is on the left and background thermal radiation of the surfaces is sub-

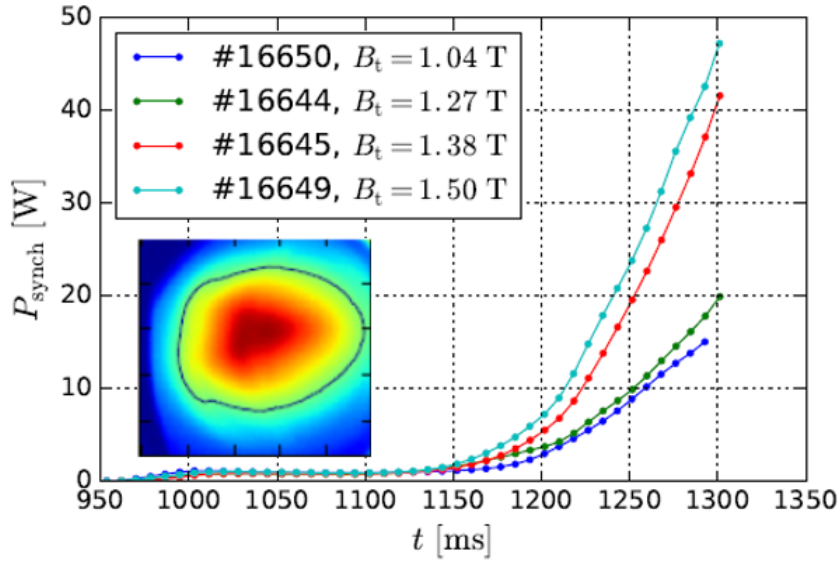


Figure 5.27: Synchrotron radiation power evolution calculated from the data of the slow infrared camera for 4 different RE discharges with different B_t at COMPASS. [165], modified

tracted. This triangular pattern pointing to the HFS is rather unexpected, as in general the HFS region should produce higher intensities and blobs broader at the HFS are more typical patterns observed at other devices due to the spatial dependencies on the magnetic field magnitude and direction. However, this specific shape can be result of the spectral sensitivity of the camera being in the long wavelength range ($\lambda = 7 - 13.5\mu m$) as the HFS areas may already radiate dominantly in shorter wavelengths. Moreover, the intensive SR reflection near the midplane may also significantly contribute to this pattern.

The set of these 4 discharges can be studied in more detail to reveal what information the synchrotron radiation can actually provide. The discharges are characterised by the same plasma current request and fuelling request and the MHD activity is also very similar in most of them, with the exception of #16650 that was studied in detail from the point of magnetic islands and losses in the previous section and where the MHD-related losses are the strongest out of this set, which might be related to the fact that it has the lowest toroidal magnetic field and q at the edge, correspondingly. All of these four discharges have also terminated at the HFS and severe damage is observed with visible range camera at a specific location of a previously damaged tile with the exposed edge. The synchrotron radiation power, and thus the detected camera intensity should be proportional to the magnetic field squared and to the energy of the RE population. Given a rather similar companion plasma properties, we can use integral of the loop voltage as a measure of acceleration force applied on the RE population for relative comparison of the discharges.

The synchrotron radiation power is also proportional to the number of RE, which we can very roughly estimate from non-Ohmic current estimate and to the pitch angle distribution, for which no independent measurement is available but it should not vary significantly in the set of the discharges. In principle, measured intensities should be a function of B_t^2 , $\int U_{loop}$ and the number of RE contributing to the radiation - essentially high energy part of the RE distribution function. The terminations of #16644,45 and 49 look very similar, with large region of the camera saturated with thermal radiation from the impact point and quite slow decay of this intensity peak in time, while the termination of #16650 seems to be less severe as saturation of camera pixels is not reached. On the other hand, the images reveal spray of glowing carbon dust released from the damaged tile. The smaller apparent heat damage suggest that some part of the high energy population was lost in the previous HXR peak events. The expected relations are investigated in the figure 5.28, where loop voltage integral, the V-ECE signal normalised by B_t^2 - a quantity proportional to a number of low energy RE and the synchrotron radiation intensity measured by the IR camera normalised by B_t^2 are shown together with the shielded HXR detector signal in logarithmic scale representing the lost high energy RE and the intensity of the final impact measured via the visible camera region of interest intensity evolution in logarithmic scale. The camera frames capturing the impact in the two extreme cases are also shown. Interestingly, the #16650 in blue is characterised by the highest loop voltage and ECE signal, but rather lower level of signals proportional to the high energy RE content. The lowest apparent severity of the final RE impact of this discharge is shown by the fastest decay of the intensity of the hot spot radiation. As mentioned above, this can be connected with the fact that some part of the RE population was lost earlier. Interestingly, there are still quite big differences in the SR radiation intensity despite the normalisation by the magnetic field. The intensity of two discharges (#16649 and #16645) is almost matched while the other two discharges reach significantly lower level, with the lowest B_t discharge #16650 overcoming the #16645 when normalised by the field. Importantly, the SR intensity seems to be reasonably correlated with the severity of the final impact. Furthermore, in the case that the SR intensity is not normalised, the discharges are ordered in exactly the same manner based on these two quantities - the synchrotron radiation and the apparent impact point damage. Therefore, it seems that the SR intensity, despite its rather complicated dependencies on numerous parameters, can give a good warning about subsequent severe termination. The fact that the severity of the impact scales with the magnetic field magnitude in a set of otherwise similar discharges points to better confinement of RE in higher field, which is expected. The effect on the confinement of RE of different energies is inconclusive based on available diagnostics and such study would need to be supported by a larger set of discharges with the same setup, which no longer possible to obtain on COMPASS. However, it could still be supported by the particle modelling, which was done for perturbed fields on COMPASS e.g. in [64].

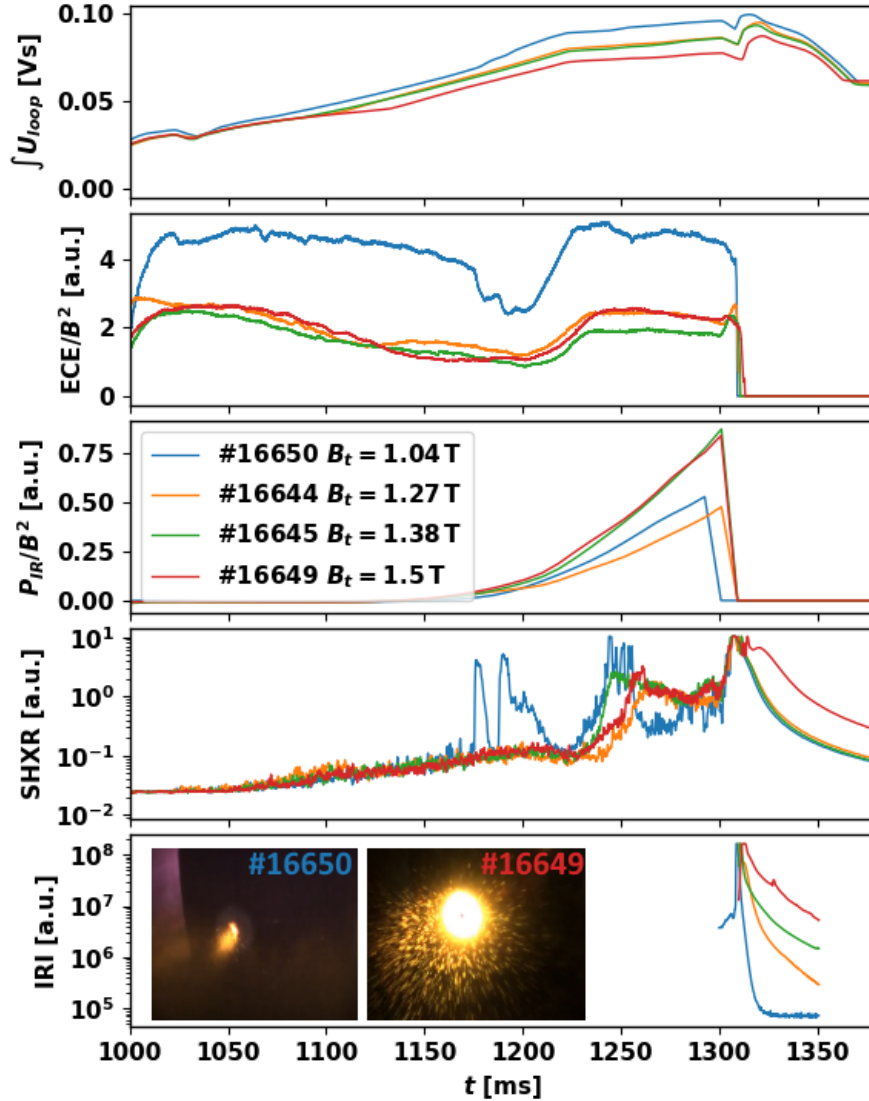


Figure 5.28: The magnetic field scan with synchrotron radiation measurement, from top: loop voltage integral, ECE normalised by magnetic field, IR camera synchrotron radiation intensity normalised by magnetic field, shielded HXR detector signal and IRI - impact region intensity of radiation as measured by fast VIS camera for four different discharges. In the last frame, the camera images of the two extreme cases are shown.

These results are listed here as they were achieved in the flattop of discharges with RE population. Unfortunately, SR measurements with cameras during the RE beam phase were not possible due to saturation and malfunction of the cameras, partly caused by extreme IR radiation intensities and partly due to high HXR flux in the tangential direction. However, spectrometric measurements using REIS were conducted as mentioned earlier in chapter 3. Furthermore, the SR measurements performed during the RE beam phase at

JET will be also briefly mentioned in the next chapter.

■ 5.6 Conclusion of start-up and flattop studies

In this chapter, the results from broad range of the RE experiments in the non-disruptive phases of the COMPASS discharges that the author organised and analysed, were described. It was shown that the early fuelling after the breakdown had a crucial effect in the suppression of the start-up runaway electrons, this hypothesis is supported by operation experience but also statistically and by simple modelling. Furthermore, a certain amount of pollution of the gas pre-fill proved to be able to contribute to the RE generation in the experiments with the Ne injection and the NBI-assisted breakdown was recognised as a scenario with significantly decreased risk of the start-up RE generation. In the second part of this chapter, various periodic losses of the RE were briefly summarised and a more detailed analysis was shown for some types of these losses with more information included in the attached papers. Finally, some examples of the measurement of synchrotron radiation in the mid-IR spectral region on COMPASS were exemplified and discussed. The final two chapters are dedicated to analysis of the full RE beams generated by the material injection and studies of their properties in COMPASS and JET, including their magnetic equilibrium.

Chapter 6

Equilibrium of the runaway electron beam

Post disruptive RE beams can be stabilised in position as well as in current in most of the present devices. However, the equilibrium of the beam formed by relativistic particles and the magnetic field of the tokamak coils and also the magnetic field arising from the current in the passive conducting structures is different from the equilibrium of high temperature plasma during normal tokamak operation.

6.1 Equilibrium in high temperature tokamak discharges

The equilibrium of the high temperature plasma in a tokamak is governed by the Grad-Shafranov equation derived from magnetohydrodynamic equilibrium, Ohm's law and Maxwell equations. The simplified magnetohydrodynamic equilibrium equation that results from the Maxwell equations and momentum equation for plasma fluid, relates the pressure with the current density and magnetic field

$$\nabla p = \mathbf{j} \times \mathbf{B}, \quad (6.1)$$

where p is pressure, \mathbf{j} is the current density vector and \mathbf{B} is the magnetic field vector. Grad-Shafranov equation is derived, see e.g. original paper [169], or text books [170][24] in cylindrical coordinates using the magnetic field description with magnetic vector potential.

$$B_R = \frac{1}{R} \frac{\partial A_z}{\partial \phi} - \frac{\partial A_\phi}{\partial z}; \quad B_\phi = \frac{\partial A_R}{\partial z} - \frac{\partial A_z}{\partial R}; \quad B_z = \frac{1}{R} \frac{\partial}{\partial R} (RA_\phi) - \frac{1}{R} \frac{\partial A_R}{\partial \phi} \quad (6.2)$$

where A_x are components of magnetic vector potential. We further define poloidal flux function that defines the flux surfaces in a tokamak and is a simple function of the toroidal component of the magnetic vector potential

$$\psi(R, z) = RA_\phi. \quad (6.3)$$

Furthermore we define also the toroidal field function which is related to the toroidal component of the magnetic field that is dominantly but not completely given by the current in the toroidal filed coils

$$F = RB_\phi. \quad (6.4)$$

Using these functions we can now define the magnetic field components as

$$B_r = -\frac{1}{R} \frac{\partial \psi}{\partial z}; \quad B_\phi = \frac{F}{R} = \frac{\mu_0 I(\psi)}{2\pi R}; \quad B_z = \frac{1}{R} \frac{\partial \psi}{\partial R} \quad (6.5)$$

where $I(\psi)$ is the current flowing in the poloidal direction inside (in terms of radius R) a region defined by the flux surface ψ . This includes the currents in the inboard segments of the TF coils as a border condition but namely poloidal currents in the plasma. Now using the components of the MHD equilibrium 6.1 and Maxwell equations and the definitions above [170],[24], we can arrive to Grad-Shafranov equation

$$\frac{\partial^2 \psi}{\partial R^2} - \frac{1}{R} \frac{\partial \psi}{\partial R} + \frac{\partial^2 \psi}{\partial z^2} = -\mu_0 r^2 \frac{dp}{d\psi} - \frac{1}{2} \frac{dF^2}{d\psi}, \quad (6.6)$$

where the special differential operator on the left hand side is often marked as Δ^* or \mathbf{L} acting on ψ . The F function term is expressed $I(\psi)$ in some sources with the differences being only in the constants, other formulations are also possible. This equation has several important conclusions and except some specific situations, it is solved numerically, e.g. using EFIT [120]. The most important conclusion for the further text here is the requirement on additional external vertical field to secure the MHD stability. This is satisfied by outer ring poloidal field coils in a tokamak. The required vertical field is

$$B_v = \frac{\mu_0 I_p}{4\pi R_0} \left[\left(\beta_p + \frac{l_i}{2} - \frac{1}{2} \right) \left(1 - \frac{a^2}{b^2} \right) + \ln \frac{b}{a} \right] \quad (6.7)$$

where I_p is the plasma current, R_0 is the major radius of the tokamak $\beta_p = \langle p \rangle / \frac{B_\theta^2}{2\mu_0}$ is the plasma kinetic pressure normalised by poloidal magnetic field pressure, the $l_i = \langle B_\theta(r) \rangle / B_\theta(a)$ is the internal inductance, i.e. the peaking factor of the plasma current density and a and b are the plasma and the conductive shell minor radius, respectively. In general, the first term is related to the compensation of the tire tube expanding force of the high temperature plasma, the second one to the compensation of the hoop force related to the internal inductance and the last one to the compensation of the hoop force related to the external inductance. The second two terms are applicable to a high current RE beam with cold plasma, while analogy of the first one does exist in this situation but takes a different form as we describe further. The important point is that the vertical field that needs to be applied carries information about the plasma pressure, i.e. also its thermal energy and temperature.

■ 6.1.1 High current betatrons

In the 1970s and 1980s, the interest in the electron accelerators peaked, focusing primarily on the high intensity bremsstrahlung radiation production. In order to achieve high intensity of the radiation, it was necessary to maximize the current in the relativistic electron beams. However, at currents reaching several kiloamperes, it was impossible to stabilise the beam in vacuum using just the vertical field proportional to the flux swing (electron energy) and vacuum tubes as in the conventional betatrons. The space charge of the negative particles present a serious complication itself, causing also other harmonic disturbances. A possible way how to introduce stable orbits and spread the space charge over a larger cross-section was to introduce helical field [171]. By addition of a toroidal component of the magnetic field and in combination with the vertical betatron field and also the poloidal field arising from the particle beam current itself, the betatrons arrived to a magnetic configuration very similar to circular cross-section tokamaks. Such configuration is referred to as a "modified betatron". While most of the instabilities appeared to be solved at this step, several new were introduced and still the problem with too large negative space charge contributed to relatively small region of operation stability. Due to this, another modification was introduced - the addition of low density background plasma [171] via injection of ionised gas. The device with both these modifications applied was then called a "Plasma-assisted modified betatron". Not surprisingly, three different regimes of its performance based on the density of the background plasma, but viewed from the acceleration perspective, have been identified:

- Accelerator regime - the background plasma works well to dilute the

spacial charge, but does not impose significant drag on the relativistic particles

- Combined regime - most of the current is still carried by the accelerated particles, i.e. runaway electrons, but due to the increased plasma density, the drag is significant and Ohmic current component may arise
- Dominantly Ohmic regime - when the background plasma density is not properly controlled and rises too much, the acceleration is inefficient due to large drag and the electric field is driving namely Ohmic current, totally useless for acceleration.

The same regimes are observed in the tokamaks as described in this thesis, with the first two being risky and undesirable in the thermonuclear fusion research. The plasma-beam system of the plasma-assisted modified betatron was also subject to periodic instabilities similar to tokamak kink and magnetic island instabilities. Therefore the literature summarising the research at these devices can be a source of interesting comparison and different approach to the RE beams in the tokamaks. The betatrons are still in use in technical and medical applications, while the physics research is now more focused on laser driven accelerators or high energy synchrotrons.

6.2 Possible modification of the magnetic equilibrium and Grad-Shafranov-like equation for RE beam

The standard magnetohydrodynamic equilibrium that contains the $\mathbf{j} \times \mathbf{B}$ and ∇p terms can be modified using a suitable description of the RE component of the current. This equilibrium was theoretically investigated by Mondelli and Ott for arbitrary toroidal magnetic configuration [172], by Manheimer from the betatron point of view [173] or by Yoshida [174] and Fujita [175] for tokamaks with significant RE population. The equilibrium equation can be written as

$$\mathbf{j} \times \mathbf{B} - \sum_{b=1}^N n_b (\mathbf{v}_b \cdot \nabla) M_b \mathbf{v}_b - \nabla p = 0 \quad (6.8)$$

,

where the middle term describes a sum of elemental beams with given density n_b , relativistic mass M_b and velocity v_b . The additional component of the force balance compared to the standard MHD equilibrium is a centrifugal

force of the elemental beams. Surprisingly, these equations are not used in the present day runaway electron experimental research extensively if at all. The very few applications include the work of the author described further in this text. The problem can be simplified in the important case of a post-disruption RE beam as this situation is characterised by a negligible Ohmic current component and temperature, therefore the companion plasma pressure can be neglected. Furthermore, in case we consider a mono-energetic beam and when we can consider the velocity of the electrons to be close enough to the speed of light to apply ultra-relativistic limit, the simplification further leads to

$$\mathbf{j} \times \mathbf{B} - (n_{RE} \cdot m_e \cdot c^2 \nabla \gamma(\mathbf{r})) = 0, \quad (6.9)$$

where $\gamma(\mathbf{r})$ is the spatial distribution of energy - relativistic factor. This formulation is consistent with a single ultra-relativistic particle moving on a circular orbit, with radius R in magnetic field B_v which is a low current limit of the presented situation, using also $j = n_{RE}ec$ we arrive to

$$eB_v = \gamma m_e c / R. \quad (6.10)$$

In other words this means that in the first approach, the external vertical field needs to be proportional to the energy of the runaway electron beam, just like in the traditional betatron. This proportionality is valid with respect to the average beam energy even in case of a more complicated energy distribution function. Also, in the case of high RE currents, the external field proportional to the average energy is still necessary to support the relativistic expansion force that is very similar to the thermal plasma pressure in effect.

In a more detailed approach, it is important to explore the differences and analogies of the relativistic beam equilibrium with respect to the standard Grad-Shafranov equilibrium. Most importantly the poloidal flux function ψ which is a primary variable in the tokamak equilibrium which is used to describe the pressure profile and contours of the equilibrium is replaced by the toroidal canonical momentum P_ϕ in case of the RE beam

$$P_\phi = \gamma m_e R c + e\psi(R, z), \quad (6.11)$$

which is still a function of ψ , but also a function of γ . This quantity describes the drift surfaces on which the RE move. The shift of RE trajectories with respect to high temperature plasma equilibrium with Ohmic current is a well known consequence that naturally arises in full orbit particle tracking codes and that was described in classical papers, e.g. [176]. However, simple approach of test particles on equilibrium background is applicable only in

the case of a negligible RE current. In the case of high RE current, the equilibrium itself is modified.

The betatron beam or tokamak RE current density and the toroidal field function F or its analogy and other parameters can be then defined as a function of P_ϕ as shown in [173], [177]. Using this approach a similar equation as the Grad-Shafranov equation can be derived for the RE beam - plasma system and accompanied by a suitable equation for the RE beam energy or momentum. A modification of the Grad-Shafranov equation (6.6) for ψ with RE beam poloidal RE current intensity I_b and toroidal RE beam current density j_b based on [174] can be written down. It includes toroidal field in the form of the poloidal external currents I_v and toroidal coil and passive structure current densities j_v as well and reads

$$L\psi = \mu_0 r^2 p'(\psi) + (I_p + I_b + I_v) I_p'(\psi) + \mu_0 r (j_b + j_v). \quad (6.12)$$

However, this naturally increases the complexity of the equilibrium equation solution as it becomes a function of the electron energy distribution. Furthermore, the distribution usually cannot be measured precisely enough and we are only able to estimate the average or maximum energy or relative changes from other diagnostics. On the other hand, the risks and damage potential of the RE beam is determined by its total kinetic and magnetic energy which can be estimated from the equilibrium in the first approach using just the average or maximum energy as well. Therefore, just the connection of the equilibrium with the average energy is an important result and we will focus on it further. Nevertheless, the proper solution of the relativistic RE beam equilibrium in tokamak conditions using experimental measurements can bring interesting implications for the distribution function shape, the beam instabilities related to rational helicity surfaces and e.g. discrimination of the spatial regions where kinetic instabilities driven by the distribution function may occur, and will be attempted in future. In this chapter we further focus namely on the direct implication for the RE beam energy diagnostics and the position control of the RE beam.

6.3 Understanding the position stability of the RE beam in COMPASS

The COMPASS tokamak was an especially interesting device to study the RE equilibrium namely due to its small major radius where the effect of energy dominates but also thanks to the relatively simple PF coil system and

position control algorithms that can be easily disentangled.

6.3.1 COMPASS Poloidal field coil system

In order to analyse the equilibrium orbits of relativistic particles in the COMPASS tokamak and stability of the RE beam, the poloidal field (PF) coil system of the machine is briefly introduced in the following section. Unlike at most other machines, where multi-variable control of individual coil power sources is implemented, COMPASS PF coil windings consist of 5 groups of coils divided based on their purpose. Each group has its own single power supply.

- **Magnetizing field circuit - MF** - primary winding of the tokamak transformer responsible for generating the flux change that drives current in the plasma + associated coils to compensate magnetic fields arising during its operation in the vacuum vessel volume
- **Equilibrium field circuit - EF** - outer poloidal field coils with respect to the plasma, but also a layer of turns in the central solenoid that together provide additional vertical component of magnetic field B_v to oppose natural plasma radial expansion forces (hoop force - current distribution and tire-tube force - pressure). This circuit is important also for maintaining the position of the RE beam as will be described in the further text.
- **Shaping field circuit - SF** - coils responsible for achieving desired shape of the plasma cross-section - elongated and D-shaped, generally quadrupole or hexapole configuration
- **Fast feedback circuits - vertical (FABR) and radial control (FABV)** - part of these coils are complementing the EF circuit in securing the radial stability with dominantly vertical field B_v , the rest is securing the fast feedback control of the vertical instability (dominantly radial field B_R) that is introduced by the elongation in case that the shaping is applied

The positions of the coils and their purpose are displayed in figure 6.1. The coils attached to the specific group/power supply are shown in specific color. The details on connections of these groups of coils can be found in the thesis [127]. The MF circuit coil geometry is organised so that it creates negligible magnetic fields inside the vacuum vessel and only secures the electric field for the current drive and Ohmic heating. Most of the RE discharges are

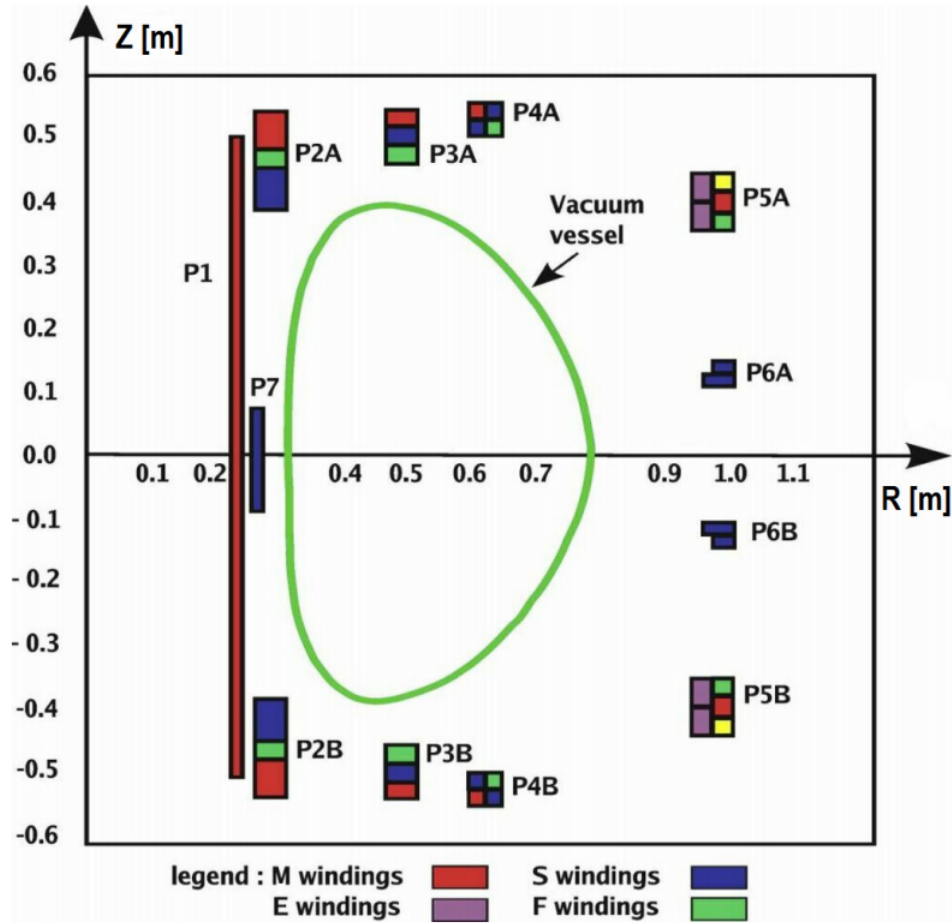


Figure 6.1: The positions and color coded purpose of the poloidal field magnetic coils around vacuum vessel of the COMPASS tokamak, adopted from [127].

run in circular configuration, meaning that the SF circuit is not used and no action of fast vertical position control (FABR) is usually required. On the other hand, the EF and FABV circuits are important for the RE beam magnetic configuration. The EF circuit is supplied by a thyristor converter power supply, that can secure up to 16 kA of current. The direction of the current in the LFS part of this coil system is always opposing the direction of the plasma current to balance the outward force. The turns are grouped to 2 times 2 coils (upper and lower) each having 8 turns with an additional layer of 48 turns in the central solenoid with opposite direction of current to optimise the spatial distribution of the magnetic field. Both top and bottom pairs of the LFS coils are effectively connected in parallel. Therefore the actual total current flowing through the entire poloidal cross-section is $16I_{\text{EFPS}}$ on the LFS and $-48I_{\text{EFPS}}$ at the HFS. On the midplane, the generated magnetic field is in the range 7.5 mT/kA to 13 mT/kA, from LFS to HFS[127]. Along the vertical line, the vertical magnetic field is almost constant inside the vacuum vessel. The EF power supply current control is based on plasma current value and error of the position. The fast winding of the radial stability

control (B_v - FABV) is powered by a fast amplifier that may achieve ± 5 kA and consists of two 2-turn coils (the green segment of P2A,B in figure 6.1) at the HFS and 2-turn coils at the LFS (the green segment of P5A,B in figure 6.1). The rate of change of the magnetic field is much higher using this coil system due to faster power source and lower inductance, however the corresponding magnetic field achieves only values of approximately 2 mT/kA at the midplane. The control loop clock is 20 kHz [127], while for EFPS it is 2 kHz. Therefore it is suitable for compensation of fast instabilities. The control of FABV current is based exclusively on the radial position deviation from the request. In the case that there is a principal error in the controller using EF circuit as an actuator, the FABV control may get into conflict with the EF control, reach saturation early and become useless in compensating fast position instabilities which is very undesirable.

6.3.2 Improved position control for the RE beam on COMPASS

The overall plasma radial position control is based on the current centroid approach and position estimation using four flux loops - two on the HFS, two on the LFS, above and below midplane in both cases. From the change of flux ratios and differences in these coils, the change of vertical or radial position is inferred. The position may then be corrected back to the reference by the available actuators which include both the EF power source and the FABV mentioned above. The two controllers of these actuator coil systems have a general form

$$I_{EFPS} = K_{p,I}I_p + K_{p,E}\Delta R + K_{i,E} \int \Delta R dt \quad (6.13)$$

$$I_{FABV} = K_{p,F}\Delta R + K_{i,F} \int \Delta R dt, \quad (6.14)$$

i.e. proportional to plasma current and proportional-integral to position error for EFPS; proportional-integral based on error of the position for FABV. K_p and K_i are proportional and integral gains respectively. The part related to the position error is a natural dependence, as the actuator is supposed to compensate the unwanted position changes, and should work under any circumstances. However, the relation to the plasma current via $K_{p,I}$ is given by the Grad-Shafranov equation and the typical vertical field arising from this equation, in this case based on typical internal plasma inductance and poloidal beta. This can be significantly altered in the following situations

- Operation with high auxiliary heating power leading to high pressure

(β_p), where optimal radial position is a function of I_p and $p = nT$.

- Large amount of runaway electrons in the discharge leading to anomalous pressure (β_p) increase where the optimal radial position is a function of I_p but importantly the same holds for the runaway electron density n_{RE} and average energy $\langle E_{RE} \rangle$ as well.

The consequences of these two cases are similar, we will further focus on the latter case. Small violations of the I_p -only dependence can be compensated by the position error-proportional component. However, for large violations, e.g. in the case of decreasing current and simultaneously increasing runaway electron energy, the position control designed in this way will fail. This situation has been occurring during the dedicated RE beam discharge scenarios and is illustrated in figure 6.2. In orange, the performance of the position control is shown for the case of standard discharge with no runaway electrons, the position controlled is very well maintained and radius is decreased in a controlled way near the termination as the plasma becomes smaller during the current ramp-down. During the whole discharge the vertical field from the EFPS and FABV divided by the plasma current - with a constant C added to avoid divergence at zero - is constant. This is expected and it can be concluded that the discharge follows the standard Grad-Shafranov equation and the control works precisely.

On the other hand, in the red case, the full RE beam is created by argon MGI (first pink rectangle) and since this moment the vertical field applied becomes more and more disproportional to the plasma (RE beam) current and at the same time, the position oscillates strongly which is further worsened by the feedback control of the plasma current where drops are compensated by changes in the loop voltage. The two interacting control loops get the system into a very unstable phase and the RE beam eventually drifts to the LFS where it hits the limiter. Most of the RE beam discharges were characterised by a similar behaviour with uncontrolled LFS termination. Furthermore, the deposited energies measured during the termination at the dedicated LFS protection limiter were very significant, well over 10 kJ [138].

In order to improve the position control the author suggested to decrease the $K_{p,I}$ by 30% in collaboration with COMPASS operators, this means reducing the constant from $4.8 \cdot 10^{-7}$ to $3.2 \cdot 10^{-7}$ in the units of the control loop. The discharge #19002 shown in blue in the figure 6.2 is run with this value of $K_{p,I}$. The discharge is otherwise very similar to the discharge marked in red including the secondary deuterium injection marked by the second pink rectangle. It is apparent that while the disproportional of the applied vertical field with current still exists, the position is stable up to $t = 1320$ ms when the position control is switched off. It can be also seen that small oscillation on the position before $t = 1250$ ms is quickly damped. This position feedback control for the RE beam therefore seems to be stable as the increased relative role of the position error in the controller is able to compensate the change of position arising from the acceleration or slow

changes of energy. On the other hand the decreased value of $K_{p,I}$ is causing failures of position control of plasmas without RE, which are lost towards HFS. The two regimes therefore need to be used in the respective situations, unless the inputs of the whole nature of the control algorithm is changed, e.g. by including independent RE energy measurement in parallel to the plasma/RE current dependence. In practice, the change of the feedback constant was programmed to occur slightly after the time of the Ar/Ne/Kr injection was applied to generate the RE beam. In this way, the successfully generated RE beams are well controlled in radial position.

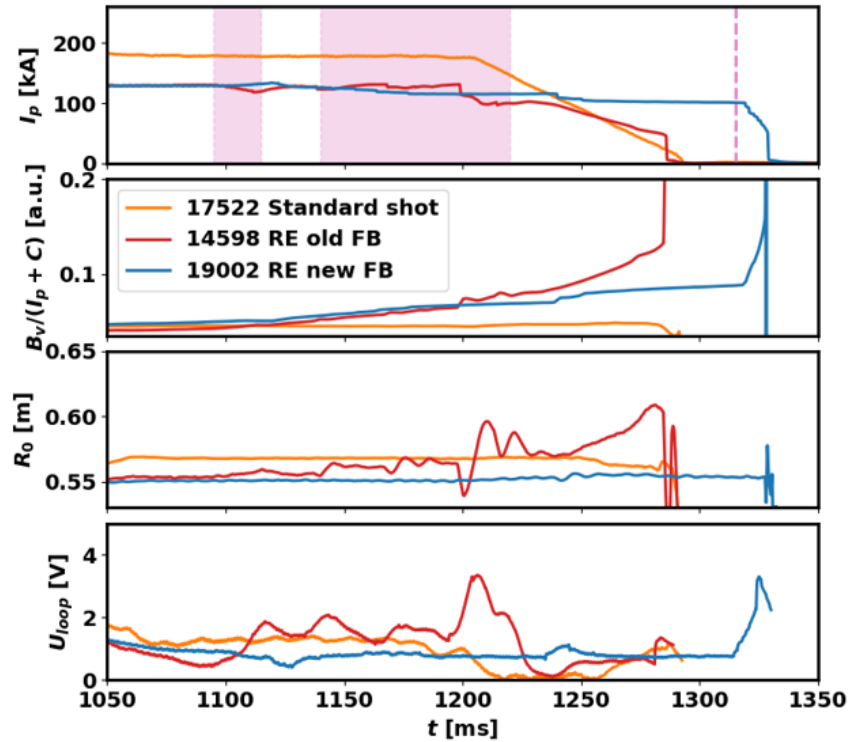


Figure 6.2: Comparison of the performance of the old and the modified radial position control policy for the runaway electron beam at COMPASS: from top plasma current and injection valve opening (colored rectangles), the normalised vertical field B_v , the radial coordinate of the plasma center R_0 and the loop voltage U_{loop} evolution.

The change in the position control of the RE beam was extremely important for interpretation of all the RE experiments at COMPASS and is one of the most important results of this thesis. However, it is not the only outcome of the experimental observations of RE equilibrium consequences at COMPASS. Importantly, the "anomalous" component of the vertical field proved to provide a very simple way to estimate the RE beam kinetic energy.

6.4 Simple energy estimate based on magnetic equilibrium in full RE beam

6.4.1 The estimate based on B_v and radial position

As was shown in the previous section, the RE beam energy affects the radial position of the RE beam. Vice versa, the simplified approach of equation (6.9) can be used to estimate average or "effective" energy of the runaway electron beam from its radial position and applied vertical field as

$$\gamma = \frac{eR_0B_{v,an}}{m_e c}. \quad (6.15)$$

This means that the gamma factor, i.e. average energy of the confined RE beam, can be calculated as a simple function of known constants - electron mass m_e , electron charge e and speed of light c ; the beam current centroid position R_0 and anomalous component of external vertical field $B_{v,an}$. This quantity is the fraction of the external field that is applied on top of the current-proportional value of vertical field that is based on the Grad-Shafranov equation as shown in equation (6.7). The current-proportional component of the request can be calculated using the feedback control constants discussed above. Using the relation (6.15), the energy in MeV can be approximately calculated as

$$E[\text{MeV}] = 300R_0B_{v,an}, \quad (6.16)$$

when the rest energy of the RE can be neglected compared to the kinetic energy. In the attached Paper B [22], figure 7, the method was applied to the special case of discharge #14592, where the RE beam current is gradually decreased to $I_{RE} = 50 \text{ kA}$ where it is kept for 200 ms in stable position even with the old feedback control approach. In this stationary phase it is obvious that the increase in the required vertical magnetic field for keeping the position stable must be connected with the beam acceleration that is a result of the applied loop voltage to maintain the current. In this case, it is even possible to match acceleration - energy increase in the electric field - with the position and discharge evolution trajectory in the B_v and $\langle E \rangle$ plane when using simple linear function of the loop voltage. The use of linear function of the signal instead of the signal itself is justified by the fact that the internal effective acceleration electric field might be lower than the one corresponding to the measured loop voltage due to geometric effects and remaining drag acting on the RE. The energies derived in this way are in the 11-16 MeV range, which is in good agreement with the largest energies measured by HXR spectroscopy in similar scenarios. The calculation using the loop voltage is not reliable during the phase with changing current as the internally induced electric fields that may not be correctly measured outside

the vessel, may play significant role. However the direct, simple estimate of energy via equation (6.16) is still possible.

6.4.2 The estimate based on the pressure from EFIT

Another way to determine the average energy of the runaway electron beam is to use one of the quantities representing plasma pressure that are calculated by the EFIT reconstruction. Despite the fact that the reconstruction is based on solving the standard high temperature plasma equilibrium, the RE beam energy effect on the equilibrium is so similar to the effect of plasma pressure that some of the output quantities can be effectively used as the measure of the total kinetic energy or average energy per particle. Typically the normalised plasma beta parameter can be used. This parameter is defined as

$$\beta_N = \frac{p}{\frac{B^2}{2\mu_0}} \frac{aB_t}{I_p[\text{MA}]}, \quad (6.17)$$

which means the plasma pressure normalised by the magnetic field pressure and further normalised by a function containing toroidal magnetic field B_t , minor radius a and plasma current I_p in megaamperes. It is worth noting that extremely high β_N values were observed in the RE campaigns at COMPASS since we have conducted first experiments and this observation motivated further investigation of the phenomenon. In the case of the RE beam, the plasma pressure can be replaced by the relativistic pressure of the runaway electron beam, based on the general relativistic pressure tensor formula [172]

$$P = \sum_{\sigma} n^{\sigma} m^{\sigma} \langle \gamma \mathbf{v} \mathbf{v} \rangle^{\sigma} \quad (6.18)$$

where σ marks component of the system (RE, plasma, neutral gas, etc.) and this definition captures the anisotropy. This definition of pressure, that is applied in the general relativistic plasma toroidal equilibrium derivation in [172] and used by Fujita in tokamak applications [175], then reads

$$p = \frac{1}{2}(p_{\phi} + \frac{1}{2}p_{\theta}) = n_{RE} m_e \gamma (\frac{1}{2}v_{\phi}^2 + \frac{1}{4}v_{\theta}^2), \quad (6.19)$$

This formula provides a direct relation between the beam energy and β_N calculated by EFIT. In the tokamak geometry, under the assumption of high safety factor q and low pitch angle ξ , the toroidal velocity component v_{ϕ} may be considered dominant and in the case of ultra relativistic beam energy, the pressure term may be simplified as

$$p = \frac{1}{2} n_{RE} m_e \gamma c^2. \quad (6.20)$$

If the value of the β_N is available, then the γ factor can be derived using the relativistic pressure definition as

$$\gamma = \frac{\beta_N I B_t}{a \mu_0 n_{RE} m_e c^2}. \quad (6.21)$$

Furthermore, if we consider the current to be carried by the RE exclusively, i.e. $I = n_{RE} e c \pi a^2$ and we simplify the constants, we may arrive to the simple formula

$$E[MeV] = 7.5 \beta_N [\%] a B_t. \quad (6.22)$$

In this equation 6.22, the β_N value is directly in percents as the factor 10^{-2} was taken into account during the simplification, the toroidal magnetic field is preset and measured in the experiments and minor radius a can be estimated from the equilibrium reconstruction or a suitable radiation diagnostics with spatial resolution, e.g. the overview camera. This method was applied to the COMPASS discharges in the attached Paper G [178] and in the further text. Note that due to the derivation neglecting the anisotropy of the situation, i.e., the factor 1/2 and 1/4 at the different velocity components in the relativistic pressure derivation, the constant used in the equation (6.22) is 3.75 in the paper G [178]. This leads to energies smaller by a factor of 2, but the same trends. For reference and comparison with the other methods we included both estimates in the figures below. The estimate neglecting the anisotropy with the value of the constant 3.75 is designated as Min E_{β_N} , the estimate that attributes all the momentum to the toroidal pressure tensor component, i.e. with the constant value 7.5 is marked as Max E_{β_N} .

Another quantity suitable for estimates of total kinetic energy is the stored/thermal energy W_{pl} calculated by EFIT. In common high temperature plasma, this would be the energy connected with the kinetic pressure, in the case of the high energy RE beam, this quantity is roughly representing the total kinetic energy of the electrons. In general it should be proportional to β_N , however based on the properties of the equilibrium, namely the pressure anisotropy, it is expected to generally reach different values than the total kinetic energy calculated as β_N -based average energy times the number of RE ($E_{tot} = \langle E_{\beta_N} \rangle * N_{RE}$).

The three methods - feedback control, β_N -based and use of the plasma energy - are compared in figure 6.3 for the discharge #14592 in the phase where all the current is carried by the RE after the injection of Ar into the flat-top of the low density discharge. The scenario is in general described in section 4.3.2. The figure 6.3 is only focused on the phases with decreasing and constant current after the generation of the RE beam.

The number of runaway electrons is calculated from the RE current density under the assumption that the RE population is ultra-relativistic ($N_{RE} = I/(ec) * 2\pi R_0$). It can be seen that all the methods predict gradual increase

in the average energy and the energy trend estimated from the radial position correlates well with the β_N -based estimate when considering the pressure is dominantly connected with the toroidal momentum component. The differences can be attributed to changes in the current profile, energy or pitch angle distributions that can have different effect on the two methods. Note that the energy reached is significant, more than 12 MeV according to both methods. The discharge requires consumption of a majority of the available Voltseconds of the central solenoid and energies well over 10 MeV are necessary for explaining the HXR and synchrotron radiation measurements in more recent similar discharges, thus the energy estimate seems to be within the expected absolute values as well. The comparison with these measurement methods is done using the suitable discharges in the attached conference paper G [178].

The total kinetic energy displayed in the third frame of the figure documents the similar trends when comparing the methods described above and the plasma energy E_{pl} which is the direct output of EFIT. The E_{pl} is showing almost exactly the same values as the β_N energy estimate when neglecting the strong relativistic pressure anisotropy and when multiplied by number of RE. This seems to agree with the expected discrepancy of the EFIT solution of the Grad-Shafranov equation and the actual situation in the terms of anisotropy. Interestingly, the total energy rises for major part of the current ramp-down and then the increase of the total energy is even more prominent when the current is kept approximately constant. The estimates tend to saturate when the loop voltage is decreased as the current is above the requested reference of 50 kA. However, the final saturation may also be connected with the maximum RE energy that can be confined in the relatively small COMPASS vessel. The maximum total kinetic energy of 10 kJ is well comparable to the measurement of the deposited energy due to the RE impact that was studied in [138] and in the thesis [84]. Indeed, the energy deposited to the calorimetry head at the LFS of the vacuum vessel reached over 10 kJ in many discharges, depending on the current and other parameters, with the maximum values recorded as high as 16 kJ.

Note that the highest deposited energy may be connected with the higher number of RE when terminated at higher current or conversion of part of the magnetic energy during the termination. This potentially dangerous mechanism is discussed in the final chapter of this thesis. The average energy per particle is not expected to get much higher than in the discharge #14592 in COMPASS as almost all available Voltseconds were invested into the RE acceleration in this case anyway.

In the last frame of the figure 6.3, the measurement of the HXR fluxes based on the detector chain 3.3.2 is shown for reference of the HXR bremsstrahlung radiation during interaction of the RE with companion plasma or vessel structures. In this case, the blind PMT serving as the least sensitive detector is replaced by blind avalanche photodiode of the SXR system that is picking up the HXR background. The PMT was unfortunately optically connected

with the tokamak and measured mixed signal of visible radiation and HXR radiation in the harsh environment and could not be used. The response of the SXR diode is less suitable for extremely high fluxes than the PMT but it is still a better option than the shielded HXR/photo-neutron detector (SHX) which is saturated for a very long period in the phase of the discharge with the highest fluxes. Interestingly, after the RE beam generation and build up of the signal, the trend of the radiation intensity/HXR flux roughly follows the total energy with some loss peaks included. This suggests that the signal can be proportional to the number of the highest energy RE, however it does not seem straightforward to distinguish whether the bremsstrahlung radiation comes from the confined RE interaction with companion plasma or lost RE dominantly. Note that even when including the third detector, the signal saturates for two short periods, roughly at the estimated total HXR rate of $1.6 \cdot 10^{16} \gamma/s$.

These methods are further applied to various parameter scans with RE beams that are further discussed in the next chapter. The β_N -based estimated of RE energy was also successfully implemented at JET, which is also reported in the next chapter and in Paper G [178]. Based on the equilibrium parameter evolution at ASDEX Upgrade and TCV, the method is also applicable at these machines and the application is foreseen in near future.

6.4.3 Energy estimate in the case of plasma discharge with RE population

It is much more difficult to estimate the RE energy using the methods described here in a discharge where Ohmic current is still present. However, we will try to attempt the estimation in a discharge with relatively high RE current fraction after taking into account several additional assumptions. Namely:

1. The RE current and the related RE density and number can be estimated as the difference between the total measured current and the Ohmic component which is estimated from the loop voltage measurement and Spitzer resistivity - a function of plasma electron temperature. The drawback of this approach is that electric field derived from the loop voltage measurement is a very approximate measurement of the actual inter electric field that drives the current. Methods how to obtain a more precise estimate of the electric field are discussed in detail in the thesis [51]. The Z_{eff} in the resistivity calculation is considered to be just slightly above 1.

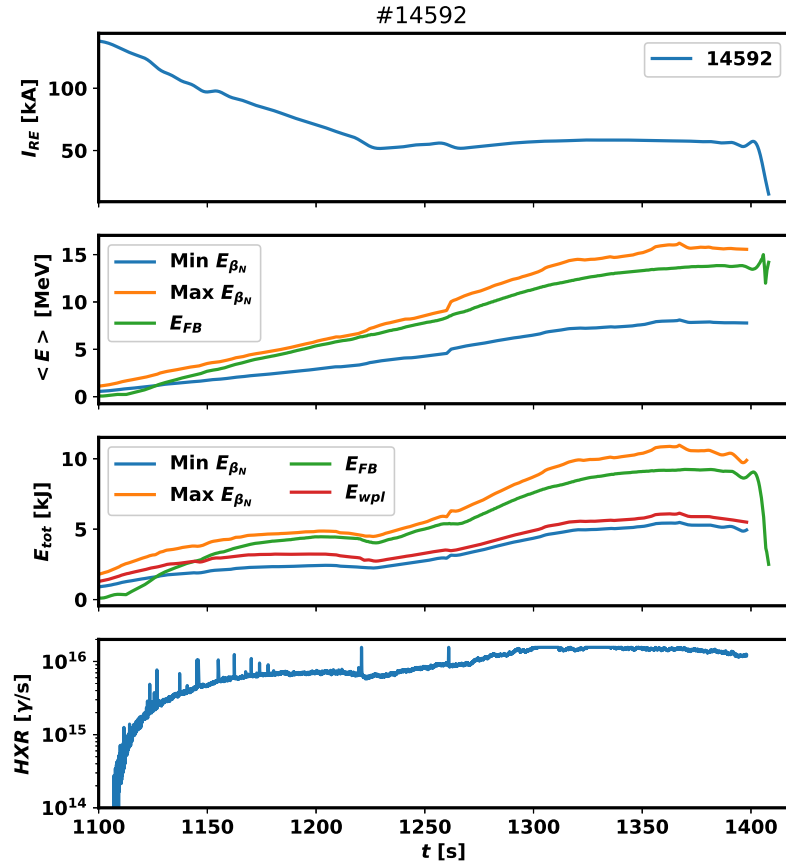


Figure 6.3: Estimate of RE kinetic energy based on equilibrium for the RE beam in COMPASS discharge #14592. From top: The RE current evolution; the three values of average kinetic energy estimates $\langle E \rangle$: minimum (blue) and maximum (orange) β_N -based estimate; the estimate based on the radial position control (green) as described above; Total kinetic energy E_{tot} for the two methods calculated from the average kinetic energy and the RE number compared to the plasma energy calculated by EFIT; last frame - the HXR flux estimate from a detector with low sensitivity.

2. The analysis is done in the phase of the plasma current flattop as the changes of magnetic energy are not take into account. In principle the analysis can be modified with inductive terms to extent the applicability in to other cases.
3. In the studied period of the time evolution, no significant sudden RE losses occur as such events tend to cause propagation of large oscillations in the signals important for the analysis.
4. The RE energies are in the MeV range so that the ultra-relativistic formulas for energy estimate can be still used without introducing significant errors. Alternatively, modified formulas taking into account the rest energy are used. In the formula for the RE current or the RE number,

the effect of substituting the speed of light c with the velocity v is indeed small, about 6% in case of 1 MeV.

5. The Ohmic plasma temperature T and density n measurement taken into account are based on the Thomson scattering measurement of the electron temperature T_e and density n_e that is available and reliable.
6. The thermal plasma pressure values are relatively small. Then, in the energy estimate method based on runaway electron position control the plasma pressure changes are not taken into account and in the case of the energy estimate based on the β_N , the Ohmic part defined in equation (6.17) is subtracted from the β_N calculated by EFIT, to obtain the fraction of pressure related to the RE

$$\beta_{N,RE}(n_{RE}, \gamma) = \beta_{N,EFIT} - \beta_{N,plasma}(n, T). \quad (6.23)$$

Interestingly, the model with the sum of thermal and RE pressure was used to estimate the RE current fraction by Fujita et al. [175] at the small tokamak NOVA-II and by Vlainić et al. [51] at COMPASS. In these works, several different analytical functions of the runaway electron velocity distributions were assumed and used for calculation of average energy and the RE density/current fraction based on the observed anomalous beta values. The current fraction can then differ significantly depending on the shape of the distribution, e.g. exponentially decaying distribution is represented by relatively small value of average energy and significantly more runaway electrons would be needed to carry the current. However, the results presented in this thesis and the various measurements of the RE beam and RE population properties at COMPASS and other large machines suggest that the distributions centered at high energies are more often observed and the RE current estimate using the Ohmic current component is a reasonable approach.

Based on the listed assumptions, the analysis of flat-top phase of the very low density discharge #8680 was done with results shown in figure 6.4. The parameters plotted in the frames are the same like in the previous figure - of course with suitably modified equations based on the listed assumptions.

In the first frame, both total current I_{tot} and the RE current calculated using the Ohmic resistivity and electric field are shown. Apparently, the RE current fraction is quickly increasing from roughly 60% to 85% in the beginning of the observed period and then gradually keeps increasing to more than 90% and in accordance with this less and less loop voltage is applied to keep the current stable. There is a fundamental difference compared to the previous case - no impurity injection and thus a very little drag and therefore the current can be carried by the stable RE population without significant

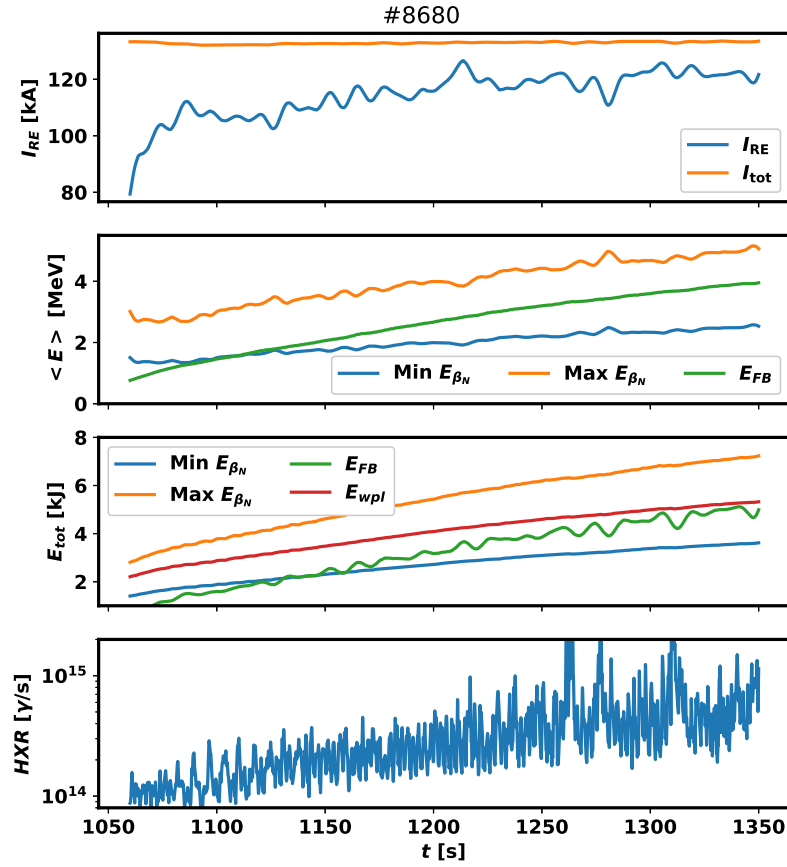


Figure 6.4: Estimate of RE kinetic energy based on RE+plasma equilibrium for the plasma current flat-top of COMPASS discharge #8680 with significant RE population. From top: The total measured current I_{tot} and evolution of the RE current I_{RE} based on the subtraction of the Ohmic fraction depending on temperature and electric field; the three values for average kinetic energy $\langle E \rangle$: minimum (blue) and maximum (orange) β_N -based estimate, the estimate based on the radial position control as described above (green); Total kinetic energy E_{tot} for the two methods calculated from the average kinetic energy and the RE number compared to the plasma energy calculated by EFIT; last frame - the signal of the shielded HXR/photoneutron detector

losses. In accordance with this, the energy is just slowly increasing as well as the signal of the detector of lost RE in the last frame. Due to the extremely low density, the majority of the HXR signal is considered to originate in the interaction of the lost RE with the limiters and vacuum vessel. The average kinetic energy per particle using different methods is again producing similar trends, with the radial position control estimate being significantly lower than the β_N estimate in this case. Furthermore, in the total kinetic energy, the direct calculation of the plasma energy by EFIT is significantly higher than the isotropic (minimum) β_N estimate which is most probably caused by the fact that the isotropic plasma pressure contribution is not subtracted from

the EFIT plasma energy. Overall the energy estimates seem to be reasonable and may improve understanding of these scenarios with slide-away electron population which may occur due to the density control failures or start-up RE events on large machines and result in significant damage comparable to the damage caused by post-disruptive RE beams. The method is however not applicable to discharges with higher density and only trace RE population as the effect of such population on the total equilibrium is negligible. However, in such discharges HXR spectrometers can provide good RE energy estimate as the fluxes are reasonably low and enable their application.

The most straightforward estimates of RE parameters based on the RE beam magnetic equilibrium can apparently provide very useful diagnostics capabilities. This gives a good hope that a full self-consistent equilibrium reconstruction could actually provide many more details, including discrimination of certain shape parameters of RE energy distribution and spatial distribution. Perhaps, the evolution of the average pitch angle of the RE population could be disentangled from the influence of the other parameters to some degree as well, as the effects of pitch angle distribution change should change both anisotropy of the pressure and the value of the current. However this option needs to be explored outside of the scope of this thesis. In the last section of this chapter, only the spatial effects of the RE equilibrium which can be directly related to experimental observations, are analysed and discussed.

6.5 Other effects of betatron/tokamak RE equilibrium

In the previous two applications a 0D/averaged approach to the RE equilibrium was considered in order to improve the feedback control or establish a simple RE energy diagnostics. However, more complicated spatial dependencies such as the shape of the beam boundary and its evolution due to changing current and energy are also of significant interest. First, the shape of the beam or the companion plasma boundary are discussed with respect to the camera observation. Second, the equilibrium leads to the spatial ordering of particle trajectories by energy which determines where the RE hit the limiters and what are the maximum confined energies.

6.5.1 HFS X-point and possible self-compression

The X-point is characterised by a zero poloidal magnetic field. With the new feedback control, the overall beam shift is prevented by sufficient increase in the vertical magnetic field. However, the HFS X-point is generated in this case and its gradual movement towards LFS with energy increase/current decrease may actually lead to a collapse of the confined plasma region and the beam itself as well. The situation is shown in figure 6.5. In the left part of the figure, evolution of separatrix (last closed flux surface) as calculated by standard EFIT reconstruction is shown for the discharge #14592 where the position as well as the current are kept stable. The time of the displayed separatrix is shown at each contour. Note that the last closed flux surface calculated by EFIT should still correspond to the region of the confined plasma while it is not necessarily the boundary for the confined RE beam electrons. The time evolution of the position of the X-point can be trusted as it is validated by measurement of the magnetic field at the vacuum vessel HFS midplane. The HFS X-point enters the vacuum vessel roughly at $t = 1261$ ms. As can be seen in the attached camera images, the entering of the HFS X-point into the vacuum vessel correlates in time with the large flash of Ar II line radiation. This is most probably caused by the abrupt ionisation and excitation and/or recombination of companion Ar plasma due to the change of the topology and size of the region where confined plasma may exist. This phenomenon may also lead to loss of some part of the RE population, but the change in the measured current is relatively small. The phenomenon of the HFS X-point in the RE beam is mostly relevant for small tokamaks.

As we can see in the figure 6.5, the X-point is further progressing towards the centre of the vessel with time which leads to shrinking of the region where the RE may coexist with the confined companion plasma. Some of the RE may exist outside this region, however the spatial charge compensation is not secured in the regions where slow ions are not confined. This means, that with increasing energy and stable position, the main part of the beam is gradually compressed. The controlled compression in minor radius is one of the methods for fast termination of the RE beam that limits re-acceleration of the runaway electrons and regeneration of the RE population and is actively studied at larger machines [146, 157]. Therefore, this phenomenon can be potentially very interesting. With the improved feedback control, a fast beam termination when the beam current reached low values - about 20-30 kA - was observed on COMPASS without any specific position instability or other obvious cause. The current understanding of the situation points to the hypothesis that these terminations can be caused by the compression. The beam compression may lead to a very low value of the edge safety factor q_a due to small minor radius and still significant current and the external kink instability could be one of the causes of the termination. Indeed, if we

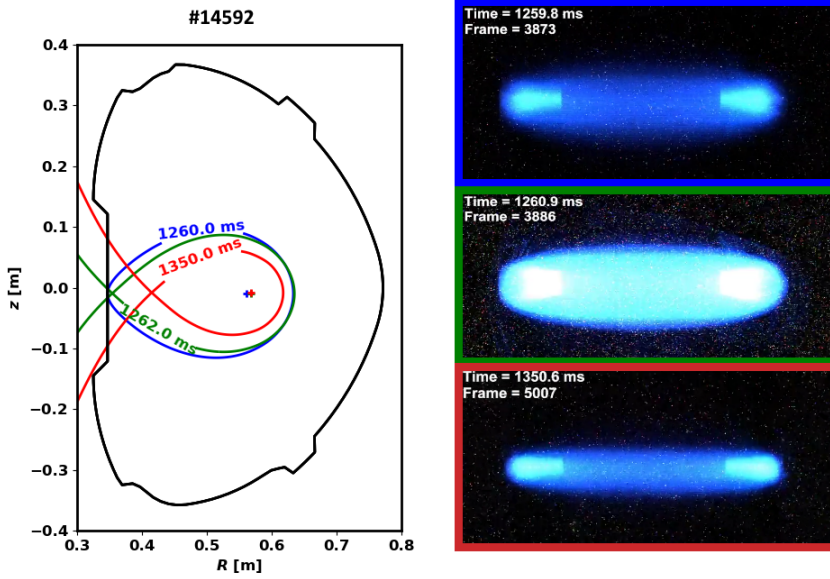


Figure 6.5: Left: Shape of last closed flux surface as calculated by EFIT. With time the HFS X-point is moving into the vessel and further outwards, Right: Consecutive wide angle visible camera images, in time instances roughly corresponding to the LCFS in the left part of the figure.

consider several very different RE beam discharges as in the figure 6.6, the evolution of the q at the edge suggests that this is a viable hypothesis for the termination. Let us remind the formula for the safety factor at the edge of circular plasma q_a before we proceed

$$q_a = \frac{a}{R_0} \frac{B_t}{B_p} = \frac{2\pi a^2 B_t}{\mu_0 I R_0} \quad (6.24)$$

where we have used the simple loop formula for the poloidal magnetic field $B_p = \frac{\mu_0 I}{2\pi a}$ in the second step. This means that the low and unstable q_a values might be achieved by the compression in minor radius a , the increase in the current I_p or decrease in the toroidal magnetic field B_t . During a normal plasma current ramp-down, the q_a would be rising as the decrease in the plasma current is similar or faster than the decrease in the minor radius. However, the situation in the RE beam with high energy and HFS X-point configuration seems to be different.

In the figure 6.6, the plasma current I_p , the q_{95} , i.e. the safety factor near the edge, the radial position of the current centroid R_0 and the lower average kinetic energy estimate based on the β_N is shown. It can be seen that except of the very quickly terminated red case #18932 which collapsed to the HFS, all the beams experience a reversal in the q_{95} trend and arrive near the value of 2 which is the limit of MHD stability in a tokamak. In the green case #16625 which drifts to the LFS due to use of the old feedback control

policy, the current reaches zero quite smoothly, however, in the case of the other discharges, fast current drops occur at the termination and they are apparently related to the decreasing distance between the magnetic axis of the beam and the HFS X-point. This is indeed a property specific to the RE beam and in case of COMPASS we may speak about the termination of the beam by a self-compression. If this termination or a controlled compression in the center of the vessel would be doable in the recombined plasma necessary for the benign termination that is discussed in the next chapter and [145], it could further decrease the risks of the tokamak damage by the runaway electrons. Currently, the termination is done against the limiters in larger machines, typically the HFS limiters.

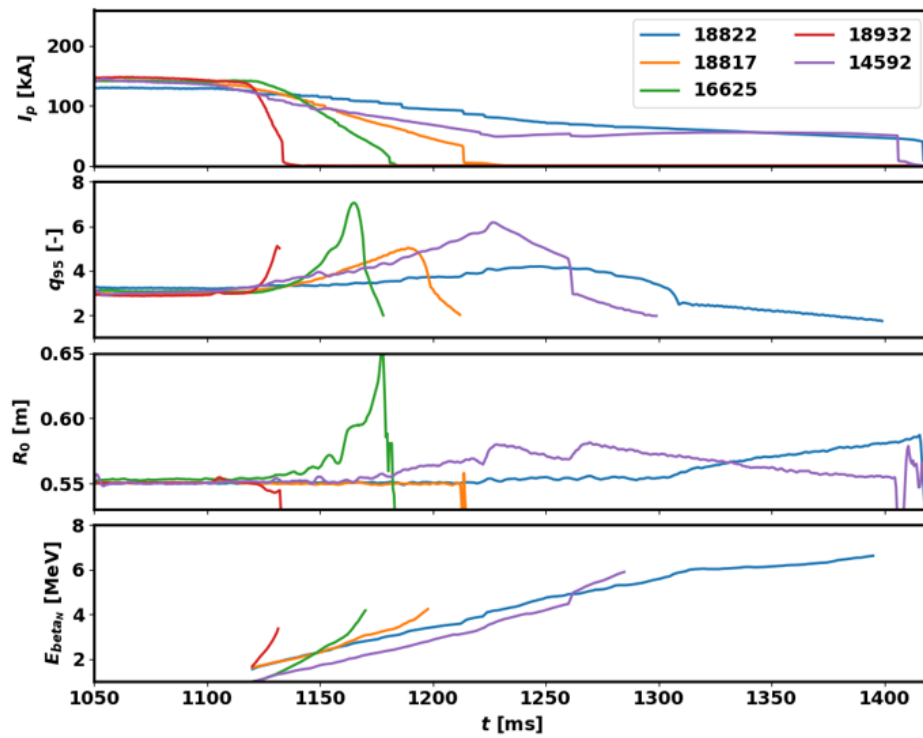


Figure 6.6: The evolution of the plasma current, the q_{95} , the radial position of the beam and the estimate of average energy based on isotropic β_N method for several COMPASS discharges. The interesting q_{95} trend reversal followed by sudden beam termination is observed and characteristic for the RE beam on COMPASS

6.5.2 Orbits for different energies and impact locations

The other important consequence of the relativistic equilibrium of the RE beam is the fact that under a stable position, the RE with higher energy are lost predominantly to the LFS midplane limiters. The situation with the RE

equilibrium in the poloidal plane is approximated using the Biot-Savart tool described in Appendix C. In this case, the current in the main equilibrium winding - the EFPS and the current in the beam/plasma is taken into account to represent the situation. Other poloidal field coil groups (shaping or magnetising) do not play significant role. However, in the case when the fast B_v power supply current is large or in saturation, its magnetic field is also considered and superposed with EF. The EF winding current is taken from the signal measuring the respective power supply current, multiplied by the number of turns and distributed to the geometric cross-section of the coils. For the EF system winding in the central solenoid this means $-48I_{\text{EPFS}}$ turns in total and for the LFS ring coils it is $16I_{\text{EPFS}}$ as there are 4 individual coils with 8 turns each, but connected as two pairs of coils in parallel [127]. The current of the beam profile itself can be represented by an arbitrary profile function, or by current density j imported from the standard equilibrium reconstruction calculated by EFIT. The tool then calculates the magnetic field map and poloidal flux ψ which determines the region of plasma confinement and can be cross-checked with EFIT. However, the most important calculated quantities are the drift orbits or in other words toroidal canonical momentum $P_\phi = \gamma m_e c^2 + e\psi$ surfaces that are corresponding to the natural primary equilibrium functions for RE of given energy. In principle a new iteration of the current density can be defined on these surfaces to obtain a better approximation of equilibrium for the RE beam, however this is not attempted in this thesis but planned for near future. In the examples below we focus on the resulting beam boundaries for different energies and situations.

In the figure 6.7, the results for the RE beam and coil currents of discharge #14592 at time $t = 1220$ ms are shown. This situation corresponds to ψ separatrix (in red) already significantly elongated in horizontal direction which is the RE effect. The average energy calculated using the methods described in previous sections and shown in figure 6.3 is about 6 MeV in this period. Interestingly, the 12 MeV P_ϕ separatrix (blue) is LFS limited. This confirms that the RE with energies higher than the equilibrium average energy terminate at the LFS limiter with gradual acceleration. Moreover, the RE can exist in a region much larger than cold plasma ions and electrons which soon reach vessel surface in case they cross separatrix. However, the density of RE outside separatrix is most probably very limited due to worse spatial charge dilution. The RE can get to the outer orbits due to magnetic perturbations or collisions with high pitch angle scattering in this case. On the other hand, in extremely low density discharges the cross-field transport of RE maybe very low and thus they can be confined on the closed orbits without a contact with the limiter.

In the figure 6.8, the situation in the same discharge #14592 right before its termination is shown. In this case the separatrix in red poses a HFS X-point, the external vertical field is very large and the confined plasma

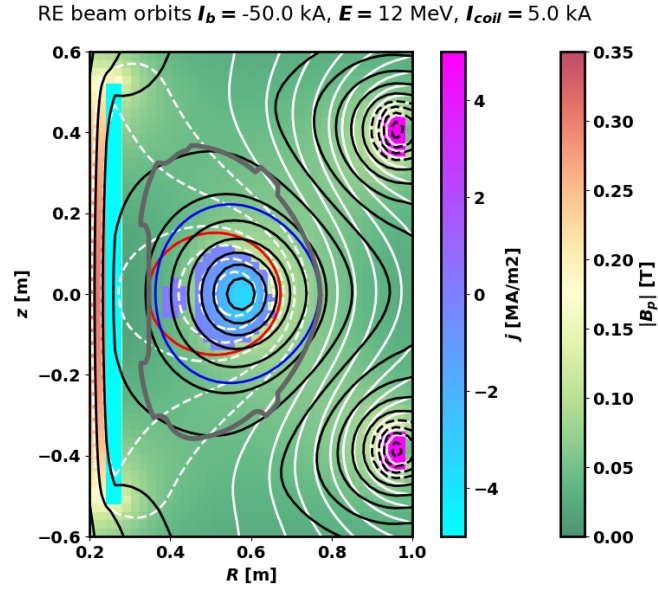


Figure 6.7: The RE quasi-equilibrium: current density from the standard EFIT calculation and current density distribution in the coils are shown in shades of magenta and blue, the magnetic field that is calculated by the Biot-Savart tool C is displayed in the shades of green-yellow-red, the flux surfaces are displayed in white with plasma separatrix in red, toroidal canonical momentum surfaces for RE of 12 MeV are displayed in black with the outermost closed orbit in blue. COMPASS #14592, $t = 1220$ ms

region extremely small. The estimated equilibrium average RE energy is about 13 MeV. In this case the 20 MeV electron orbits are still HFS limited, however the RE of significantly larger energies tend to terminate on the LFS. The region which can be occupied by the RE is much larger than the confined plasma region in this case. However with further increasing vertical field, the leading to a self-compression of the confined plasma region may occur as well as a quick loss of the RE population. A very interesting observation in this and the previous case is that the current density supplied from EFIT is having opposite direction than the dominant plasma current in the outer regions and near the HFS X-point. This is most probably an artefact of EFIT due to not being 'aware' of the relativistic pressure of the RE. It is not probable that these counter-current densities would be connected with the return currents that do exist in some plasma-beam systems. However to prove this, it would be necessary to apply a special particle-in-cell simulation or similar complicated models.

To compare the effect of different energies on RE location in a more common plasma and external vertical field configuration, the last closed orbits and separatrix are shown in figure 6.9 for #14592 equilibrium before the RE beam generation, at $t = 1110$ ms. It is clearly visible that in this configuration 5 MeV electrons may terminate at the HFS, while all the other displayed

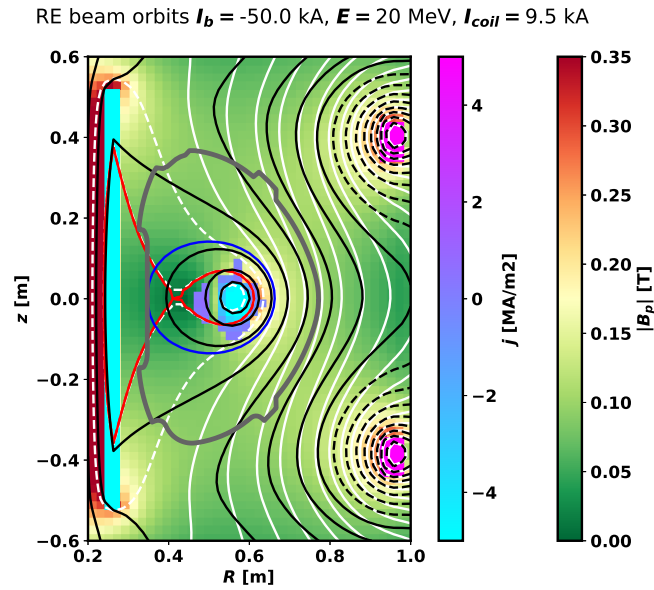


Figure 6.8: The RE quasi-equilibrium: current density from the standard EFIT calculation and current density distribution in the coils are shown in shades of magenta and blue, the magnetic field that is calculated by the Biot-Savart tool Appendix C is displayed in the shades of green-yellow-red, the flux surfaces are displayed in white with plasma separatrix in red, the toroidal canonical momentum surfaces for RE of 20 MeV are displayed in black with the outermost closed orbit in blue. COMPASS #14592, $t = 1399$ ms.

energies are LFS limited. This situation corresponds to the drift orbits on the standard equilibrium background that are commonly studied and taken into account in modelling, however in case of dominant RE population the RE existing on these orbits can alter the magnetic equilibrium and the feedback control reaction as shown in previous paragraphs. This separation of RE impact location by a certain energy is a very interesting consequence and may help to explain some of the observations by other diagnostics at COMPASS that are listed in the next paragraph.

■ 6.5.3 Diagnostics evidence for RE orbits limited at HFS and at LFS

The magnetic configuration calculation in fact helps to understand several different diagnostics observations, corresponding to RE impacts on both HFS and LFS limiters during different parts of the discharge. Namely:

- Fast IR camera measurement of heat fluxes varying with periodic losses

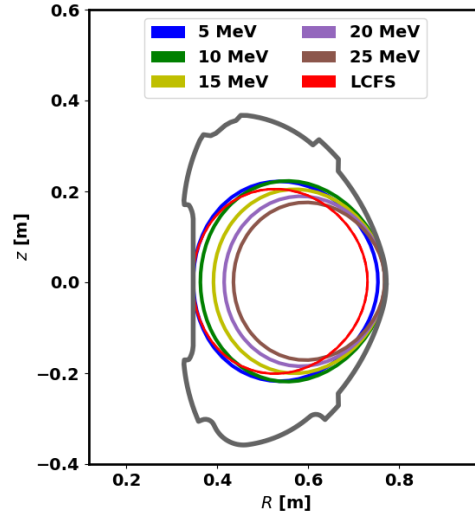


Figure 6.9: The last closed RE orbits for different energies in a typical circular plasma of the COMPASS tokamak, in red the standard plasma separatrix is shown.

of RE at the HFS limiter and gradual increase in RE-related heat-fluxes at the LFS limiter shown e.g. in attached paper A [18].

- The variation of HXR signal corresponding to gradual movement of very low density plasma towards LFS and towards HFS [163].
- Observation of RE interaction with the HFS limiters mostly just during the plasma current ramp-up in the beginning of the discharge and during the fast collapses of radial position towards the HFS. Indeed, the RE interaction with HFS can be observed in dedicated scenarios on fast camera or even 2D SXR pinhole cameras [132, 134] only during the ramp-up phase, corresponding to a phase with relatively lower energies. The signal disappears later despite the RE population grows further. On the other hand, the HFS limiter damage due to RE impacts can be significant, as shown in the the attached paper C [21].
- Gradual increase of temperature of the LFS calorimetric limiter before the final termination, that can be only explained by gradual deposition of lost RE [84, 138].
- The small carbon pellets injected into a RE beam tangentially from the LFS seem to explode before reaching the beam separatrix suggesting that non-negligible RE population may exist in these locations.
- The AXUV tomography with special modifications for RE beam as shown below.

The AXUV tomographic reconstruction, using the bottom camera that is the only one that does not suffer from strong non-directional HXR pick-up in RE beam discharges was performed for several interesting discharges and time slices. Apart from the very rough beam/companion plasma radiation profile, it shows either LFS or HFS interaction point. In figure 6.10, with the HFS X-point configuration, very large intensities are observed at the LFS by the respective AXUV camera line-of-sight and are also nicely visualised by the reconstruction. This observation then corresponds to very high energies of RE that are hitting the LFS limiters. Apart from the observation of the limiter, the fact that the largest radiation intensity does not come from the confined plasma region but from the X-point region is very interesting observation as well. This observation probably corresponds to the large number of recombining Ar ions that can be expected in this region.

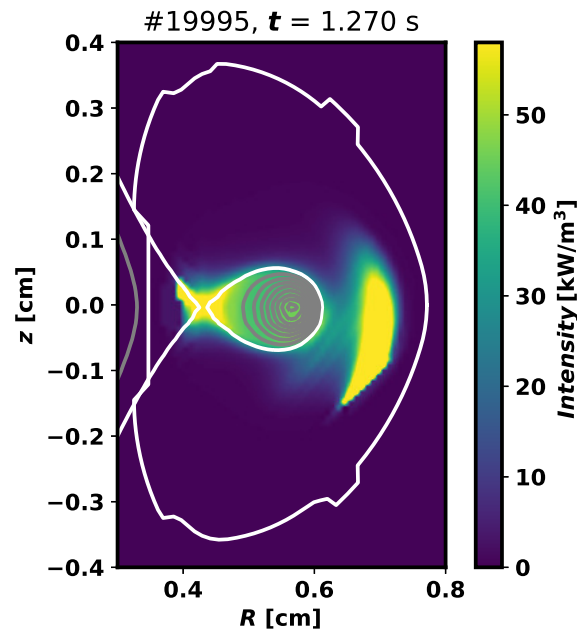


Figure 6.10: The tomographic reconstruction using the single 20-channel bottom AXUV detector showing radiation during the high energy RE beam phase with LFS limiter interaction at beam termination

A different situation is displayed in the figure 6.11. In this case, the full RE beam generation was not successful and the population most probably contained only lower energy RE or an amount of higher energy RE insufficient to drive the current. The population was therefore lost to the HFS limiter and the discharge was terminated. The interaction with the HFS limiter is again noticeable as increased intensity in the AXUV reconstruction corresponding to the time instance shortly before the total loss of the current.

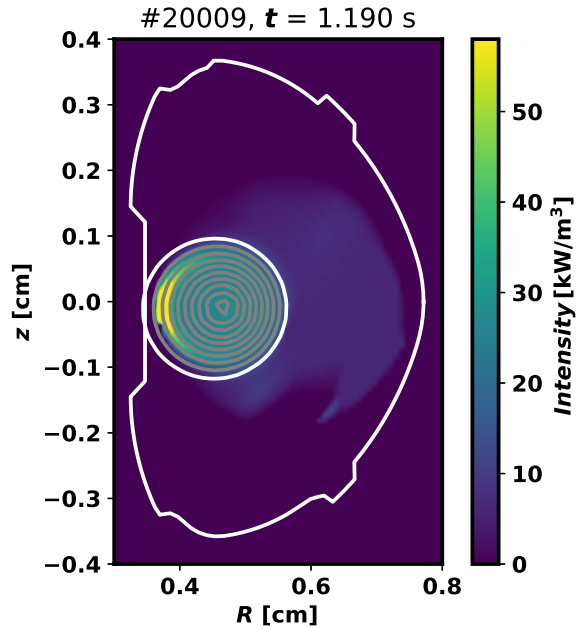


Figure 6.11: The tomographic reconstruction using the single 20-channel bottom AXUV detector showing radiation during the lower energy RE beam phase with HFS limiter interaction

6.6 Summary of RE equilibrium applications

In this chapter, the theoretical background for the relativistic RE beam magnetic equilibrium in tokamak configuration was discussed and applied to COMPASS data. Most importantly, the fact that the outward force acting on the plasma/beam current ring scales with the RE energy was employed in improving the position control of the RE beam. Furthermore, it was shown that based on magnetic measurements or standard equilibrium reconstruction, the average or total kinetic energy can be obtained and that it is an efficient energy diagnostics method of a low cost, readily available on all tokamaks. Moreover, other consequences, like the magnetic beam self-compression via the X-point "guillotine" effect and energy-dependent limiter point location for the RE orbits calculated with the use of magnetic field Biot-Savart calculator are included among the results presented in this chapter. All these consequences and methods are applicable at larger devices with modifications, the applications of some of these is discussed in the next chapter. COMPASS has proven itself as the most suitable device for investigation of these effects due to its small size and simple coil current control system.

Chapter 7

Analysis of RE in COMPASS and JET discharges in support of RE beam mitigation techniques

The final chapter of this thesis, contains a collection of results achieved in the two RE beam scenarios at COMPASS and some selected results achieved at JET where the methods described in this thesis were also applied. The text is focused on the most important physics conclusions that the author has achieved or contributed to significantly and on the related open questions in the RE beam physics. The first section is focused on the ramp-up RE beam generation scenario of COMPASS.

7.1 The ramp-up scenario RE beam analysis

The ramp-up scenario described in chapter 4, is of a special interest in terms of the RE generation. Extensive analyses of various parameter scans and other measurements in this scenarios were done within the thesis [20]. However, the low reproducibility of the scenario has been puzzling. The most important findings that may help to explain the variation in the RE beam generation and confinement are discussed here with references to the material published by the author.

■ 7.1.1 RE beam reproducibility

The most important and clearest correlation that was identified in terms of the RE beam generation is that between the toroidal magnetic field B_t and the resulting RE beam current I_{RE} . The higher is the magnetic field the higher is the fraction of the RE current after the disruption and also the reproducibility of achieving the similar fraction in repeated discharges within the same session, i.e. with similar wall conditions. The result is included as fig. 2 in the attached paper C [21], but also shown in figure 7.1. The dependence seems to point to a threshold behaviour and almost total conversion of current into RE current is reached for higher toroidal magnetic field. A similar dependence on magnetic field amplitude was observed at JET [69] - with large Ar fractions in the disruption mitigation mixture and large magnetic field the runaway beam generation is guaranteed at JET. At ASDEX Upgrade, strong dependence on the magnetic field was also observed with respect to the q_{95} value during the disruption - there were no RE beams generated in case $q_{95} < 3$ while the reproducibility of the RE beam generation is good with $q_{95} > 3$.

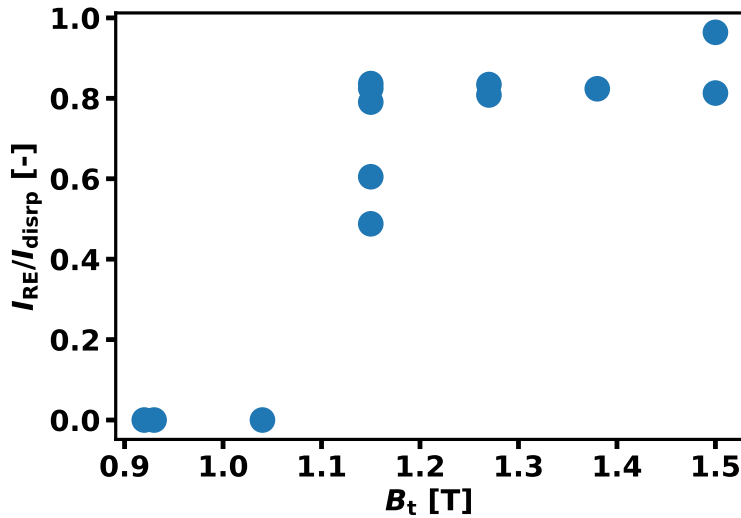


Figure 7.1: The runaway electron current I_{RE} reached in the confined RE beam after Ar MGI into the ramp-up scenario on COMPASS at different magnetic fields B_t .

There can be two main reasons for the strong influence of B_t . First, in terms of the generation, the q_a values at the same current with higher B_t are higher, which is in general good for MHD stability and thus the plasma can resist the disruptive effects of the gas injection at the edge longer. Moreover, before the magnetic configuration is destroyed, it takes longer for the ionised Ar atoms to travel across the magnetic field surfaces as the diffusion coefficient

typically scales with $r_L \sim B^{-2}$. These mechanisms may increase the duration of period suitable for acceleration of the RE. Indeed, such slowing down of the Ar penetration would prolong the situation with closed magnetic field lines and already increased electric field due to the decay of the current in the external layers of the plasma ring.

The cause of the dependence on the magnetic field can be also related to better RE confinement in higher B_t with respect to the sources of external stray poloidal fields that decrease the confinement through induced magnetic instabilities. Such instabilities have larger relative effect in smaller B_t . The origin of these stray fields can be in the currents induced in the vessel and other passive structures during the disruption and in general due to the redistribution of the currents during the TQ and the CQ. Interestingly, the RE beam generation after a disruption in COMPASS seem to be in contrast to results obtained at the Alcator C-mode that were explained by modelling and with the magnetic field threshold for RE beam generation at TEXTOR. At Alcator C-mode, a machine slightly larger than COMPASS, the RE beams were never generated in the disruptions, despite that the machine was operated at very high B_t up to 9T, this was explained by the scaling of the RE confinement with machine size in [179]. It is worth noting that ALCATOR C-mode also had a very conductive ($R_{tor} = 40\mu\Omega$) vacuum vessel where large currents were induced during the disruption and could contribute to prevention of the RE beam generation. COMPASS on the other hand has a thin, resistive ($R_{tor} = 630\mu\Omega$) vessel where relatively small currents are generated during the disruption. At TEXTOR, magnetic perturbations were identified to prevent the RE generation below the magnetic field limit of $B_t = 2$ [180]. Given the results achieved in this scenario on COMPASS, this limit is by far not universal and other parameters specific for the machine and the scenario come into play. However, the relative strength of magnetic perturbations can influence the probability of generating the confined RE beam from the ramp-up scenario as shown in the figure 2 of the attached Paper E [181]. At the higher levels of the magnetic perturbation amplitude, the RE beam was not generated, while at lower levels the spread in the current of the generated RE beam is rather large.

Given that RE are generated, the equilibrium conditions discussed in the previous chapter may affect its macroscopic stability, which is further complicated by the ongoing current quench. Indeed, the terminations of the weak RE populations that did not form a confined RE beam usually occur at the HFS. This can be observed using the position control signals, but also based on the AXUV or SXR radiation tomography that is possible at this phase of the discharge. A comparison of two cases, #15824 with a confined RE beam and #15820 with insufficient RE population is shown in the figure 2 of Paper F [182]. In both cases, the radiation at the plasma edge is visible after the Ar injection. However, with progressing current

quench, the radiation center of mass moves to the HFS in the case of the failed RE beam generation. At the end, the interaction with the wall is the only source of radiation. On the other hand, in the case of the confined beam, the UV and visible radiation builds up in the core as the beam is formed, stable in position. Later on, the confined beams typically drift to the LFS in accordance with the role of the low current and increasing average RE energy in the equilibrium and position control. This further corresponds with the fact that the RE beams with the highest current (smallest drop during the CQ) are the most stable ones.

■ 7.1.2 Detailed look on the ramp-up RE beam generation

The understanding of the ramp-up RE beam generation on COMPASS was significantly improved after the fast cameras (several thousands frames per second in high resolution) were installed. This includes the color fast visible camera Phothron Mini UX100 and monochromatic very fast camera Phothron SA-X2, the former offering a very crude resolution of the element or ionisation state based on the dominant color of the line radiation and the latter offering extremely large frame rate of more than 100 000 fps still with a good spatial resolution. These cameras allowed observation of interesting phenomena at the edge of the plasma or the RE beam in all stages of the ramp-up scenario, namely

- Penetration of the impurity into the plasma during the injection in the form of filament structures following the magnetic field lines in the case of observation of the line radiation of Ar ions (Ar II, dominantly blue color) and rotation of these structures. The line radiation of the neutral Ar peaks in the IR region and therefore it is not visible in the fast camera data.
- Penetration of the neon gas plume into the plasma - in the case of Ne, the neutral atoms are visualised as the Ne I dominantly radiate in the orange region. This provides qualitatively different observation of the gas injection compared to Ar.
- Observation of very bright, short living, thin filaments outside of the main RE beam volume shortly after its generation or in phases with elevated electric field
- Observation of turbulence-like structures at the edge of the RE beam or the confined companion plasma during the current decay

The first two observations from the list above are shown together with the relevant signals in figure 7.2. In this case the images are taken with the monochromatic fast visible camera and are shown in the bottom part of the figure - the image capturing the neon injection is characterised by the saturated region of the gas plume, while the image capturing the Ar injection shows broad filaments as the argon ions follow the field lines. In both cases, the RE beam was not generated. However, from the displayed signals, it is obvious that the amount of HXR corresponding to the generated and lost RE is larger in the Ar case. There is also a small bump in the current signal during the current quench corresponding to a very short living RE beam. Despite the same timing of the injection and similar gas quantity, the sequence of events (density rise, current decay, etc.) is significantly faster in the case of the neon injection. It can be related to both the neutral neon speed in the injection tubes and to the more significant effect on the plasma, which could be related to the higher ionisation potential of Ne compared to Ar. Due to this difference, the neutral Ne atoms may penetrate deeper in the plasma. As a matter of fact discussed for the older discharges in [20], the RE beam after generation by Ne MGI in a disruption with partial CQ was never observed on COMPASS. With the Ne injection, the RE beam is either not generated with all the RE lost at CQ or, with sufficient seed, the full current conversion into RE beam and its slow decay is observed. At other machines, RE beams can be generated in disruptions initiated by Ne MGI, however at JET and ASDEX-U the Ar injection is used almost exclusively as a standard and reliable scenario. For the comparison of the color images of Ar II and Ne I in evolved RE beam, see the attached paper F [182], figure 3.

The bright, very short living filaments (small tens of μs) that are listed in the interesting camera observations above were found to correspond to events in several other diagnostics and to this date are a very unique observation of the COMPASS experiments. The situation is shown in the figure 7.3 that captures a transition from the current quench to the RE beam plateau. The vertical ECE registers the most distinct events in a form of short peaks, these can be directly related to observation of filaments in the camera data, furthermore if there is a peak group in the ECE data, the observed filament structure is typically more complicated as well. The peaks come from a relatively flat background as the density in the main beam volume is rather large and can be well over the cut-off for the ECE diagnostics at COMPASS so the measured signal from the core region can be significantly attenuated. The magnetic perturbation typically shows oscillations close to the peak in V-ECE. Moreover, the direct RE measurement by the Cherenkov detector or indirect RE measurement by HXRs shows peaks following some of the filaments.

Based on this description of the situation, the explanation that the filaments are connected with low energy RE just generated outside the RE beam volume

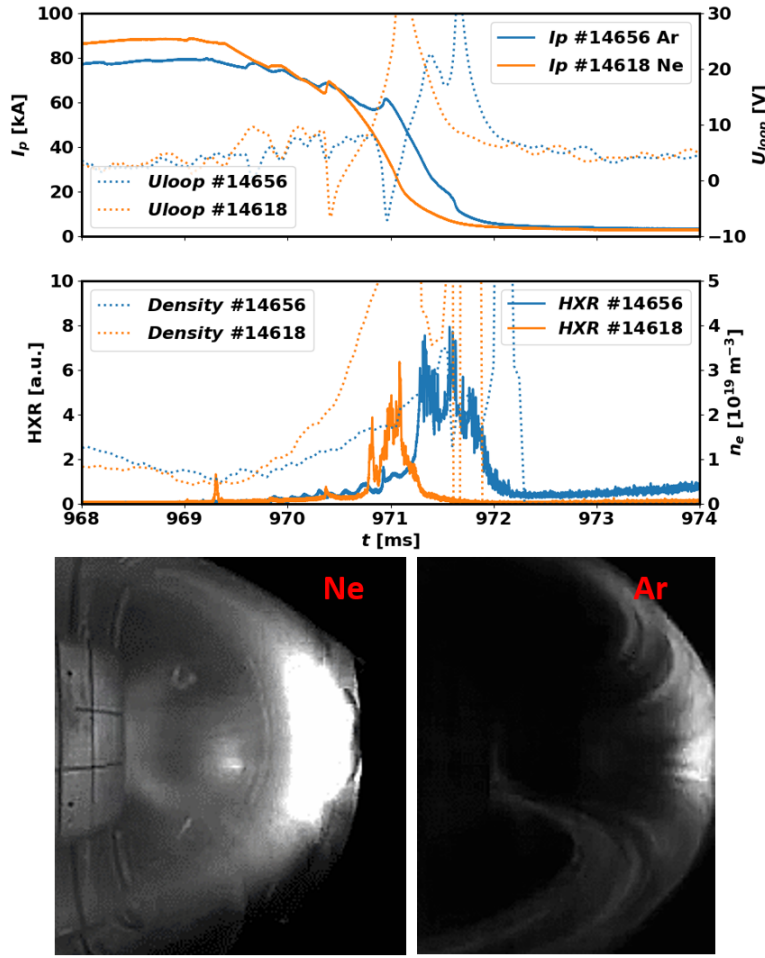


Figure 7.2: Comparison of Ar (blue curves) and Ne (orange curves) MGI into the ramp-up scenario for the case of unsustained RE beam: top frame shows the plasma current I_p and the loop voltage U_{loop} , the bottom frame shows the density n_e and the evolution of the HXR measurement, The respective camera images taken shortly after the current started to decrease are shown in the bottom part of the figure.

on the rational surfaces is the most viable one. This is based on the fact that the V-ECE can see electrons of energies below or near 100 keV [79] and the fact that the HXR and the Cherenkov detector signals, sensitive to RE, seem to be affected slightly later perhaps after the RE from the filament drift away and are lost to the wall. The electrons ionise the Ar in a narrow channel of a rational surface. The mode number is not clear from the camera image of the filament. The the number of apparent toroidal and poloidal transits of the filament would suggest 2/1 mode however, the q values provided by EFIT as well as inclination of the filament suggest that the poloidal mode number should be higher. Anyway, the rational surface field line can be easily highlighted by line radiation of Ar II ionised and excited by the passing RE as it is the shortest one outside the beam in terms of

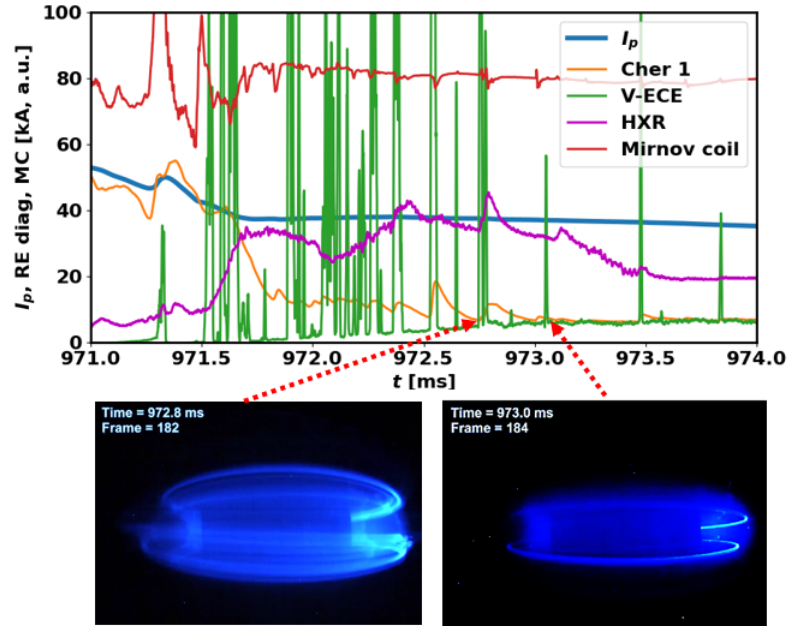


Figure 7.3: The detailed look on the early RE beam phase generated in the disruption from the plasma current ramp-up - the plasma current I_p in blue, the low energy (<57 keV) local measurement RE by the Cherenkov detector in orange, the vertical ECE in green, the HXR detector signal in magenta and the magnetic perturbation measured by the LFS midplane Mirnov coil in red. Two frames from fast visible camera corresponding to the indicated features in the signals.

transit time and thus sufficient amount of radiating ions is secured by RE repeatedly crossing the same region. In general, the conditions in this phase are beneficial for the RE generation in terms of E/E_c . The only circumstance necessary for this hypothesis about the filament nature that can be hard to explain is why only discrete filaments are observed in the situation when all the field lines covering the rational surface are equivalent. This can be caused by the density or electric field fluctuation in particular location on the $q = 2$ surface, where RE generation is initiated. The short life of the filament can be explained by two options: either the RE are accelerated to higher energies where interaction with Ar and detection by ECE is much less probable; or due to the acceleration or drifts the RE gradually leave the rational surface, then they are spread around on irrational surfaces and long field lines and eventually they are lost. The latter hypothesis is more probable. In principle the concentration of RE in the filament could also alter the magnetic configuration and create a thin magnetic island.

This observation is not just very interesting from the point o view of RE

physics, but also provide a unique insight into the RE generation during the fast phases of the disruption at larger devices that can work in similar way in terms of role of the rational surfaces, but cannot be diagnosed in such a detail as this particular phase of the ramp-up scenario at COMPASS.

Last but not least, similar filaments were also observed in the situation with very elevated electric field in case of RE generation from the flattop scenario.

■ 7.2 RE beam generated from the flat-top scenario - brief overview of results

In this section, the most important results achieved with the primary gas injection (RE beam generation) and secondary gas injection (effects on existing RE beam) into the flattop scenario are discussed. Some of the findings were reported in the the attached paper B [22] and other references that will be cited throughout the text.

■ 7.2.1 Conditions for RE generation using gas injection valve and MGI

In general, the RE beam generation from the low density flattop discharge is very reliable, however in the case that the RE seed is too small it may fail as well. In terms of timing with the standard gas valve, successful attempts in generating the RE beam in the ramp-up as well as in an arbitrary time during the flattop were performed. The unreliability of the beam generation was encounter in some campaigns and was apparently connected with different wall conditions or MHD instabilities. Therefore the reliability could have been restored by the change of the initial fuelling or by a slight change of the plasma current. The situation when using the MGI for the generation of the quickly decaying RE beam is much more interesting. In the attached paper B [22], figure 4-right, the threshold in time for successful RE beam generation can be observed. Indeed in a scan of MGI timing and otherwise the same plasma scenario and injection parameters, early injections resulted in disruption without a RE beam generation while injections happening a couple of ms later resulted in the sustained RE beam generation. The boundary of the two different cases seem to be $t = 1195$ ms. This threshold seems to be related to the seed population based on the evolution of the loop voltage

that is decreasing and thus suggesting growing seed over the time. For the MGI injection with faster thermal quench compared to the slow gas valve, larger seed is apparently needed to overtake the current. However, the energy of the seed electrons that is gradually growing due to acceleration can also play a role through the equilibrium effect and improved position stability during the thermal plasma current decay. In these scans, RE plateau with partial pre-disruption current was never observed, although it would seem probable that around the threshold for the beam generation it could occur as a transitional state. However, it is most probably the MHD stability related to relatively low q_a values and macroscopic stability of the position, that prevent the partial current quench followed by the RE beam plateau.

7.2.2 Effect of different gas species and amounts on the RE current decay after the injection

As the RE beam generation scenario is admittedly quite different compared to those performed at large machines (no pre-disruption seed needed, acceleration due to CQ), we will further focus on the effects of different gases in the fully evolved RE beam stage. Four different gases were tested for the RE beam generation in the flattop scenario: Ar, Ne, Kr and N₂ (the order is given by the number of discharges performed with these gases).

In general, with similar amount injected into similar target plasmas, the higher Z gas companion plasma causes faster decay of the RE beam current and thus larger increase of average energy due to the induced voltage and the fact that the faster electrons are the more effective carriers of the current in this environment. Indeed, as can be seen in figure 7.4, argon and krypton definitely cause faster current decay than neon and nitrogen. Similarly, the amount of HXRs produced by the heavier gasses is significantly higher compared to the lighter gases. The external loop voltage is kept 0 in all these cases, thus the electric field present during the decay is induced by the decay of the beam current. With faster decay of the current, larger increase in the energy derived from, the β_N -minimum estimate is found. The set of discharges displayed in figure 7.4 contains discharges with two different values of current: 130 kA in the case of N₂ and Ar and 150 kA in the case of Kr and Ne. There are also differences in the gas propagation among the species, however these differences do not affect the conclusions.

From this comparison it is quite obvious that in the case that the current decay is too fast, the conversion of magnetic to kinetic energy is very efficient. On COMPASS, the too large current decay can be induced already by relatively small quantities of heavier impurity gas. This might be connected

with the small size of the beam and significant particle losses. The neon or nitrogen thus seem to be a more preferable option from the point of view of minimising the kinetic energy at the RE beam impact.

Moreover, the current decay slope in nitrogen is decreased after a couple of tens of ms and this is connected with the change of the color in the camera, therefore most probably with the nitrogen recombination. After the recombination the energy increase is almost stopped and the current decay continues in a very slow manner, but steadily. This is in effect very similar to the deuterium secondary injection that is discussed in the next section.

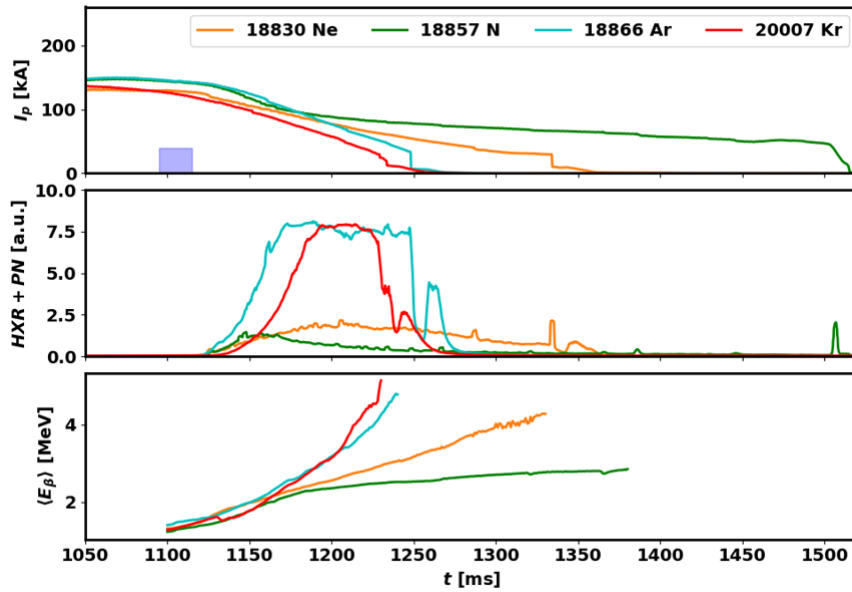


Figure 7.4: The comparison of injection of 4 different gas species into the low density COMPASS plasma discharge, triggering the RE beam and governing the decay of its current. The top frame shows the evolution of the plasma current after the injection - marked by the blue rectangle, the second frame shows the evolution of the shielded HXR scintillator signal and the last frame shows the estimate of energy based on the β_N -minimum estimate as discussed in chapter 6.

The scaling of the current decay rate and the produced HXR radiation and photo-neutrons - that is an rough measure of energy - with the impurity amount was also studied for Ar and Ne. The results are presented in the attached papers in the form of point graphs where each point represents one discharge with RE beam decay. More specifically, in the attached Paper C [21], figure 3, a graph of the average current decay rate is shown as a function of injected impurity amount, based on the valve calibration and also pressure increase during the discharge. This includes 8 discharges in Ar and Ne each with gas injected using the piezo-valve, where the amount is modified by the duration of the injection or reservoir pressure, and 4 Ar/3 Ne MGI cases

where the amount was modified by the duration of the injection. For both types of valves, there is an increase of current decay with increased injected amount and higher decay rate in Ar compared to Ne. However the overall image shows that orders of magnitude higher amounts of gas injected by MGI cause only a couple of times larger current decay rate and the whole dependence tends to saturate at high injected gas amount ($N/V \sim 10^{21}$).

The same set of discharges was further analysed in the attached Paper B [22], figure 9 in terms of average and maximum radiated power (measured and calculated by the AXUV tomography modified for the use in the RE beam phase, as described in paper), the photoneutron measurement by ^3He detectors and HXR measurement by the least sensitive detector. The general conclusion is that all the studied quantities rise with the current decay rate (i.e. with injected gas amount based on trend discussed in the previous paragraph). Furthermore the Ne injection results in higher radiated powers while Ar injection results in much larger amount of hard radiation (HXR and photoneutrons), corresponding to larger amount of kinetic energy deposited in bremsstrahlung interaction with impurity gas or the plasma facing component material. These results seem to be consistent with the comparison of gases in figure 7.4 and with the hypothesis that faster current decay rate is not beneficial and leads to increase of the energy via induced electric field.

Total impact energies of the RE beams in different gases were also measured by the calorimetry head outside the scope of this thesis and the results are consistent with the results discussed above - the impact heating power is much larger for beams in Ar, however the longer current decay of the beams in Ne may actually result in relatively large total deposited impact energy [138, 84]. The latter option is still more beneficial regarding the risks of damage during the termination.

Based on these results, it can be concluded, that lighter impurities form more beneficial companion plasma for harmless deposition/decay of the RE beam kinetic and magnetic energy.

However, in the case that a stable position can be secured during the decay, all the impurities eventually help to dissipate the RE energy without local damage.

In the next section secondary injection of light impurities is discussed as it is now considered as a very promising mitigation technique worldwide. Note that the secondary injection of heavy impurities is essentially only increasing the effect of the first injection in this scenario - i.e. accelerating the current decay but at the same time causing the increase of the energy.

■ 7.2.3 Secondary injection of deuterium in COMPASS

The secondary injection of deuterium into existing RE beam in Ar or Ne was first attempted in the 7th RE campaign on COMPASS (2017), roughly at the same time as the effect was explored at DIII-D in detail [146]. Later this injection scheme was found to be the most promising RE mitigation method at JET [145] and other machines as well.

At COMPASS, the secondary injection was always performed via the standard gas fuelling valve. On other machines, MGI, SPI or standard fuelling pellet injectors are used as well. The gas valve is usually set to 100 ms of full opening in the COMPASS scenario.

The injection causes a gradual recombination of the Ar, but only in the case of small Ohmic power - zero loop voltage request. The comparison of the evolution of relevant parameters after secondary deuterium injection into Ar-triggered beam with zero loop voltage request and Ar triggered RE beam with constant current request with the standard RE beam current decay without secondary beam injection is shown in the attached Paper C [21], figure 4. Indeed the plasma current decay in the zero external loop voltage cases is slowed down by the deuterium injection and the shielded HXR detector signal is decreased (note that this signal is in the PMT saturation in the other cases so the drop is most probably much more significant). Moreover, the density is decreased after the deuterium injection in the zero loop voltage case, while it is not decreased in the case of the constant current control, which can only mean that the plasma is neutralised but just in the case without additional Ohmic power applied. The last frame of the described figure shows the evolution of the radiated power in the spectral regions covered by the AXUV diodes.

The radiated power evolution is also plotted below in the figure 7.5 with Ne + deuterium injection and zero applied loop voltage case included instead of the pure Ar case. It can be clearly seen that even the higher Ne radiation (compared to Ar) is drastically reduced after the D2 arrives and causes the recombination ($t=1120$ ms).

Within the community, the D2 effect is sometimes referred to as "flushing" of Ar. However as we show further, the Ar or Ne in fact remain in the vessel and can be re-ionised under suitable circumstances. This is consistent with the fact that the vacuum pumps are not that efficient to pump out the impurity on the relevant time scales.

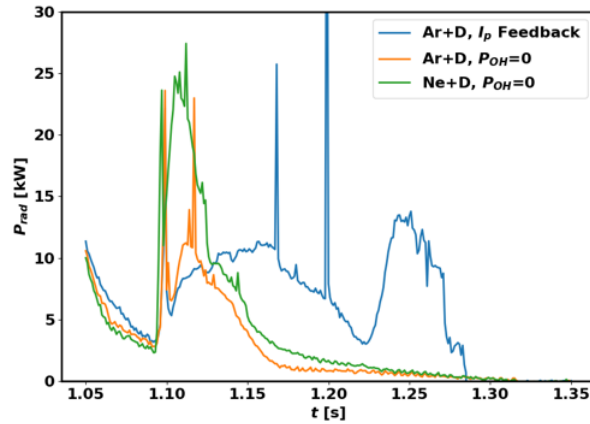


Figure 7.5: The comparison of the radiated power in the AXUV spectral region calculated using tomography for 3 discharges with different injection and Ohmic power control schemes.

In the two following figures we will cross-check the understanding of the situation with the visible radiation spectra measurement by a suitable minispectrometer available during the COMPASS discharges. First, in the figure 7.6, the evolution of the ionised Ar line radiation intensity and the D_α (H_α) radiation is shown. Apparently the Ar II line radiation peaks after the primary injection, while it is completely mitigated and replaced by the deuterium (hydrogen) line after the deuterium injection. This suggests that the recombination is very efficient.

On the other hand in the case of the secondary deuterium injection into the RE beam created by the neon injection, we are able to observe the line of Ne I, i.e. neutral atoms in the visible range. This is shown in figure 7.7. In this case the Ne I persists from the injection till the end of the discharge, despite a drastic reduction in the electron density after the deuterium injection, when the Ne I line is joined by the D_α line at high intensity. This observation confirms that the heavier impurity, in this case Ne, remains in the volume of the RE beam after the recombination.

Last but not least, the fast colour camera contributes to the improved understanding of the recombination and re-ionisation phenomena and fast events during the beam existence. An example of evolution of the images in a pair of discharge with the same injection parameters but different current control schemes is shown in figure 7.8. It is apparent that while in the case of zero loop voltage request, the recombination is complete and sustained and the blue Ar II radiation disappears completely, in the case of the plasma current feedback, the recombination is only partial. The deuterium prevails near the north valve where it is injected, while Ar II resists near the south. Both blue and magenta colors are visible, furthermore, right after a partial

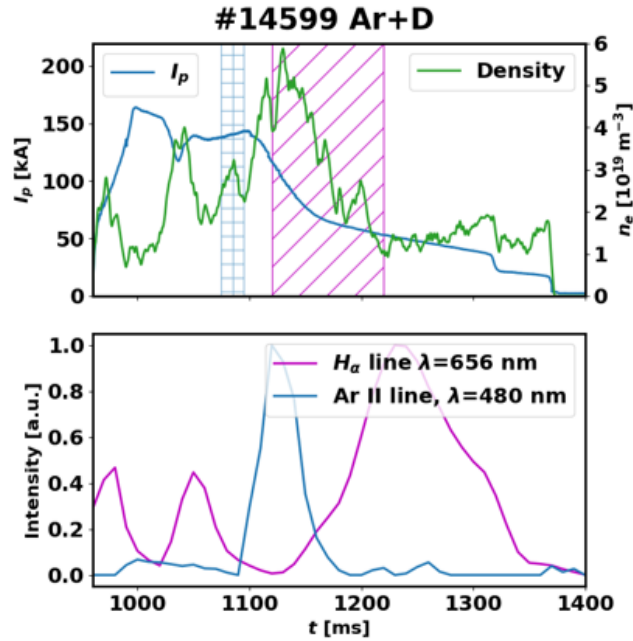


Figure 7.6: The evolution of the selected Ar II and D_α (H_α) spectral lines during the experiments with RE beam generated by primary injection of argon and affected by secondary generation of D2. For the time reference, the plasma current, the density and the injection periods (blue and magenta rectangles filled with a pattern) are shown.

current crash, the filaments discussed in the ramp-up scenario section appear in several bursts in the phase with large electric field. Ultimately, the ionised Ar prevails after the deuterium injection is stopped. This suggests that the Ohmic power input is crucial for the recombination and with higher current and/or loop voltage, it can cause failure of the recombination or triggering of the re-ionisation. This is a very important finding.

In the case that the kinetic energy evolution based on the two equilibrium methods described in chapter 6 is calculated for a pair of Ar, a pair of Ne injection cases and the secondary deuterium injection case in discharge #14599 and plotted in figure 7.9, it is obvious that injection of heavier impurity and larger amount leads to a faster energy increase. Most importantly, the deuterium injection completely stops the increase or even causes the energy to slowly decay. This is the very unique attribute of the secondary deuterium injection that can be only partly matched by the nitrogen, that recombines without any additional deuterium injection after some period as discussed in description of figure 7.4 above. None of the heavier impurities shows similar behaviour. The unique behaviour was confirmed in all machines where the secondary deuterium injection was attempted.

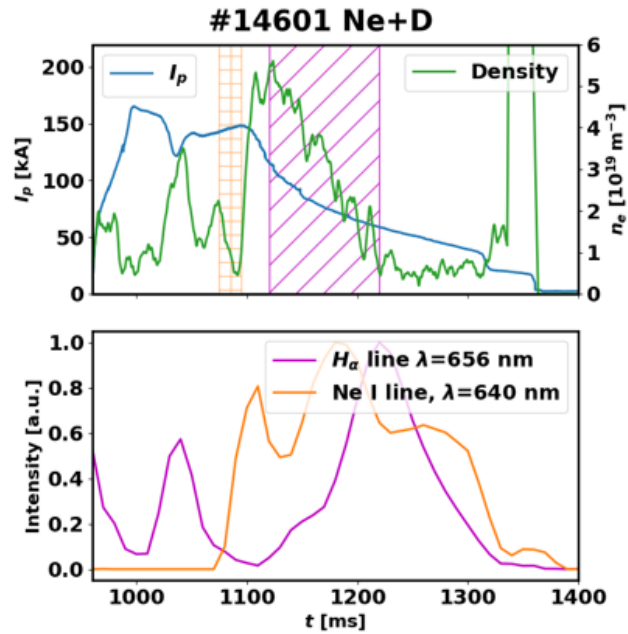


Figure 7.7: The evolution of the selected Ne I and D_α (H_α) spectral lines during the experiments with RE beam generated by the primary injection of neon and affected by secondary generation of deuterium. For the time reference, the plasma current, the density and the injection periods (orange and magenta rectangles filled with a pattern) are shown

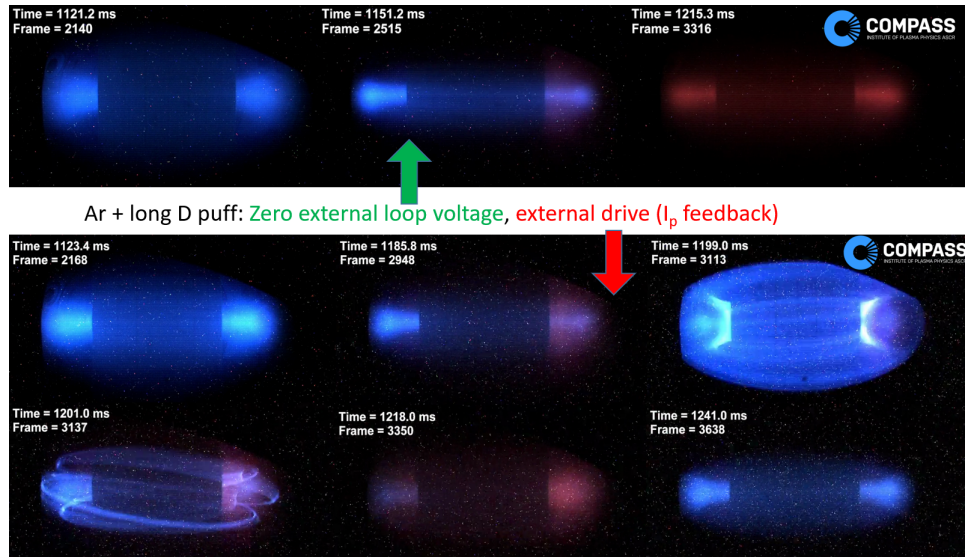


Figure 7.8: The evolution of the fast camera images for the Ar injection followed by deuterium injection and the two cases with different control policy: #14599 with zero loop voltage request marked by a green arrow and #14598 with constant plasma current request marked by a red arrow.

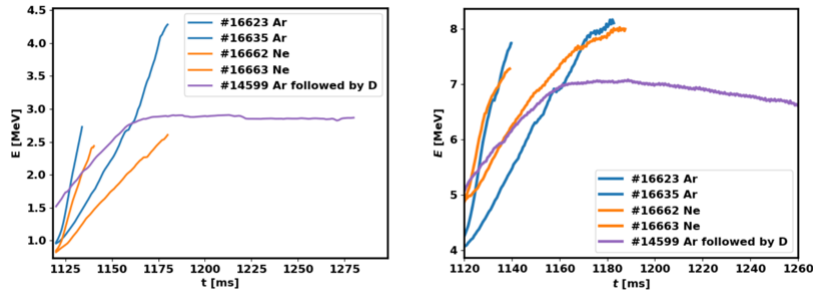


Figure 7.9: Energy derived using the two RE equilibrium methods based on relativistic pressure (isotropic - minimum) - left and radial position control - right calculated for discharges with different gas injection species and amounts, in the case of the pairs marked by same color in one frame, the faster increase corresponds to MGI injection while the slower one to the slow valve injection.

7.2.4 Acceleration and deceleration of the RE beam

The other option to affect the RE beam energy and current in a way that is suitable for physics analysis is to use fixed external positive or negative loop voltage through the control of the current in the central solenoid. The positive external loop voltage provides additional current drive and acceleration, while the negative loop voltage provides additional drag and accelerates the current decay. However the overall effect on the RE population and its average kinetic energy might be more complicated due to the induced electric field. Several different cases are compared in the figure 7.10. Note that the sign conversion of the current, central solenoid current derivative and loop voltage is modified so the positive value of each quantity always corresponds to acceleration of RE in both groups of discharges run in standard and reversed current direction on COMPASS. It can be seen that, as expected, the highest positive current drive with $U_{loop} \sim 1$ V (red line) that is generated by the central solenoid current change dI_{CS}/dt marked in the legend leads to largest average energy and relatively smallest current decay rate. The current decay rate, however, is still significant and given the fact that the current is namely given by the number of RE at this stage, it corresponds to the significant particle losses due to the ionised Ar background plasma. These particle losses are not sufficiently compensated by the RE generation mechanisms like the avalanche and thus the current decays. The blue case with no drive and no secondary injection presents the reference for comparison with all the other cases. The green case corresponds to significant loop voltage opposing the RE current, turned on at 1200 ms. This accelerates the current decay as expected, however, the average energy actually rises with even a higher rate than without any drive and in the situation with the acceleration. This situation must be caused by the large induced magnetic electric field - the lower energy RE could be lost due

to the enhanced drag (collisions and electric force) and the RE that remain are further accelerated. The externally measured loop voltage is roughly 2x lower than expected - it should be the same as in the red case with an opposite value. This confirms that the induced loop voltage is significant. It might be so significant that it can overcome the external one inside the RE beam.

In the purple case with slightly lower opposing loop voltage and deuterium injection the increase in the energy is less significant, but still noticeable and the current decay is not changed compared to the reference. This however means that the deuterium is slowing down the current decay - with significant external deceleration, it reaches the same value as in the case with no external loop voltage and ionised Ar background plasma. Last but not least, the orange case corresponding to secondary deuterium injection and no external drive in the already discussed discharge #14599 shows slowing down of the current decay after the injection and most importantly leads to the decrease of average energy as the only scenario studied at COMPASS. Interestingly, the current decay rate is approximately the same as in the Ar background plasma with significant current drive, however the energy estimate leads to drastic difference in the kinetic energy of these discharges.

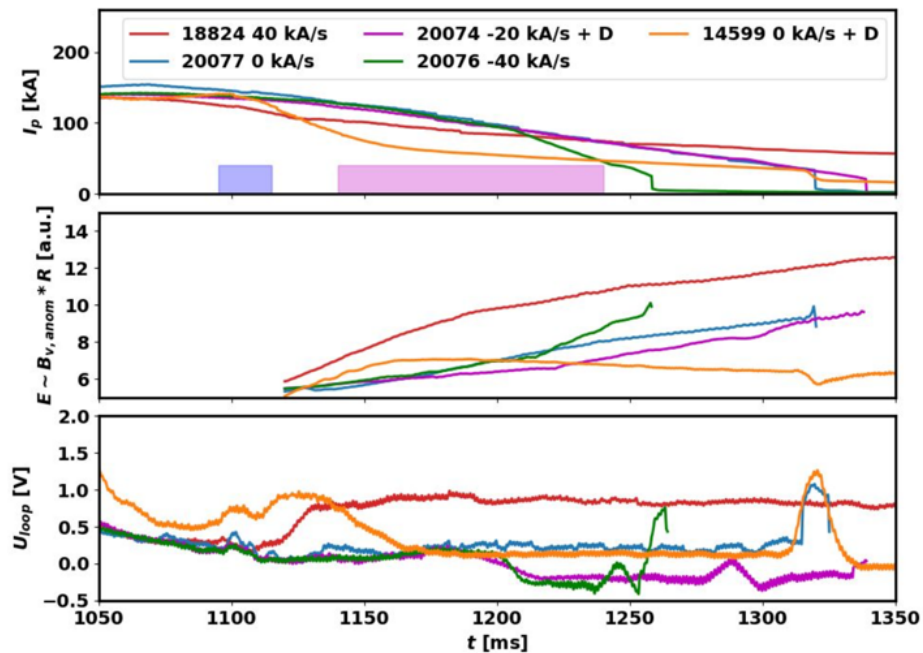


Figure 7.10: Energy estimates and plasma current decay behaviour for different rate of current change in the central solenoid - from top the evolution of the plasma current I_p together with rectangles marking the opening of the primary Ar injection valve and secondary deuterium injection valve (applicable to curves with + D in the legend), the evolution of the average energy based on the radial position control request and in the last frame the evolution of the loop voltage measured outside the vessel.

Based on this set of experiments it is clear that in the case of COMPASS, the

effect of the deuterium is very beneficial and allows for significant decrease of kinetic and magnetic energy of the RE beam simultaneously, which is required for safe and steady termination of the RE beam. In this way, using the improved position control, deuterium injection and limited current drive, the RE beam can be brought to very low energy termination gradually on COMPASS. The RE beam current decay rate can be also significantly affected by the RMP application, however, this is out of the scope of this thesis, with results published in [137] and publications in preparation.

In other devices it was shown that the deuterium is a key ingredient to allow for fast RE beam termination without any damage as well. Some details of this benign termination scenario in case of JET, where the author has performed relevant analysis, are discussed in the next sections.

■ 7.3 Analysis of the RE beams at JET

As discussed in chapter 4, the JET RE beams are similar to the COMPASS ones, however reach significantly higher currents up to the order of MA and duration from tens of ms to several seconds. The RE beams are generated from a flattop plasma with relatively low density but without any pre-disruption seeds, usually through injection of pure Ar MGI with amount close to 1 bar-litre. The post-injection particle density in the vacuum vessel is comparable to COMPASS MGIs. Throughout the last decade, various pre-injection parameters were scanned, see e.g. [69] as well as various actions on the existing RE beam were tested. Regarding the diagnostics available for analysis of the RE parameters and parameters of the background plasma, JET has excellent equipment that was further enhanced during the recent years. The plasma density measurement is performed using interferometry with multiple vertical and horizontal chords and high time resolution option. Before the disruption, the temperature and density profiles are measured using the high resolution Thomson scattering. The density profiles can be measured by the reflectometer as well. The post-disruption RE losses and interaction with the companion plasma are characterised by HXR and neutron flux monitors. The energy resolved HXR measurements are available via multiple spectrometers including a system of 19 collimated LOS. The radial ECE radiometer provides spectra of suprathreshold ECE radiation from the runaway electrons, however the optical properties of the environment set by the background plasma are important for evaluation of this signal. Last but not least, the capability to measure synchrotron radiation in the visible and infrared ranges was greatly enhanced before the 2019 RE experiments. In the previous campaigns, only hints in the form of saturated blobs and reflections suggested observation of synchrotron radiation in the post-disruption RE beams. This is documented

for one of the longest pre-2019 RE beams in figure 7.11. The views of various cameras presented in the figure, considering that the IR range should be free of line radiation and hot spots on the plasma facing components can be identified and excluded, suggest that the radiation source shining tangentially from the plasma in the direction of RE flight is observed. However, a better camera set was necessary in order to confirm this observation.

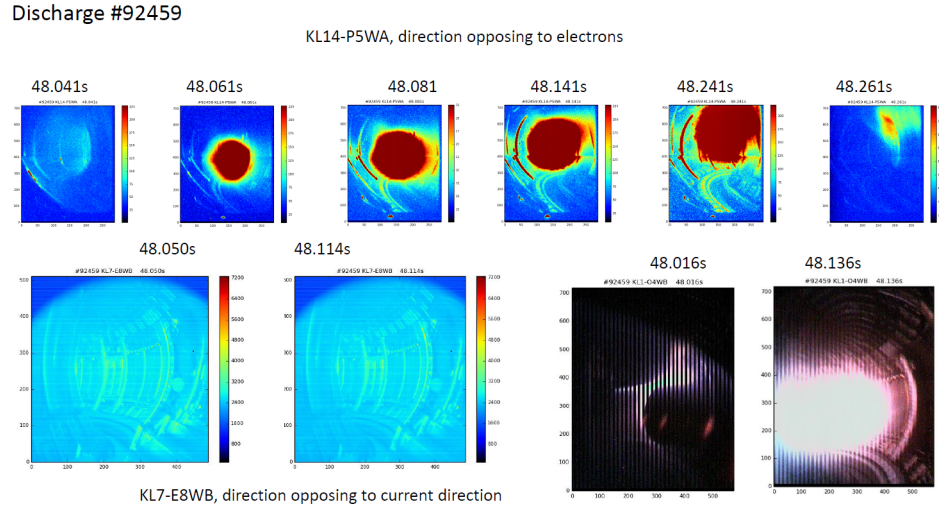


Figure 7.11: RE beam following the MGI disruption in JET discharge #92459. The time sequence of frames with suspected synchrotron radiation observation from 3 different cameras: top - co-current tangential view NIR camera showing saturated radiating blob, bottom left - counter current IR observation of reflections on limiters suggesting light source directed away from the camera, bottom right - visible camera directed co-current showing a saturated view of radiating blob as well. Images displayed using the JUVIL software [183]

In 2017, the KLDT camera system [184], [185] which is characterised by a very long optical paths based on periscopes to allow camera placement outside of the main radiation shielding was installed. The cameras of this system covering different wavelength ranges, have beneficial tangential view in opposition to the electron flight direction. The view of this camera system is shown, e.g. in figure 1 of [185]. The most important camera for observation of synchrotron radiation is the KLDT-E5WC which is a mid-IR camera with wavelength range $\lambda = 3 - 3.5 \mu\text{m}$. The analysis of SR using this camera can be complement with the KL7 camera looking in the opposite direction. The KLDT-E5WE is a fast visible camera that is also very useful for the synchrotron radiation, however it is polluted by line radiation unlike the KLDT-E5WC camera. The visible range camera is complemented by the KL8 fast camera that is observing vacuum vessel in the opposite tangential direction.

Interestingly, advanced high temperature plasma diagnostics can have unexpected applications with respect to the RE beam. For example the

collecting part of the motional Stark effect diagnostics, normally used for spectroscopic measurement of plasma current profile based on the Stark effect on the D_α line of excited neutral beam atoms, can be applied for polarised measurements of the synchrotron radiation. Indeed, the collection optics geometry is suitable and the diagnostics can bring valuable information as was proved at Alcator C-mod [82]. The system is characterised by a narrow wavelength window around the D_{α} line. The use of this diagnostics was attempted at JET as well and the measurements were successful as the observed light intensity was huge.

Last but not least, the methods of kinetic energy estimates using the equilibrium results and derived in this thesis were applied to the JET discharges as well.

The evolution of the relevant signals in the discharge where RE beam is triggered by the Ar MGI and then affected by secondary D₂ SPI is shown in figure 7.12. The current quench, RE beam plateau and beam termination phases are clearly visible in the current trace and the beam lasted almost 700 ms in this cases. The evolution of the other signals is described further in the text in a relevant paragraph.

■ 7.3.1 Application of tomography for analysis of RE beam properties on JET

The tomography was successfully applied in various stages of the discharges with the RE beam. In the RE beam stage, various diagnostics with multiple LOS that are available at JET, namely bolometry, SXR, HXR and neutrons are of interest for the tomographic analysis. However, in some of the cases, the diagnostics signals have to be used with caution regarding the harsh ionising radiation environment and possible inaccuracies in the magnetic equilibrium. In the figure 7.13, an example of the SXR tomographic reconstruction after secondary heavy impurity injection into existing beam is shown. A clear radiation ring can be recognised and this shape is consistent with the line-integrated data. It could be interpreted as a failure of the Kr penetration into the RE beam core - it radiates only at the peripheral region. However, as the vertical position control of the RE beam is gradually lost, the interpretation is difficult. However, from other experiments it is apparent that injection of large amounts of heavy gases is not a good mitigation method and can lead to significant localised heat loads. [69, 145].

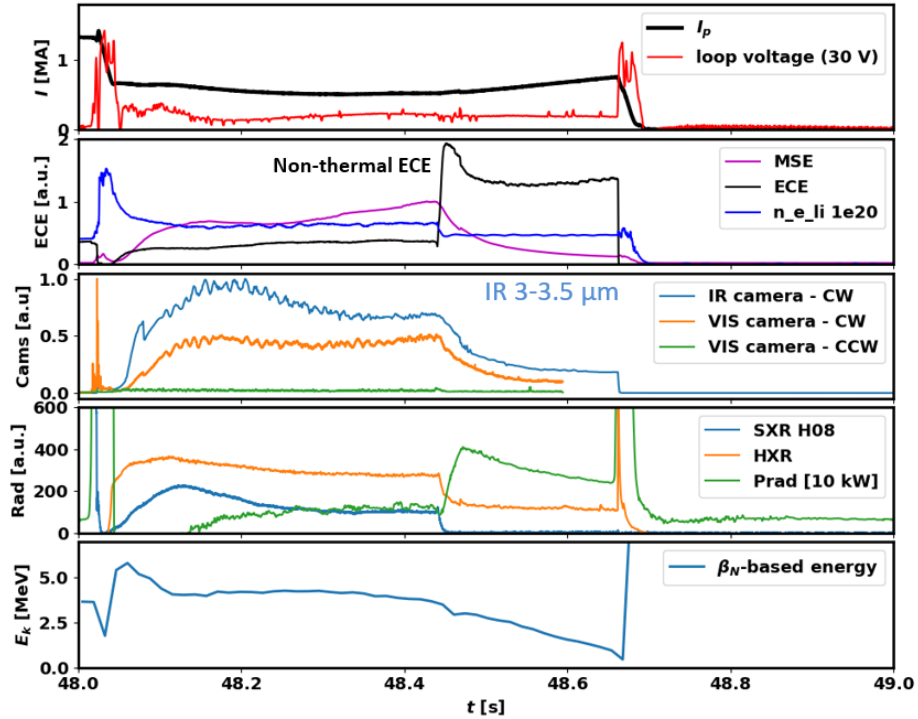


Figure 7.12: Evolution of relevant discharge and RE parameters in the JET discharge #95135: The plasma current and the loop voltage; line integrated electron density n_e , electron cyclotron radiation and synchrotron radiation measured by the MSE system; the synchrotron radiation intensity measured by tangential visible range and the mid-IR camera and compared to visible camera measurement in the opposite direction; The central SXR, HXR and total radiated power during the RE beam phase and in the last frame the average RE kinetic energy calculated from β_N

7.3.2 Secondary injection of deuterium and benign termination

Among the various parameter scans in terms of RE beam generation and mitigation, the secondary deuterium injection significantly stands out, providing the most surprising and promising results. Indeed as is shown in the attached paper D [145], last frame of figure 1, while the heat loads on the walls due to terminations of unmitigated or high Z RE beams are very significant and scaling with the beam current, the terminations occurring after secondary deuterium injections via SPI or other injection method, lead to negligible heat loads, independently on the plasma current. This must mean that total deposited kinetic energy including the part of magnetic energy converted in the termination into RE acceleration is significantly smaller and/or that the area of deposition is significantly larger so the heat loads are spread. It appears that both options might play a role as the paper

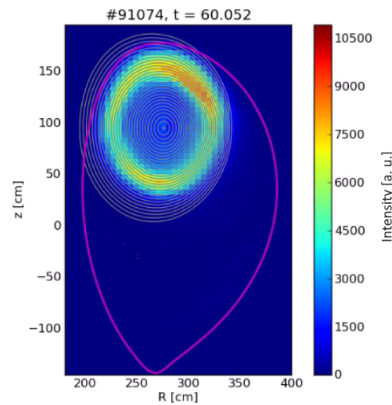


Figure 7.13: The SXR radiation map in poloidal cross-section of RE beam, JET discharge #91074, time 20.062 s after the breakdown (60.062 s on JET time axis) showing radiation ring and significantly vertically displaced RE beam after secondary Kr injection.

explains - the reacceleration or regeneration of RE is prevented due to large deuterium neutral pressure and the heat loads can be spread as majority of RE is lost within a very fast MHD collapse which leads to fast stochastisation of field lines and thus to increasing the number and size of locations of the RE impacts. The non-linear modelling using JOREK shows [145, 156] that such instability is possible when starting from hollow current profile. This profile shape is very unusual, however confirmed by the mode numbers of islands observed in the synchrotron radiation and namely the simulation of the observed hollow synchrotron radiation profile. The hollow SR radiation profile simulations at JET were run by the author of this thesis in SOFT using the JET magnetic equilibrium and some details are given in the last section of this chapter. However, based on the evolution of various RE and companion plasma diagnostics, it seems that significant changes of the RE population that may affect the kinetic energy at impact occur gradually after the injection, not just at the beam termination. This is a very interesting open topic of the RE research. In the next lines we will discuss these diagnostics observations on a couple of examples of RE beams.

In the figure 7.12 the injection of deuterium (at $t = 48.4$ s) lead to recombination of the Ar companion plasma and the plasma current started to increase despite the external loop voltage is the same, like in the previous phase with ionised companion plasma and current decay. The current of a runaway beam with very low temperature plasma can be increased by the avalanche multiplication as primary mechanisms are more or less excluded due to the very low companion plasma temperature. The avalanche can lead to increase of number of the RE on one hand, but decrease of average energy per particle on the other hand in the case that the electric field acting on the system is not sufficient.

Furthermore, the detectors of the synchrotron radiation, including the visible range camera, the MSE collection system and the mid-IR camera show fast decay of the radiation intensity - as the current and therefore the RE number is increased, the intensity decay can be only caused by decay of energy and/or decrease of the pitch angle. The ECE on the other hand shoots up, but this is related rather to the companion plasma recombination than to a change in the RE population - as the plasma is becoming transparent for the radiation at these frequencies. Last but not least, the average kinetic energy derived using the β_N estimate is gradually decreasing after the deuterium injection. Such decrease in anisotropic pressure can be hardly attributed only to profile changes or drop in the pitch angle. At the same time, the SXR, i.e. the RE interaction with companion plasma ions as well as photoneutron production drop significantly, HXR signal is also decreased. These changes can mean decrease in the high energy population but also just a decrease in the interaction with the companion plasma. However, together with the negligible heat loads during the benign termination occurring after the deuterium injection, most of the diagnostics evidence points to the decrease in energy.

The estimate of average kinetic energy using the equilibrium quantities was compared to the HXR spectrometry (provided by A. Dal Molin at JET) in three different cases of the JET RE beams - no secondary injection, secondary Ar SPI and secondary D2 SPI in the attached paper G - qualitatively, the trends of the energy evolution measured by both methods are very similar - the energy seems to be largest just after the RE generation, while it decays with time if the beam current is not decreasing too quickly, there is an increase of energy in case of secondary SPI. In the case of secondary deuterium SPI, the count rate of the HXR spectrometry drops so much that the statistics does not allow to measure the energy spectrum. However, it seems to be confirmed even with this comparison that the estimate of average energy evolution from the equilibrium is reasonable.

In figure 7.14, multiple JET discharges are compared by the means of average energy estimate from equilibrium, the peaking just after the beam generation is apparent in all cases. In the blue case #94508, with active current drive, the beam average energy is kept rather high while in the red case #95132 it is increase just at the termination with the secondary Ar SPI, in green case #95135 it decays with secondary deuterium SPI up to the termination. In the orange case with decaying RE current the energy estimate oscillates and increases again at the low current - the behaviour seems to be rather complicated and requires deeper analysis.

More detailed, statistical cross-comparison of different methods to estimate the energy is currently in progress and planned to be presented at the IAEA

Fusion energy conference in October 2023.

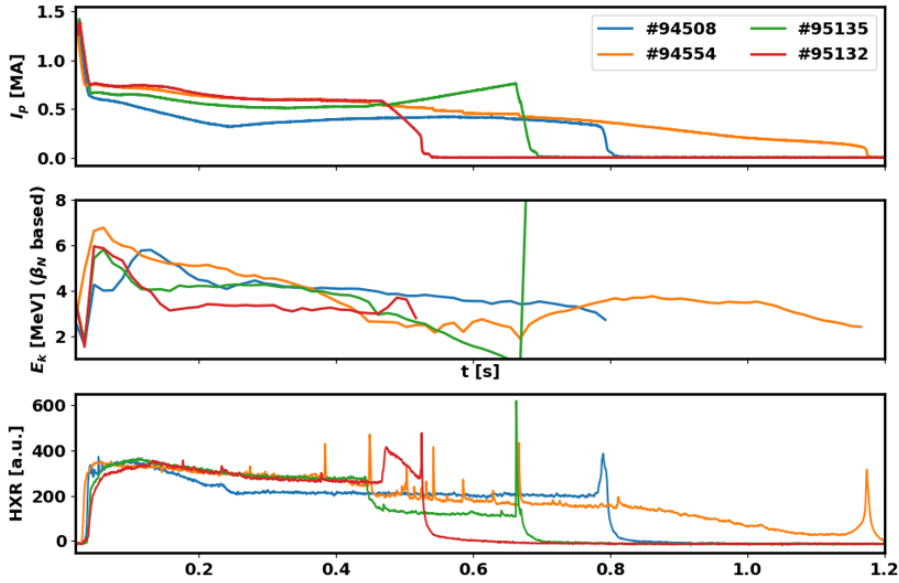


Figure 7.14: JET runaway electron beams comparison: plasma current I_p , average energy derived from the beta normalised and HXR signal

■ 7.3.3 Interpretation of synchrotron radiation at JET and analysis using SOFT synthetic diagnostics

The synchrotron radiation has clearly become a very useful diagnostics technique in the past years. The total intensity evolution as well as gradual evolution or abrupt changes of the pattern observed by the IR camera does bring interesting information, however the interpretation is often complicated due to many parameters involved. Therefore the use of suitable synthetic diagnostics tool in order to narrow down the interpretation of observed phenomena is inevitable. Several synchrotron radiation synthetic diagnostics numerical tools are available in the community, in this application SOFT (Synchrotron Orbit-Following Toolkit) [53] is used. It allows for simulating the radiation pattern, using simple pinhole camera model with arbitrary spectral sensitivity and distribution function of the RE e.g. in the form $f(r, p, \theta_p)$, i.e. function of normalised minor radius, momentum magnitude and pitch angle cosine. The phase space covered by the distribution function is then sampled and particles of given properties are followed along the magnetic field lines for one poloidal transit in the guiding centre approach, the synchrotron radiation models include hollow cone that simulates the effect of gyration or full angular distribution. The magnetic field configuration can be either given analytically or imported from equilibrium reconstruction, e.g. EFIT. The latter option was used in the case of JET simulations, the interpolation

and export of the field from the JET database was prepared via adding JET data reader and SOFT format data exporter to the Pleque package [186], this extension was code by the author of this thesis. It can provide SOFT with magnetic field from arbitrary JET or COMPASS discharge. With all the inputs ready, SOFT can calculate the particle orbits and namely the radiation contribution from these particles to individual images or alternatively the Green's functions that can be multiplied by arbitrary distribution function in order to quickly obtain images corresponding to different RE beam population. In order to understand the diagnostics capabilities of JET cameras for synchrotron radiation observation, the output of the SYRUP code [52], the predecessor of SOFT is shown in the figure 7.15. It can be seen that the main too. i.e. the mid-IR camera measures SR near the peak of the spectrum for the relevant energies, while nir-IR camera - the one that provided first signatures of SR described above - and the VIS range camera measure rather the quickly growing high energy edge of the spectra. Therefore, these cameras provide a very interesting diagnostic set.

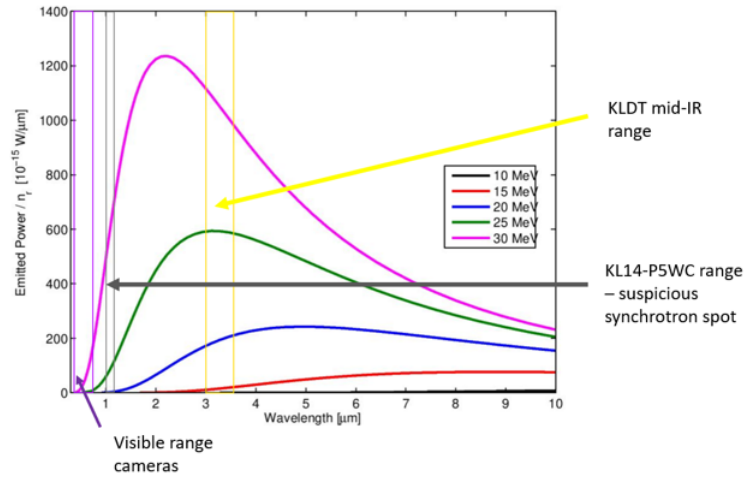


Figure 7.15: The synchrotron radiation spectra for the monoenergetic RE beam modelled using SYRUP, the wavelength ranges of different camera sensitivities are also included.

In the figure 7.16, the Green's function of the total image intensity in variables p and θ_p for JET mid-IR camera an typical JET magnetic equilibrium is shown. It is apparent that the high energy and high pitch angle particles are the most important contributors to the total intensity. In the same scale the top right region with significant contribution would be much smaller for the case of the visible range camera.

The Green's functions in (p, θ_p) were combined with the Green's functions in r in order to study namely the spatial RE distribution profile effect on the image pattern as the images observed in experiment suggested that the profile could be hollow or extremely peaked in different phases of the RE beams.

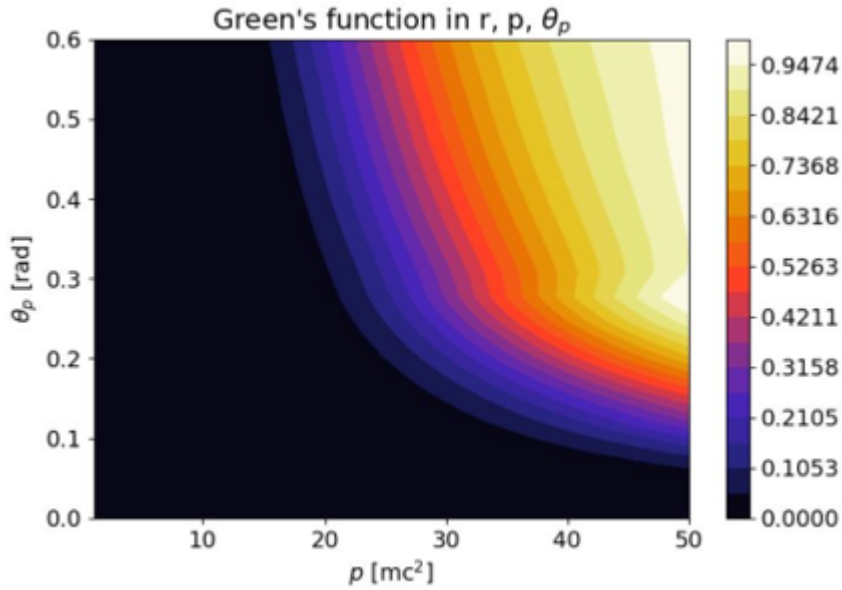


Figure 7.16: The Green's function in p, θ_p for the SR intensity measurement using JET mid-IR camera

Indeed using the described methodology and in the first approach qualitative or very simple numerical comparison. The profile being hollow seems to be confirmed in the case of #95135 before the final collapse as was published in [145] (attached paper G) and in slightly more detail in [156].

Furthermore, in these papers, the same hollow profile that was used in SOFT simulation was applied as the initial condition for the JOREK+RE fluid simulation [114] of the fast RE beam collapse - and indeed, the mode evolution from this point seems to lead to the fast mode overlapping and loss of RE confinement on the sub-ms timescales. The role of the SR radiation analysis and simulation was essential here. Below in the figure 7.17, the example comparison of camera observation and model SR images by SOFT for the hollow profile and for mix of parabolic profile with a very prominent peak in the RE density are shown. In part (a) of the figure, various profiles used in the simulation are shown. In part (b) a two selected frames from the mid-IR camera observation of RE beam in pulse #95135 are documented and in (c), the 5 SR images corresponding to the profiles in (a) are simulated using SOFT. A qualitative comparison may indeed help to discriminate the profiles. Note that the specific camera optics and the reflections or hot spots on the limiters contribute to the experimental image but cannot be captured by SOFT. Despite these limitations, the given experimental images most probably correspond to the specific RE density profiles that were simulated or their combinations. In this way, the SR radiation has become a really important element in the comprehensive analysis of the RE beam evolution.

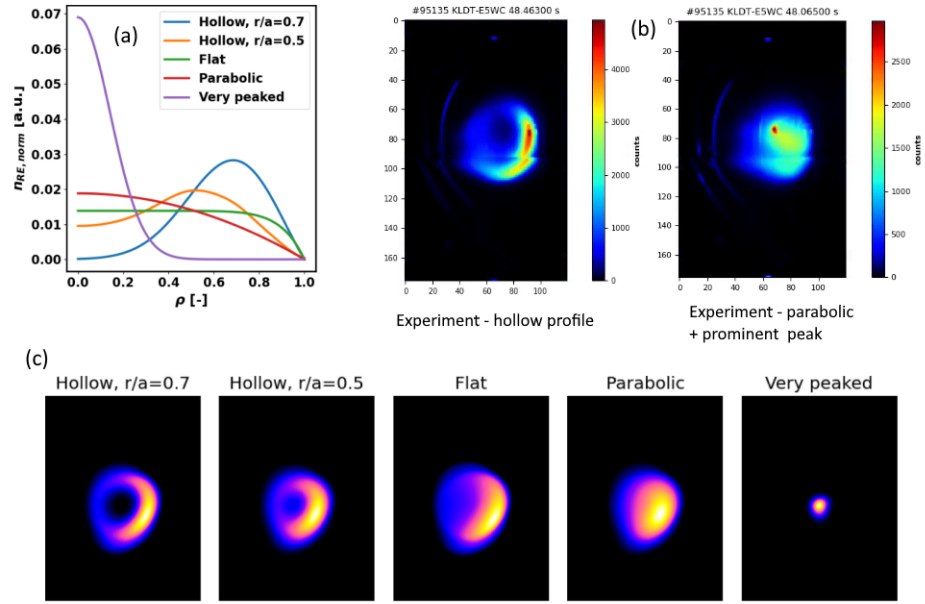


Figure 7.17: (a): the RE density radial profiles used in the simulation, (b) the two experimental observations of mid-IR camera displayed using JUVIL [183], (c) the 5 images corresponding to different RE density profiles in (a) simulated in SOFT.

A more detailed analysis of the role of pitch angle and momentum magnitude was done but is not included here due to space constraints. The synchrotron radiation was lately also simulated in a large detail by other members of the experimental team at JET, with some advice from the author of this thesis.

7.3.4 Summary of the RE generation and mitigation results analysed in this thesis

Within this chapter, the brief summary of gas injection experiments with RE beam generation on COMPASS is given. Namely, the important role of the magnetic field magnitude and the position control in the ramp-up post-disruption RE beam generation is discussed together with the observation of filamentary structures that seem to be composed of newly generated RE electrons on the rational flux surfaces. The generation of RE beam from the flattop scenario seems to be sensitive to timing when MGI is used. Importantly, the current decay rate, produced HXR radiation and kinetic energy estimate is affected by the injected gas amount and species. More specifically it scales with the charge or mass of the injected atoms. Higher Z materials lead to faster current decay but based on the RE beam equilibrium and HXR diagnostics also to increased kinetic energy deposition on the limiters.

The secondary deuterium injection may help to decrease the average RE kinetic energy in the beam while maintaining moderate plasma current decay. Similar behaviour is suggested by the diagnostics observation at JET, where the evolution of the RE energy derived from the magnetic was compared to the HXR spectrometry. Last but not least within this chapter the methodology to discriminate the RE density profile of the beam in given phased based on the observation of the synchrotron radiation pattern via mid-IR camera was described in this chapter in relation to the published results.



Chapter 8

Conclusions and outlook

The understanding of the runaway electron phenomenon via experiments on present devices is the key method to secure safe operation of future large tokamak reactors. The summary of runaway electron physics in chapter 2 shows that runaways can be generated during multiple discharge phases and that the generation mechanisms as well as radiation of runaway electrons and mitigation methods are topics with gradually improving understanding via both modelling and experiments. The chapter 3 summarises the diagnostics methods that can be used to measure RE parameters and the signal processing methods that are typically involved in these measurements. The chapter also includes original contribution of the thesis author to these diagnostics and processing methods applied on COMPASS, namely construction of improvised HXR detector chain to cover large range of photon fluxes or modification of tomographic algorithm for the use in the environment with strong background radiation. The following chapter 4 includes description of the RE discharge scenarios developed at COMPASS and comparison of these to the typical RE beams and RE discharges at ASDEX Upgrade, TCV and JET. The reproducible scenarios allowed for relevant contribution to the international RE research. The chapter 4 also included brief overview of experiments that were conducted on COMPASS and are not further detailed in the following chapters as they were led by other members of COMPASS RE team. This chapter is also complemented with the technical overviews of RE campaigns in appendix B which might be useful for future analysis of the COMPASS RE experiment database.

The chapter 5 summarises results of the studies of RE generation during the COMPASS tokamak discharge start-up and periodic RE losses due to various causes during the discharge current flattop. Via dedicated experiments,

statistical analysis of majority of COMPASS discharges and application of simple numerical model, it is confirmed that early plasma density increase after the breakdown can stop runaway generation and acceleration. Furthermore, a certain level of impurity concentration in pre-fill is found to lead to increased RE generation. In terms of periodic losses more than 7 different classes of plasma instabilities or oscillations due to coil power sources were identified to modulate the RE confinement. The most interesting data includes the periodic losses of RE through edge transport barrier via ELM instabilities and the fact that magnetic islands can both decrease and increase the RE confinement depending on the position. The most important results of this thesis are included in the chapter 6. The features of the RE equilibrium that is also applicable in high current betatrons are discussed with respect to the standard high temperature plasma equilibrium. The applications of the theory that RE kinetic energy behave as anisotropic pressure have allowed for significant improvement of radial position control at COMPASS. Furthermore, the estimate of total RE kinetic energy can be obtained via this dependence and the location of the RE impact depending on energy can be studied.

In the final chapter 7, the diagnostics methods described in previous sections are applied to the analysis of gas injection experiments with RE at COMPASS and JET. It is found, that the generation of RE beam via massive gas injection strongly depends on magnetic field and timing. On the other hand, when small amount of gas is used, the current is transformed fully to the RE and the current decay rates scale with the atomic number of the injected gas. Importantly, the higher current decay rate seem to lead to increase of average kinetic energy, HXR and photoneutron production which is consistent with conversion of magnetic to kinetic energy via induced electric field. Simultaneous decay of both kinetic and magnetic energy seem to be only reached with the companion plasma neutralised by the secondary deuterium injection. This is in agreement with the beneficial effects of deuterium injection studied at JET and other machines in Europe and the world. At JET the harmless termination with deuterium injection and fast deconfinement of RE was studied by the means of synchrotron radiation pattern observation via infrared camera and qualitative comparison with modelling. The comparison leads to a conclusion that the RE density profile and thus current profile is most probably hollow. Furthermore, the decay of synchrotron radiation intensity, estimate of kinetic energy through equilibrium, decay of photoneutron rate and a couple of other indicators suggest gradual decay of energy after the deuterium injection which may contribute to the fact that damage is not observed at all with the secondary deuterium injection. However the main mechanism of annihilating the damage potential of the RE beam by the secondary deuterium injection is most probably linked to the spread of heat loads due to fast MHD instability and removal of RE re-acceleration mechanism as discussed in the [145].

The analyses included in the thesis naturally lead to more research questions, that can be answered via more detailed analysis of existing databases or more dedicated experiments and modelling. The author is currently participating in coordination of RE and disruption mitigation experiments at JET, AUG and TCV that address the details of runaway electron avoidance and mitigation scenarios for ITER. In particular, a publication on the performance of various RE diagnostics during these experiments at various machines is in preparation. Publications covering other unpublished results from the thesis are also planned in near future. The signature result of this thesis, included in chapter 6, is the application of RE equilibrium that is not often considered and has potential to become the most simple RE kinetic energy diagnostics, suitable also for real-time control applications.

In general the COMPASS RE experiments made relatively significant impact in the international community, especially given the small size of the machine. The number of RE discharges conducted within the RE campaigns is very large and the work done within this thesis on RE experiment execution lead to acquisition of huge amount of interesting data that makes other student theses, analyses and publications possible. Furthermore, the large amount of experience with RE phenomena gained during the dedicated campaigns helps with diagnostics design and RE avoidance in the future COMPASS-Upgrade tokamak, where RE can present significantly larger threat due to significantly larger plasma thermal and magnetic energy.

Acknowledgments

Děkuji svému vedoucímu prof. Janu Mlynářovi a všem svým kolegům z týmu tokamaku COMPASS, zejména Evě Macúšové, Jaroslavu Čeřovskému a Miloši Vláníčovi za vynikající spolupráci při experimentálních kampaních.

Furthemore, I would like to thank all the colleagues and experimental team from JET, ASDEX Upgrade and TCV and the colleagues from Chalmers Technical university in Gothenburg, Sweden, for all the discussions, comments and fruitful collaboration during experiments and in the data interpretation.

Děkuji své ženě Hance a synovi Matoušovi za trpělivé snášení mého vědeckého bádání, za podporu a zázemí. Také děkuji svým rodičů a celé rodině.

This work has been carried out within the framework of the EUROfusion Consortium and has received funding from the Euratom research and training programme 2014-2018 and 2019-2020 under grant agreement No 633053. The views and opinions expressed herein do not necessarily reflect those of the European Commission. This work was co-funded by MEYS projects 8D15001 and LM2018117 and Czech science Foundation project GA18-02482S and grant no. SGS19/180/OHK4/3T/14 of the Grant Agency of CTU in Prague.

Prohlašuji, že jsem tuto disertaci vypracoval samostatně a použil jsem pouze podklady (literaturu, projekty, SW, atd.) uvedené v příloženém seznamu.

Nemám závažný důvod proti použití tohoto školního díla ve smyslu § 60 Zákona č. 121/2000 Sb., o právu autorském, o právech souvisejících s právem autorským a o změně některých zákonů (autorský zákon).

V Praze dne 30.3.2023



Bibliography

- [1] Vaclav Smil. *Energy Transitions: Global and National Perspectives, 2nd Edition*. English. 2nd edition. Santa Barbara, California: Praeger, Dec. 2016.
- [2] R. Aymar, P. Barabaschi, and Y. Shimomura. “The ITER design”. en. In: *Plasma Physics and Controlled Fusion* 44.5 (2002), p. 519. DOI: 10.1088/0741-3335/44/5/304.
- [3] John Wesson, D. J. Campbell, J. W. Connor, and R. D. Gill. *Tokamaks*. English. 2 edition. Oxford : New York: Clarendon Press, Mar. 1997.
- [4] R. G. Mills. “Lawson Criteria”. In: *IEEE Transactions on Nuclear Science* 18.4 (Aug. 1971), pp. 205–207. DOI: 10.1109/TNS.1971.4326341.
- [5] A. Gibson. “Fusion relevant performance in JET”. en. In: *Plasma Physics and Controlled Fusion* 32.11 (1990), p. 1083. DOI: 10.1088/0741-3335/32/11/018.
- [6] T. Fujita et al. “High performance reversed shear plasmas with a large radius transport barrier in JT-60U”. en. In: *Nuclear Fusion* 38.2 (1998), p. 207. DOI: 10.1088/0029-5515/38/2/305.
- [7] J. G. Cordey et al. “Plasma confinement in JET H mode plasmas with H, D, DT and T isotopes”. en. In: *Nuclear Fusion* 39.3 (1999), p. 301. DOI: 10.1088/0029-5515/39/3/301.
- [8] D. M. Duffy. “Fusion power: a challenge for materials science”. en. In: *Philosophical Transactions of the Royal Society of London A: Mathematical, Physical and Engineering Sciences* 368.1923 (July 2010), pp. 3315–3328. DOI: 10.1098/rsta.2010.0060.
- [9] Mitsuru Kikuchi. *Fusion Physics*. English. IAEA, 2012.

- [25] Nicholas A. Krall and Alvin W. Trivelpiece. *Principles of Plasma Physics*. English. First Edition, Thus. San Francisco: San Francisco Pr, June 1986.
- [26] Hyun-Tae Kim and A. C. C. Sips and. “Physics of plasma burn-through and DYON simulations for the JET ITER-like wall”. en. In: *Nuclear Fusion* 53.8 (2013). Publisher: IOP Publishing, p. 083024. DOI: 10.1088/0029-5515/53/8/083024.
- [27] V V Plyusnin, V G Kiptily, A E Shevelev, E M Khilkevitch, M. Brix, S Gerasimov, and G. F. Matthews. “Parameters and Stability of Runaway Electron Dominating Discharge in JET with ITER-Like Wall”. In: *Europhysics Conference Abstracts*. Lisbon, Portugal, June 2015, P2.127.
- [28] Mathias Hoppe. “Runaway electron model development and validation in tokamaks”. en. PhD. Gothenburg: Chalmers university of technology, 2021.
- [29] H. K. Wimmel. “Lagrangian Formulation of a Consistent Relativistic Guiding Center Theory”. en. In: *Zeitschrift für Naturforschung A* 38.6 (June 1983). Publisher: De Gruyter Section: Zeitschrift für Naturforschung A, pp. 601–607. DOI: 10.1515/zna-1983-0601.
- [30] Boris N. Breizman, Pavel Aleynikov, Eric M. Hollmann, and Michael Lehnen. “Physics of runaway electrons in tokamaks”. en. In: *Nuclear Fusion* 59.8 (June 2019). Publisher: IOP Publishing, p. 083001. DOI: 10.1088/1741-4326/ab1822.
- [31] H. Dreicer. “Electron and Ion Runaway in a Fully Ionized Gas. I”. In: *Physical Review* 115.2 (July 1959). Publisher: American Physical Society, pp. 238–249. DOI: 10.1103/PhysRev.115.238.
- [32] H. Dreicer. “Electron and Ion Runaway in a Fully Ionized Gas. II”. In: *Physical Review* 117.2 (Jan. 1960). Publisher: American Physical Society, pp. 329–342. DOI: 10.1103/PhysRev.117.329.
- [33] J. W. Connor and R. J. Hastie. “Relativistic limitations on runaway electrons”. en. In: *Nuclear Fusion* 15.3 (June 1975). Publisher: IOP Publishing, pp. 415–424. DOI: 10.1088/0029-5515/15/3/007.
- [34] A. Stahl, E. Hirvijoki, J. Decker, O. Embréus, and T. Fülöp. “Effective Critical Electric Field for Runaway-Electron Generation”. In: *Phys. Rev. Lett.* 114.11 (Mar. 2015). Publisher: American Physical Society, p. 115002. DOI: 10.1103/PhysRevLett.114.115002.
- [35] Linnea Hesslow. “Kinetic modeling of runaway-electron dynamics in partially ionized plasmas”. en. PhD. Gothenburg: Chalmers university of technology, 2020.
- [36] S. T. Beliaev and G. I. Budker. “The Relativistic Kinetic Equation”. In: *Soviet Physics Doklady* 1 (Oct. 1956). ADS Bibcode: 1956SPHD....1..218B, p. 218.

- [37] Bastiaan J. Braams and Charles F. F. Karney. “Differential form of the collision integral for a relativistic plasma”. In: *Phys. Rev. Lett.* 59.16 (Oct. 1987). Publisher: American Physical Society, pp. 1817–1820. DOI: 10.1103/PhysRevLett.59.1817.
- [38] Bastiaan J. Braams and Charles F. F. Karney. “Conductivity of a relativistic plasma”. In: *Physics of Fluids B: Plasma Physics* 1.7 (July 1989). Publisher: American Institute of Physics, pp. 1355–1368. DOI: 10.1063/1.858966.
- [39] A. Stahl, M. Landreman, O. Embréus, and T. Fülöp. “NORSE: A solver for the relativistic non-linear Fokker–Planck equation for electrons in a homogeneous plasma”. en. In: *Computer Physics Communications* 212 (Mar. 2017), pp. 269–279. DOI: 10.1016/j.cpc.2016.10.024.
- [40] Mathias Hoppe, Ola Embreus, and Tünde Fülöp. “DREAM: A fluid-kinetic framework for tokamak disruption runaway electron simulations”. In: *Computer Physics Communications* 268 (2021), p. 108098. DOI: 10.1016/j.cpc.2021.108098.
- [41] L. Hesslow, L. Unnerfelt, O. Vallhagen, O. Embreus, M. Hoppe, G. Papp, and T. Fülöp. “Evaluation of the Dreicer runaway generation rate in the presence of high-impurities using a neural network”. en. In: *Journal of Plasma Physics* 85.6 (Dec. 2019). Publisher: Cambridge University Press. DOI: 10.1017/S0022377819000874.
- [42] H. M. Smith and E. Verwichte. “Hot tail runaway electron generation in tokamak disruptions”. In: *Physics of Plasmas* 15.7 (July 2008). Publisher: American Institute of Physics, p. 072502. DOI: 10.1063/1.2949692.
- [43] Ida Svenningsson, Ola Embreus, Mathias Hoppe, Sarah L. Newton, and Tünde Fülöp. “Hot-Tail Runaway Seed Landscape during the Thermal Quench in Tokamaks”. In: *Phys. Rev. Lett.* 127.3 (July 2021). Publisher: American Physical Society, p. 035001. DOI: 10.1103/PhysRevLett.127.035001.
- [44] M. N. Rosenbluth and S. V. Putvinski. “Theory for avalanche of runaway electrons in tokamaks”. en. In: *Nucl. Fusion* 37.10 (1997). Publisher: IOP Publishing, pp. 1355–1362. DOI: 10.1088/0029-5515/37/10/I03.
- [45] L. Hesslow, O. Embréus, O. Vallhagen, and T. Fülöp. “Influence of massive material injection on avalanche runaway generation during tokamak disruptions”. en. In: *Nucl. Fusion* 59.8 (2019). Publisher: IOP Publishing, p. 084004. DOI: 10.1088/1741-4326/ab26c2.
- [46] S. Sridhar, C. Reux, P. Beyer, M. Lehnen, I. Coffey, R. Guirlet, and N. Fedorczak. “Characterization of cold background plasma during the runaway electron beam mitigation experiments in the JET tokamak”. en. In: *Nucl. Fusion* 60.9 (Aug. 2020). Publisher: IOP Publishing, p. 096010. DOI: 10.1088/1741-4326/ab9dd0.

- [47] Allen H. Boozer. “Pivotal issues on relativistic electrons in ITER”. en. In: *Nucl. Fusion* 58.3 (Jan. 2018). Publisher: IOP Publishing, p. 036006. DOI: 10.1088/1741-4326/aaa1db.
- [48] H. Bethe, W. Heitler, and Paul Adrien Maurice Dirac. “On the stopping of fast particles and on the creation of positive electrons”. In: *Proceedings of the Royal Society of London. Series A, Containing Papers of a Mathematical and Physical Character* 146.856 (Aug. 1934). Publisher: Royal Society, pp. 83–112. DOI: 10.1098/rspa.1934.0140.
- [49] GEORGE R. BLUMENTHAL and ROBERT J. GOULD. “Bremsstrahlung, Synchrotron Radiation, and Compton Scattering of High-Energy Electrons Traversing Dilute Gases”. In: *Rev. Mod. Phys.* 42.2 (Apr. 1970). Publisher: American Physical Society, pp. 237–270. DOI: 10.1103/RevModPhys.42.237.
- [50] O. Embréus, A. Stahl, and T. Fülöp. “Effect of bremsstrahlung radiation emission on fast electrons in plasmas”. en. In: *New J. Phys.* 18.9 (Sept. 2016). Publisher: IOP Publishing, p. 093023. DOI: 10.1088/1367-2630/18/9/093023.
- [51] M. Vlainic, O. Ficker, J. Mlynar, and E. Macusova. “Experimental runaway electron current estimation in COMPASS tokamak”. In: *Atoms* 7.1 (2019). DOI: 10.3390/atoms7010012.
- [52] A. Stahl, M. Landreman, G. Papp, E. Hollmann, and T. Fülöp. “Synchrotron radiation from a runaway electron distribution in tokamaks”. In: *Physics of Plasmas* 20.9 (Sept. 2013). Publisher: American Institute of Physics, p. 093302. DOI: 10.1063/1.4821823.
- [53] M. Hoppe, O. Embréus, R. A. Tinguely, R. S. Granetz, A. Stahl, and T. Fülöp. “SOFT: a synthetic synchrotron diagnostic for runaway electrons”. en. In: *Nuclear Fusion* 58.2 (2018), p. 026032. DOI: 10.1088/1741-4326/aa9abb.
- [54] E. Hirvijoki, I. Pusztai, J. Decker, O. Embréus, A. Stahl, and T. Fülöp. “Radiation reaction induced non-monotonic features in runaway electron distributions”. en. In: *Journal of Plasma Physics* 81.5 (Oct. 2015). Publisher: Cambridge University Press. DOI: 10.1017/S0022377815000513.
- [55] O. Embréus, K. Richards, G. Papp, L. Hesslow, M. Hoppe, and T. Fülöp. “Dynamics of positrons during relativistic electron runaway”. English. In: vol. 42A. Prague, Czech Republic: EPS Mulhouse, France, 2018, P5.4011.
- [56] J. Chadwick and M. Goldhaber. “A Nuclear Photo-effect: Disintegration of the Dipion by γ -Rays”. en. In: *Nature* 134.3381 (Aug. 1934). Number: 3381 Publisher: Nature Publishing Group, pp. 237–238. DOI: 10.1038/134237a0.
- [57] O. N. Jarvis. “Neutron measurement techniques for tokamak plasmas”. en. In: *Plasma Physics and Controlled Fusion* 36.2 (1994), p. 209. DOI: 10.1088/0741-3335/36/2/002.

- [58] Lukáš Lobko. “Statistická analýza měření fúzních neutronů a fotoneutronů na tokamaku COMPASS”. en. Master’s. Prague: Czech Technical University in Prague, 2022.
- [59] M. Lehnen et al. “Disruptions in ITER and strategies for their control and mitigation”. en. In: *Journal of Nuclear Materials*. PLASMA-SURFACE INTERACTIONS 21 463 (Aug. 2015), pp. 39–48. DOI: 10.1016/j.jnucmat.2014.10.075.
- [60] S. Putvinski and et al. “Disruption Mitigation in ITER”. In: Daejeon, Republic of Korea: IAEA, Vienna, Oct. 2010, ITR/1–6.
- [61] T. C. Jernigan, L. A. Baylor, S. K. Combs, D. A. Humphreys, P. B. Parks, and J. C. Wesley. “Massive Gas Injection Systems for Disruption Mitigation on the DIII-D Tokamak”. In: *21st IEEE/NPS Symposium on Fusion Engineering SOFE 05*. ISSN: 2155-9953. Sept. 2005, pp. 1–3. DOI: 10.1109/FUSION.2005.252977.
- [62] T. E. Gebhart, L. R. Baylor, M. N. Ericson, S. J. Meitner, A. L. Qualls, and D. A. Rasmussen. “Recent progress in shattered pellet injection technology in support of the ITER disruption mitigation system \ast ”. en. In: *Nuclear Fusion* 61.10 (Sept. 2021). Publisher: IOP Publishing, p. 106007. DOI: 10.1088/1741-4326/ac1bc4.
- [63] J. Mlynar et al. “Current Research into Applications of Tomography for Fusion Diagnostics”. In: *Journal of Fusion Energy* 38.3-4 (2019), pp. 458–466. DOI: 10.1007/s10894-018-0178-x.
- [64] Yueqiang Liu et al. “Toroidal modeling of runaway electron loss due to 3-D fields in DIII-D and COMPASS”. In: *Physics of Plasmas* 27.10 (Oct. 2020). Publisher: American Institute of Physics, p. 102507. DOI: 10.1063/5.0021154.
- [65] D. B. Weisberg, C. Paz-Soldan, Y. Q. Liu, A. Welander, and C. Dunn. “Passive deconfinement of runaway electrons using an in-vessel helical coil”. en. In: *Nuclear Fusion* 61.10 (Sept. 2021). Publisher: IOP Publishing, p. 106033. DOI: 10.1088/1741-4326/ac2279.
- [66] D. A. Spong et al. “First Direct Observation of Runaway-Electron-Driven Whistler Waves in Tokamaks”. In: *Physical Review Letters* 120.15 (Apr. 2018). Publisher: American Physical Society, p. 155002. DOI: 10.1103/PhysRevLett.120.155002.
- [67] Chang Liu, Eero Hirvijoki, Guo-Yong Fu, Dylan P. Brennan, Amitava Bhattacharjee, and Carlos Paz-Soldan. “Role of Kinetic Instability in Runaway-Electron Avalanches and Elevated Critical Electric Fields”. In: *Physical Review Letters* 120.26 (June 2018). Publisher: American Physical Society, p. 265001. DOI: 10.1103/PhysRevLett.120.265001.
- [68] R. de Luca, P. Fanelli, S. Mingozi, G. Calabrò, F. Vivio, F. Maviglia, and J. H. You. “Parametric design study of a substrate material for a DEMO sacrificial limiter”. en. In: *Fusion Engineering and Design* 158 (Sept. 2020), p. 111721. DOI: 10.1016/j.fusengdes.2020.111721.

- [69] C. Reux et al. “Runaway electron beam generation and mitigation during disruptions at JET-ILW”. en. In: *Nuclear Fusion* 55.9 (Aug. 2015). Publisher: IOP Publishing, p. 093013. DOI: 10.1088/0029-5515/55/9/093013.
- [70] C. Reux, E. Petit, A. Torre, S. Nicollet, F. Saint-Laurent, A. Le Luyer, and P. Moreau. “TOROIDAL FIELD COIL QUENCH CAUSED BY RUNAWAY ELECTRONS ON THE WEST TOKAMAK”. In: Nice, France: IAEA, Vienna, May 2021, p. 1055.
- [71] M. Rabinski et al. “Development of a Cherenkov-type diagnostic system to study runaway electrons within the COMPASS tokamak”. en. In: *Journal of Instrumentation* 12.10 (2017), p. C10014. DOI: 10.1088/1748-0221/12/10/C10014.
- [72] P. Svihra et al. “Runaway electrons diagnostics using segmented semiconductor detectors”. In: *Fusion Engineering and Design* 146 (2019), pp. 316–319. DOI: 10.1016/j.fusengdes.2018.12.054.
- [73] P. Dhyani, V. Svoboda, V. Istokskaia, J. Mlynář, J. Čerovský, O. Ficker, and V. Linhart. “Study of Runaway Electrons in GOLEM Tokamak”. In: *Journal of Instrumentation* 14.9 (2019). DOI: 10.1088/1748-0221/14/09/C09029.
- [74] J. Cerovsky et al. “Progress in HXR diagnostics at GOLEM and COMPASS tokamaks”. en. In: *Journal of Instrumentation* 17.01 (Jan. 2022). Publisher: IOP Publishing, p. C01033. DOI: 10.1088/1748-0221/17/01/C01033.
- [75] D. Rigamonti et al. “The upgraded JET gamma-ray cameras based on high resolution/high count rate compact spectrometers”. In: *Review of Scientific Instruments* 89.10 (Oct. 2018). Publisher: American Institute of Physics, p. 10I116. DOI: 10.1063/1.5038839.
- [76] D. C. Pace et al. “Gamma ray imager on the DIII-D tokamak”. In: *Review of Scientific Instruments* 87.4 (Apr. 2016). Publisher: American Institute of Physics, p. 043507. DOI: 10.1063/1.4945566.
- [77] Nuvia Group. *NuDET NEUTRON specification sheet*. 2017.
- [78] A. Murari et al. “New developments in the diagnostics for the fusion products on JET in preparation for ITER (invited)”. eng. In: *The Review of Scientific Instruments* 81.10 (Oct. 2010), 10E136.
- [79] M. Farník et al. “Radiometry for the vertical electron cyclotron emission from the runaway electrons at the COMPASS tokamak”. In: *Review of Scientific Instruments* 90.11 (Nov. 2019). Publisher: American Institute of Physics, p. 113501. DOI: 10.1063/1.5099463.
- [80] A. Perek et al. “MANTIS: A real-time quantitative multispectral imaging system for fusion plasmas”. In: *Review of Scientific Instruments* 90.12 (Dec. 2019). Publisher: American Institute of Physics, p. 123514. DOI: 10.1063/1.5115569.

- [92] P. Chandrikamohan and T. A. DeVol. “Comparison of Pulse Shape Discrimination Methods for Phoswich and CsI:Tl Detectors”. In: *IEEE Transactions on Nuclear Science* 54.2 (Apr. 2007), pp. 398–403. DOI: 10.1109/TNS.2007.892943.
- [93] Van Chuan Phan and Xuan Hai Nguyen. “Evaluating four neutron-gamma discrimination methods with EJ-301 scintillator”. en. In: *Analog Integrated Circuits and Signal Processing* 98.1 (Jan. 2019), pp. 75–84. DOI: 10.1007/s10470-018-1324-0.
- [94] Steven W. Smith. *The Scientist and Engineer’s Guide to Digital Signal Processing*. en. Newnes, 2002.
- [95] Petre Stoica and Randolph L. Moses. *Spectral Analysis of Signals*. English. 1st edition. Upper Saddle River, N.J: Pearson, Mar. 2005.
- [96] Andrey Nikolayevich Tikhonov. “Solution of incorrectly formulated problems and the regularization method”. en. In: *Soviet Mathematics* 4 (1963), pp. 1035–1038.
- [97] Ondřej Ficker. “Dekonvoluce dat z aktivační sondy jako metoda ke stanovení energií ionizujícího záření v tokamacích”. cs. Bachelor thesis. Prague: Czech Technical University, 2013.
- [98] Ondřej Ficker. “Unfolding of energies of fusion products measured by the activation probe at JET”. eng. In: Conference of Czech and Slovak Physicists/18./ (2015). Ed. by A. Murari, Jan Mlynář, G. Bonheure, and S. Popovichev.
- [99] L. C. Ingesson et al. “Soft X ray tomography during ELMs and impurity injection in JET”. en. In: *Nuclear Fusion* 38.11 (1998), p. 1675. DOI: 10.1088/0029-5515/38/11/307.
- [100] Michael L. Walker, Peter De Vries, Federico Felici, and Eugenio Schuster. “Introduction to Tokamak Plasma Control”. In: *2020 American Control Conference (ACC)*. ISSN: 2378-5861. July 2020, pp. 2901–2918. DOI: 10.23919/ACC45564.2020.9147561.
- [101] D. Humphreys et al. “Novel aspects of plasma control in ITER”. In: *Physics of Plasmas* 22.2 (Feb. 2015). Publisher: American Institute of Physics, p. 021806. DOI: 10.1063/1.4907901.
- [102] A. Shevelev et al. “Study of runaway electrons in TUMAN-3M tokamak plasmas”. en. In: *Plasma Physics and Controlled Fusion* 60.7 (2018), p. 075009. DOI: 10.1088/1361-6587/aac0d5.
- [103] J. Buermans. *Measurement of hard X-rays intensity generated by runaway electrons*. Prague, Czech Republic, 2019.
- [104] Paul K. Romano, Nicholas E. Horelik, Bryan R. Herman, Adam G. Nelson, Benoit Forget, and Kord Smith. “OpenMC: A state-of-the-art Monte Carlo code for research and development”. en. In: *Annals of Nuclear Energy*. Joint International Conference on Supercomputing in Nuclear Applications and Monte Carlo 2013, SNA + MC 2013. Pluri- and Trans-disciplinarity, Towards New Modeling and Numerical

- Simulation Paradigms 82 (Aug. 2015), pp. 90–97. DOI: 10.1016/j.anucene.2014.07.048.
- [105] Jonathan Shimwell, John Billingsley, Ariful Islam Pranto, Katie Taylor, Patrick Shriwise, and Ross Worrall. *A workshop covering a range of fusion relevant analysis and simulations with OpenMC, DAGMC and the Paramak*. original-date: 2021-07-15T09:10:29Z. Oct. 2021.
- [106] M.J. Berger et al. “XCOM: Photon Cross Sections Database”. en. In: *NIST* (Sept. 2009). Last Modified: 2019-11-26T11:20-05:00.
- [107] G. Weber. *X-Ray attenuation & absorption calculator*. web application.
- [108] J. Svoboda, J. Cavalier, O. Ficker, M. Imříšek, J. Mlynář, and M. Hron. “Tomotok: python package for tomography of tokamak plasma radiation”. en. In: *Journal of Instrumentation* 16.12 (Dec. 2021). Publisher: IOP Publishing, p. C12015. DOI: 10.1088/1748-0221/16/12/C12015.
- [109] J. Cavalier. *Calibration of the piezo valve*. Presentation. Institute of Plasma Physics of the CAS, 2016.
- [110] Pfeiffer Vacuum. *Compact FullRange Gauge PKR 251 - Operating instruction*.
- [111] Karl Jousten. “On the gas species dependence of Pirani vacuum gauges”. In: *Journal of Vacuum Science & Technology A* 26.3 (May 2008). Publisher: American Vacuum Society, pp. 352–359. DOI: 10.1116/1.2897314.
- [112] M. Hoppe, I. Ekmark, E. Berger, and T. Fülöp. “Runaway electron generation during tokamak start-up”. en. In: *Journal of Plasma Physics* 88.3 (June 2022). Publisher: Cambridge University Press, p. 905880317. DOI: 10.1017/S002237782200054X.
- [113] C. Sommariva, E. Nardon, P. Beyer, M. Hoelzl, and G. T. A. Huijsmans and. “Electron acceleration in a JET disruption simulation”. en. In: *Nuclear Fusion* 58.10 (Aug. 2018). Publisher: IOP Publishing, p. 106022. DOI: 10.1088/1741-4326/aad47d.
- [114] V. Bandaru, M. Hoelzl, F. J. Artola, G. Papp, and G. T. A. Huijsmans. “Simulating the nonlinear interaction of relativistic electrons and tokamak plasma instabilities: Implementation and validation of a fluid model”. In: *Physical Review E* 99.6 (June 2019). Publisher: American Physical Society, p. 063317. DOI: 10.1103/PhysRevE.99.063317.
- [115] O. Linder, E. Fable, F. Jenko, G. Papp, G. Pautasso, and and. “Self-consistent modeling of runaway electron generation in massive gas injection scenarios in ASDEX Upgrade”. en. In: *Nuclear Fusion* 60.9 (Aug. 2020). Publisher: IOP Publishing, p. 096031. DOI: 10.1088/1741-4326/ab9dcf.

- [116] T. Goorley et al. “Initial MCNP6 Release Overview”. In: *Nuclear Technology* 180.3 (Dec. 2012). Publisher: Taylor & Francis _eprint: <https://doi.org/10.13182/NT11-135>, pp. 298–315. DOI: 10.13182/NT11-135.
- [117] J. Allison et al. “Recent developments in Geant4”. en. In: *Nuclear Instruments and Methods in Physics Research Section A: Accelerators, Spectrometers, Detectors and Associated Equipment* 835 (Nov. 2016), pp. 186–225. DOI: 10.1016/j.nima.2016.06.125.
- [118] F. Ballarini et al. “The FLUKA code: an overview”. en. In: *Journal of Physics: Conference Series* 41 (May 2006). Publisher: IOP Publishing, pp. 151–160. DOI: 10.1088/1742-6596/41/1/014.
- [119] A. E. Shevelev et al. “Reconstruction of distribution functions of fast ions and runaway electrons in fusion plasmas using gamma-ray spectrometry with applications to ITER”. en. In: *Nuclear Fusion* 53.12 (Nov. 2013). Publisher: IOP Publishing, p. 123004. DOI: 10.1088/0029-5515/53/12/123004.
- [120] L. L. Lao, H. St John, R. D. Stambaugh, A. G. Kellman, and W. Pfeiffer. “Reconstruction of current profile parameters and plasma shapes in tokamaks”. en. In: *Nuclear Fusion* 25.11 (Nov. 1985). Publisher: IOP Publishing, pp. 1611–1622. DOI: 10.1088/0029-5515/25/11/007.
- [121] Y. Q. Liu, A. Bondeson, C. M. Fransson, B. Lennartson, and C. Breitholtz. “Feedback stabilization of nonaxisymmetric resistive wall modes in tokamaks. I. Electromagnetic model”. In: *Physics of Plasmas* 7.9 (Sept. 2000). Publisher: American Institute of Physics, pp. 3681–3690. DOI: 10.1063/1.1287744.
- [122] M. Carr et al. “Towards integrated data analysis of divertor diagnostics with ray-tracing”. In: *Europhysics Conference Proceedings*. Belfast, UK: European Physical Society, 2017.
- [123] R. Pánek et al. “Reinstallation of the COMPASS-D tokamak in IPP ASCR”. en. In: *Czechoslovak Journal of Physics* 56.2 (Oct. 2006), B125–B137. DOI: 10.1007/s10582-006-0188-1.
- [124] R. Pánek et al. “Status of the COMPASS tokamak and characterization of the first H-mode”. en. In: *Plasma Physics and Controlled Fusion* 58.1 (2016), p. 014015. DOI: 10.1088/0741-3335/58/1/014015.
- [125] M. Hron et al. “Overview of the COMPASS results *”. en. In: *Nuclear Fusion* 62.4 (May 2022). Publisher: IOP Publishing, p. 042021. DOI: 10.1088/1741-4326/ac301f.
- [126] J. Decker et al. “Full conversion from ohmic to runaway electron driven current via massive gas injection in the TCV tokamak”. en. In: *Nuclear Fusion* 62.7 (May 2022). Publisher: IOP Publishing, p. 076038. DOI: 10.1088/1741-4326/ac544e.

- [127] Josef Havlíček. “Study of Equilibrium Magnetic Configuration in Tokamak Type Devices”. en. PhD. Prague, Czech Republic: Charles University in Prague, Sept. 2015.
- [128] V. V. Plyusnin et al. “Study of runaway electron generation during major disruptions in JET”. en. In: *Nuclear Fusion* 46.2 (Jan. 2006). Publisher: IOP Publishing, pp. 277–284. DOI: 10.1088/0029-5515/46/2/011.
- [129] R. S. Granetz et al. “An ITPA joint experiment to study runaway electron generation and suppression”. In: *Physics of Plasmas* 21.7 (July 2014). Publisher: American Institute of Physics, p. 072506. DOI: 10.1063/1.4886802.
- [130] Michal Farník. “Suprathermal electron diagnostics for the COMPASS tokamak using EC emission”. MA thesis. Prague: Czech Technical University, 2018.
- [131] Jan Mlynar et al. “Effects of Plasma Control on Runaway Electrons in the COMPASS Tokamak”. In: *Europhysics Conference Proceedings*. Lisbon, Portugal: EPS Mulhouse, France, 2015, P4.102.
- [132] L. Novotny et al. “Runaway electron diagnostics using silicon strip detector”. en. In: *Journal of Instrumentation* 15.07 (July 2020). Publisher: IOP Publishing, pp. C07015–C07015. DOI: 10.1088/1748-0221/15/07/C07015.
- [133] V. Linhart et al. “First Measurement of X-rays Generated by Runaway Electrons in Tokamaks Using a TimePix3 Device with 1 mm thick Silicon Sensor”. In: *2018 IEEE Nuclear Science Symposium and Medical Imaging Conference Proceedings (NSS/MIC)*. ISSN: 2577-0829. Nov. 2018, pp. 1–9. DOI: 10.1109/NSSMIC.2018.8824534.
- [134] S. Kulkov et al. “Detection of runaway electrons at the COMPASS tokamak using a Timepix3-based semiconductor detector”. en. In: *Journal of Instrumentation* 17.02 (2022). Publisher: IOP Publishing, P02030. DOI: 10.1088/1748-0221/17/02/P02030.
- [135] J. Zebrowski et al. “Studies of runaway electrons via Cherenkov effect in tokamaks”. en. In: *Journal of Physics: Conference Series* 959.1 (2018), p. 012002. DOI: 10.1088/1742-6596/959/1/012002.
- [136] Jaroslav Čerovský. “Studies of trajectories of relativistic electrons in the magnetic field of tokamak”. MA thesis. Prague: Czech Technical University, 2018.
- [137] Eva Macusova, Ondrej Ficker, Tomas Markovic, Matej Tomes, Yueqiang Liu, and et al. *The impact of resonant magnetic perturbations on runaway electron dynamics*. Invited contribution. Ghent, Belgium, 2019.

- [138] Jakub Caloud, Eva Macusova, Ondrej Ficker, Jaroslav Cerovsky, Jan Mlynar, and et al. “Calorimetry probe measurements of the runaway electron impact energy on plasma facing components at COMPASS tokamak”. In: *Europhysics Conference Proceedings*. Vol. 2022. Maastricht, Netherlands (Online): EPS Mulhouse, France, 2022, P2b.118.
- [139] FTU Team et al. “First Intrashot Observation of Runaway-Electron-Driven Instabilities at the Lower-Hybrid Frequency Range under ITER-Relevant Plasma-Wave Dispersion Conditions”. In: *Physical Review Letters* 129.4 (July 2022). Publisher: American Physical Society, p. 045002. DOI: 10.1103/PhysRevLett.129.045002.
- [140] S. Coda et al. “Overview of the TCV tokamak program: scientific progress and facility upgrades”. en. In: *Nuclear Fusion* 57.10 (2017), p. 102011. DOI: 10.1088/1741-4326/aa6412.
- [141] D. Carnevale et al. “Runaway electron beam control”. In: *Plasma Physics and Controlled Fusion* 61.1 (2019). DOI: 10.1088/1361-6587/aaef53.
- [142] Papp, G., G. Pautasso, and J. Decker. “Runaway Electron Generation and Mitigation on the European Medium Sized Tokamaks ASDEX-Upgrade and TCV”. In: IAEA-CN-234 INIS Reference Number: 49068105. Kyoto, Japan: International Atomic Energy Agency (IAEA), Oct. 2016, EX/9-4.
- [143] M. Gobbin et al. “Runaway electron mitigation by 3D fields in the ASDEX-Upgrade experiment”. en. In: *Plasma Physics and Controlled Fusion* 60.1 (Nov. 2017). Publisher: IOP Publishing, p. 014036. DOI: 10.1088/1361-6587/aa90c4.
- [144] G. Pautasso et al. “Generation and dissipation of runaway electrons in ASDEX Upgrade experiments”. en. In: *Nuclear Fusion* 60.8 (2020). Publisher: IOP Publishing, p. 086011. DOI: 10.1088/1741-4326/ab9563.
- [145] Cédric Reux et al. “Demonstration of Safe Termination of Megaampere Relativistic Electron Beams in Tokamaks”. In: *Physical Review Letters* 126.17 (Apr. 2021). Publisher: American Physical Society, p. 175001. DOI: 10.1103/PhysRevLett.126.175001.
- [146] C. Paz-Soldan et al. “Kink instabilities of the post-disruption runaway electron beam at low safety factor”. en. In: *Plasma Physics and Controlled Fusion* 61.5 (Mar. 2019). Publisher: IOP Publishing, p. 054001. DOI: 10.1088/1361-6587/aafd15.
- [147] K. Insulander Björk et al. “Modelling of runaway electron dynamics during argon-induced disruptions in ASDEX Upgrade and JET”. en. In: *Plasma Physics and Controlled Fusion* 63.8 (2021). Publisher: IOP Publishing, p. 085021. DOI: 10.1088/1361-6587/ac07b5.

- [148] V. V. Plyusnin et al. “Comparison of runaway electron generation parameters in small, medium-sized and large tokamaks—A survey of experiments in COMPASS, TCV, ASDEX-Upgrade and JET”. en. In: *Nuclear Fusion* 58.1 (2018), p. 016014. DOI: 10.1088/1741-4326/aa8f05.
- [149] J. Mailloux and et al. “Overview of JET results for optimising ITER operation”. en. In: *Nuclear Fusion* 62.4 (Apr. 2022). Publisher: IOP Publishing, p. 042026. DOI: 10.1088/1741-4326/ac47b4.
- [150] L. R. Baylor et al. “Design and performance of shattered pellet injection systems for JET and KSTAR disruption mitigation research in support of ITER”. en. In: *Nuclear Fusion* 61.10 (Aug. 2021). Publisher: IOP Publishing, p. 106001. DOI: 10.1088/1741-4326/ac1bc3.
- [151] P. C. de Vries et al. “Analysis of runaway electron discharge formation during Joint European Torus plasma start-up”. en. In: *Plasma Physics and Controlled Fusion* 62.12 (Nov. 2020). Publisher: IOP Publishing, p. 125014. DOI: 10.1088/1361-6587/abbe34.
- [152] J. A. Wesson et al. “Disruptions in JET”. en. In: *Nuclear Fusion* 29.4 (Apr. 1989). Publisher: IOP Publishing, pp. 641–666. DOI: 10.1088/0029-5515/29/4/009.
- [153] R. D. Gill, B. Alper, A. W. Edwards, L. C. Ingesson, M. F. Johnson, and D. J. Ward. “Direct observations of runaway electrons during disruptions in the JET tokamak”. en. In: *Nuclear Fusion* 40.2 (2000). Publisher: IOP Publishing, pp. 163–174. DOI: 10.1088/0029-5515/40/2/302.
- [154] G. Papp et al. “The effect of ITER-like wall on runaway electron generation in JET”. en. In: *Nuclear Fusion* 53.12 (Nov. 2013). Publisher: IOP Publishing, p. 123017. DOI: 10.1088/0029-5515/53/12/123017.
- [155] C. Reux et al. “Physics of runaway electrons with shattered pellet injection at JET”. en. In: *Plasma Physics and Controlled Fusion* 64.3 (2022). Publisher: IOP Publishing, p. 034002. DOI: 10.1088/1361-6587/ac48bc.
- [156] Vinodh Bandaru, Matthias Hoelzl, Cedric Reux, Ondřej Ficker, Scott Alan Silburn, Michael Lehnen, and Nicholas W. Eidietis. “Magnetohydrodynamic simulations of runaway electron beam termination in JET”. en. In: *Plasma Physics and Controlled Fusion* (2021). DOI: 10.1088/1361-6587/abdbcf.
- [157] C. Paz-Soldan et al. “A novel path to runaway electron mitigation via deuterium injection and current-driven MHD instability”. en. In: *Nuclear Fusion* 61.11 (Oct. 2021). Publisher: IOP Publishing, p. 116058. DOI: 10.1088/1741-4326/ac2a69.
- [158] P. Vondracek et al. “Preliminary design of the COMPASS upgrade tokamak”. en. In: *Fusion Engineering and Design* 169 (Aug. 2021), p. 112490. DOI: 10.1016/j.fusengdes.2021.112490.

- [159] Hane Thienpondt, Evangelos Baslis Pallidis, Ondřej Ficker, Eva Marcusova, and Jan Mlynar. *Analysis of Breakdown Runaway Electrons in COMPASS*. winter school report. Prague, Czech Republic: IPP of the CAS, Dec. 2019.
- [160] Jozef Varju et al. “Neutral beam assisted plasma breakdown on tokamak COMPASS”. In: *30th Symposium on Fusion Technology*. Giardini Naxos, Italy, Sept. 2018, P4.007.
- [161] P. C. de Vries and Y. Gribov. “Size matters: ITER breakdown and plasma initiation revisited”. In: *Europhysics Conference Proceedings*. Vol. 42A. Prague, Czech Republic: EPS Mulhouse, France, 2018, O3.109.
- [162] Emelie Nilsson. “Dynamics of runaway electrons in tokamak plasmas”. en. PhD thesis. CEA, Sept. 2015.
- [163] O Ficker and et al. “Long slide-away discharges in the COMPASS tokamak”. In: *Bulletin of the American Physical Society*. Vol. Volume 61, Number 18. San Jose, USA: American Physical Society, 2016, GP10.00101.
- [164] E. Matveeva et al. “Statistical analysis of disruptions in COMPASS”. In: vol. 2018-July. cited By 0. 2018, pp. 333–336.
- [165] Petr Vondracek. “Plasma Heat Flux to Solid Structures in Tokamaks”. en. PhD. Prague, Czech Republic: Charles University in Prague, Apr. 2019.
- [166] M. Imrisek et al. “Use of soft x-ray diagnostic on the COMPASS tokamak for investigations of sawteeth crash neighborhood and of plasma position using fast inversion methods”. In: *Review of Scientific Instruments* 85.11 (Sept. 2014), 11E433. DOI: 10.1063/1.4894528.
- [167] J. W. Connor, A. Kirk, and H. R. Wilson. “Edge Localised Modes (ELMs): Experiments and Theory”. In: *AIP Conference Proceedings* 1013.1 (May 2008). Publisher: American Institute of Physics, pp. 174–190. DOI: 10.1063/1.2939030.
- [168] H.R. Wilson. “Neoclassical Tearing Modes”. In: *Fusion Science and Technology* 57.2T (Feb. 2010). Publisher: Taylor & Francis _eprint: <https://doi.org/10.13182/FST10-A9407>, pp. 164–173. DOI: 10.13182/FST10-A9407.
- [169] Harold Grad and Hanan Rubin. “Hydromagnetic equilibria and force-free fields”. en. In: *Journal of Nuclear Energy (1954)* 7.3-4 (Sept. 1958), pp. 284–285. DOI: 10.1016/0891-3919(58)90139-6.
- [170] Stephen Jardin. *Computational Methods in Plasma Physics*. en. CRC Press, June 2010. DOI: 10.1201/EBK1439810958.
- [171] W. M. Manheimer. “THE PLASMA ASSISTED MODIFIED BETA-TRON”. In: *Part. Accel.* 17 (1985), pp. 157–170.

- [172] Alfred Mondelli and Edward Ott. “Straight and toroidal plasma equilibria with an intense relativistic electron current component”. en. In: *The Physics of Fluids* 17.5 (Aug. 2003). Publisher: American Institute of Physics AIP, p. 1017. DOI: 10.1063/1.1694807.
- [173] W. M. Manheimer and J. M. Finn. “SELF-CONSISTENT THEORY OF EQUILIBRIUM AND ACCELERATION OF A HIGH-CURRENT ELECTRON RING IN A MODIFIED BETATRON”. In: *Particle Accelerators* 14 (1983), 29=38. DOI: 0031-2460/83/1401/002918.50/0.
- [174] Z. Yoshida. “Numerical analysis of runaway tokamak equilibrium”. en. In: *Nuclear Fusion* 30.2 (1990), p. 317. DOI: 10.1088/0029-5515/30/2/010.
- [175] Takaaki Fujita et al. “High-Current Runaway Electron Beam in a Tokamak Plasma”. In: *Journal of the Physical Society of Japan* 60.4 (Apr. 1991). Publisher: The Physical Society of Japan, pp. 1237–1246. DOI: 10.1143/JPSJ.60.1237.
- [176] H. Knoepfel and D. A. Spong. “Runaway electrons in toroidal discharges”. en. In: *Nuclear Fusion* 19.6 (1979), p. 785. DOI: 10.1088/0029-5515/19/6/008.
- [177] John M. Finn and Wallace M. Manheimer. “Self-consistent equilibrium and adiabatic evolution of a high-current electron ring in a modified betatron”. In: *The Physics of Fluids* 26.11 (Nov. 1983). Publisher: American Institute of Physics, pp. 3400–3417. DOI: 10.1063/1.864078.
- [178] O Ficker et al. “Analysis of RE beams in COMPASS and JET using betatron equilibrium and radiation diagnostics”. en. In: *Europhysics Conference Proceedings*. Sitges, Spain (virtual): EPS Mulhouse, France, June 2021, P3.1034.
- [179] V. A. Izzo et al. “Runaway electron confinement modelling for rapid shutdown scenarios in DIII-D, Alcator C-Mod and ITER”. en. In: *Nuclear Fusion* 51.6 (May 2011), p. 063032. DOI: 10.1088/0029-5515/51/6/063032.
- [180] L. Zeng et al. “Experimental Observation of a Magnetic-Turbulence Threshold for Runaway-Electron Generation in the TEXTOR Tokamak”. In: *Physical Review Letters* 110.23 (June 2013). Publisher: American Physical Society, p. 235003. DOI: 10.1103/PhysRevLett.110.235003.
- [181] O Ficker et al. “RE beam generation in MGI disruptions on COMPASS”. en. In: *Europhysics Conference Proceedings*. Belfast, UK: EPS Mulhouse, France, June 2017, P5.126.
- [182] O Ficker et al. “Analysis of MGI disruptions and runaway electron beams at COMPASS using tomography and fast camera data”. en. In: *Europhysics Conference Proceedings*. Prague, Czech Republic: EPS Mulhouse, France, July 2018, P1.1062.

- [183] Valentina Huber et al. “JUVIL: A new innovative software framework for data analysis of JET imaging systems intended for the study of plasma physics and machine operational safety”. en. In: *Fusion Engineering and Design*. Proceedings of the 29th Symposium on Fusion Technology (SOFT-29) Prague, Czech Republic, September 5-9, 2016 123 (Nov. 2017), pp. 979–985. DOI: 10.1016/j.fusengdes.2017.03.005.
- [184] V. Huber et al. “The software and hardware architecture of the real-time protection of in-vessel components in JET-ILW”. en. In: *Nuclear Fusion* 59.7 (May 2019). Publisher: IOP Publishing, p. 076016. DOI: 10.1088/1741-4326/ab1a79.
- [185] U. Losada et al. “Observations with fast visible cameras in high power Deuterium plasma experiments in the JET ITER-like wall tokamak”. en. In: *Nuclear Materials and Energy* 25 (Dec. 2020), p. 100837. DOI: 10.1016/j.nme.2020.100837.
- [186] L. Kripner. *PLEQUE - PLasma EQUilibrium Enjoyment module*. original-date: 2018-07-31T09:05:49Z. Mar. 2023.
- [187] L. Urankar. “Vector potential and magnetic field of current-carrying finite arc segment in analytical form, Part III: Exact computation for rectangular cross section”. In: *IEEE Transactions on Magnetics* 18.6 (Nov. 1982). Conference Name: IEEE Transactions on Magnetics, pp. 1860–1867. DOI: 10.1109/TMAG.1982.1062166.
- [188] Ondrej Grover. *Numerical integration routines of the Biot-Savart law*. original-date: 2019-09-28T08:21:36Z. Mar. 2020.
- [189] Bruce Charles Breneman, John Russell Purcell, and Sibley Charles Burnett. “Magnetic resonance imaging system and method of manufacturing thereof”. en. EP0310212A2. Apr. 1989.



Appendix A

List of acronyms

AUG	ASDEX-Upgrade - Axially Symmetric Divertor Experiment, tokamak in Garching, Germany
AXUV	Absolute eXtreme Ultra-Violet
COMPASS	Compact Assembly - tokamak formerly in Prague, Czech Republic
ECRH	Electron Cyclotron Resonance Heating
EFPS	Equilibrium field power supply
EFIT	Equilibrium FITting
FABV	Fast vertical field power supply - radial control
FABR	Fast radial field power supply - vertical control
HFS	High field side
HFS	Hard X-ray
IPP	Institute of Plasma Physics (of the Czech Academy of Sciences)
JET	Joint European Torus, tokamak in Culham, UK
LFS	Low field side
LOS	Line of sight
MFPS	Magnetising field power supply

A. List of acronyms

MFI	Minimum Fisher Regularisation - tomography
MGI	Massive gas injection
NBI	Neutral beam injection/injectors
PID	Proportional-Integral-Differential (Controller)
PMT	Photomultiplier - general or particular detector at COMPASS
PN	Photoneutrons
RE	Runaway electrons
RMP	Resonant magnetic pertrurbation
RT	Real time control
HX	basic HXR detector at COMPASS
SHX	Shielded HXR - a particular dector at COMPASS
SPI	Shattered pellet Injection (Injector)
SR	Synchrotron Radiation
SXR	Soft X-ray
TCV	Tokamak à configuration variable - operated in Lausanne, Switzerland
TS	Thomson scattering
VV	Vacuum vessel

Appendix B

Plasma diagnostics setups and overviews of COMPASS RE campaigns

B.1 5th-12th RE campaign

Overview of the last 8 RE campaigns is given here while the first 4 are sufficiently described in [20]. The author of the present thesis was the main proponent and coordinator of approximately half of the experiments in these campaigns, which accounts for nearly 1000 discharges. The work on the experiments has included coordination of shutdowns with installation of special diagnostics, some of which was delivered and installed by external guest or installed/designed directly by the COMPASS team; communication with the machine operators including modifications of the feed-back control schemes; proposal and result presentations on COMPASS meetings; management of the experiment execution; calibrations; data analysis and visualisation and some minor modelling support to the experiments in some cases.

B.1.1 5th RE campaign

- Date: from 27/6/2016 till 1/7/2016
- Discharge range: #12076 - #12202

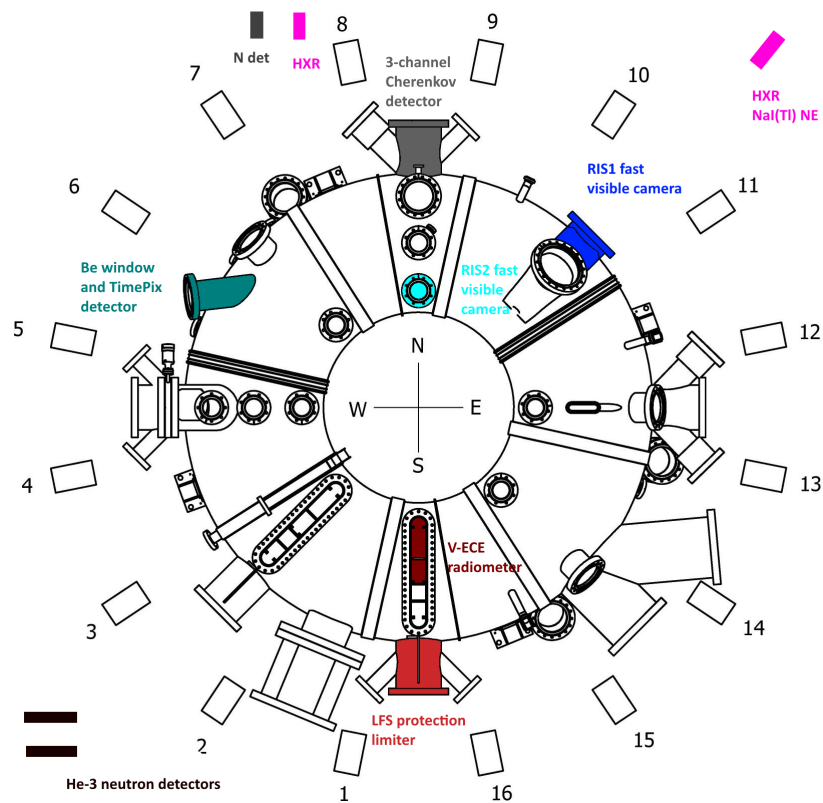


Figure B.2: Scheme of locations of ports with special diagnostics used during the 6th RE campaign

of RE beams triggered in the current ramp-up phase using massive gas injection. This time, observations using fast color camera have revealed gradual penetration of Ar II ions across the field lines and very thin filamentary structure just after the beam generation period, these filaments follow the field lines, live only approximately $30 \mu\text{s}$ and may be formed by low energy RE. This phenomena is described in more detail in chapter 7.

■ B.1.2 6th RE campaign

- Date: from 9/12/2016 till 21/12/2016
- Discharge range: #13054 - #13207
- Special diagnostics installed: 3-channel Cherenkov detector, microwave radiometer on the vertical port, Timepix detector viewing plasma tangentially via Be window

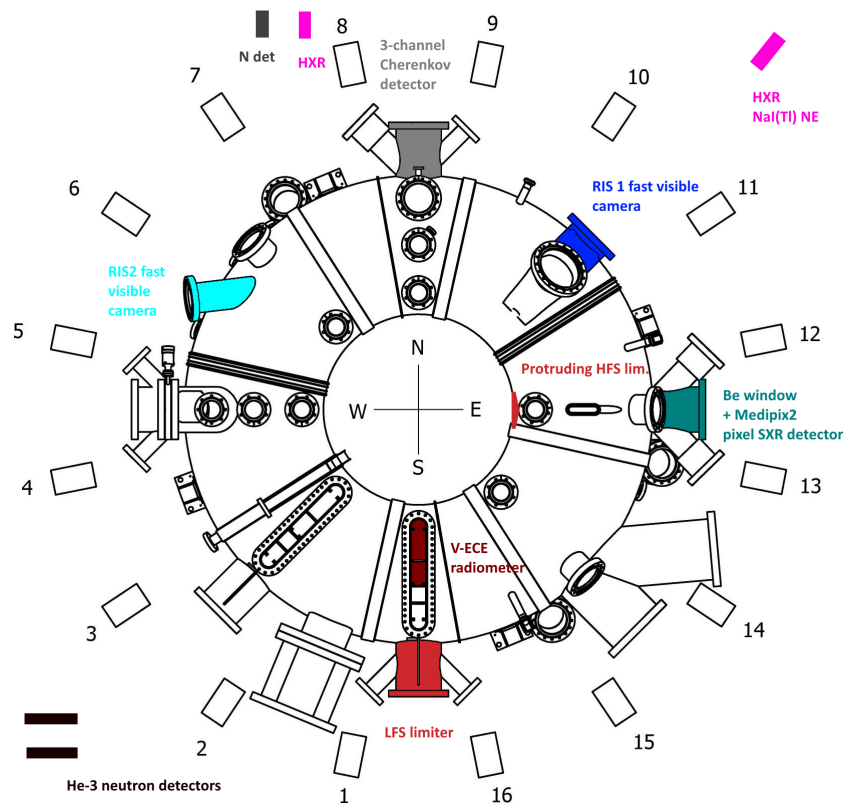


Figure B.3: Scheme of locations of ports with special diagnostics used during the 7th campaign

on the runaway electron losses. For the first time on COMPASS this has been done systematically, in this campaign with $n = 1$ toroidal mode number and different gases and also application of the RMP before and after the disruption and RE beam generation. It was clearly shown that a specific spacial phase shift of top and bottom row RMPs accelerates the decay of runaway electron beam without any observable hot spots on the wall. Results have been reported in [21] as well.

■ B.1.4 8th RE campaign

- Date: from 16/11/2017 to 30/11/2017
- Discharge range: #15619 - #15894
- Special diagnostics installed: 3 channel Cherenkov detector, vertical ECE, super-fast camera Phtoron SA-X2 observing plasma in a wide-angle view, one additional borrowed NaI(Tl) detector, LFS protection limiter now on the reciprocating probe manipulator

■ B.1.5 9th RE campaign

- Date: from 3/4/2018 to 12/4/2018
- Discharge range: #16536 - #16724
- Special diagnostics installed: TimePix3 pixel detector observing plasma via the Be window radially, NaI(Tl) detector with fast data acquisition, slow IR cam observing synchrotron radiation tangentially, super-fast camera Photron SA-X2 observing massive gas injection nozzle, microwave radiometer on the vertical port, LFS protection limiter on reciprocating manipulator

The main topics and achievements: The RMP effects on the flattop scenario were further studied with $n=1$ and $n=2$ toroidal mode numbers of the perturbation, within Ar or Ne and applied before or after the injection. The magnetic field B_t scan run with the very low density discharges for measurements of synchrotron radiation. Attempts of ramp-up MGI scenario were slightly less successful. Flattop MGI timing scan run with solid result pointing to a threshold in necessary RE seed density and/or energy for successful RE beam generation [22]. HXR energies measured for the first time with NaI(Tl) scintillation detector in the counting mode and fast data acquisition - HXR of energies up to 7 MeV detected.

■ B.1.6 10th RE campaign

- Date: from 28/5/2019 to 7/6/2019
- Discharge range: #18790-#19003
- Special diagnostics installed: 3-channel Cherenkov detector, microwave radiometer on the vertical port, X-chip detector placed at one of the bottom ports, pixel detector with neutron conversion layer, limiter on the horizontal reciprocating manipulator as a calorimeter (equipped with temperature sensors) and observed by IR camera, multiple scintillators in a lead bunker, fast cameras including SA-X2, compact NIR camera for wide-angle view
- Guests: Marco Gobbin, Harshita Raj, Roch Kwiatkowski and Marek Rabinski

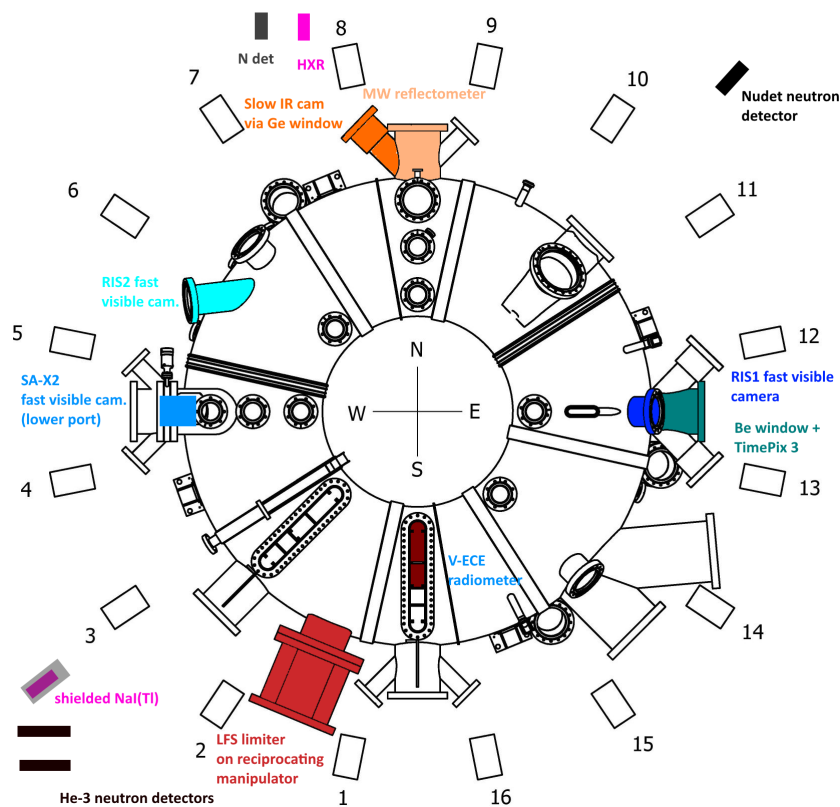


Figure B.5: Scheme of locations of ports with special diagnostics used during the 9th campaign

The main topics and achievements: successful implementation of the RE beam position stability algorithm modification that takes into account the beam energy, RE beam generated in diverted configuration, scan of external electric field values during the RE beam phase, RMPs - influence of the HFS and LFS midplane segment error coils studied. Dedicated discharges run for the measurements of the total beam impact energy via the calorimeter. Use of multiple gas injections (piezo-electric valve followed by MGI), fast timing of TS provides the T_e profile during the slow TQ.

B.1.7 11th RE campaign

- Date: from 27/1/2020 to 4/2/2020
- Discharge range: #19933-#20077
- Special diagnostics installed: 3-channel Cherenkov detector, microwave radiometer on the vertical port, Timepix3 detector viewing plasma radially through Be window, calorimetry head on the horizontal reciprocating

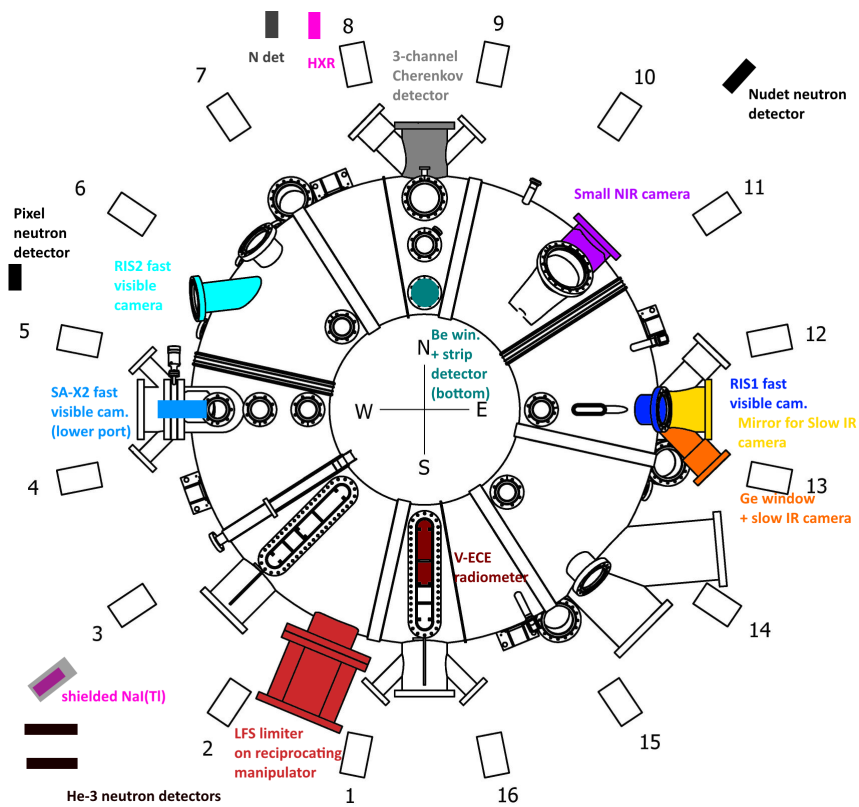


Figure B.6: Scheme of locations of ports with special diagnostics used in the 10th campaign

manipulator and observed by IR camera, 2 NuDET neutron detectors - one outside the hall, precise HXR spectrometer based on $\text{LaBr}_3(\text{Ce})$ scintillator outside the hall, 3 fast cameras + a compact NIR camera, room temperature solid state pellet injector injecting carbon or boron-nitride pellets

- Guests: Marcin Jakubowski, Marek Rabinski; Marco Tardocchi, Enrico Perelli Cipo, Davide Rigamonti; Michal Marčíšovský, Sergei Kulkov

The main topics and achievements: HXR spectra measured with the RE-GARDS spectrometer brought by Italian colleagues, up to 20 MeV HXR photons were detected. RTSP injector was successfully commissioned and used during the experiments - carbon pellet injected into plasma and into an existing RE beam and spectacular videos were recorded. Injection of heavier gas - krypton was tested in the flat-top RE beam generation scenario and also together with the application of RMPs. The negative electric field/loop voltage was applied during the beam decay. The impact energy was measured by the calorimeter during all suitable discharges. Measurements of synchrotron radiation using high resolution NIR camera, which seemed to have insufficient spectral range for the synchrotron radiation detection, unfortunately.

temperature solid state pellet injector with carbon or boron-nitride pellets, spectrometric system for observation of synchrotron radiation spectra REIS, system of 2 in-vessel and 2 ex-vessel antennas for measurements of electromagnetic waves in the range of 100 kHz - 1GHz

The main topics and achievements: Further experiments with RTSP, measurements with REIS-E synchrotron radiation detection system and measurements of HXR's using multiple spectrometers, measurement with upgraded design of the calorimeter. Observation of kinetic instabilities and high frequency instabilities using the loop antennas, active launching of 500 kHz 50W waves into the plasma to observe the effects on the RE population. Various scans with RMPs and fixed Ohmic current drive run, measurements with various radiation detectors by a group from specialised dosimetry institute conducted.

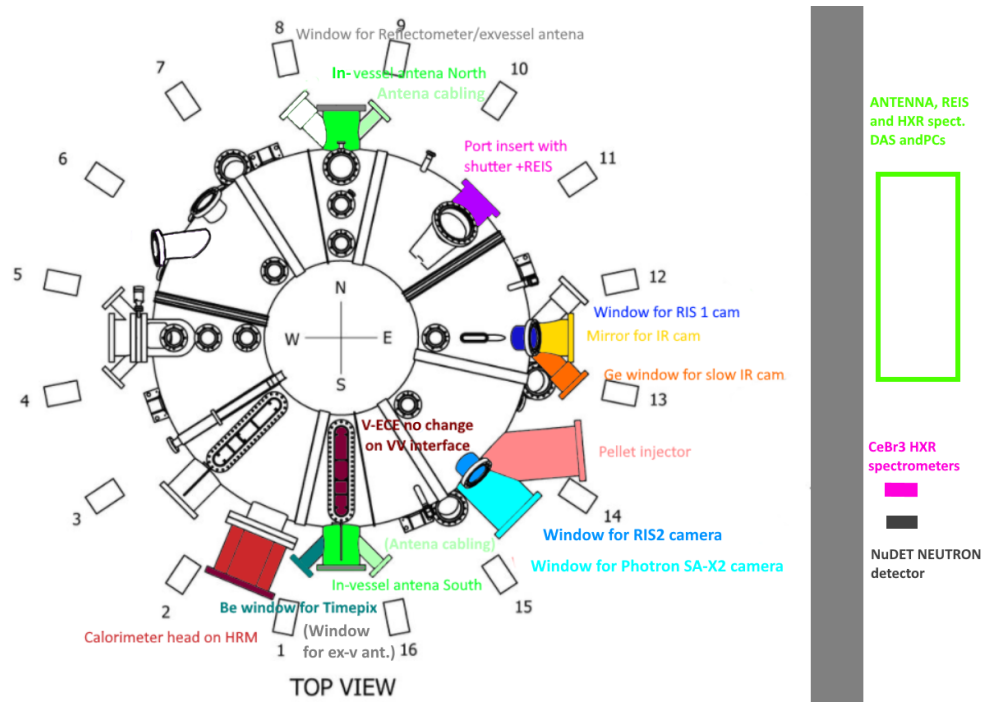


Figure B.8: Scheme of locations of ports with special diagnostics used in the 12th campaign

Appendix C

Biot-Savart solver for investigation of RE equilibrium

In order to better understand and visualise the difference between the standard tokamak equilibrium and possible stable RE orbits a numerical tool in Python that is based on the Biot-Savart integrator of elemental wires with cyclic symmetry was proposed and written by the author. The code is applicable also to various other tasks, e.g. for the optimisation of plasma breakdown with respect to the stray magnetic field from the currents induced in passive structures. It was used for this purpose as well. The code is more flexible for the less traditional applications, like the RE equilibrium, than the codes already available in the community. The program contains two options for calculation of the magnetic field - full Biot-Savart integration that is precise but slower and calculation based on analytical result for toroidal loops that uses elliptic integrals, the details are given below.

Calculating the magnetic field of toroidally symmetric current loops is possible using the Biot-Savart law and simplified formulas. The following formula can be used to calculate the magnetic field of an element $d\mathbf{l}$ of infinitely thin wire carrying current I

$$\mathbf{B} = \frac{\mu_0}{4\pi} I \int \frac{d\mathbf{l} \times (\mathbf{r} - \mathbf{r}_l)}{|\mathbf{r} - \mathbf{r}_l|^3}, \quad (\text{C.1})$$

where $\mu_0 = 4\pi \cdot 10^{-7} \text{H/m}$ is the permeability of vacuum, r is the position where magnetic field is calculated and r_l is the location of the wire element. In our application, this definition is used for a set of loops filling up the poloidal cross-section of a tokamak. Modifications of the integration formula for finite width rectangular cross-section loops applicable here have been derived in [187].

The full integration is done using the Biot-Savart integrator package [188] which allows for calculation of contributions to magnetic field at a given point or a cross-section grid element from each loop in the grid. The field at the point is then evaluated by applying the geometry operator/matrix on the current density matrix for the given grid. The contribution matrices can be then calculated for all elements of the grid and essentially provide a Green's function given that only needs to be multiplied by the current density matrix to obtain the complete magnetic field distribution. Such approach makes any subsequent calculations very fast and competitive with elliptic integral approach described below.

Alternatively, The magnetic field of a loop or a set of loops with arbitrary R , z position that are toroidally symmetric can be calculated analytically using the elliptic integrals of the first and second kind $K(q)$ and $E(q)$. The formulae for this calculation can be found e.g. in the patent [189]. For the magnetic field in arbitrary location R_p , z_p that is generated by a loop positioned at z_l with a diameter R_l we define

$$a = (Z_p - Z_l)^2 + R_l^2 + R_p^2 \quad (\text{C.2})$$

$$b = 2R_l R_p \quad (\text{C.3})$$

$$c = R_l^2 - (Z_p - Z_l)^2 - R_p^2 \quad (\text{C.4})$$

$$d = (Z_p - Z_l)^2 + (R_l - R_p)^2 \quad (\text{C.5})$$

$$e = \sqrt{(Z_p - Z_l)^2 + (R_l + R_p)^2} \quad (\text{C.6})$$

$$q = \sqrt{2b}/e \quad (\text{C.7})$$

using these parameters and the elliptic integrals, we can calculate the magnetic field from single current loop as

$$B_R(R_p, Z_p) = \frac{\mu_0 I}{2\pi e} \frac{Z_p - Z_l}{R_p} \left(\frac{a}{d} E(q) - K(q) \right) \quad (\text{C.8})$$

$$B_Z(R_p, Z_p) = \frac{\mu_0 I}{2\pi e} \left(\frac{c}{d} E(q) + K(q) \right). \quad (\text{C.9})$$

In the magnetostatic calculation, contributions from magnetic field of elemental loops forming the coils, passive structures and plasma/RE beam can be summed up together to get the total field, while in the time dependent case, the mutual inductance has to be considered. The full Biot-Savart integration for rectangular wires is used in chapter 6 when dealing with runaway electron equilibrium.

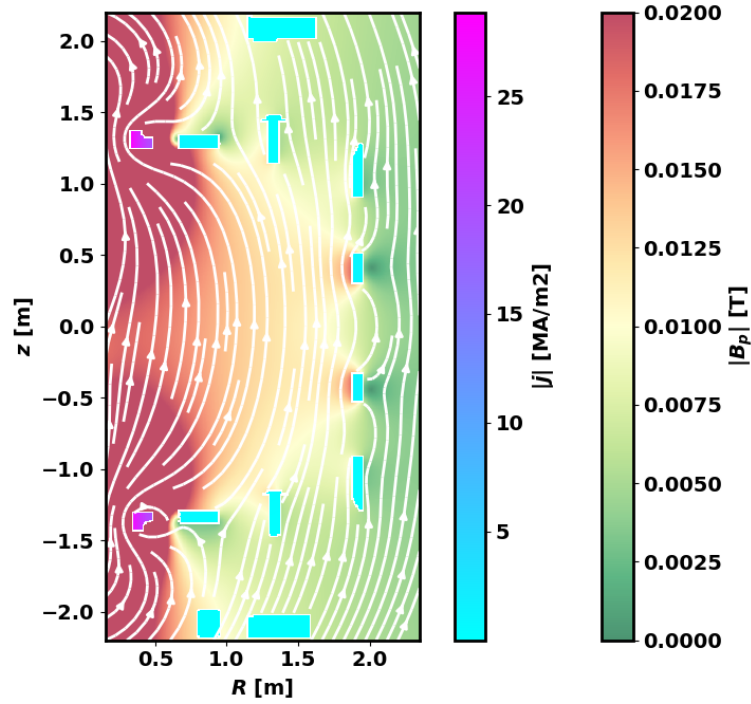


Figure C.1: The output of the Biot-Savart calculation tool described in this appendix for the example of current induced in the support structure of the COMPASS-Upgrade tokamak

It is possible to import the geometry of the cross-section as a bitmap image with the conductor shapes, generated e.g. from a section of the CAD 3D model of the respective structure. Separate image is to be used for loops with different power sources. The image is then scaled to the dimensions and required pixel resolution of the simulation and current distribution is assigned to the coils or plasma based on total current and current profile shapes, loop voltage or externally supplied current distribution e.g. from EFIT. Alternatively it is possible to generate conductors of rectangular and circular cross-section within the program. The program output is shown in fig. C.1. This is an example of calculation of stray magnetic fields caused by currents induced in the closed loops of the support structure of the COMPASS-Upgrade tokamak that is currently being designed.

The figure shows overlay of two images with different colormaps, the green-red colormap shows the magnetic field magnitude and the cyan-magenta colormap shows the current density in the conductors. The white arrows show local direction of the magnetic field. In the case of the application to runaway electron equilibrium in chapter 6, contours of different colours were used to show the flux function Ψ or the toroidal canonical momentum P_ϕ . Various other quantities, e.g. forces can be calculated based on the results.

Appendix D

The attached publications and declaration

The following pages contain a full list of publications (as a main author or a co-author) and four relevant journal papers (two as a first author and two as a coauthor) and three conference contributions connected with runaway electrons that are attached in the following order:

- A. **Ficker O**, Mlynar J, Vlainic M, Cerovsky J, Urban J, Vondracek P, Weinzettl V, Macusova E, Decker J, Gospodarczyk M, Martin P, Nardon E, Papp G, Plyusnin V V, Reux C, Saint-Laurent F, Sommariva C, Cavalier J, Havlicek J, Havranek A, Hronova O, Imrisek M, Markovic T, Varju J, Paprok R, Panek R and Hron M, Losses of runaway electrons in MHD-active plasmas of the COMPASS tokamak, *Nuclear Fusion* 57 076002 (2017)

Author contribution: proposal of the experiments, contribution to the execution of the experiments, analysis of majority of the experimental data included in the paper, figures except Fig 1,2, 6, 7, the whole text of the paper.

- B. **Ficker O**, Macusova E, Mlynar J, Bren D, Casolari A, Cerovsky J, Farnik M, Grover O, Havlicek J, Havranek A, Hron M, Imrisek M, Jerab M, Krbec J, Kulhanek P, Linhart V, Marcisovsky M, Markovic T, Naydenkova D, Panek R, Sos M, Svihra P, Svoboda V, Tomes M, Urban J, Varju J, Vlainic M, Vondracek P, Vrba V, Weinzettl V, Carnevale D, Decker J, Gobbin M, Gospodarczyk M, Papp G, Peysson Y, Plyusnin V V, Rabinski M and Reux C, Runaway electron beam stability and decay in COMPASS, *Nuclear Fusion* 59 (2019)

Studium v doktorském studijním programu

PUBLIKAČNÍ LIST

Jméno: Ing. Ondřej Ficker

Publikace se vztahem k tématu disertační práce/Publications related to the PhD thesis topic:

Publikace v impaktovaných časopisech s afiliací FJFI, Publications in impacted journals with FNSPE affiliation:

Jako hlavní autor/As main author:

1. O. **Ficker**, J. Mlynar, M. Vlainic, J. Cerovsky, J. Urban, P. Vondracek, V. Weinzettl, E. Macusova, J. Decker, M. Gospodarczyk, P. Martin, E. Nardon, G. Papp, V. V. Plyusnin, C. Reux, F. Saint-Laurent, C. Sommariva, J. Cavalier, J. Havlicek, A. Havranek, O. Hronova, M. Imrisek, T. Markovic, J. Varju, R. Paprok, R. Panek, M. H. and, “Losses of runaway electrons in MHD-active plasmas of the COMPASS tokamak,” en, *Nuclear Fusion*, vol. 57, no. 7, May 2017
2. O. **Ficker**, E. Macusova, J. Mlynar, D. Bren, A. Casolari, J. Cerovsky, M. Farnik, O. Grover, J. Havlicek, A. Havranek, M. Hron, M. Imrisek, M. Jerab, J. Krbec, P. Kulhanek, V. Linhart, M. Marcisovsky, T. Markovic, D. Naydenkova, R. Panek, M. Sos, P. Svihra, V. Svoboda, M. Tomes, J. Urban, J. Varju, M. Vlainic, P. Vondracek, V. Vrba, V. Weinzettl, D. Carnevale, J. Decker, M. Gobbin, M. Gospodarczyk, G. Papp, Y. Peysson, V. Plyusnin, M. Rabinski, C. Reux, “Runaway electron beam stability and decay in COMPASS,” *Nuclear Fusion*, vol. 59, no. 9, 2019

Jako spoluautor/As co-author:

3. J. Mlynar, O. **Ficker**, E. Macusova, T. Markovic, D. Naydenkova, G. Papp, J. Urban, M. Vlainic, P. Vondracek, V. Weinzettl, O. Bogar, D. Bren, D. Carnevale, A. Casolari, J. Cerovsky, M. Farnik, M. Gobbin, M. Gospodarczyk, M. Hron, P. Kulhanek, J. Havlicek, A. Havranek, M. Imrisek, M. Jakubowski, N. Lamas, V. Linhart, K. Malinowski, M. Marcisovsky, E. Matveeva, R. Panek, V. Plyusnin, M. Rabinski, V. Svoboda, P. Svihra, J. Varju, J. Zebrowski, “Runaway electron experiments at COMPASS in support of the EUROfusion ITER physics research,” *Plasma Physics and Controlled Fusion*, vol. 61, no. 1, 2019
4. J. Cerovsky, O. **Ficker**, V. Svoboda, E. Macusova, J. Mlynar, J. Caloud, V. Weinzettl, M. Hron,

- “Progress in HXR diagnostics at GOLEM and COMPASS tokamaks,” en, *Journal of Instrumentation*, vol. 17, no. 01, Jan. 2022
5. J. Mlynar, T. Craciunescu, D. Ferreira, P. Carvalho, O. **Ficker**, O. Grover, M. Imrisek, J. Svoboda, c. JET, “Current Research into Applications of Tomography for Fusion Diagnostics,” *Journal of Fusion Energy*, vol. 38, no. 3-4, 2019
 6. M. Vlainić, J. Mlynář, V. Weinzettl, R. Papřok, M. Imříšek, O. **Ficker**, P. Vondráček, J. Havlíček, “First dedicated observations of runaway electrons in the COMPASS tokamak,” *Nukleonika*, vol. 60, no. 2, 2015
 7. M. Vlainic, J. Mlynar, J. Cavalier, V. Weinzettl, R. Papřok, M. Imrisek, O. **Ficker**, M. Varavin, P. Vondracek, J.-M. Noterdaeme, t. C. Team, “Post-disruptive runaway electron beams in the COMPASS tokamak,” en, *Journal of Plasma Physics*, vol. 81, no. 5, Oct. 2015
 8. M. Farník, J. Urban, J. Zajac, O. Bogár, M. Varavin, A. Casolari, J. Čerovský, O. **Ficker**, J. Mlynář, E. Macúšová, V. Weinzettl, M. Hron, “Radiometry for the vertical electron cyclotron emission from the runaway electrons at the COMPASS tokamak,” *Review of Scientific Instruments*, vol. 90, no. 11, Nov. 2019
 9. M. Hron, J. Adánek, J. Cavalier, R. Dejarnac, O. **Ficker**, O. Grover, J. Horáček, M. Komm, E. Macúšová, E. Matveeva, R. Pánek, M. Peterka, J. Seidl, D. Tskhakaya, V. Yanovskiy, F. J. Artola, S. Atikukke, P. Bartoň, A. Bencze, M. Berta, P. Bílková, W. Bin, K. Bogár, O. Bogár, P. Böhm, I. Borodkina, S. Brezinsek, F. Brochard, P. Buratti, J. Čaloud, A. Casolari, C. Castaldo, J. Čečrdle, J. Čerovský, D. Čipciar, A. Devitre, M. Dimitrova, I. Ďuran, S. Entler, M. Farník, H. Fernandes, D. Fridrich, Š. Fuková, E. Gauthier, J. Gerardin, M. Gobbin, G. Grenfell, Y. Gribov, M. Grof, J. Gunn, P. Háček, J. Havlíček, A. Havránek, C. Hidalgo, K. Hromasová, O. Hronova, M. Iafrati, M. Imříšek, N. Isernia, F. Jaulmes, M. Jeřáb, M. Jirsa, P. Junek, A. Kallenbach, O. Kovanda, K. Kovařík, J. Krbec, L. Kripner, L. Krlín, P. Kulhánek, M. Lehnen, N. Lemoine, X. Litaudon, Y. Q. Liu, N. C. Logan, T. Loarer, A. Loarte, P. Lourenco, S. Lukes, P. Mácha, M. Rabinski, A. M. Roldan, T. Markovič, J. Matějček, G. Mazzitelli, J. Mlynář, I. Mysiura, F. Napoli, D. Naydenkova, J.-K. Park, N. Patel, P. Pavlo, R. Pitts, A. Podolník, M. Poradzinski, J. Preinhaelter, A. Prishvitsin, D. Refy, R. Roccella, D. Šesták, O. Shyshkin, V. Škvára, M. Šos, M. Spolaore, J. Stöckel, J. Svoboda, M. Tomeš, A. Torres, P. Turjanica, G. Tynan, M. Valovič, G. V. Oost, M. Varavin, J. Varju, P. Veis, M. Vilemova, F. Villone, P. Vondráček, V. Weinzettl, F. Žáček, G. Zadviskiy, J. Zajac, D. R. Zaloga, J. Zebrowski, S. Zoletnik, “Overview of the COMPASS results *,” en, *Nuclear Fusion*, vol. 62, no. 4, May 2022
 10. V. Linhart, D. Bren, A. Casolari, J. Čerovský, M. Farník, O. **Ficker**, M. Hetflejš, M. Hron, J. Jakůbek, P. Kulhánek, E. Macúšová, M. Marčíšovský, J. Mlynář, P. Švihra, V. Svoboda, J. Urban, J. Varju, V. Vrba, “First Measurement of X-rays Generated by Runaway Electrons in Tokamaks Using a TimePix3 Device with 1 mm thick Silicon Sensor,” in *2018 IEEE Nuclear Science Symposium and Medical Imaging Conference Proceedings (NSS/MIC)*, Nov. 2018
 11. L. Novotny, J. Cerovsky, P. Dhyani, O. **Ficker**, M. Havranek, M. Hejtmanek, Z. Janoska, V. Kafka, S. Kulkov, M. Marcisovska, M. Marcisovsky, G. Neue, P. Svihra, V. Svoboda, L. Tomasek, M. Tunkl, V. Vrba, “Runaway electron diagnostics using silicon strip detector,” en, *Journal of Instrumentation*, vol. 15, no. 07, Jul. 2020
 12. S. Kulkov, M. Marcisovsky, P. Svihra, M. Tunkl, M. v. Beuzekom, J. Caloud, J. Cerovsky, O. **Ficker**, E. Macusova, J. Mlynar, V. Weinzettl, V. Svoboda, “Detection of runaway electrons at the COMPASS tokamak using a Timepix3-based semiconductor detector,” en, *Journal of Instrumentation*, vol. 17, no. 02, 2022
 13. P. Svihra, D. Bren, A. Casolari, J. Cerovsky, P. Dhyani, M. Farnik, O. **Ficker**, M. Havranek, M. Hejtmanek, Z. Janoska, V. Kafka, P. Kulhanek, V. Linhart, E. Macusova, M. Marcisovska, M. Marcisovsky, J. Mlynar, G. Neue, L. Novotny, V. Svoboda, L. Tomasek, J. Urban, P. Vancura,

J. Varju, V. Vrba, V. Weinzettl, “Runaway electrons diagnostics using segmented semiconductor detectors,” *Fusion Engineering and Design*, vol. 146, 2019

14. P. Vondracek, E. Gauthier, O. **Ficker**, M. Hron, M. Imrisek, R. Panek, “Fast infrared thermography on the COMPASS tokamak,” *Fusion Engineering and Design*, Proceedings of the 29th Symposium on Fusion Technology (SOFT-29) Prague, Czech Republic, September 5-9, 2016, vol. 123, Nov. 2017

Publikace v impaktovaných časopisech bez afilice FJFI/Publications in impacted journals without FNSPE affiliation:

15. C. Reux, C. Paz-Soldan, P. Aleynikov, V. Bandaru, O. **Ficker**, S. Silburn, M. Hoelzl, S. Jachmich, N. Eidietis, M. Lehnen, S. Sridhar, JET contributors, “Demonstration of Safe Termination of Megaampere Relativistic Electron Beams in Tokamaks,” *Physical Review Letters*, vol. 126, no. 17, Apr. 2021
16. C. Reux, C. Paz-Soldan, N. Eidietis, M. Lehnen, P. Aleynikov, S. Silburn, V. Bandaru, O. **Ficker**, M. Hoelzl, E. M. Hollmann, S. Jachmich, E. Joffrin, P. J. Lomas, F. Rimini, L. Baylor, A. Bleasdale, L. Calacci, F. Causa, D. Carnevale, I. Coffey, D. Craven, A. D. Molin, E. d. l. Luna, G. D. Tommasi, J. Garcia, T. Gebhart, L. Giacomelli, A. Huber, E. Khilkevich, C. Lowry, E. Macusova, A. Manzanares, M. Nocente, E. Panontin, G. Papp, G. Pautasso, A. Peacock, V. Plyusnin, A. Shevelev, D. Shiraki, C. Sommariva, C. Sozzi, S. Sridhar, R. Sweeney, G. Szepesi, R. A. Tinguely, J. Wilson, “Physics of runaway electrons with shattered pellet injection at JET,” en, *Plasma Physics and Controlled Fusion*, vol. 64, no. 3, 2022
17. V. Bandaru, M. Hoelzl, C. Reux, O. **Ficker**, S. A. Silburn, M. Lehnen, N. W. Eidietis, “Magnetohydrodynamic simulations of runaway electron beam termination in JET,” en, *Plasma Physics and Controlled Fusion*, 2021
18. M. Vlainic, O. **Ficker**, J. Mlynar, E. Macusova, “Experimental runaway electron current estimation in COMPASS tokamak,” *Atoms*, vol. 7, no. 1, 2019
19. C. Paz-Soldan, C. Reux, K. Aleynikova, P. Aleynikov, V. Bandaru, M. Beidler, N. Eidietis, Y. Q. Liu, C. Liu, A. Lvovskiy, S. Silburn, L. Bardoczi, L. Baylor, I. Bykov, D. Carnevale, D. D.-C. Negrete, X. Du, O. **Ficker**, S. Gerasimov, M. Hoelzl, E. Hollmann, S. Jachmich, S. Jardin, E. Joffrin, C. Lasnier, M. Lehnen, E. Macusova, A. Manzanares, G. Papp, G. Pautasso, Z. Popovic, F. Rimini, D. Shiraki, C. Sommariva, D. Spong, S. Sridhar, G. Szepesi, C. Zhao, t. D.-D. Team, J. E. T. Contributors, “A novel path to runaway electron mitigation via deuterium injection and current-driven MHD instability,” en, *Nuclear Fusion*, vol. 61, no. 11, Oct. 2021
20. J. Decker, G. Papp, S. Coda, B. P. Duval, U. Sheikh, P. Blanchard, D. Choi, C. Galperti, L. Calacci, D. Carnevale, O. **Ficker**, M. Gobbin, B. Labit, E. Macusova, J. Mlynar, V. Plyusnin, O. Sauter, t. T. Team, t. E. M. Team, “Full conversion from ohmic to runaway electron driven current via massive gas injection in the TCV tokamak,” en, *Nuclear Fusion*, vol. 62, no. 7, May 2022
21. U. A. Sheikh, P. David, O. **Ficker**, M. Bernert, D. Brida, M. Dibon, B. P. Duval, M. Faitsch, M. Maraschek, G. Papp, G. Pautasso, C. Sozzi, “Disruption mitigation efficiency and scaling with thermal energy fraction on ASDEX Upgrade,” en, *Nuclear Fusion*, vol. 60, 2020
22. P. Dhyani, V. Svoboda, V. Istokskaia, J. Mlynář, J. Čerovský, O. **Ficker**, V. Linhart, “Study of Runaway Electrons in GOLEM Tokamak,” *Journal of Instrumentation*, vol. 14, no. 9, 2019
23. D. Carnevale, M. Ariola, G. Artaserse, F. Bagnato, W. Bin, L. Boncagni, T. Bolzonella, F. Bombarda, P. Buratti, L. Calacci, F. Causa, S. Coda, F. Cordella, J. Decker, G. Tommasi, B. Duval, B. Esposito, G. Ferro, O. **Ficker**, L. Gabellieri, A. Gabrielli, S. Galeani, C. Galperti, S. Garavaglia, A. Havranek, M. Gobbin, M. Gospodarczyk, G. Granucci, E. Joffrin, M. Lennholm, A. Lier, E. Macusova, F. Martinelli, J. Martin-Solis, J. Mlynar, L. Panaccione, G. Papp, M. Passeri, G. Pautasso, Ž. Popovic, C. Possieri, G. Pucella, U. Sheikh, G. Ramogida, C. Reux, F. Rimini, A. Romano, M.

- Sassano, B. Tilia, O. Tudisco, D. Valcarcel, “Runaway electron beam control,” *Plasma Physics and Controlled Fusion*, vol. 61, no. 1, 2019
24. V. V. Plyusnin, C. Reux, V. G. Kiptily, G. Pautasso, J. Decker, G. Papp, A. Kallenbach, V. Weinzettl, J. Mlynar, S. Coda, V. Riccardo, P. Lomas, S. Jachmich, A. E. Shevelev, B. Alper, E. Khilkevitch, Y. Martin, R. Dux, C. Fuchs, B. Duval, M. Brix, G. Tardini, M. Maraschek, W. Treutterer, L. Giannone, A. Mlynek, O. **Ficker**, P. Martin, S. Gerasimov, S. Potzel, R. Paprok, P. J. McCarthy, M. Imrisek, A. Boboc, K. Lackner, A. Fernandes, J. Havlicek, L. Giacomelli, M. Vlainic, M. Nocente, U. Kruezi, C. team, TCV team, A.-U. team, E. M. Team, J. E. T. contributors, “Comparison of runaway electron generation parameters in small, medium-sized and large tokamaks—A survey of experiments in COMPASS, TCV, ASDEX-Upgrade and JET,” en, *Nuclear Fusion*, vol. 58, no. 1, 2018
 25. Y. Liu, C. Paz-Soldan, E. Macusova, T. Markovic, O. **Ficker**, P. B. Parks, C. C. Kim, L. L. Lao, L. Li, “Toroidal modeling of runaway electron loss due to 3-D fields in DIII-D and COMPASS,” *Physics of Plasmas*, vol. 27, no. 10, Oct. 2020
 26. M. Rabinski, L. Jakubowski, K. Malinowski, M. J. Sadowski, J. Zebrowski, M. J. Jakubowski, R. Mirowski, V. Weinzettl, O. **Ficker**, J. Mlynar, R. Panek, R. Paprok, M. Vlainic, “Development of a Cherenkov-type diagnostic system to study runaway electrons within the COMPASS tokamak,” en, *Journal of Instrumentation*, vol. 12, no. 10, 2017

Příspěvky na konferencích, ve sbornících abstraktů/Publications at conferences, in proceedings:

Jako hlavní autor/As main author:

27. O. Ficker, et al., “Long slide-away discharges in the COMPASS tokamak,” in *Bulletin of the American Physical Society*, vol. Volume 61, Number 18, American Physical Society, 2016; 58th Annual Meeting of the APS Division of Plasma Physics, San Jose, USA, 31/10-4/11/2016 [poster]
28. O. **Ficker**, J. Mlynar, E. Macusova, M. Vlainic, V. Weinzettl, J. Urban, J. Cerovsky, M. Farnik, T. Markovic, R. Paprok, P. Vondracek, M. Imrisek, M. Tomes, J. Havlicek, J. Varju, M. Varavin, O. Bogar, A. Havranek, M. Gospodarczyk, M. Rabinski, M. Jakubowski, K. Malinowski, J. Zebrowski, V. Plyusnin, G. Papp, R. Panek, M. Hron, “RE beam generation in MGI disruptions on COMPASS,” en, in *Europhysics Conference Proceedings*, EPS Mulhouse, France, Jun. 2017; 44th EPS Conference on Plasma Physics, Belfast, UK, 26 - 30 June 2017 [poster]
29. O. **Ficker**, M. Imrisek, J. Mlynar, E. Macusova, J. Svoboda, V. Weinzettl, J. Urban, A. Havranek, J. Cerovsky, M. Farnik, O. Grover, M. Hron, R. Panek, V. Plyusnin, M. Vlainic, “Analysis of MGI disruptions and runaway electron beams at COMPASS using tomography and fast camera data,” en, in *Europhysics Conference Proceedings*, EPS Mulhouse, France, Jul. 2018; 45th EPS Conference on Plasma Physics, Prague Czech Republic, 2-6 July 2018 [poster]
30. O. **Ficker**, E. Macusova, J. Cerovsky, L. Kripner, A. D. Molin, S. Silburn, C. Reux, M. Hoppe, C. Sommariva, E. Joffrin, G. Ghillardi, R. A. Tinguely, J. Mlynar, E. Panontin, M. Nocente, M. Tardocchi, S. Jachmich, C. Paz-Soldan, P. Vondracek, A. Casolari, M. Farnik, J. Caloud, V. Weinzettl, J. Cavalier, J. Havlicek, A. Havranek, M. Imrisek, J. Svoboda, M. Hron, “Analysis of RE beams in COMPASS and JET using betatron equilibrium and radiation diagnostics,” en, in *Europhysics Conference Proceedings*, EPS Mulhouse, France, Jun. 2021; 47th EPS Conference on Plasma Physics, Sitges, Spain (virtual), 21-25 June, 2021 [poster]

Dále ustní příspěvky na významných mezinárodních setkáních, například/Oral contributions and important international meetings such as:

Losses of runaway electrons in MHD-active plasmas of the COMPASS tokamak

O. Ficker^{1,2}, J. Mlynar¹, M. Vlaine^{1,2,3}, J. Cerovsky^{1,2}, J. Urban¹,
P. Vondracek^{1,4}, V. Weinzettl¹, E. Macusova¹, J. Decker⁵, M. Gospodarczyk⁶,
P. Martin⁷, E. Nardon⁸, G. Papp⁹, V.V. Plyusnin¹⁰, C. Reux⁸,
F. Saint-Laurent⁸, C. Sommariva⁸, J. Cavalier^{1,11}, J. Havlicek¹,
A. Havranek^{1,12}, O. Hronova¹, M. Imrisek^{1,4}, T. Markovic^{1,4}, J. Varju¹,
R. Paprok^{1,4}, R. Panek¹, M. Hron¹ and The COMPASS Team¹

¹ Institute of Plasma Physics of the CAS, CZ-18200 Praha 8, Czechia

² FNSPE, Czech Technical University in Prague, CZ-11519 Praha 1, Czechia

³ Department of Applied Physics, Ghent University, 9000 Ghent, Belgium

⁴ FMP, Charles University, CZ-12116 Praha 2, Czechia

⁵ Swiss Plasma Centre, EPFL, CH-1015 Lausanne, Switzerland

⁶ Università di Roma Tor Vergata, 00133 Roma, Italy

⁷ Consorzio RFX, 35127 Padova, Italy

⁸ CEA, IRFM, F-13108 Saint-Paul-lez-Durance, France

⁹ Max Planck Institute for Plasma Physics, Garching D-85748, Germany

¹⁰ Instituto de Plasmas e Fusão Nuclear, IST, Lisbon, Portugal

¹¹ Institut Jean Lamour IJL, Université de Lorraine, 54000 Nancy, France

¹² FEE, Czech Technical University in Prague, CZ-12000 Praha 2, Czechia

E-mail: ficker@ipp.cas.cz

Received 16 December 2016, revised 3 March 2017

Accepted for publication 3 April 2017

Published 11 May 2017



CrossMark

Abstract

The significant role of magnetic perturbations in mitigation and losses of runaway electrons (REs) was documented in dedicated experimental studies of RE at the COMPASS tokamak. REs in COMPASS are produced both in low density quiescent discharges and in disruptions triggered by massive gas injection (MGI). The role of the RE seed produced in the beginning of the discharge on the subsequent RE population proved significant. Modulation of the RE losses by MHD instabilities was observed at several characteristic frequencies, as well as by magnetic field oscillations related to power supplies. Magnetic islands seem to suppress the losses as the HXR signal is low and coherent with the island rotation frequency. Moreover, periods of increased losses of REs observed in the current quench (CQ) and early RE beam plateau phase of the MGI disruptions seem to be linked to the bursts of magnetic perturbation, and to the observation of filaments in the fast visible camera images.

Keywords: tokamaks, runaway electrons, MHD instabilities, disruptions

(Some figures may appear in colour only in the online journal)

1. Introduction

Control and/or mitigation of runaway electrons (REs) present one of the key tasks for experimental work of present tokamaks in support of the ITER programme. Indeed, models of ITER disruption evolution predict generation of RE beams with several tens of MeV to carry up to 70% of pre-disruptive plasma

current [1]. As the deposition of the RE current can be highly localised, the deposited energy could severely damage plasma facing components and blanket modules of ITER. Following previous experiments [2] and recent modelling efforts [3], it appears that improved understanding of the link between the complex dynamics of evolution of perturbed magnetic surfaces during the disruption and RE generation and losses represents

a key contribution towards safe operation of ITER. However, this task is quite challenging, due to short timescales and significant radiation loads that can lead to saturation or degradation of many diagnostic signals. Equilibrium reconstruction, e.g. EFIT that is applied to COMPASS discharges, is also ruled out for a fast discharge termination. In this respect it is essential to understand the response of REs to magnetic perturbations under controlled conditions, i.e. in the current flat-top phase of the discharge. Subsequently, the knowledge so acquired can be extended towards plasma disruption timescales with support of the relevant MHD codes (e.g. Jorek [4]).

The COMPASS tokamak [5, 6] has been systematically contributing to dedicated RE research since 2014. It is an experimental device with ITER-like plasma cross-section, major radius $R_0 = 0.56$ m and minor radius $a = 0.23$ m. The typical toroidal field is $B_T = 1.2$ T and plasma current in the flat-top phase is $I_p < 400$ kA. The COMPASS plasmas can be operated in both limiter and divertor configuration, the latter allowing for routine H-mode operation [5]. Neutral beam heating at 40 keV can inject up to 600 kW of additional power. The main advantages of the machine are its flexibility and low operational costs. Population of REs is observed in COMPASS even at relatively high plasma densities $n_e \sim 4\text{--}6 \cdot 10^{19} \text{ m}^{-3}$, with a strong dependence on the gas fuelling scenario in the initial phase as well as on the plasma shape [7]. The COMPASS experiments are normally deuterium fuelled, and the typical pulse length is about 0.4 s, although the low current circular discharge with high fraction of REs can last up to one second [8]. The disruptive scenario with RE beam generation following argon puff was achieved in COMPASS [9], and currently presents an important topic for further investigation.

1.1. MHD and RE related diagnostics

The COMPASS tokamak features a rich set of magnetic diagnostics [10], allowing for rather detailed measurements of both poloidal and toroidal characteristics of magnetic perturbation in the plasma, including magnetic islands and TAEs (toroidal Alfvén eigenmodes). It consists of three poloidal arrays of internal Mirnov (pick-up) coils (MC) at different toroidal positions covering all three components of magnetic field (r, θ, ϕ) by 24 coils each (i.e. $3 \times 3 \times 24$ coils in total), see figure 1. Furthermore, 16 internal partial Rogowski (IPR) coils circumventing poloidal cross section (so that their combined signal provides a direct measure of the plasma current), several flux loops and an extensive number of saddle coils may be used in studies of magnetic configuration and perturbations. For the analysis reported further in this paper, specifically the outer midplane (OMP) coils of all arrays have been used.

The primary means of RE research at COMPASS relies on standard hard x-ray (HXR) diagnostics, based on a pair of NaI(Tl) scintillation detectors with photomultiplier tube (PMT) and a composite scintillator (EJ410—ZnS(Ag) embedded in a plastic matrix) with PMT shielded by 10 cm of lead. Although the latter detector features an enhanced sensitivity to photoneutrons, experience at COMPASS tokamak has demonstrated that the relative intensity of HXR is sufficiently high to overrun the neutron signal and

form the main component of the ZnS(Ag) data in most of the RE dedicated experiments. Therefore, in the following it will be referred to as the shielded HXR detector, sensitive to HXR energies of approx. 500 keV and above. The energy range of the unshielded NaI(Tl) scintillation detectors starts at approximately 50 keV. Due to the high intensity of the HXR signal in the RE experiments—note that there is no collimation—the detectors typically work in current mode operation. The approximate distance of both detectors from the tokamak main axis is 4 m; for their location see figure 2.

Plasma density was monitored and controlled using the 2 mm interferometer with central vertical line of sight. In recent experimental campaigns the fast IR camera—Telops FAST-IR 2K—was located at a tangential port in direct view of the OMP protection limiter (made of graphite). The camera was used for studies of first wall heat loading due to RE losses, which was monitored with frame-rates up to 30 kfps and spatial resolution ~ 1 mm/pixel. Further, for investigation of the MGI induced disruptions with runaway beam generation, the fast visible spectrum camera—Photron Mini UX100—proved to be very useful. This camera is situated at the midplane, and covers a wide angle at a standard frame-rate of 8 kfps.

1.2. RE generation control via plasma density

Based on previous experience [7], the RE seed generated in the plasma current ramp up phase proves to be well controlled by plasma fuelling just before the plasma breakdown and in the initial 10 ms of the discharge. Without the RE seed, RE generation in the current flat-top phase appears only at very low plasma densities, approximately $n_e < 1.5 \cdot 10^{19} \text{ m}^{-3}$ that corresponds to $E/E_c \geq 10$, where $E_c = \frac{e^3 n_e \ln \Lambda}{4\pi \epsilon_0^2 m_e c^2}$ and E is an estimate of the electric field inferred from the loop voltage measurement. Once the RE seed is present, the RE confinement is much better in the divertor configuration and in the elongated limited plasma compared to the circular limited plasma [7]. Indeed, in the circular limited configuration it suffices to increase the density to $n_e = 3 \cdot 10^{19} \text{ m}^{-3}$ in order to initiate relatively fast decay of the RE population.

The following sections accentuate the influence of the background plasma and external coil current oscillations on the runaway electron population and are organised as follows: in section 2.1 the effect of ST instability on RE in discharges with controlled RE population is presented, section 2.2 outlines the effect of magnetic islands on RE losses, section 3 details direct (section 3.1) and indirect (section 3.2) effects of poloidal field power supply oscillations, and in section 4 the interplay of magnetic perturbations and RE losses during disruptions is reported.

2. RE losses due to MHD instabilities

2.1. Increased losses during sawtooth crashes

A comparison of a series of similar discharges with a rather high flat-top density ($n_e \sim 6 \cdot 10^{19} \text{ m}^{-3}$) in the divertor configuration was carried out, in order to better understand the

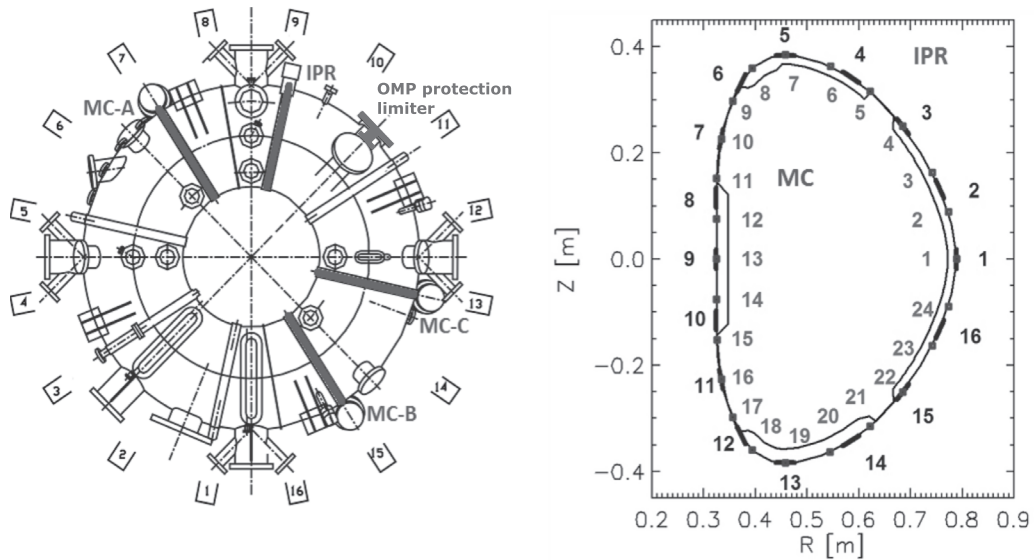


Figure 1. The COMPASS tokamak, left: top view with toroidal positions of the MHD coil arrays (all located inside the vacuum vessel), limiter position corresponding to section 2.2, right: vacuum vessel poloidal cross-section with the distribution of MC and IPR coils.

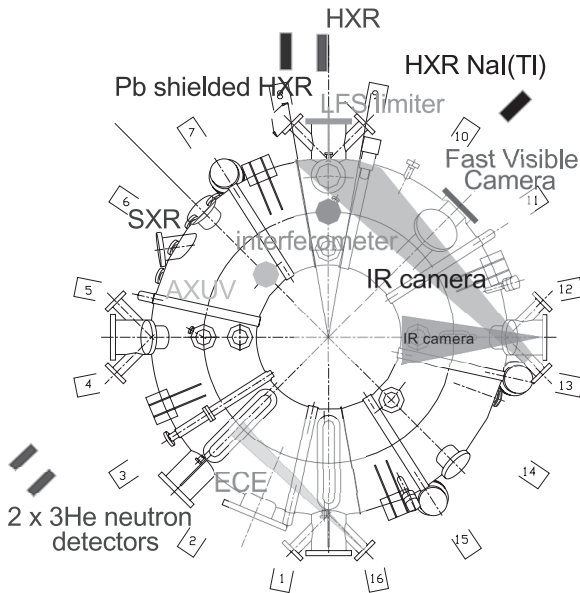


Figure 2. The most recent layout of the RE-related diagnostics.

influence of different plasma fuelling waveforms on the RE population. Furthermore, the discharges were characterised by a relatively high frequency sawtooth instability (with period close to 2 ms). It can be concluded that the changes in the magnetic topology and induced radial plasma flow substantially increase RE losses. Note that from the measured data it cannot be inferred whether REs are lost from the core or from the edge in these crashes, as sawtooth instability is known to strongly affect edge physics in COMPASS [11]. Sawtooth instability represents an especially important case with respect to its potential to generate a population of energetic electrons due to the local electric field induced in fast reconnection theoretically considered and even observed in TCV [12]. Although it seems unlikely that such a population could be confined for a sufficient time in order to become an RE seed and eventually lead to a significant RE current, this

generation source was investigated during COMPASS fuelling experiments. The result is negative at the detection level of the utilised HXR detectors—see figure 3. In the discharge where the initial fuelling and thus also the density were kept at higher levels to prevent RE seed generation (#8634), negligible HXR signal was observed during the current flat-top even though the sawtooth instability showed the same behaviour as in the reference discharge with the same initial parameters except the initial fuelling (#8636), where the HXR signal was clearly correlated with sawtooth crashes. This result has proved to be reproducible. No clear correlation between the size of the sawtooth crash or the period of the instability and the size of HXR peaks has been identified so far.

2.2. RE losses and magnetic islands

Magnetic islands appear often in COMPASS plasmas, depending on the safety factor profile $q(r)$ [13]. The oscillations of the pick-up coil signal that are caused by the rotating magnetic island may be identified using a time-resolved frequency analysis. In COMPASS discharges without auxiliary heating, the typical frequency of rotation of stable magnetic islands with toroidal mode number $n = 1$ is 8–10 kHz. This section is focused on discharges with plasma densities n_e from 1 to $3 \cdot 10^{19} \text{ m}^{-3}$ and a rather high loop voltage. In these discharges, REs are present while carrying just a small fraction of plasma current, and the interaction of REs with the background plasma can be studied. From figure 4 it is obvious that the presence of the magnetic islands completely alters the dynamics of the RE losses compared to MHD-quiescent plasma discharges. It seems that the magnetic islands can behave as a barrier for REs, and the losses are significantly lowered until the end of the discharge when the rest of the RE population is released. The density as well as the initial fuelling was kept the same in each pair of discharges presented ($n_e = 1.5 \cdot 10^{19} \text{ m}^{-3}$ in #10004 and #10006, $n_e = 1.8 \cdot 10^{19} \text{ m}^{-3}$ in #13084 and #13085). Furthermore,

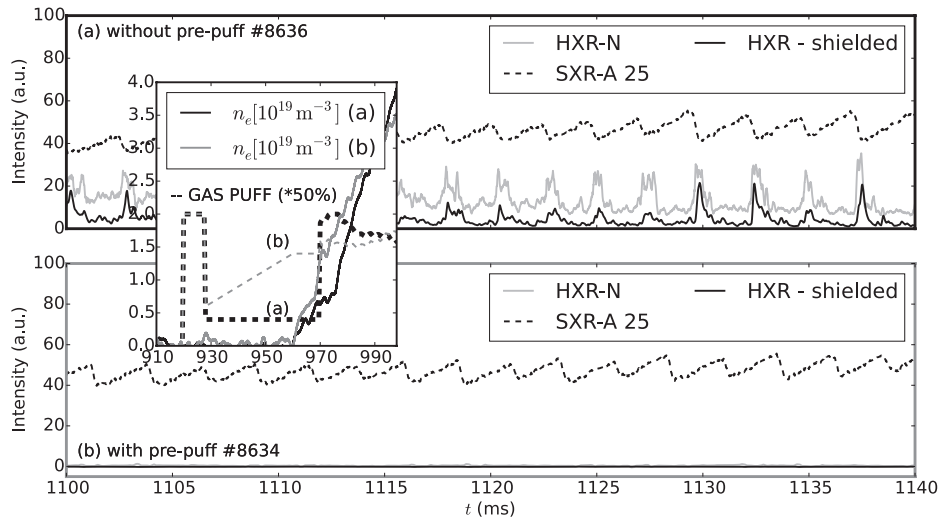


Figure 3. The initial fuelling and density evolution just after the plasma breakdown (inserted image) for two otherwise identical discharges where REs are affected by the sawtooth instability. Increase of the initial fuelling results in a strong suppression of RE seed and subsequently no HXR burst connected to sawtooth crashes are observed.

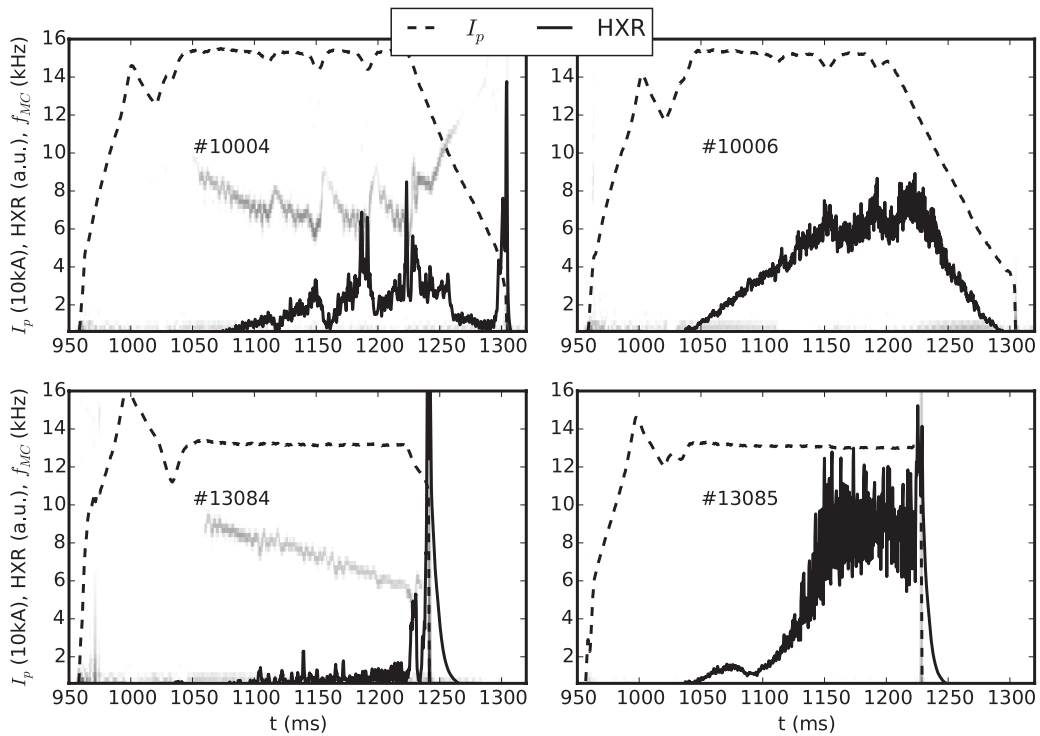


Figure 4. Comparison of two pairs of almost identical COMPASS discharges (the top pair differ in elongation #10004: $\epsilon = 1.0$ and #10006: $\epsilon = 1.1$, the discharges of the second pair were using identical waveforms for all pre-set parameters). Spectrogram of outer midplane Mirnov coil is in the background (grey), plasma current I_p in a dashed line and signal of shielded HXR/PN detector in solid, the scale is the same in all frames.

the measured loop voltage in the discharges with magnetic islands is significantly lower compared to the quiescent discharges. This supports the hypothesis of a decreased radial transport of REs due to magnetic islands. Besides, the intentional decreases in the plasma current seem to affect the RE losses much more in the discharges with perturbed topology of magnetic surfaces. In order to completely understand the effect of magnetic islands on REs, the role of the size, position and rotational frequency of magnetic islands must be studied and compared with MHD models, e.g. JOREK.

Observation of oscillations in the HXR signal intensity with frequencies similar to the frequency of island rotation on COMPASS was first briefly reported in [13]. The interplay between the HXR data and the magnetic data was later confirmed in dedicated COMPASS RE campaigns in discharges with a measurable population of REs, and with magnetic oscillations of a sufficient amplitude. From these measurements, it can be concluded that the magnetic islands considerably influence confinement of REs at the plasma edge. Indeed, the coherence diagram in figure 5 shows that the HXR oscillations

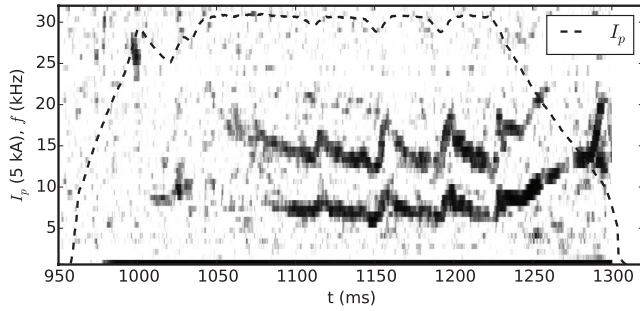


Figure 5. Coherence diagram of the Mirnov coil signal and the signal of the HXR detector, together with the time evolution of the plasma current (dashed line), COMPASS discharge #10004. The magnetic island rotation clearly correlates with the modulated HXR signal visible at approx. 8 kHz, and with the second harmonic.

follow the changes of the island rotation frequency. The changes were induced by small decreases in the plasma current waveform. Furthermore, the second harmonic—practically undetectable in the simple spectrogram calculated from the Mirnov coil signal—appears in the coherence diagram.

In order to investigate whether the coherent RE losses correspond to the O-point or the X-point of the magnetic island—in simplified terms, whether the HXR intensity is in phase or in counter phase to the magnetic oscillations—a method was developed using the available data, i.e. the non-localised HXR measurements and the signals from the rich and localised magnetic diagnostics on COMPASS. The method presented here is based on the assumption that most of the REs are lost to the OMP protection limiter and the magnetic islands have toroidal mode number $n = 1$, although the method might be modified for higher toroidal mode numbers. The method uses the cross-correlation, which helps to identify the time delays between similar signals, in our case the magnetic fluctuation signals and the HXR signal (reference). The cross-correlation is more efficient than simple comparison of signals as it highlights common components of the time series. Before applying the cross-correlation analysis, the signals were band-pass filtered ($f_l = 100$ Hz, $f_u = 100$ kHz). An example of the delays derived from the cross-correlation analysis for one segment of the signals for discharge #10004 is shown in the left part of figure 6. The time evolution of the cross-correlation delays τ is then shown in the right part of figure 6 (for each time the delays are detected as the left part of the figure shows). The changes in the frequency of the island rotation appear in this figure again, and further support our assumptions. The time delays may be transformed to the toroidal phase shifts by a multiplication with the instant value of the angular frequency, but in such a case the changes in the time evolution (due to the plasma current variation in #10004) would not be visible anymore. From the analysis of the phase shifts between the integrated signals of the OMP coils of the four poloidal arrays (for the set-up see figure 1) it can be concluded that the enhanced RE losses correspond to the O-point of the magnetic islands.

Similar results were also achieved in FTU using the Cherenkov detector [14, 27] (localised measurement of the RE

losses, recently tested on COMPASS as well)—for the detailed analysis see [15]. However, this technique is not fully reproducible for all COMPASS discharges due to multiple reasons, including the significant presence of higher toroidal mode component, saturation in the HXR data and also the limited validity of the key assumption that the HXR intensity oscillations originate in the OMP limiter. Note that significant damage from the REs was also observed on the HFS. Nevertheless, these results highlight the importance of the edge magnetic topology for RE losses.

3. Effects of the poloidal magnetic field power source oscillations on the RE losses

In the COMPASS experiments, it turned out that RE losses are not modulated just by the plasma MHD instabilities but also by other frequencies linked to the power supplies (PS) of the magnetic field. The main power supplies of the COMPASS tokamak consist of two flywheel generators (FWG) and a set of thyristor AC/DC converters [6, 16]. For the experiments presented in this part only one FWG was used with stored energy up to 45 MJ. The FWG typically rotates at 1400 RPM at the beginning of the discharge, the rotation frequency decreases approximately by 100–200 RPM towards the end of the discharge. The poloidal field PS use 12-pulse converters, while the toroidal field PS use 24-pulse converters. Due to these technical constraints, the current in the poloidal field windings—and therefore the measured signals of the loop voltage, the equilibrium poloidal field and the shaping poloidal field—exhibit an oscillating component with a typical frequency of approx. 800 Hz, while in the case of the toroidal field, this frequency is doubled. The effect of these PS oscillations on the COMPASS plasma is in general negligible; however, it becomes very important in the case of sensitive phenomena, e.g. RE losses.

3.1. Direct effect due to radial position change

Small oscillations in the radial position of the order of several millimetres with frequency approximately 400 Hz appear in COMPASS as a reaction of the real-time position control (PID controller) to the abovementioned PS oscillations. These oscillations modulate the losses of REs, specifically in discharges with large RE population. Modulation of the RE losses by radial position was recently confirmed by the fast IR camera data as corresponding to heat flux on the OMP protection limiter [17]—see figure 7. The left part of the figure also indicates that the increasing heat flux comes primarily from the growing RE population: the heat flux increases with the decreasing electron density, while the plasma temperature does not change significantly according to the Thomson scattering measurement. Moreover, in discharges where intentional radial movements were applied [8] it was shown that the losses might also be increased by slow outward movement. These results indicate that specifically the losses of the runaway electrons from the very edge of plasma are modulated by this mechanism.

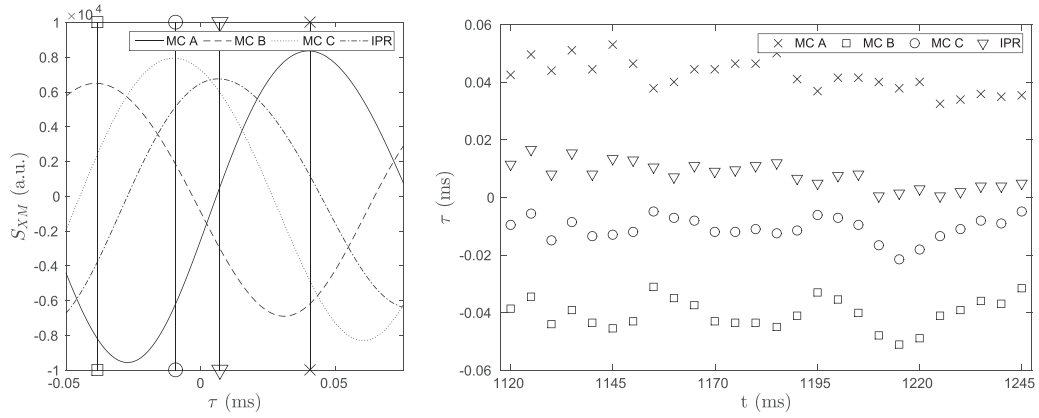


Figure 6. Left: an example of delays derived from cross-correlation analysis between the reference HXR data and the data from magnetic coils located at four different toroidal positions (see figure 1). The vertical lines correspond to the detected maxima of the cross-correlation functions S_{XM} , τ is the lag (delay) of the cross-correlation functions. Right: time evolution of the lag, demonstrating that the RE losses culminate when the maximum of the field perturbation passes the OMP limiter.

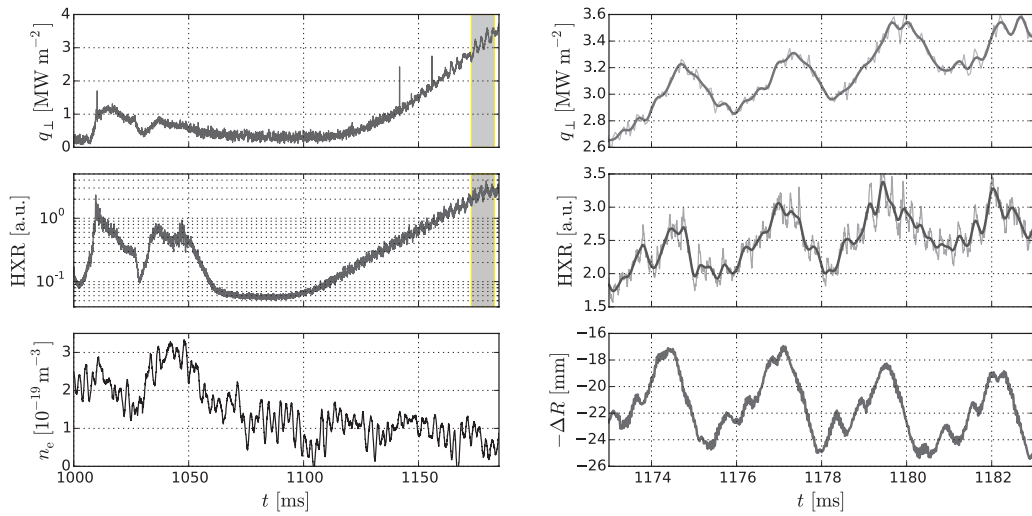


Figure 7. Left: time evolution of the heat flux q_{\perp} calculated from the fast IR camera data, HXR signal and the electron density n_e as measured in the COMPASS discharge with strong RE generation (#12084). Right: detail of the highlighted region including the oscillation of the radial position (outer clearance—distance of the separatrix and the OMP limiter as calculated by EFIT—shown in the figure).

3.2. Indirect effect due to interaction with plasma MHD perturbations

The radial oscillations of the plasma position do not represent the only occurrence of interplay between the RE losses and the PS oscillations. Interestingly, in the case of smaller RE populations, very pronounced periodic peaks with a frequency close to 1 kHz were observed in the signals of all HXR detectors, and even in the form of bursts of saturated pixels in the fast visible camera images. In order to determine whether this phenomenon was connected to the power source oscillations, the initial frequency of the FWG was changed in a series of almost identical discharges. Comparison of a pair of these discharges is presented in figure 8. Indeed, the results demonstrate that the change in the FWG rotation frequency (which drives the oscillations of the loop voltage signal) causes a proportional change of the frequency of the HXR intensity peaks.

The fact that the HXR peak frequency in this regime of RE losses changes when the FWG rotation frequency is changed presents a very robust result. However, it was also clearly

observed that in different discharge scenarios the frequency of the HXR periodic peaks may have different values with the same FWG frequency. Therefore, 14 relevant discharges were systematically analysed in order to determine the key parameters behind this phenomenon. It was found that the frequency of the losses show significant dependence on the value of the edge safety factor q_{95} : the lower the q_{95} , the higher the frequency of the HXR peaks. In order to cancel the dependence on the FWG frequency, figure 9 gives the ratio of the HXR and the loop voltage oscillation frequencies as a function of q_{95} . Although it seems that the value of the studied ratio may reach any number in the continuous interval, the values of the ratio could be primarily only rational numbers (e.g. $\{1, 3/2, 2\}$) with the scatter being caused by different effects.

It is worth noting that a weak magnetic structure, probably a small magnetic island, can be observed in the spectrogram of the outer mid-plane diagnostic coils at 6–10 kHz during this type of RE loss (see figure 10). Based on these observations a proposed explanation of the HXR peak frequencies is

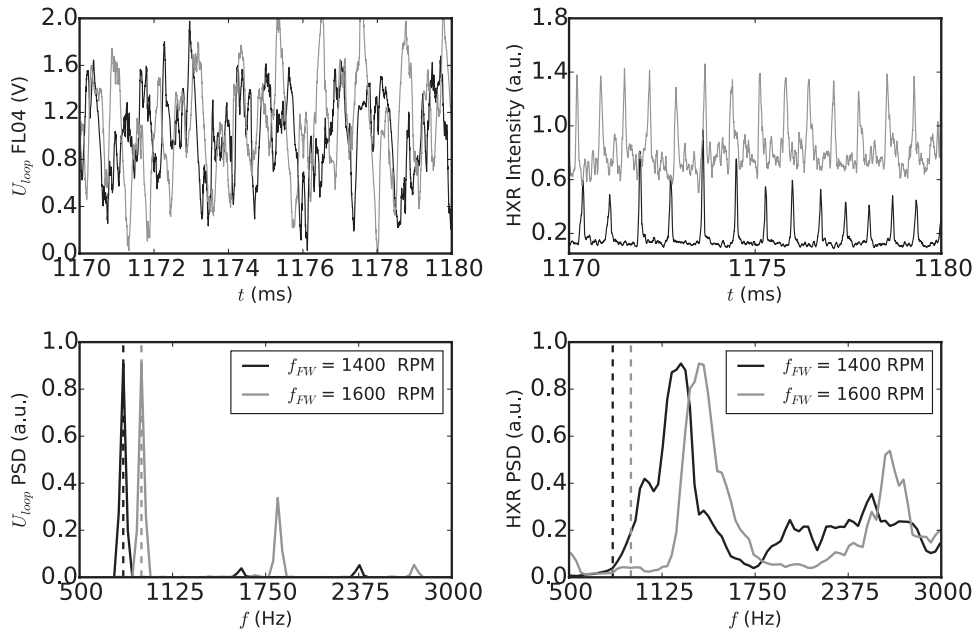


Figure 8. Comparison of the loop voltage (left) and HXR (right) oscillations in the two discharges with different FWG rotation frequencies (1400 RPM in the discharge #10874, 1600 RPM in discharge #10875). Time traces of the signal (top) and the frequency analysis (bottom). Vertical lines correspond to oscillations in the loop voltage signal in both graphs.

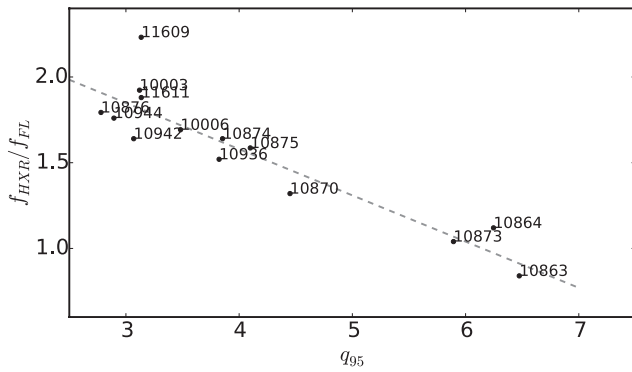


Figure 9. Dependence of the ratio of the frequency of periodic peaks of HXR signal f_{HXR} and the dominant frequency of the poloidal field oscillations as measured by the flux loop f_{FL} on the safety factor value at the edge q_{95} . Discharge numbers are also shown.

a resonant interaction of the power source oscillations with weak magnetic islands. This hypothesis can explain the weak trace in the spectrogram and the transitions from this mechanism of the RE losses to the mechanism dominated by large magnetic islands that was described in the previous section. Provided that the magnetic islands behave like a barrier for REs (see section 2.2), this mechanism may correspond to a repeating destruction of such barriers. Details of the interaction between the PS oscillations and the magnetic islands, dependent on their mode number, are yet to be disclosed.

4. RE losses and MHD activity during current quench and beam plateau phase

The wide variety of periodic RE loss phenomena identified in quiescent discharges—and described in the preceding text—shows that even minor changes in the topology of

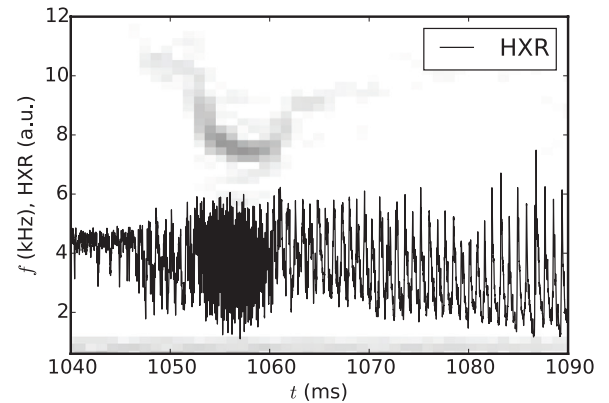


Figure 10. Spectrogram of the OMP IPR coil signal and the HXR intensity signal for discharge #10945, three regimes of RE losses may be identified—aperiodic regime in the very beginning, periodic peaks with frequency above 1 kHz accompanied by a weak trace in the spectrogram and 8 kHz losses coherent with the magnetic island.

magnetic surfaces may critically affect RE losses. This presents an important conclusion for the generation of runaway electron beams during a massive gas injection (MGI) triggered or mitigated disruption. Generation of the post-disruptive beams has been systematically studied on many large and medium size tokamaks [20–23, 25, 26, 29, 30], while the most thorough analysis of the interplay between the magnetic perturbation level and RE beam current was performed at TEXTOR [2, 28]. The scenario was also developed and studied on COMPASS [9]. A typical COMPASS post-disruption RE beam is generated in a MGI-triggered (argon) disruption in the current ramp-up phase of circular limited discharges at 12–25 ms after the plasma breakdown. Argon pressure in the range 0.8–2.8 bar was used, with the number of injected particles being in the order of 10^{19} – 10^{20} [9]. The radial stability of the plasma during the disruption and of the subsequent beam,

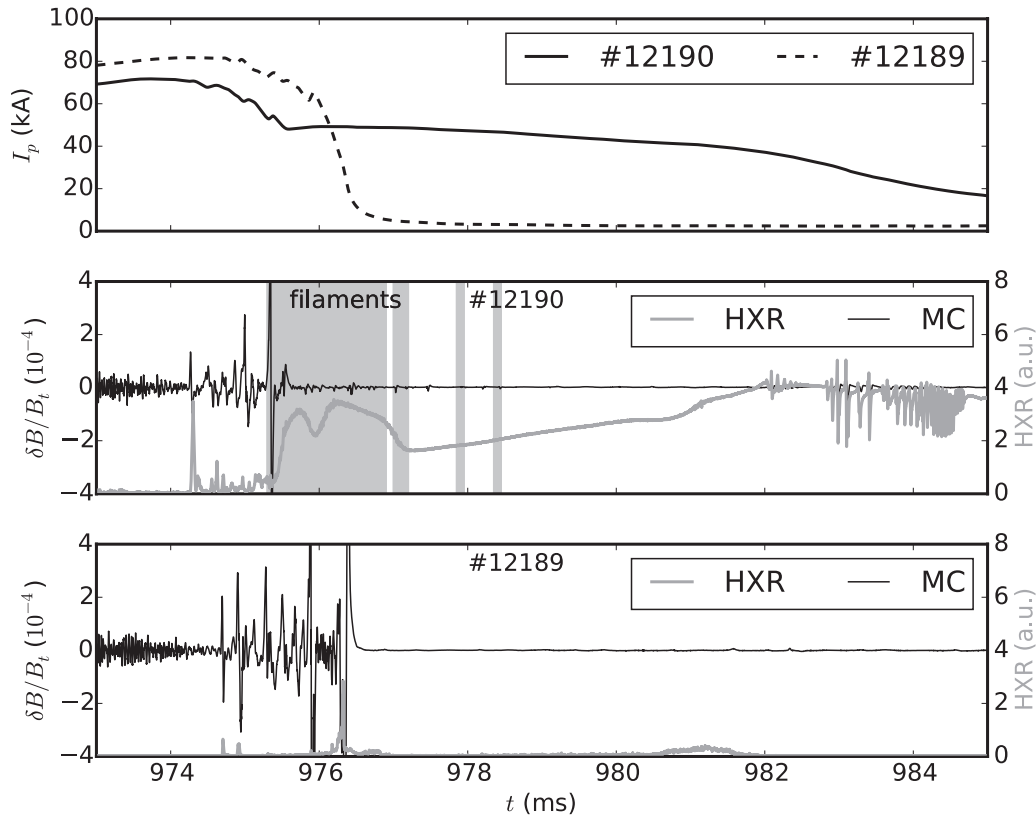


Figure 11. Detail of the current quench and early RE plateau phase of the discharges #12189 (no beam) and #12190 (beam produced), comparison of magnetic fluctuation level measured by HFS Mirnov coil and HXR signal, the scale of signals is the same in both subplots. Grey areas represent the frames where the filaments were detected.

as well as sufficient control of the initial density, present the main challenges in these experiments on COMPASS—and for the statistical analysis. The COMPASS post-disruption RE beams were obtained in $B_t = 1.15$ T, thus it seems that there is a different threshold for the beam generation than the one found on TEXTOR ([2], $B_t \geq 2$ T required for RE beam generation). The large current spike typically occurring during the disruption is replaced by multiple smaller events in the case of MGI disruption on COMPASS—see the evolution of I_p in figure 11. These events are always accompanied by a negative loop voltage peak, bursts of magnetic perturbations and usually also by HXR spikes. This character of the CQ phase is common to both disruptions with and those without RE beam generation. In figure 11 a comparison of the two cases is displayed: multiple MHD bursts (strongest at the HFS—MC C13 signal is displayed in the graphs) often accompanied by HXR spikes occur in both cases; however, the perturbations are smaller in the case when an RE beam is generated (#12190). The magnetic fluctuations then almost disappear, and the HXR signal becomes rather continuous, while in the case of the other discharge (#12189) the fluctuations continue until the plasma current disappears. The dependence of the post-disruptive RE beam current on the level of magnetic perturbations was statistically analysed for COMPASS MGI disruptions. However, no clear threshold value—nor any trend—was found, as the discharges conducted in different campaigns are very hard to compare, partly due to the position instability and different distance from the Mirnov coils. On

the other hand, the level of magnetic perturbation displayed in figure 11 is close to the theoretically predicted threshold value where perturbations should prevent RE beam generation ($\delta B/B_t > 10^{-3}$, [24]), and the two subsequent discharges displayed in figure 11 follow the expected trend.

Disruption evolution was also recently monitored by a fast visible radiation camera (8 kfps). During the studied disruptions, the camera specifically detects the line radiation of argon. In figure 12, four selected frames are displayed: in the top left frame Ar radiates at the plasma edge close to the MGI valve just after the injection; the top right frame shows thick helical structures in the current quench when argon is already toroidally distributed. In the bottom left frame the thin filamentary structures appear within the phase where I_p stops decreasing and minor bursts of magnetic perturbation still occur. The last, bottom right frame displays the late post-disruptive RE beam phase that seems to be very homogeneous.

The filaments in the early beam phase are accompanied by increased HXR signal (see the marked time range in figure 11) that seems to be almost continuous and tends to decrease after the main filamentary phase. Later in the beam phase, isolated filaments may be still observed, but the Mirnov coil data are generally quiescent. The frames with the filaments can be linked to the small bursts of magnetic turbulence; however, the camera might miss some of the filaments and measurements using higher frame rate are necessary in order to confirm the correlation. The post-disruptive RE beam typically terminates at the LFS as the control system fails to prevent radial

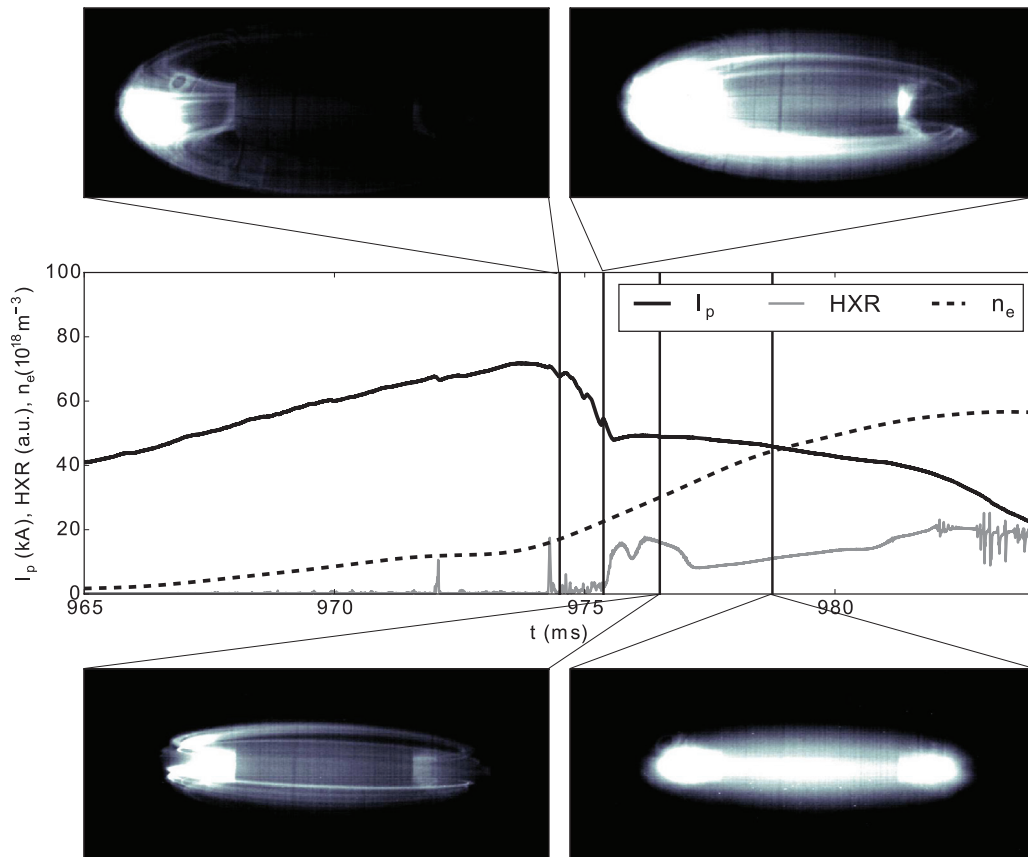


Figure 12. Time evolution of plasma current I_p , electron density n_e and HXR signal during an Ar-induced disruption at the COMPASS tokamak with four frames from the fast camera capturing plasma at the indicated time stamps.

expansion. Furthermore, in the particular discharge #12190 the faster dissipation of the beam current is accompanied by large periodic HXR spikes (see figure 12 from $t = 982$ ms) and small magnetic perturbation bursts. Relatively large measured radial position of the beam at this phase indicates that this event occurs due to the interaction of the beam with the protection limiter. Both the filamentary phase and the beam dissipation are definitely worth further study.

5. Conclusions

RE losses have been studied on COMPASS, in both quiescent low density discharges and Ar-induced disruptions with RE beam generation. These experiments benefit from the experience with the influence of initial fuelling on the RE generation in the current ramp-up phase of the discharge. The effect of the magnetic field perturbations on the RE losses in the COMPASS tokamak was studied using a rich set of magnetic diagnostics and HXR scintillation detectors. It was found that REs are extremely sensitive to any magnetic field perturbation, as the RE losses are modulated in a wide range of frequencies (hundreds of Hz to tens of kHz). In the flat-top of the low density discharges the effect of periodic RE losses to the OMP limiter caused by magnetic island rotation was observed and from the identified phase order it was concluded that maximum of the losses occurs when the O point of the island passes the limiter. The amplitudes of losses were found

to be considerably lower in some discharges with magnetic islands—REs seem to be confined by them. Furthermore, it was observed that the power source oscillations cause periodic HXR intensity peaks with a frequency dependent also on the edge safety factor. Unlike the simple effect that can be directly related to the oscillations of magnetic axis position caused by the power sources, the higher frequency of HXR peaks seems to result from an interaction between the power source oscillations and plasma MHD instabilities.

The link between the MHD perturbations and losses of RE was also observed during the MGI disruptions, specifically in those accompanied by RE beam generation. Beam generation has been achieved despite the low toroidal field in COMPASS. Observation of thin filaments in the early beam plateau phase, which corresponds to a final stage of the formation of the beam, is accompanied by increased HXR losses and rather small magnetic turbulence bursts. In agreement with previous studies, the disruptions with RE beam generation are generally characterised by a smaller level of high frequency magnetic fluctuations. However, no clear threshold magnetic perturbation magnitude has been found in this respect. The MHD dynamics of the post-disruption beam itself merits further investigation on COMPASS, with results contributing, among others, to benchmarking of the advanced RE models. Importantly, the influence of transient MHD phenomena on the RE losses has to be taken into account in order to quantify the RE related risks, and to verify the mitigation schemes for ITER.




























Acknowledgments

This work has been supported by MEYS projects LG14002 and LM2015045 and carried out within the framework of the EUROfusion Consortium. It has also received funding from the Euratom research and training programme 2014–2018 under grant agreement No 633053 with the Co-fund by MEYS project number 8D15001. The views and opinions expressed herein do not necessarily reflect those of the European Commission.

References

- [1] Hender T.C. 2007 *Nucl. Fusion* **47** S128–202
- [2] Zeng L. et al 2013 *Phys. Rev. Lett.* **110** 235003
- [3] Sommariva C. et al 2016 Modeling runaway electron dynamics in realistic fields from 3D non-linear MHD disruption simulations *43rd EPS Conf. on Plasma Physics (Leuven, Belgium, 4–8 July 2016)* P2.006 (<http://ocs.ciemat.es/EPS2016ABS/pdf/P2.006.pdf>)
- [4] Czarny O. and Huysmans G. 2008 *J. Comput. Phys.* **227** 7423–45
- [5] Panek R. et al 2016 *Plasma Phys. Control. Fusion* **58** 014015
- [6] Panek R. et al 2016 *Czech. J. Phys.* **56** B125–37
- [7] Mlynar J. et al 2015 Effects of plasma control on runaway electrons in the COMPASS Tokamak *42nd EPS Conf. on Plasma Physics (Lisbon, Portugal, 22–26 June 2015)* P4.102 (<http://ocs.ciemat.es/EPS2015PAP/pdf/P4.102.pdf>)
- [8] Ficker O. et al 2016 *58th Ann. Meeting APS DPP (San Jose, USA)* G10.101
- [9] Vlaine M. et al 2015 *J. Plasma Phys.* **81** 475810506
- [10] Weinzettl V. et al 2011 *Fusion Eng. Des.* **86** 1227–31
- [11] Imrisek M. et al 2014 *Ref. Sci. Instrum.* **83** 11E433
- [12] Klimanov I. et al 2011 *Plasma Phys. Control. Fusion* **49** L1–6
- [13] Weinzettl V. et al 2013 Experimental evidence of neoclassical tearing modes on COMPASS tokamak *40th EPS Conf. on Plasma Physics (Espoo, Finland, 1–5 July 2013)* P5.143 (<http://ocs.ciemat.es/EPS2013PAP/pdf/P5.143.pdf>)
- [14] Rabinski M. et al 2011 *Vopr. At. Nauki Tekh.* **41** 164–6
- [15] Causa F. et al 2015 *42nd EPS Conf. on Plasma Physics (Lisbon, Portugal)* O4.134
- [16] Havlicek J. et al 2013 *Annual Conf. of Doctoral Students WDS (Prague, Czech Republic, 4–7 June 2013)* (www.mff.cuni.cz/veda/konference/wds/proc/proc-contents.php?year=2013)
- [17] Vondracek P. et al 2016 *Fusion Eng. Des.* submitted
- [18] Granetz R.S. et al 2014 *Phys. Plasmas* **21** 072506
- [19] Moyer R.A. et al 2014 Impact of core modes, islands, and instabilities on runaway electron confinement *Proc. 25th IAEA FEC (St. Petersburg, Russia, 13–18 October 2014)* (General Atomics Report GA-A27773) (www-pub.iaea.org/MTCD/Meetings/PDFplus/2014/cn221/cn221ProvisionalProgramme.pdf)
- [20] Reux C. et al 2015 *Nucl. Fusion* **55** 093013
- [21] Plyusnin V. et al 2017 *Nucl. Fusion* submitted
- [22] Martin P. et al 2016 Physics, control and mitigation of disruptions and runaway electrons in the EUROfusion medium size tokamaks science programme *Preprint: 2016 IAEA Fusion Energy Conf. (Kyoto, Japan, 17–22 October 2016)* EX/P6-23 (www.euro-fusionscipub.org/wp-content/uploads/WPJET1CP16_15187_submitted.pdf)
- [23] Papp G. et al 2016 Runaway electron generation and mitigation on the European medium sized tokamaks ASDEX Upgrade and TCV *Preprint: 2016 IAEA Fusion Energy Conf. (Kyoto, Japan, 17–22 October 2016)* EX/9-4 (www.euro-fusionscipub.org/wp-content/uploads/WPMST1CP16_15157_submitted.pdf)
- [24] Helander P. et al 2000 *Phys. Plasmas* **7** 4106–11
- [25] Esposito B. et al 2016 First experimental results of runaway beam control in TCV *Preprint: 2016 IAEA Fusion Energy Conf. (Kyoto, Japan, 17–22 October 2016)* EX/P8-27 (www.euro-fusionscipub.org/wp-content/uploads/WPMST1CP16_15196_submitted.pdf)
- [26] Carnevale D. et al 2016 Analysis of runaway beam suppression experiments in FTU *Preprint: 2016 IAEA Fusion Energy Conf. (Kyoto, Japan, 17–22 October 2016)* EX/P8-22 (www.euro-fusionscipub.org/wp-content/uploads/WPMST2CP16_15186_submitted.pdf)
- [27] Plyusnin V.V. et al 2008 *Rev. Sci. Instrum.* **79** 10F505
- [28] Abdullaev S.S. et al 2015 *J. Plasma Phys.* **81** 475810501
- [29] Hollmann E.M. et al 2013 *Nucl. Fusion* **53** 083004
- [30] Coda S. et al 2016 *Nucl. Fusion* submitted

Runaway electron beam stability and decay in COMPASS

O. Ficker^{1,2}, E. Macusova¹, J. Mlynar¹, D. Bren², A. Casolari¹, J. Cerovsky^{1,2}, M. Farnik^{1,2}, O. Grover^{1,2}, J. Havlicek¹, A. Havranek¹, M. Hron¹, M. Imrisek^{1,3}, M. Jerab¹, J. Krbec^{1,2}, P. Kulhanek¹, V. Linhart², M. Marcisovsky², T. Markovic^{1,3}, D. Naydenkova¹, R. Panek¹, M. Sos^{1,2}, P. Svihra², V. Svoboda¹, M. Tomes^{1,3}, J. Urban¹, J. Varju¹, M. Vlainic⁴, P. Vondracek^{1,3}, V. Vrba², V. Weinzettl¹, D. Carnevale⁵, J. Decker⁶, M. Gobbin⁷, M. Gospodarczyk⁵, G. Papp⁸, Y. Peysson⁹, V.V. Plyusnin¹⁰, M. Rabiniski¹¹, C. Reux⁹, COMPASS Team¹ and the EUROfusion MST1 Team^a

¹ Institute of Plasma Physics of the CAS, CZ-18200 Praha 8, Czech Republic

² FNSPE, Czech Technical University in Prague, CZ-11519 Praha 1, Czech Republic

³ FMP, Charles University, Ke Karlovu 3, CZ-12116 Praha 2, Czech Republic

⁴ Institute of Physics, University of Belgrade, 11080 Belgrade, Serbia

⁵ Universita' di Roma Tor Vergata, 00133 Roma, Italy

⁶ Swiss Plasma Centre, EPFL, CH-1015 Lausanne, Switzerland

⁷ Consorzio RFX, Corso Stati Uniti 4, 35127 Padova, Italy

⁸ Max Planck Institute for Plasma Physics, Garching D-85748, Germany

⁹ CEA, IRFM, F-13108 Saint-Paul-lez-Durance, France

¹⁰ Instituto de Plasmas e Fusão Nuclear, IST, Lisbon, Portugal

¹¹ National Centre for Nuclear Research (NCBJ), Otwock-Swierk, Poland

E-mail: ficker@ipp.cas.cz

Received 8 February 2019, revised 29 April 2019

Accepted for publication 10 May 2019

Published 2 August 2019



Abstract

This paper presents two scenarios used for generation of a runaway electron (RE) beam in the COMPASS tokamak with a focus on the decay phase and control of the beam. The first scenario consists of massive gas injection of argon into the current ramp-up phase, leading to a disruption accompanied by runaway plateau generation. In the second scenario, injection of a smaller amount of gas is used in order to isolate the RE beam from high-temperature plasma. The performances of current control and radial and vertical position feedback control in the second scenario were experimentally studied and analysed. The role of RE energy in the radial position stability of the RE beam seems to be crucial. A comparison of the decay phase of the RE beam in various amounts of Ar or Ne was studied using absolute extreme ultraviolet (AXUV) tomography and hard x-ray (HXR) intensity measurement. Argon clearly leads to higher HXR fluxes for the same current decay rate than neon, while radiated power based on AXUV measurements is larger for Ne in the same set of discharges.

Keywords: tokamaks, disruptions, runaway electrons, tomography

(Some figures may appear in colour only in the online journal)

^a See the author list in Meyer *et al* [39].

1. Introduction

Runaway electrons (REs) have been extensively studied at COMPASS within the framework of the EUROfusion work package MST1 (medium sized tokamaks) because they still present an issue with respect to the safe operation of ITER [1]. ITER can hardly succeed without securing mitigated disruptions with no RE being generated and/or without developing a fully reliable technique for runaway beam mitigation. It seems that the typical timescales for disruptions in ITER will be crucial for the beam generation [2] and that the position stability in the post-disruptive phase remains the critical issue [3]. Enough time to mitigate the RE beam can only be secured in the case when the beam position is stabilised, which may be extremely difficult. Alternatively, the speed of the position instability must be known to optimise the mitigation method. In ITER, it is expected that the shaping field may cause vertical instability of the beam just after the disruption, while correct stabilizing of the vertical field can be hard to optimise early enough to also secure stability of the radial position. However, stability of the beam can be achieved on currently operated machines, and various mitigation techniques, including injection of large amounts of noble gases or shattered pellets [4], can be studied under controlled conditions. In fact, if the position control is reliable enough, the amount of gas already present in the chamber from mitigation of the disruption may be sufficient to slowly mitigate the beam. Detailed understanding of the behaviour of beam position stability under different conditions provide useful information for ITER. Control and mitigation of the RE beam is one of the key topics in European fusion research, see [5, 6] and also [7].

1.1. COMPASS and RE experiments

The COMPASS tokamak is one of the European compact, highly flexible facilities that has been operated at IPP Prague since 2008. The vacuum chamber is D-shaped with an open divertor. The major radius is $R_0 = 0.56$ m and the minor radius is $a = 0.21$ m. The toroidal magnetic field B_t ranges from 0.8 to 1.6 T while a plasma current I_p of up to 350 kA can be driven in the tokamak. The machine is equipped with two 40 keV neutral beam injectors with heating power up to 350 kW and capable of routine H-mode operation [8, 9]. The RE research on COMPASS gains from flexibility of the machine, increasing experience in RE experiments at EUROfusion MST1 machines and cooperation with groups working on relevant development of diagnostics and models.

During the COMPASS RE experiments, the RE generation in quiescent scenarios and losses related to various magneto-hydrodynamics (MHD) phenomena and external field errors were studied as well as disruptions triggered by massive gas injection (MGI) in the ramp-up scenario [10, 11]. In the flat-top discharges without gas injection the losses of RE are modified to a large extent by sawtooth instability, magnetic island rotation and oscillations in the poloidal field power supply (introduced by flywheel rotation and a set of 12-pulse

converters) [12]. The reaction of REs to the perturbed magnetic fields was recognized as an important topic. Thanks to the rich variety of possible resonant magnetic perturbation (RMP) coil configurations at COMPASS, it is possible to run very detailed scans of the RMP effect on the RE beam. So far, $n = 1$ and $n = 2$ low-field side (LFS) off-midplane coil configurations were tested with promising results [13, 14] and good agreement with the results achieved at ASDEX-U [15]. Despite the fact that ITER edge-localised mode control coils are probably unable to affect the RE orbits in the confined RE beam because they are too far from the plasma, the COMPASS experiments can contribute to the understanding of the beam behaviour in the perturbed fields and to the validation of theoretical predictions and models of RE transport in perturbed fields. The most urgent task of RE research is to find an effective method for RE beam mitigation that can be reliably extrapolated to ITER. Termination of the unmitigated RE beam may occur on timescales an order of magnitude shorter than a typical plasma disruption. At COMPASS, terminations of extremely low-density plasmas in the slide-away regime due to radial position instability were recorded on microsecond timescales [13]. These sudden terminations also caused very localised hotspots. On the other hand, after injection of even a minor amount of high-Z impurity gas the current decay has been rather moderate and no severe hotspots were observed.

1.2. Diagnostics and gas injection valves

COMPASS is equipped with a rich set of magnetic diagnostics [16], which contributes not only to equilibrium reconstruction and control of the discharge parameters but also to the study of the magnetic fluctuations related to various instabilities. The line-averaged density is determined and controlled using a 2 mm microwave interferometer; the density and temperature profiles are measured using a Thomson scattering (TS) system [17]. The detection of REs is carried out using multiple methods: low-energy (about 100 keV) REs confined in the vessel volume are detected using a vertical electron cyclotron emission (ECE) system [18] and lost REs can be detected by the Cherenkov detector [19, 20], but mainly using several hard x-ray (HXR) detectors that measure the secondary radiation (unshielded and shielded with HXR energy thresholds roughly $E > 50$ keV and $E > 500$ keV). Photoneutrons may be also detected by multiple neutron detectors, but the contribution of photoneutrons is mixed with HXRs in the case of large fluxes that affect even the shielded detectors. A wide-angle view and detailed observations of the RE beam in the visible range are provided by the fast cameras Photron MINI UX-100 [21] and Photron SA-X2, respectively. Spectral data in the visible, near-IR and near-UV regions are acquired using various minispectrometers. To some degree, soft x-ray (SXR) cameras and absolute extreme ultraviolet (AXUV) cameras may also contribute to the analysis of RE experiments, despite the fact that they can be affected by HXR radiation from the walls, see section 1.3. The gas injection experiments use two very different valves: (i) the ex-vessel piezoelectric valve injecting

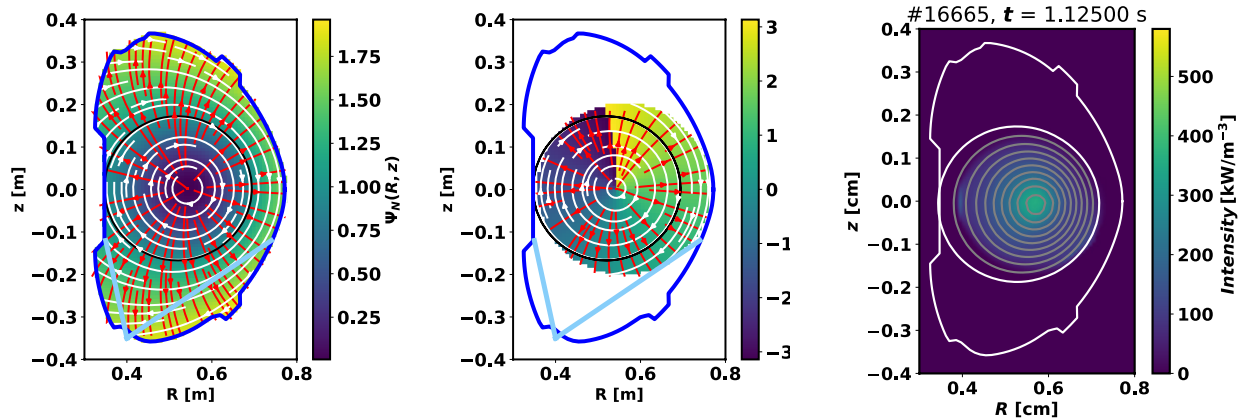


Figure 1. Tomographic procedure for a reduced set of lines of sight. Left: COMPASS vessel with the field of view of AXUV camera F (light blue lines) marked over the $\Psi(R, z)$ map; center: modified reconstruction domain with preferential smoothing direction parameter—the ratio of $\nabla\Psi$ components with respect to the flux contours; right: typical radiation pattern of an evolved RE beam from the flat-top Ar gas puff scan described further in the text.

a smaller amount of gas from the divertor region on the high-field side (HFS) (also used for seeding experiments) can inject gas atoms at a rate of roughly $2 \times 10^{20} \text{ s}^{-1}$ when used with Ar and pressures around 1 bar. With a standard opening time of 20 ms, this gives $4\text{--}5 \times 10^{18}$ injected gas particles according to the calibration; (ii) the ex-vessel MGI solenoid valves at three different toroidal positions at the outer mid-plane can inject at rates of roughly $1 \times 10^{22} \text{ s}^{-1}$ when used with Ar and at a pressure of 2 bar, while pressures up to 5 bar can be used. As typical opening times of the valve are close to 10 ms, the number of injected gas particles is up to 1×10^{20} .

1.3. Modified tomographic inversion

The hard x-ray radiation affecting the LFS angular cameras during runaway electron beam scenarios causes an unknown contribution to the SXR and AXUV signals, and a special modified procedure needs to be used for the tomographic reconstruction. The bottom HFS AXUV camera F (for field of view see figure 1) is the one least affected, providing peaked profiles of radiation even during high-energy and high-current RE beams. It provides radial resolution; however, use of a single camera in the unconstrained minimum Fisher regularisation (MFR) tomography (for application on COMPASS see [22]) would cause vertically spread artefacts. On the other hand, application of Abelian inversion is too dependent on the use of magnetic equilibrium data, which are not sufficiently correct for the RE beam. Therefore, MFR using smoothing given by a gradient map of the $\Psi(R, z)$ function [23] and a modified reconstruction domain (circular area on the mid-plane) was developed and used to obtain the radiation patterns and approximate (due to non-uniform AXUV spectral response) radiated power values. This treatment helps to avoid both the artefacts and the contribution from the limiter radiation. An example of the smoothing functions used and a typical axis-peaked radiation profile with a low-intensity halo during the RE beam phase are shown in figure 1.

2. Runaway electron beam scenarios

2.1. Ramp-up scenario

COMPASS is characterised by relatively low toroidal magnetic field, which should not be beneficial for the post-disruptive RE beam generation as was shown, e.g., in TEXTOR [24]. On the other hand, RE beams in the ramp-up phase following a classical disruption triggered by massive gas injection (fast thermal quench (TQ), often current spike, current quench (CQ) and beam plateau) were achieved irregularly; see an example discharge in figure 2, where $B_t = 1.15$ T. The scenario includes a carefully tuned fuelling waveform, injection at early times (low currents/high q_{95}), optimised position reference and argon MGI (see section 1.2 for a description of the valve) at a pressure of 1–3 bar and a short valve opening time. Despite the relatively low reproducibility, a systematic analysis yielded valuable results [10, 11]. Recently the crucial role of the toroidal magnetic field has been confirmed in a dedicated scan [13]. No RE beams were created in the very same scenario at fields lower than 1.1 T, although the beam was reliably produced at higher fields. Based on magnetic measurements and on AXUV inversion and camera data, it is concluded that discharges where Ar MGI does not lead to RE beam generation terminate on the HFS. In contrast, in discharges where a beam is generated following the current quench, the radiation pattern shrinks to the vicinity of the vessel axis during the TQ and CQ [25]. In this case, the low-energy channel of the Cherenkov detector ($E > 57$ keV) indicates the existence of a fast electron population already in the phase of current quench. These beams are often characterised by a very interesting first stage, where bright filaments in the camera images correlate with the short spikes in the ECE and Mirnov coil data and later also in the HXR and Cherenkov detector data [26]. Typically, the generated RE beams are radially unstable—the instability is more severe in the case of a smaller beam current, i.e. a larger drop of current during the current quench. Well confined beams increase their

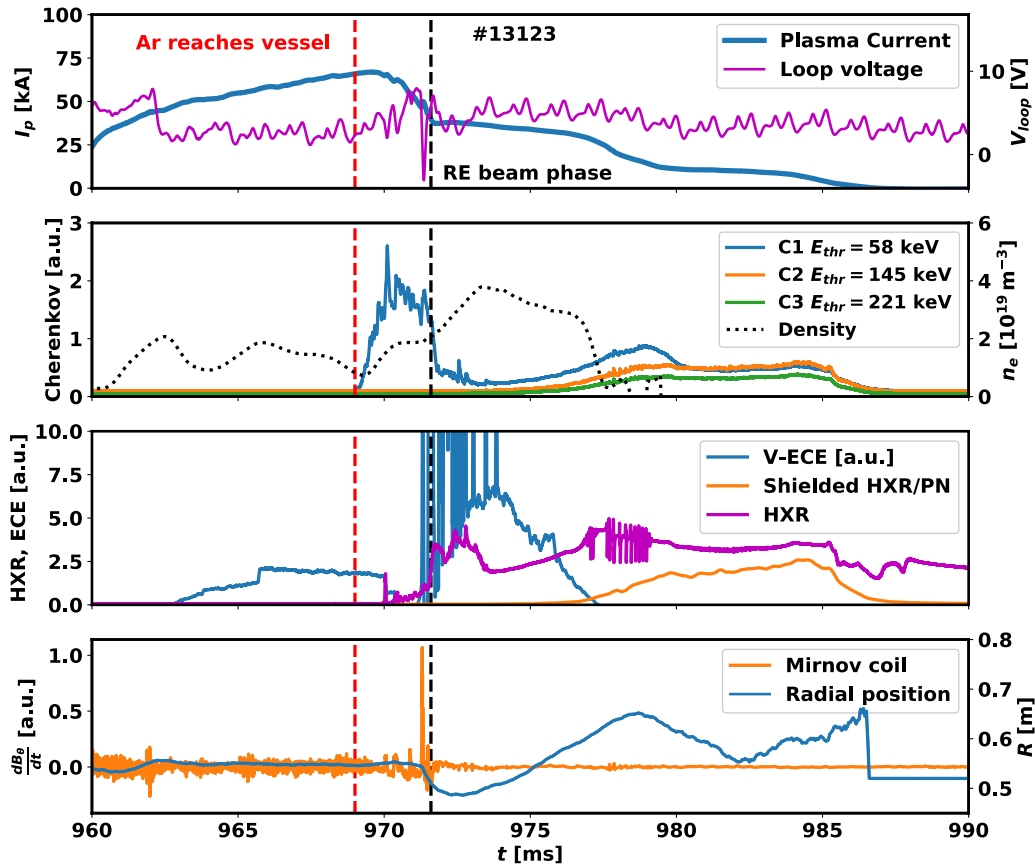


Figure 2. The ramp-up scenario for RE beam generation. Ramp-up of plasma current is interrupted by Ar MGI, which leads to a current quench and RE generation. The density (black dashed line) increases, and the early beam phase is accompanied by spikes in the ECE data and an increased level of HXR. Later the signals of higher-energy Cherenkov detector channels and the shielded HXR detector increase as well.

major radius and are lost to the LFS, or partially lost and then stabilised as in the case of the discharge in figure 2.

2.2. Flat-top scenario

Due to the low reproducibility of the ramp-up scenario, which would be problematic in RE beam decay experiments and scans, an alternative, more quiescent scenario was developed. In these discharges, the current flat-top is reached and the fuelling is turned off, which leads to a decay of the thermal plasma density and a rise of the RE current fraction in several tens of milliseconds. Ar or Ne injection is then introduced using a piezoelectric gas puff or MGI (see section 1.2). MGI causes a significantly faster decay of the RE current, see [13]. During a short delay (5 ms) after the injection, when the gas fills the poloidal cross section, the derivative of the current in the primary windings (which creates the external loop voltage) is set to zero; see figure 3 for a detailed overview. During this stage, additional puffs or RMPs [13, 14] may be applied to investigate the influence on the decay of the beam. The puff causes the quench of the thermal plasma, while the REs are preserved almost unaffected and fully overtake the remaining current. The TQ is very slow in the case of a piezoelectric gas puff, lasting roughly 5 ms (see the evolution of the profile T_e in figure 4), while it lasts less than 1 ms in the case of MGI. The

amount and duration of the gas injection play a crucial role. While this scenario works reliably with the piezoelectric valve injection (slow TQ) at almost any time during the low-density discharge, including the late phase of the ramp-up, the MGI typically causes an immediate current quench when injected too early, while RE beam generation and gradual beam decay are the result of a later injection; see figure 4. This indicates that the slower TQ allows a sufficient RE energy and/or current to be reached during the injection itself, while the fast MGI may only preserve the beam in the case when the RE population is already well evolved. All the results described further in this article are based on this scenario.

Advantages and possible applications of the flat-top scenario include:

- Reproducible conditions—suitable for scans (e.g. n_e , B , RMP effects, etc).
- Natural or controlled current decay of the RE beam.
- Average RE energy can be modified by timing or prescribed U_{loop} waveforms.
- Optimisation of position control algorithms.
- Validation of models or elements of models that include the RE interaction with impurities (e.g. CODE [27, 28]).
- Investigation of the RE transport in perturbed fields.
- Exploitation of diagnostic methods under well controlled conditions.

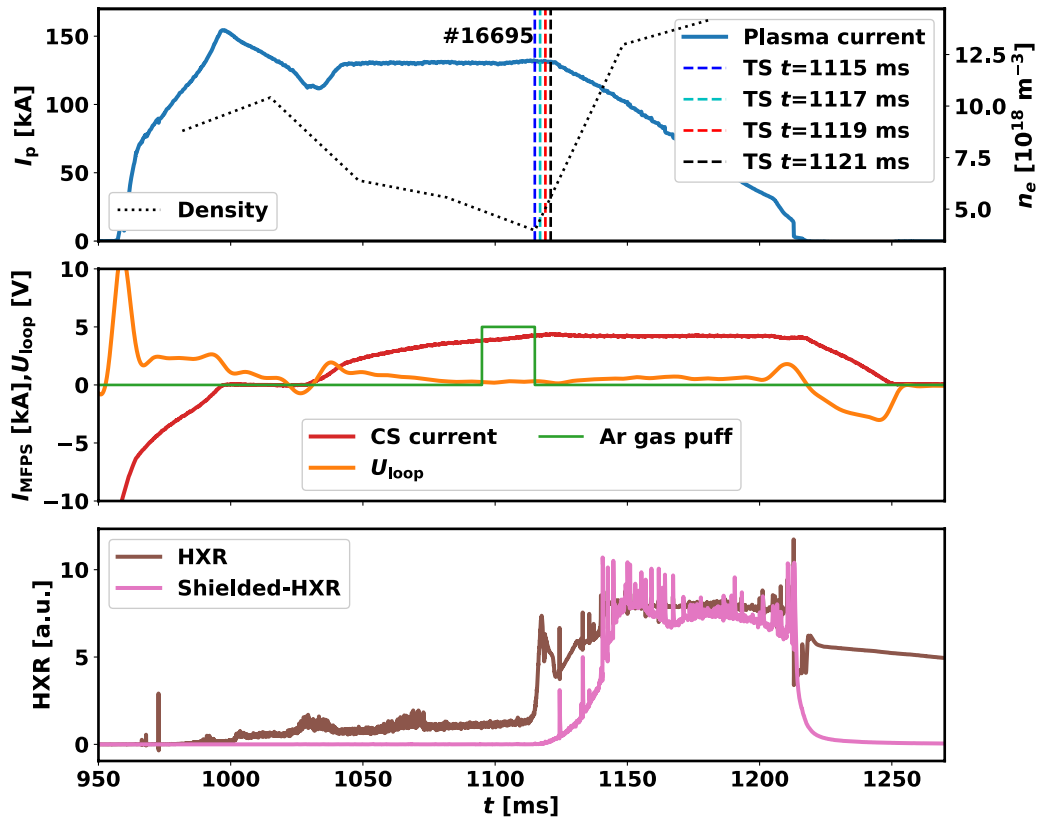


Figure 3. The flat-top scenario with RE beam generation. Top: time evolution of plasma current (blue) and electron density measured by TS (black dotted line); center: loop voltage U_{loop} (orange), current in the primary windings (red) and Ar gas puff opening (green); bottom: HXR detector signals (brown: >50 keV, pink: >500 keV).

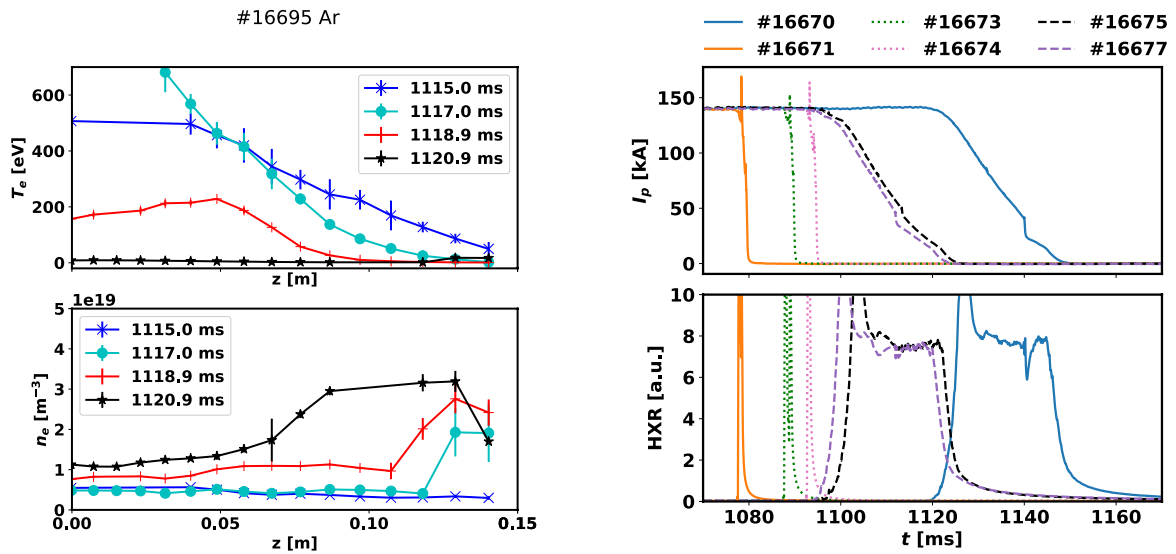


Figure 4. Left: profiles of temperature and density from the TS diagnostics measured at times indicated in figure 3. Right: the timing scan with MGI Ar injection shows that sufficient RE seed or sufficient RE energy is needed for creation and slow termination of an RE beam.

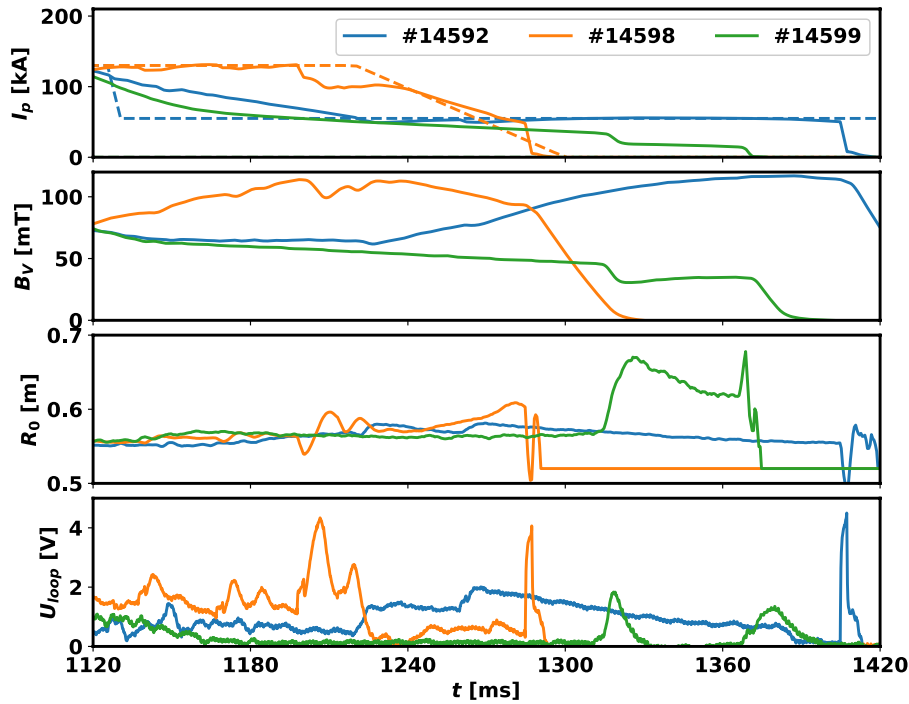


Figure 5. Different attempts to control the current of the runaway electron beam. First frame: measured current and feedback reference (dashed)—in the case of discharge #14599, zero loop voltage is requested; second frame: total external vertical field—approximate value at R_0 ; third frame: radial position of the plasma current centroid; bottom frame: loop voltage measured on the HFS. In the discharges #14599 and #14598, deuterium was injected during the RE beam phase (1120–1220 ms) [13], which led to a slower natural current decay.

- Measurements of RE–wall or RE–limiter interactions during forced terminations.
- Analysis of mutual interaction of REs with various instabilities.

3. Position stability of the runaway electron beam and analogies with a plasma-assisted modified betatron

3.1. Current control

The current of the RE beam on COMPASS can be partly controlled in the case of impurity injections using a low amount of Ar or Ne (piezoelectric valve injection). However, the simultaneous control of radial position and beam current proved to be difficult. When the external loop voltage is removed, the beam current decreases with an average rate related to the type and amount of injected gas(es) [23] and the beam slowly drifts to the low-field side. The application of a feedback control on the plasma current at values above 100 kA requires loop voltage up to 2–4 V and the radial position is driven unstable. However, the beam current was successfully sustained when the current set-point was decreased; see figure 5, discharge #14592, blue line. The current is typically related to the number of runaway electrons because the change in velocity is small for further accelerated relativistic electrons. Therefore, sustaining the RE beam current in the cold plasma background means compensating for the loss of particles by creating new REs. However, due to the high loop voltage, the energy of confined REs is further increased. This can be clearly seen in

figure 5, where the external vertical magnetic field B_v based on current flowing in the LFS poloidal coils [29] is indicated: although a constant beam current is maintained, the vertical field necessary to sustain the radial position increases up to very large values (over 100 mT). Moreover, the effect of an ongoing increase in kinetic energy of REs occurs also in the case of spontaneously decaying current, e.g. in discharge #16695 in figure 3, where zero external loop voltage was applied. The loop voltage induced by the current decay might not be sufficient for primary RE generation but it is sufficient for further acceleration of existing confined REs. Therefore, the position is unstable also during this type of discharge.

3.2. Radial stability of the relativistic electron beam and the role of RE energy

The runaway orbits in equilibrium magnetic field and even the contribution of the runaway current to the total equilibrium have been studied in many publications, including [30, 31]. In present devices, the policy on radial position feedback during the RE beam stage is often modified based on empirical results and adaptive control (see [6, 32]) because the physical model of this situation turns out to be rather complicated. The radial stability of the RE beam is incompatible with the standard feedback scheme applied on COMPASS and must be modified. The radial position on COMPASS is actuated by two different systems—equilibrium field power supply (EFPS) and fast vertical magnetic field power supply (FABV) [33]. The controller of the first one contains a term proportional to the plasma current (as a result of the Grad–Shafranov equilibrium, see equation (2)) and proportional–integral terms of the radial

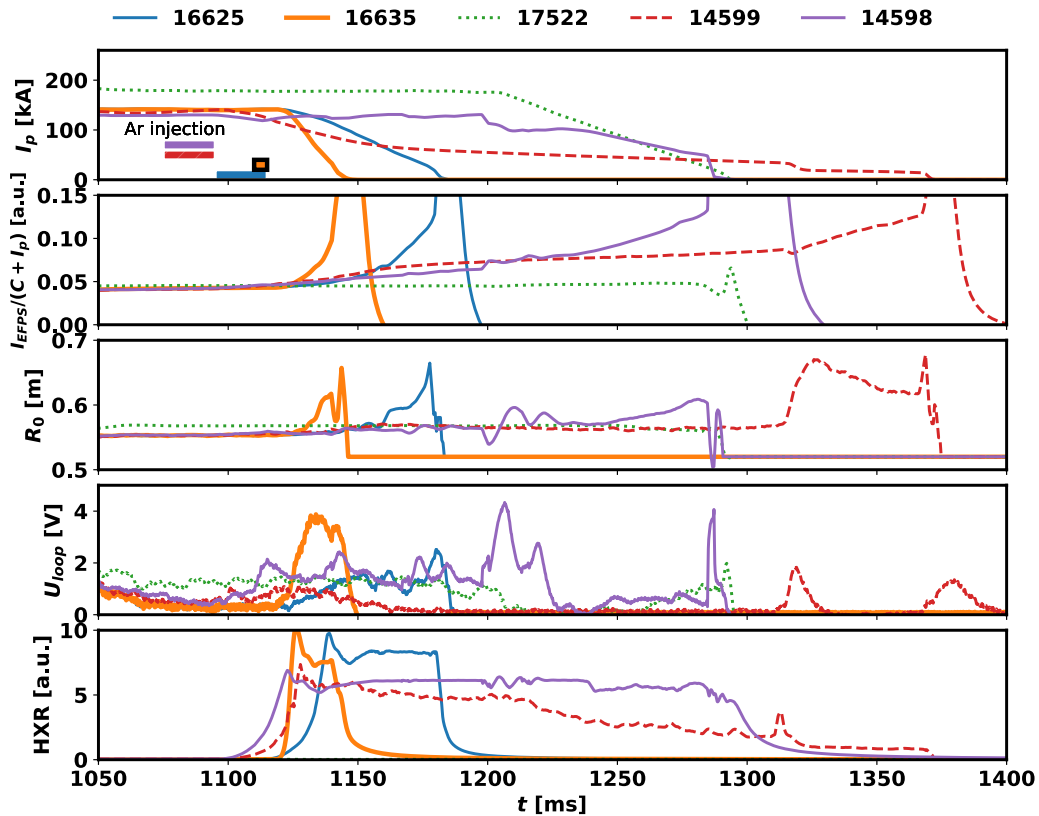


Figure 6. Comparison of radial control performance in the standard discharge (green) and various RE beam scenarios: Ar injection by MGI (#16635), piezo valve injection (#16625) or Ar injection followed by D injection (1120–1220 ms, #14598, #14599). The first frame shows the evolution of plasma current and color-coded rectangles marking the opening time of the gas injection valves; MGI is marked by a black outline. The second frame shows that the current requested from external poloidal field coils for radial position control is not a function of I_p only in case of the RE beam. The third frame displays the evolution of radial position, the fourth shows the loop voltage values and the last one the signal from the shielded HXR detector.

position error of the current centroid with respect to the reference. The FABV is dependent only on the position error and is also approximately five times weaker in maximum amplitude than EFPS. The system performs excellently in the case of a high-temperature plasma without RE; however, the performance is poor with an RE beam in the low-temperature plasma background, as can be seen in figure 6. In the figure, various scenarios are compared in terms of evolution of plasma current, normalised value of current in the EFPS windings ($I_{\text{EFPS}}/(7000 + I_p)$)—the constant is added so the function is stable when approaching zero), radial position and loop voltage that drives the current in plasma or accelerates the runaway electrons. It is obvious that while the value of the function in the second frame is constant in the case displayed using a green dotted line (standard discharge), this quantity is quickly increasing in the case of various RE scenarios: RE beams triggered by MGI (#16635—thick orange line) or piezoelectric valve Ar gas injection with plasma current feedback (#14598—violet line) or zero loop voltage applied (#16625—blue line, #14599—red dashed line + additional D injection added). The faster the current decay of the RE-dominated plasma or loop voltage, the higher the request for the vertical field normalised by the plasma current value due to a higher loop voltage induced during the current decay and a subsequent increase in RE energy. Notice that despite large values of current in the stabilising windings the beam still drifts to

the LFS. From this observation it is obvious that the dependence of radial feedback on plasma current is too strong. The standard tokamak request for a vertical field that results from the Grad–Shafranov equation can be expressed as [34]

$$2\pi R_0 I_p B_v = \frac{1}{2} I_p^2 \frac{\partial}{\partial R_0} (L_e + L_i) - 2\pi^2 \int dr r^2 \frac{p' - FF'}{R_0^2}, \quad (1)$$

where the first term on the right-hand side is related to external and internal parts of the ‘hoop force’ (force between the current elements within the plasma ring), the second term (with p') to the ‘tire tube force’, i.e. expansion due to the kinetic pressure gradient, and the FF' term changes the direction with the value of β_p . The terms—except the FF' contribution—are always outward and typically depend on plasma current squared (the pressure term via the β_N value). This means that vertical magnetic field should also be dependent on I_p . If we consider the case of the runaway electron beam, the hoop force terms should still be valid but the current density profile and therefore the internal inductance of the beam might be very different compared to thermal plasma. However, the gradient of classical thermal pressure is practically negligible for a low-temperature plasma background that may even have a large neutral fraction. Therefore, the dependence of vertical field on current in the beam ring should be weaker in the case of REs. Note that the size of the beam in terms of minor radius may also affect the feedback efficiency.

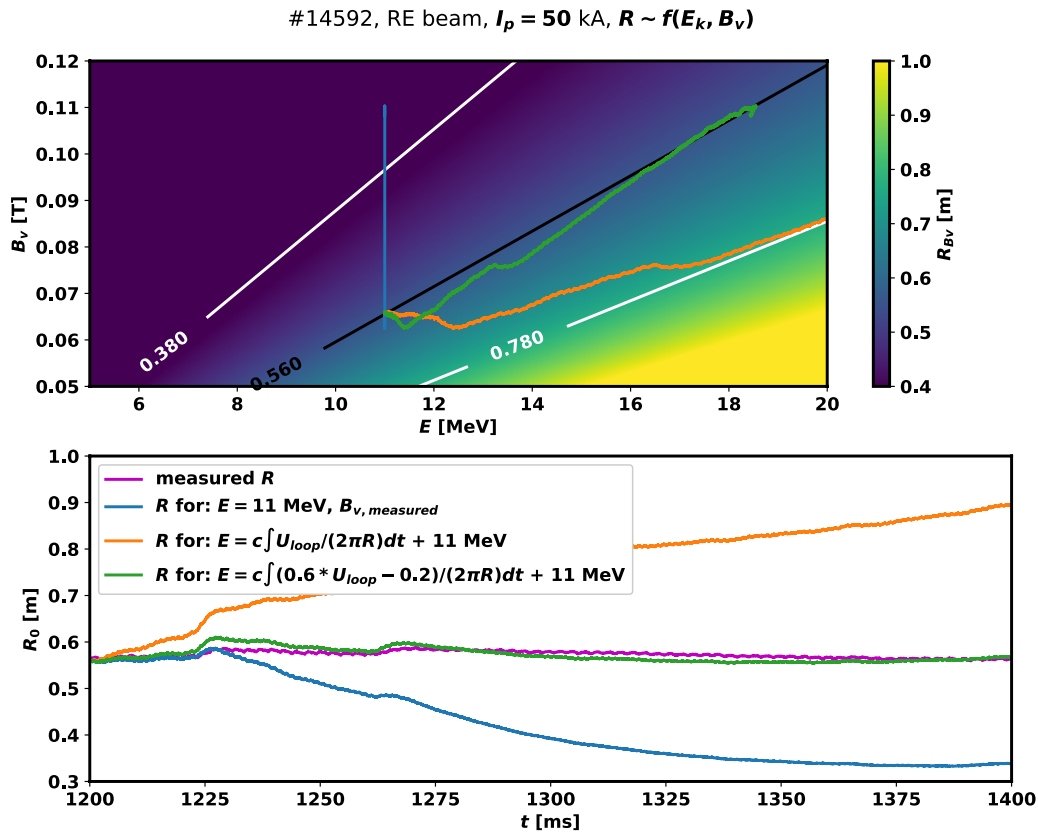


Figure 7. Top: 2D plane with ultra-relativistic electron Larmor radius as a function of energy and vertical field with curves of calculated R_{B_v} for the signals of discharge #14592. Bottom: comparison of measured radial position signal and hypothetical position corresponding to B_v evolution and energies obtained using different functions of electric field as marked in the legend.

3.3. Radial stabilisation of the RE beam

A comparison of RE beams in a tokamak with those in high-current betatrons—specifically the modified ones (including the toroidal stabilising field) [35]—turns out to be appropriate. The average energy of a beam of electrons plays a crucial role in determining the B_v value necessary to keep the beam particles on radially stable orbits. If the Larmor radius in a vertical magnetic field is considered (which applies in the case of a low beam current), the vertical field should be proportional to the change in flux or the average kinetic energy $\langle E_k \rangle$ of the accelerated electrons as in the classical betatron. The value of the vertical field necessary to confine a high-current RE beam in the tokamak should be proportional to the sum of this contribution and the hoop force compensation:

$$B_v \sim \frac{1}{4\pi R_0} I_p \frac{\partial}{\partial R_0} (L_e + L_i) + \frac{\langle E_k \rangle}{ecR_0}, \quad (2)$$

in the ultra-relativistic case. Based on the theory for plasma-assisted modified betatrons, the beam in the plasma background should always be paramagnetic, unlike in the vacuum variant of the modified betatron, where a diamagnetic to paramagnetic transition occurs during the acceleration of a high-current beam according to conditions indicated in [35]. The paramagnetism is responsible for an additional confining force. In order to achieve a suitable feedback policy it is often sufficient to simply decrease the relative contribution of the part proportional to I_p with respect to the contribution of term

due to radial position error in the controller. Most tokamaks are close to the situation where the B_v term—based primarily on I_p —is close to optimum for the given major radius and energies of REs in the range of tens of MeV. On COMPASS, as a small device, the beam is typically drifting to the LFS in the quiescent stage, while overestimated vertical field may push the RE beam to the HFS or cause position oscillations in the case of loss of some part of the current—see discharge #14598 in figure 6. Standard feedback with decreased I_p dependence may perform sufficiently well, but equation (2) or a more complex model taking the average runaway electron energy into account should increase the efficiency of the feedback. On the other hand, the feedback algorithm disturbed in a controlled way may be a source of information on the average energy of REs in the beam or even on the range of the energies. To investigate whether information on the change in flux (electric field integral) is useful for estimating the optimal vertical field for radial position feedback, the discharge #14592 can be further analysed. Let us assume that at the beginning of the 50 kA RE beam plateau (240 ms after the breakdown), the total requested vertical field is balancing well both the ‘hoop force’ and the relativistic pressure arising from the change in energy. If only the second part of equation (2) were taken into account (low-current betatron approximation), the energy corresponding to the applied vertical field would be roughly 10–11 MeV at the beginning of the constant-current phase. This is in a reasonable agreement

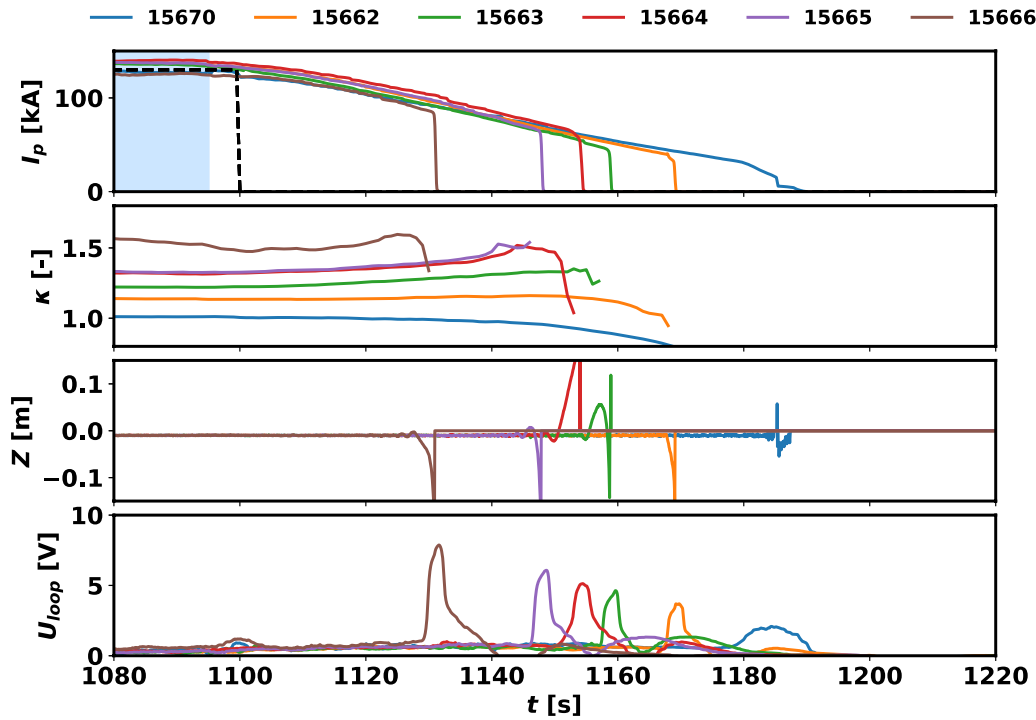


Figure 8. Elongation scan with piezoelectric gas puff Ar injection (1075–1095 ms). First frame: evolution of RE beam current in the regime of zero external loop voltage (common reference—black dashed line, elongation increased with the discharge number); second frame: elongation as calculated by EFIT; third frame: measured vertical position; last frame: measured U_{loop} .

with other methods of determination of the upper energy limit for REs originating from the breakdown in various COMPASS discharges:

- Non-collimated HXR spectrometry shows that the energy limit of HXR reliably measurable with the 2'' crystal (7 MeV) is reached after approximately 150 ms of acceleration of REs in the COMPASS standard discharge with a trace RE population. This measurement is unfortunately not available directly for the studied discharge due to extremely large HXR fluxes.
- Measurements of synchrotron radiation using a camera in the mid-IR range (15–25 μm) placed at a suitable tangential port show the start of an increase in the measured power due to synchrotron radiation roughly 190 ms after the breakdown. This measurement is also an approximation because it is measured in a low-density discharge without gas injection. Based on the synchrotron radiation model SYRUP [36] using the single-energy approximation, only electrons with energy higher than 8–10 MeV give a non-negligible contribution in the spectral sensitivity range of the camera and the COMPASS magnetic field ($B_t = 1\text{--}1.6$ T).
- Last but not least, the energy calculated using the vacuum acceleration approximation based on the loop voltage measured at the HFS reaches roughly 20 MeV at the point of the start of the RE beam plateau in discharge #14592. The vacuum approximation provides overestimated values in general.

From the start of the constant-current request phase, the beam current is stable, but the radial distribution of the current

density might be changing and there is definitely a change in energy. In figure 7, it can be seen that the increase in applied vertical field is proportional to the evolution of electric field through the relation marked in the legend of the graph; however, a decreased value of the field derived from loop voltage measurement must be used in order to get a complete fit. This may result from the drag force due to impurities, imprecision of electric field measurement (loop external to the vessel) or other effects such as a change in the RE density profile and the RE energy distribution along the minor radius.

3.4. MHD equilibrium approximation for the RE beam

The description mentioned above as a first approach is based on rather simplistic assumptions. A more suitable approach to the RE beam feedback is to use relativistic pressure. This was applied in the calculation of RE current fraction in thermal plasma in [37] and more recently in [38]. In this case, it is suitable to use the relativistic pressure formula given by the equation [37]

$$p_{RE} = \frac{1}{2}m_e\langle n_{RE}\rangle\langle\gamma v_{\parallel}^2\rangle + \frac{1}{4}m_e\langle n_{RE}\rangle\langle\gamma v_{\perp}^2\rangle, \quad (3)$$

where the RE density $\langle n_{RE}\rangle$ is averaged over beam volume and the velocity squared times Lorentz factor $\langle\gamma v_{\bullet}^2\rangle$ over both spatial and velocity distributions. Assuming that the relativistic pressure gradient is given primarily by the density gradient—rather than by the change in the average energy with the radius—the gradient of the RE pressure can be approximated by

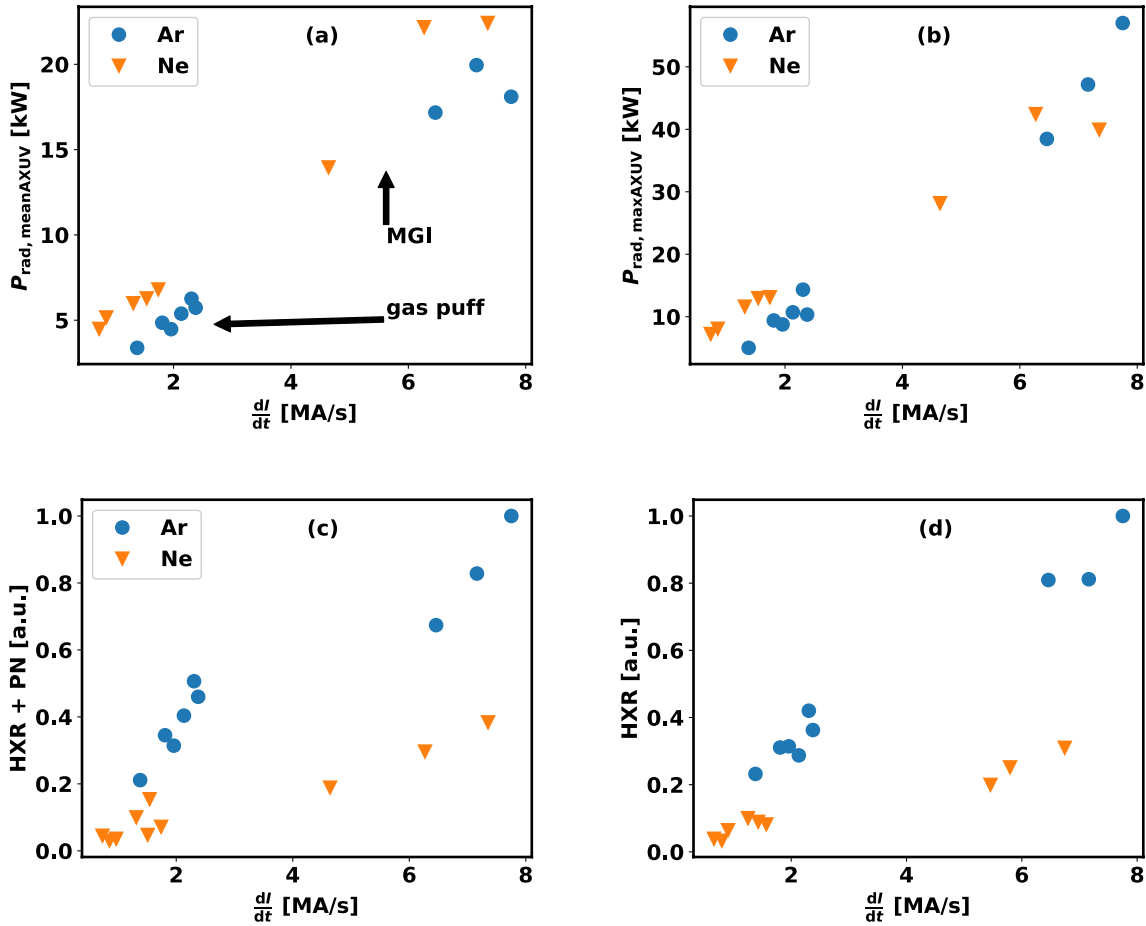


Figure 9. Scans of gas amount for Ar and Ne, quantities plotted with respect to the average current decay rate of the RE beam: (a) the average radiated power during the beam decay calculated using AXUV tomography; (b) maximum AXUV radiated power during the beam decay; (c) number of counts of the ^3He neutron detector (HXRs and photoneturons) normalised to duration of beam decay; (d) average HXR as measured by a blind photomultiplier during the beam decay.

$$\begin{aligned} \nabla p_{\text{RE}} &= m_e \nabla n_{\text{RE}}(r) \left(\frac{1}{2} \langle \gamma v_{\parallel}^2 \rangle + \frac{1}{4} \langle \gamma v_{\perp}^2 \rangle \right) \\ &\sim m_e \frac{\langle n_{\text{RE}} \rangle}{r_b} \left(\frac{1}{2} \langle \gamma v_{\parallel}^2 \rangle + \frac{1}{4} \langle \gamma v_{\perp}^2 \rangle \right), \end{aligned} \quad (4)$$

where r_b is the beam minor radius. However, the effect of the radial profile of the average energy needs to be included as well to fully reconstruct the possible equilibria. The relativistic pressure gradient can be used in the MHD equilibrium $\nabla p = \mathbf{j} \times \mathbf{B}$ and modified equilibrium can be found. This introduces an additional component of vertical field. The measured electric field integral or evolution of electric field as an output of a benchmarked disruption model seems to be a suitable input for a physics-based proportional controller of radial position in the case of a relativistic beam. Such an approach may further increase the performance of the well performing adaptive control algorithms currently run on medium sized devices. The relations will be tested on COMPASS during future RE experiments.

3.5. Vertical stability

To investigate the vertical stability of the RE beam created using the flat-top recipe with Ar, a scan in the amplitude of the elongating field was carried out. It seems that the generation of the RE beam by a mitigation of the thermal plasma component via gas injection is not significantly affected by plasma elongation. As expected, the beam is prone to a vertical instability during the decay of its current, and the instability occurs earlier for a higher elongating field—this is reported in figure 8. It seems that at the highest value of the elongation requested in the scan ($\kappa \sim 1.6$) it is more difficult for the control system to sustain the current during the injection, and slightly higher U_{loop} is requested. The vertical displacement events last several milliseconds and are characterised by large spikes in loop voltage.

4. Decay rate and energy loss channels

The beam energy (magnetic and kinetic) can be lost through several channels—direct particle loss, radiation due to decay

of excited atomic states of the background plasma species, induced currents in the vessel structures due to loss of the beam current, etc. Based on the scans of gas amount with Ar and Ne, it seems that the two gases behave very differently in terms of the beam energy loss channels—while the RE beam in Ne radiates with larger power in the AXUV spectral region, Ar causes a larger averaged signal of the ^3He neutron counter and photomultiplier-based detector measuring high HXR fluxes during the beam decay while other HXR detectors are already saturated; see figure 9. Note that the ^3He neutron counter can also be affected by the HXR if the fluxes are too large. The radiated power was calculated using the modified tomography algorithm presented in section 1.3. More Ne is injected and a higher pressure of the injected gas is measured if the same setup of valves is used for the given pressure—the gas is lighter and therefore moving faster both during the expansion into the vacuum and in the supply tubes. However, the current decay rate of the RE beam is comparable for both gases with the same gas injection setup (see figure 3 in [13], discharges with various amount of injected Ar or Ne particles) and therefore the effect of the gases on the two energy loss channels can be directly compared. Their relation may be a useful argument to prefer one gas over the other for different tasks. Argon seems to be a better choice to cause fast scattering of REs as a last layer of defence. On the other hand, if the RE beam position is stable and controlled, injecting large amounts of Ne can terminate the RE beam in a significantly more quiescent manner with a large fraction of the energy being radiated in the visible, UV and SXR spectral regions.

5. Conclusions

Experiments using two different scenarios with RE beam generation triggered by gas injection are under investigation at COMPASS: the ramp-up scenario and the flat-top scenario. The former includes typical disruption features such as current quench and is more relevant to larger machines in terms of RE generation. However, the reproducibility and control possibilities were not sufficient in this scenario on COMPASS. Therefore, a flat-top scenario with a high-current RE beam was developed using various amounts of Ar or Ne to isolate the beam from the thermal plasma component. The current of the RE beam generated in this way may be kept at the desired value in the Ar or Ne background plasma at the cost of a relatively high loop voltage. However, it is even more interesting to switch off the external drive and observe the self-consistent decay of the beam. The radial position feedback was not performing very well, possibly due to: (i) the absence of a thermal pressure gradient that would require a vertical magnetic field proportional to beam current and (ii) the role of RE energy missing in the request on the vertical magnetic field that would secure stable orbits. This hypothesis will be tested in the next campaigns. Regarding the vertical position, the elongated RE beam seems to be stable even at relatively high values of elongation, unless the current decreases below a certain threshold. During the RE beam decay, some of the total energy is lost in the interaction with the gas (excitation,

ionization and subsequent radiation) or directly through RE loss to the wall. Ar and Ne seem to behave oppositely: while Ar causes more high-energy HXR signal indicating larger RE losses, Ne causes stronger radiation in the AXUV spectral region. The work on this scenario will further continue with the feedback optimization, puffing of gas mixtures, analysis of instabilities and investigation of the influence of magnetic field perturbation in order to provide a large set of reliable results for medium sized and large machines, where safety constraints are more limiting than on COMPASS, and to validate the key elements of runaway electron models.

Acknowledgments

The work has been supported by the grant GA18-02482S of the Czech Science Foundation and also by the grant No. SGS19/180/OHK4/3T/14 of the Grant Agency of the Czech Technical University in Prague. The experiments were supported by project Nos. CZ.02.1.01/0.0/0.0/16_019/0000768 and LM2015045, co-funded from European structural and investment funds and carried out within the framework of the EUROfusion Consortium. The work has also received funding from the Euratom research and training programme 2014–2018 under grant agreement No. 633053 with the Co-fund by the MEYS project number 8D15001. The views and opinions expressed herein do not necessarily reflect those of the European Commission.















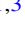






ORCID iDs

O. Ficker  <https://orcid.org/0000-0001-6418-9517>
 E. Macusova  <https://orcid.org/0000-0002-0381-9244>
 J. Mlynar  <https://orcid.org/0000-0003-4718-4321>
 A. Casolari  <https://orcid.org/0000-0002-5074-402X>
 M. Farnik  <https://orcid.org/0000-0002-7106-0719>
 O. Grover  <https://orcid.org/0000-0002-7695-8050>
 J. Havlicek  <https://orcid.org/0000-0002-7047-5007>
 M. Hron  <https://orcid.org/0000-0003-3987-8040>
 M. Imrisek  <https://orcid.org/0000-0003-0967-7758>
 J. Krbec  <https://orcid.org/0000-0002-3780-6257>
 P. Kulhanek  <https://orcid.org/0000-0003-1364-2486>
 M. Marcisovsky  <https://orcid.org/0000-0003-0860-7897>
 T. Markovic  <https://orcid.org/0000-0003-4607-3881>
 D. Naydenkova  <https://orcid.org/0000-0003-0307-2301>
 R. Panek  <https://orcid.org/0000-0002-6106-3422>
 P. Svihra  <https://orcid.org/0000-0002-7811-2147>
 J. Urban  <https://orcid.org/0000-0002-1796-3597>
 J. Varju  <https://orcid.org/0000-0002-6888-6077>
 P. Vondracek  <https://orcid.org/0000-0003-0125-9252>
 V. Weinzettl  <https://orcid.org/0000-0001-8936-7578>
 D. Carnevale  <https://orcid.org/0000-0001-6214-7938>
 J. Decker  <https://orcid.org/0000-0003-0220-2653>
 M. Gobbin  <https://orcid.org/0000-0001-5261-3683>
 M. Gospodarczyk  <https://orcid.org/0000-0002-9299-6495>
 G. Papp  <https://orcid.org/0000-0003-0694-5446>
 V.V. Plyusnin  <https://orcid.org/0000-0003-1277-820X>
 M. Rabinski  <https://orcid.org/0000-0002-9875-370X>

References

- [1] Hender T.C. et al 2007 *Nucl. Fusion* **47** S128
- [2] Boozer A.H. 2017 *Nucl. Fusion* **57** 056018
- [3] Lukash V. et al 2013 Study of ITER plasma position control during disruptions with formation of runaway electrons *40th EPS Conf. on Plasma Physics (Aalto, Finland, 1–5 July 2013)* (<http://ocs.ciemat.es/EPS2013PAP/pdf/P5.167.pdf>)
- [4] Shiraki D. et al 2016 Shattered pellet injection as the primary disruption mitigation technique for ITER *Preprint: 2016 IAEA Fusion Energy Conf. (Kyoto, Japan, 17–22 October 2016)* EX/9-2
- [5] Esposito B. et al 2017 *Plasma Phys. Control. Fusion* **59** 014044
- [6] Carnevale D. et al 2019 *Plasma Phys. Control. Fusion* **61** 014036
- [7] Saint-Laurent F. et al 2013 *Fusion Sci. Technol.* **64** 711
- [8] Panek R. et al 2016 *Plasma Phys. Control. Fusion* **58** 014015
- [9] Panek R. et al 2018 ITER-relevant research on the COMPASS tokamak *Preprint: 2018 IAEA Fusion Energy Conf. (Gandhinagar, India, 22–27 October 2018)* OV/P-3
- [10] Vlainic M. et al 2015 *J. Plasma Phys.* **81** 475810506
- [11] Plyusnin V.V. et al 2018 *Nucl. Fusion* **58** 016014
- [12] Ficker O. et al 2017 *Nucl. Fusion* **57** 076002
- [13] Mlynar J. et al 2019 *Plasma Phys. Control. Fusion* **61** 014010
- [14] Macusova E. et al 2018 The role of gas injection and magnetic perturbations in runaway electron experiments at COMPASS tokamak *60th Annual Meeting of the APS Division of Plasma Physics (Portland, OR, USA, 5–9 November 2018)* (<http://meetings.aps.org/Meeting/DPP18/Session/CP11.96>)
- [15] Gobbin M. et al 2018 *Plasma Phys. Control. Fusion* **60** 014036
- [16] Havlicek J. et al 2010 Status of magnetic diagnostics on COMPASS *WDS Proc. Contributed Papers (Prague, Czech Republic, 1–4 June 2010)* pp 12–17 (www.mff.cuni.cz/veda/konference/wds/proc/pdf10/WDS10_202_f2_Havlicek.pdf)
- [17] Bilkova P. et al 2018 *J. Instrum.* **13** C01024
- [18] Farnik M. et al 2018 Runaway electron diagnostic for the COMPASS tokamak using EC emission *45th EPS Conf. on Plasma Physics (Prague, Czech Republic, 1–6 July 2018)* (<http://ocs.ciemat.es/EPS2018PAP/pdf/P1.1010.pdf>)
- [19] Rabinski M. et al 2017 *J. Instrum.* **12** C10014
- [20] Cerovsky J. et al 2018 Simulation of trajectories of runaway electrons for support of diagnostics at the COMPASS tokamak *45th EPS Conf. on Plasma Physics (Prague, Czech Republic, 1–6 July 2018)* (<http://ocs.ciemat.es/EPS2018PAP/pdf/P2.1006.pdf>)
- [21] Weinzettl V. et al 2017 *J. Instrum.* **12** C12015
- [22] Mlynar J. et al 2012 *Rev. Sci. Instrum.* **83** 10E531
- [23] Mlynar J. et al 2019 *J. Fusion Energy* **38** 458–66
- [24] Zeng L. et al 2013 *Phys. Rev. Lett.* **110** 235003
- [25] Ficker O. et al 2018 Analysis of MGI disruptions and runaway electron beams at COMPASS using tomography and fast camera data *45th EPS Conf. on Plasma Physics (Prague, Czech Republic, 1–6 July 2018)* (<http://ocs.ciemat.es/EPS2018PAP/pdf/P1.1062.pdf>)
- [26] Ficker O. et al 2017 RE beam generation in MGI disruptions on COMPASS *44th EPS Conf. on Plasma Physics (Belfast, UK, 26–30 June 2017)* (<http://ocs.ciemat.es/EPS2017PAP/pdf/P5.126.pdf>)
- [27] Stahl A. et al 2016 *Nucl. Fusion* **56** 112009
- [28] Hesslow L. et al 2018 *Plasma Phys. Control. Fusion* **60** 074010
- [29] Havlicek J. et al 2008 *WDS Proc. Contributed Papers (Prague, Czech Republic, 3–6 June 2008)* pp 221–6 (www.mff.cuni.cz/veda/konference/wds/proc/pdf11/WDS11_238_f2_Havlicek.pdf)
- [30] Knoepfel H. et al 1979 *Nucl. Fusion* **19** 785
- [31] Yoshida Z. 1990 *Nucl. Fusion* **30** 317
- [32] Hollmann E.M. et al 2013 *Nucl. Fusion* **53** 083004
- [33] Janky F. et al 2014 *Fusion Eng. Des.* **89** 186
- [34] Freidberg J.P. 2014 *Ideal MHD* (New York: Cambridge University Press)
- [35] Manheimer W.M. 1985 *Part. Accel.* **17** 157
- [36] Stahl A. et al 2013 *Phys. Plasmas* **20** 093302
- [37] Fujita T. et al 1991 *J. Phys. Soc. Japan* **60** 1237
- [38] Vlainic M. et al 2019 *Atoms* **7** 12
- [39] Meyer H et al 2017 *Nucl. Fusion* **57** 102014

Runaway electron experiments at COMPASS in support of the EUROfusion ITER physics research

J Mlynar^{1,2} , O Ficker^{1,2} , E Macusova¹ , T Markovic^{1,3} ,
D Naydenkova¹ , G Papp⁴ , J Urban¹ , M Vlainic^{5,6}, P Vondracek^{1,3},
V Weinzettl¹ , O Bogar^{1,7}, D Bren², D Carnevale⁸ , A Casolari¹ ,
J Cerovsky^{1,2}, M Farnik^{1,2} , M Gobbin⁸ , M Gospodarczyk⁹ , M Hron¹,
P Kulhanek^{1,10} , J Havlicek¹, A Havranek¹, M Imrisek^{1,3} ,
M Jakubowski¹¹, N Lamas¹², V Linhart², K Malinowski¹¹, M Marcisovsky² ,
E Matveeva¹, R Panek¹ , V V Plyusnin¹³ , M Rabinski¹¹ , V Svoboda²,
P Svihra² , J Varju¹ , J Zebrowski¹¹ and the COMPASS Team and the EUROfusion MST1 Team¹⁴

¹Institute of Plasma Physics of the CAS, CZ-18200 Praha 8, Czechia

²FNSPE, Czech Technical University in Prague, CZ-11519 Praha 1, Czechia

³FMP, Charles University, Ke Karlovu 3, CZ-12116 Praha 2, Czechia

⁴Max Planck Institute for Plasma Physics, Garching D-85748, Germany

⁵Department of Applied Physics, Ghent University, Ghent B-9000, Belgium

⁶Institute of Physics, University of Belgrade, PO Box 68, 11080 Belgrade, Serbia

⁷Faculty of Mathematics, Physics and Informatics, Comenius University in Bratislava, 842 48 Bratislava, Slovakia

⁸Consorzio RFX, Corso Stati Uniti 4, I-35127 Padova, Italy

⁹Universita di Roma Tor Vergata, I-00133 Roma, Italy

¹⁰FEE, Czech Technical University in Prague, CZ-12000 Praha 2, Czechia

¹¹National Centre for Nuclear Research (NCBJ), PL-05-400 Otwock-Swierk, Poland

¹²University of Lorraine, F-54000 Nancy, France

¹³Instituto de Plasmas e Fusao Nuclear, IST, PT-1049-001 Lisbon, Portugal

E-mail: mlynar@ipp.cas.cz

Received 6 July 2018, revised 5 September 2018

Accepted for publication 11 September 2018

Published 13 November 2018



CrossMark

Abstract

The role of the COMPASS tokamak in research of generation, confinement and losses of runaway electron (RE) population is presented. Recently, two major groups of experiments aimed at improved understanding and control of the REs have been pursued. First, the effects of the massive gas injection ($\sim 10^{21}$ Ar/Ne particles) and impurity seeding ($\sim 10^{18}$ particles) were studied systematically. The observed phenomena include generation of the post-disruption RE beam and current conversion from plasma to RE. Zero loop voltage control was implemented in order to study the decay in simplified conditions. A distinctive drop of background plasma temperature and electron density was observed following an additional deuterium injection into the RE beam. With the loop voltage control the parametric dependence of the current decay rate dI/dt can be studied systematically and possibly extrapolated to larger facilities. Second, recent results of experiments focused on the role of the magnetic field in physics of RE were analysed. In this contribution, special attention is given to the observed effects of the resonant magnetic perturbation on the RE population. The benefits of the RE experiments on COMPASS was reinforced by diagnostic enhancements (fast cameras, Cherenkov detector, vertical ECE etc) and modelling efforts (in particular, coupling of the METIS and LUKE codes).

¹⁴ See the author list of Meyer *et al* 2017 *Nucl. Fusion* **57** 102014.

Keywords: tokamaks, runaway electrons, MHD instabilities, disruptions, diagnostics, RMP

(Some figures may appear in colour only in the online journal)

1. Introduction

Thermal equilibrium in plasmas can be disturbed, among others, by applying external electric field that accelerates in particular the light electrons. Up to a certain electric field intensity, the acceleration is mitigated by collisional drag. However, there exists a *critical electric field* [1] above which net acceleration of the high energy part of the electron thermal distribution is possible, which generates a highly directional population of non-thermal electrons denoted by the term runaway electrons (RE). The process described above is the most common mechanism of the primary RE generation, usually referred to as *Dreicer generation* [2]. In the classical model with full relativistic treatment [1] the critical electric field is

$$E_c = \frac{e^3 n_e \ln \Lambda}{4\pi \epsilon_0^2 m_e c^2}. \quad (1)$$

The critical field increases with plasma density n_e , and is only a weak function of temperature through the Coulomb logarithm $\ln \Lambda$. A more detailed introduction into the primary RE generation can be found e.g. in the paper by Granetz *et al* [3]. Relation of the critical field to the experiments will be mentioned in section 2.

RE are crucial in producing lightning discharges in thunderstorms [4]. In these events, the secondary mechanism of the RE production—the RE avalanche which may severely amplify the primary generation—plays a significant role. In the avalanche, close collisions between RE and thermal electrons (knock-on collisions) cause the latter to achieve sufficient velocity to become a part of the RE population, while the former often remain in the RE population [5], albeit with a lower velocity and/or a slightly modified trajectory [6]. In tokamaks, the RE generation is driven by the toroidal electric field induced in order to ramp-up and maintain toroidal electric current in plasma. The RE population may appear in practice in three different phases of the tokamak discharge, depending on its parameters:

- (i) In the initial phase of the discharge, i.e. in the plasma breakdown, burn-through and the current ramp-up [7]. Primary energetic electrons (the RE seed) are generated within the initial ionisation and/or the burn-through phase due to the high level of the induced toroidal electric field, which remains elevated during the subsequent current ramp-up phase. While the field is above-critical (which can be controlled via fuelling) both the RE current and energy steadily increase.
- (ii) In the current plateau phase of the discharge, provided that the plasma density is sufficiently low [3, 8, 9] so that the toroidal electric field is above the critical field given by equation (1). The case of these *quiescent RE discharges* at COMPASS tokamak are mentioned in section 2.
- (iii) Following a disruption of the plasma discharge. The rapid thermal quench after the disruption results in a temporary accumulation of supra-thermal electrons due to their lower collisionality. The subsequent current quench increases the toroidal electric field that accelerates the supra-thermal electrons. This form of the primary RE generation is referred to as the hot-tail mechanism [10]. Modelling suggests that the above mentioned Dreicer generation mechanism can also convert a significant fraction of the pre-disruption plasma current into a RE seed [11, 12]. The RE seed generated by these primary generation mechanisms is further multiplied by avalanche [5], in particular in large devices [13]. Compton scattering of hard x-rays (HXRs) on electrons and tritium decay would also contribute to the RE generation in large facilities [14].

In the current ramp-up phase, the RE population can be well controlled by the fuelling scenario [15] due to its low energy. The plateau phase is safe against RE generation for fusion relevant plasma densities. However, REs generated following a plasma disruption raise a serious issue for operation of the future tokamak fusion reactors [12, 16]. The highly undesirable, violent event of plasma disruption can incidentally occur in tokamak operation due to multiple reasons and produce major mechanical and heat shocks [17, 18]. The RE beam generated in a disruption can take over a substantial part of the original plasma current. At ITER it is predicted that the post-disruption RE beam with several tens of MeV can carry up to 70% of pre-disruptive plasma current [18]. The RE beam could cause substantial damage to the first wall of ITER (for the damage in COMPASS see figure 1) and in an extreme case result in an in-vessel coolant leak. Therefore, unmitigated post-disruption RE beams are not acceptable in fusion reactors, including ITER.

The RE beams in tokamaks prove difficult to control [19] and challenging to mitigate by any external intervention as yet, which strongly stimulates research in the field of RE generation, confinement and losses. Unfortunately, the results are far from conclusive due to

- limited scope of the RE relevant diagnostics [20–23],
- highly demanding preconditions for theory and modelling, see e.g. [24, 25], and
- limited expertise in the position control of the RE beams [19].

In order to progress efficiently, the RE research efforts in Europe have been coordinated by the EUROfusion consortium within its ITER Physics Research programme which intermediates, among others, RE relevant experiments at tokamaks JET [26], AUG [27, 28], TCV [27, 29, 30], FTU [31] and COMPASS [32–34].

The COMPASS tokamak has been operating in Prague since 2008, with systematic contributions to RE research in

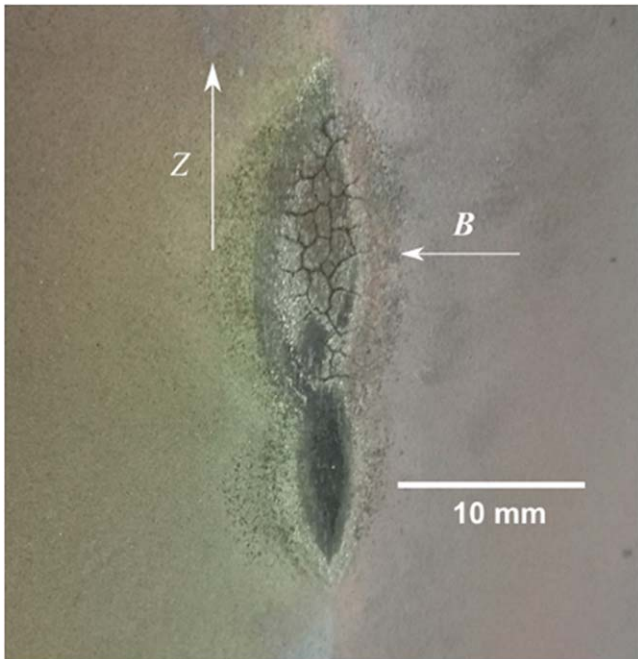


Figure 1. Wall damage due to interaction with runaway electrons (RE) at COMPASS. The damage was provoked on a protruding graphite inner limiter tile in several tens of RE discharges. The two locations of the damage correspond to two separate vertical positions of the RE beam in this set of experiments.

dedicated experimental campaigns since 2014. The facility features ITER-like plasma shapes with major radius $R_0 = 0.56$ m and minor radius $a = 0.23$ m, typical toroidal field $B_T = 0.9$ – 1.5 T, plasma current in the flat-top phase $I_p < 350$ kA, up to 600 kW neutral beam heating and a routine H-mode operation [35]. Directions of the B_T and I_p can be changed flexibly and independently. Within work published in this contribution, the B_T field as well as I_p were oriented clockwise from the top view. The toroidal magnetic field was $B_T = 1.15$ T if not stated otherwise.

The following diagnostic tools have been instrumental in the RE experiments:

- rich magnetic diagnostics [36] consisting, among others, of three poloidal arrays of 24 internal pick-up (Mirnov) coils covering radial, poloidal and toroidal components, 16 internal partial Rogowski coils and 8 flux loops,
- fast visible cameras (Photron Mini UX100 and Photron SA-X2) and fast IR camera Telops FAST-IR 2K,
- a pair of unshielded NaI(Tl) scintillation detectors to observe HXR radiation (energy range approx. 50 keV–10 MeV) and a composite ZnS(Ag) scintillation detector shielded by 10 cm of lead, therefore sensitive to neutrons and HXR approx. above 500 keV,
- 2 mm microwave interferometer with central vertical line of sight for monitoring and control of the plasma density,
- Thomson scattering (TS) data to determine temperature and density profiles; TS consists of core and edge subsystems covering the upper half of the plasma with 54 spatial points, sharing the laser beams of four Nd:YAG lasers with 30 Hz repetition rate each [37],

- six pinhole cameras with 20 channel AXUV bolometers applied for measurements of spatial distribution of total plasma radiation with high ($1 \mu\text{s}$) temporal resolution [38]; the AXUV bolometers often proved helpful in understanding the RE evolution, however, their failures during disruptions present a common problem,
- three high-resolution minispectrometers (combined range 250–1080 nm) also proved valuable in the preliminary interpretation of the RE processes related namely to injected gas ionisation and excitation—the spectroscopic data have significant potential for further intensive data analyses, provided that a sophisticated transport model with atomic data is available.

2. Results of the RE research at COMPASS

The early RE dedicated experiments at COMPASS tokamak surprisingly proved permanence of the RE population in the HXR data even at relatively high plasma densities $n_e \sim (4\text{--}6) \times 10^{19} \text{ m}^{-3}$ in the D-shaped plasmas [15]. This might be partly sustained by the secondary avalanching process, for the key role of the seed RE population from the ramp-up phase at these densities was demonstrated. Indeed, a simple secondary puff in the fuelling within the current ramp-up can inhibit the early RE population. In that case, RE appear in the current plateau only at very low plasma densities, approximately $n_e < 2 \times 10^{19} \text{ m}^{-3}$ [33]. This density value corresponds to the critical field $E/E_c \geq 10$ where E_c is defined by equation (1). The favourably high experimental value of the critical field as compared to the predicted one is in agreement with other facilities [3, 27, 29, 30] and it is probably linked to the magnetic field fluctuations, although other interpretations can be found, see e.g. [39, 40].

In the extremely low density RE dominated discharges, record length of COMPASS discharges were achieved (above 1 s) and, importantly, synchrotron radiation of the RE beam was observed [41]. From these measurements in combination with modelling, the upper limit of RE energy at COMPASS was determined to be 40 MeV [41]. In this respect, HXR photons up to 7 MeV were recorded during the RE experiments, approaching the limit given by the size of the scintillation detector. Herefrom it can be concluded that the maximum RE energies can reach a few tens of MeV.

Post-disruption RE beams were observed at COMPASS following massive gas injection (MGI) into the current ramp-up phase [33]. This scenario is particularly important due to its relevance to ITER, however, it suffers with low reproducibility which is probably linked to the role of a precise field helicity at disruption. Clear filamentation was documented in the RE beam following the MGI triggered disruption in the fast visible camera data [42]. The filaments connected with the collapse of magnetic surfaces were also captured by the V-ECE, HXR and by magnetic diagnostics [42, 43]. The same data show rather stable vertical position of the RE beam and its initially slow instability in the radial position that can be improved with a dedicated controller as mentioned below.

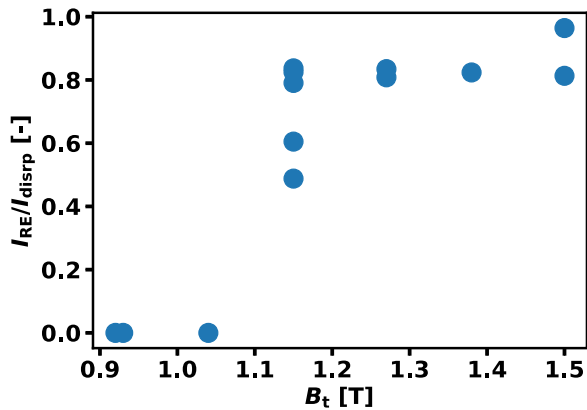


Figure 2. The RE current amplitude following an MGI disruption, normalised to pre-disruption plasma current, as a function of the toroidal magnetic field. A clear threshold level at about $B_T = 1.15$ T is disclosed.

Besides, if elongated, the RE beam usually terminates in vertical instability. In order to clarify the role of magnetic field in this scenario, a scan of the RE beam current as a function of the B_T field amplitude was measured recently, see figure 2. In this scan, the direction of the I_p was anti-clockwise so the B_T and I_p were antiparallel. As expected according to [44] a clear threshold level of the B_T field for generation of the RE beam at COMPASS was observed, although at a rather low level—at about $B_T = 1.15$ T. The reproducibility was also improved by optimising the radial position reference and in tests of the new RE controller [19].

In another scenario, inspired by the TCV RE experiments [27, 29, 30] the plateau plasma current was converted to a strong RE population following an impurity gas puff. The injection was applied on the high field side in the divertor region, with impurity density comparable to the plasma density, $n_e \approx 1 \times 10^{19} \text{ m}^{-3}$. The conversion proved to be highly reproducible and robust, providing a solid base for a systematic experimental work. Results presented in the following subsections, including the resonant magnetic perturbation (RMP) experiments, were achieved in this scenario.

2.1. Multiple effects of gas injection

An impurity gas puff (Ar or Ne) into the current flat-top of very low density discharges ($n_e \approx 10^{19} \text{ m}^{-3}$) causes a rapid thermal quench, clearly visible in the TS data. Depending on the pre-puff density, RE seed amount and gas injection amount, the thermal quench is sometimes intertwined with a current quench that terminates the discharge promptly without any RE beam generation or, more often, the current level shows no abrupt change while the HXR radiation steeply rises. This implies that a major part of the current is converted into the RE population. Consequently, the final part of this scenario i.e. the discharge following the plasma thermal quench due to the impurity puff will be referred to as the RE dominated discharge.

A surprising observation was done with respect to the MGI timing in experiments with a fixed amount of injected gas particles at approx. the threshold amount 10^{21} m^{-3} , given

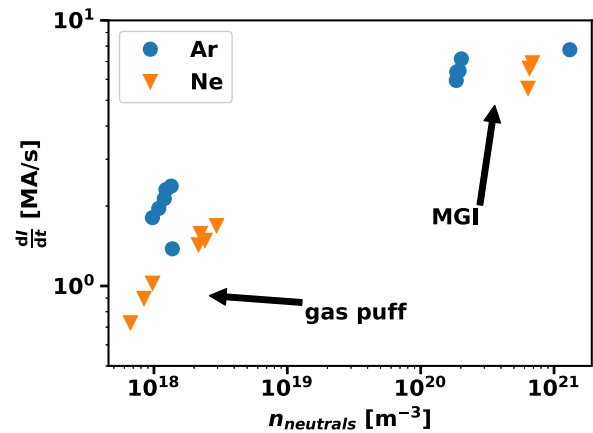


Figure 3. Current decay rate in the gas amount scan, showing both gas puff and MGI into a late stage of the current plateau ($I_p = 140$ kA). In this scan, current in the COMPASS Central Solenoid was fixed at a constant level in order to maintain U_{loop} close to zero.

$B_T = 1.5$ T and constant fuelling. In these experiments, the terminal current quench appeared only until a threshold instant in the current plateau. A later timing of the MGI single inlet resulted in a RE dominated discharge with a substantially longer current decay time. This robust result was observed in discharges #16670–#16677 with a threshold time 1090 ms (i.e. 130 ms after the plasma breakdown) and precision < 2 ms. This can be interpreted in terms of a significant role of parameters of the pre-disruption RE population. Notice that both RE density and energy increase steadily during the current plateau due to low plasma density and the avalanching effect. However, the avalanche multiplication of the RE population shall be less significant for the COMPASS conditions compared to larger facilities. The runaway fraction originating from knock-on collisions is $< 5\%$ for $E/E_c \approx 90$ and $T_e \approx 0.6$ keV and the avalanche time (τ_{ava}) can reach up to hundreds of milliseconds, as shown in [45]. In the case of smaller E/E_c (10–50), the RE avalanche fraction can significantly increase and τ_{ava} decrease, see [46].

In order to quantify the role of the impurity gas in the RE dominated discharges, a novel current control technique was introduced: following the gas puff, the power control of the tokamak was switched from the constant plasma current feedback to the constant central solenoid current regime. As a result, the induced toroidal electric field was actively kept close to zero ($U_{\text{loop}} \approx 0$ V) in this scenario. This is significant for validation of theory and models as it allows to study an acceleration-free decay of the RE population. The subsequent results—including the resonant magnetic perturbation (RMP) experiments in section 2.2—were collected in this scenario, if not stated otherwise.

In the slow, RE dominated current decay following the thermal quench the current decay rate (CDR) was observed to be a function of the injected gas amount, see figure 3. It is apparent that with a low impurity density, the RE dominated discharge can sustain CDR less than 1 MA s^{-1} in neon. The results for argon, with lower ionisation energy than neon, indicate approx. double CDR as compared to neon due to the

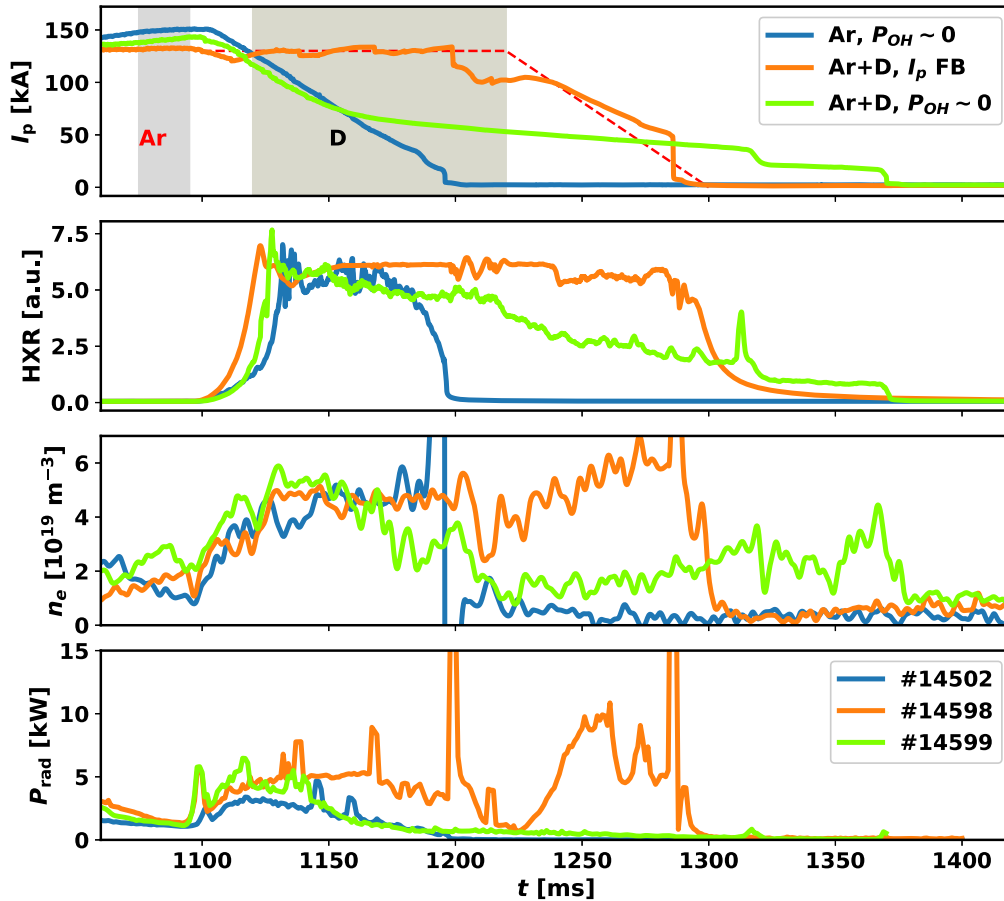


Figure 4. Three scenarios of RE dominated discharge following the thermal quench due to the Ar gas puff into the low density current plateau at COMPASS. Orange (medium grey in print) line: current feedback and additional deuterium fuelling (current reference in dashed line), blue (black) line: zero U_{loop} with no additional fuelling, green (light grey) line: zero U_{loop} and additional fuelling. Note that with the thermal quench due to the gas puff, T_e drops below 10 eV.

stronger drag force. In order to further elaborate on these results, experiments with plasma deuterium fuelling in the RE dominated discharge were undertaken, see figure 4. In the figure, three different scenarios after Ar gas puff are compared, documenting the following current decay mechanisms:

- (i) The RE dominated discharge with constant current feedback control and D fuelling (in red line, mid-grey in printed version). Deuterium supports the current feedback by neutralising the argon impurity and therefore by decreasing the RE drag. This interpretation is strengthened by fast visible camera data that shows temporal decrease of the Ar II radiation. The discharge suffers with instabilities linked to rational magnetic field surfaces, accompanied by filamentation visible in the camera data as well as by peaks in other signals [42]. With a termination of the deuterium fuelling and due to the Ohmic heating, the Ar impurity takes over again as a strong radiative component.
- (ii) The RE dominated discharge with zero U_{loop} , with no additional fuelling (in blue line, black in printed version). The current decay in this scenario is smooth, with a relatively high CDR.
- (iii) The RE dominated discharge with zero U_{loop} and deuterium fuelling (in green line, light grey in printed

version). Deuterium neutralises the argon impurity, which considerably decreases the electron density and RE drag and results in a substantially lower CDR. Notice that in this scenario the RE dominated discharge eventually lives longer than the similar discharge with the current feedback.

The above understanding is further supported by HXR data evolution, in particular in the case of the current feedback where the high levels of the HXR radiation (leading to saturation of the detector) reflect high energies of the lost RE due to high U_{loop} . Furthermore, evolution of the total radiated power (bottom frame in the figure) demonstrates that the radiative losses are higher in the case of the current feedback than in the other scenarios, and that the losses strongly increase when deuterium fuelling stops. The total losses were determined from 2D tomography of the AXUV signals calculated by the minimum Fisher regularisation (MFR) tomography [47]. A hollow belt of the radiation profile following the gas puff was clearly reconstructed by the tomographic analysis. The MFR tomography application in this task present a straightforward continuation of our initial contributions to the dedicated RE studies at JET, see [48].

Typical CDRs of discharges with large to dominant RE population are compared in table 1.

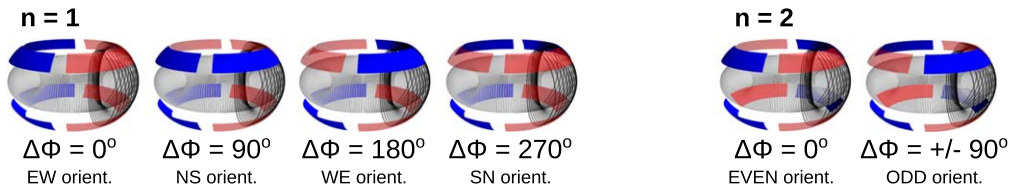


Figure 5. Configuration of the RMP coils in the RE experiments at COMPASS. The red (light grey in print) and blue colours (dark grey) correspond to positive (direction out of plasma) and negative B_r field perturbation, respectively.

Table 1. Typical current decay rates at COMPASS in different discharge terminations.

Discharge termination	CDR (MA s^{-1})	Effects
Natural decay	0.1–0.2	Moderate HXR
Ar/Ne gas puff + D	0.2–0.3	Intensive HXR, changes in colour of visible light
Ar/Ne gas puff	1.5–2.5	Faster decay, saturated HXR
Ar/Ne gas puff and RMP	5.0–9.0	Fast decay, saturated HXR
Ar/Ne MGI	6.0–9.0	Intensive line radiation, steep but shorter burst of HXR
Plasma disruption	200–700	A very short HXR burst
Disruption of RE dominated plasma without impurity gas	4000–7000	Immediate, localised damage, high peak in HXR

Numerical simulations of selected quiescent RE flat-top discharges with zero U_{loop} scenario and high Z impurity seeding were performed with the linearised Fokker–Planck solver CODE [49, 50]. The simulations included the effect of partial screening [39, 51], large-angle collisions [6] and self-consistent calculation of the electric field, but no radial transport losses due to magnetic field fluctuations. Including partial screening gives more accurate results than previous theoretical predictions (the ratio E/E_c is more than 2 times closer to the E/E_c value from experiment if partial screening is included than without), however, there is still a factor of 3–5 discrepancy between the simulation and experiment. The discrepancy might be explained by RE transport losses due to magnetic fluctuations. Note that in all the above studied cases fluctuations in the radial magnetic field ($\delta B/B \geq 5 \times 10^{-4}$) were observed.

2.2. RE in perturbed magnetic fields

The key role of magnetic field perturbations on the RE losses was clearly identified already in past RE research at COMPASS and reported in [33]. Among others, an undisputable link between plasma MHD activity and the RE confinement was documented, and a relation between the switching of the power supply and modulation of the HXR radiation was revealed. Next, a minor modulation in plasma position due to the feedback system properties proved to produce a well correlated effect between HXR radiation and infrared radiation from the limiter, which directly confirmed that RE interaction with the limiter makes a significant contribution to the overall HXR radiation intensity [33].

In this subsection, the main results from recent RE experiments with RMP system at COMPASS [52, 53] are presented. The work was partly inspired by recent work of the ASDEX Upgrade team in RMP experiments on post-

disruption RE beam [54]. Subsequently the RMP configurations were limited to the low field side off-midplane coils only, see figure 5, while the effect of coils at high field side midplane, low field side midplane, or top and bottom may be subject to the future RE research. The perturbation can reach up to $B_r/B_T \approx 10^{-2}$. However, the magnitude of the perturbation was always kept below the empirical threshold of MHD mode locking in order to avoid significant perturbation of background plasma. Similarly to [54], we study the effect of the RMP on RE beam in context of coupling of the RMP to rational surfaces m/n of the magnetic equilibrium. However, presence of external magnetic perturbation leads to induction of screening currents on these surfaces [55] that alter this coupling. Thus, the screened RMP has been calculated using a resistive MHD code MARS-F [56].

In order to achieve high reproducibility under well-defined conditions, the scenario described in section 2.1 was exploited. The different effects of gas puff and RMP field in the RE dominated discharge following a gas puff and featuring an active control of the zero U_{loop} is summarised in figure 6. Although the thermal quench due to the gas puff obviously played a dominant role in the CDR (i.e. in the discharge length), it is also clear that the RMP effect systematically increased the RE losses—as observed in the HXR data—and therefore caused a faster CDR. The effect of the gas puff and the RMP field on the plasma centre position in vertical and radial directions is visible in two bottom panels. The vertical position remains stable, whereas the radial position is unstable as mentioned previously. In the figure, CDR with phase $\Delta\Phi = 270^\circ$ of the top with respect to the bottom RMP coils is presented (see figure 5). The role of the phase was determined in a separate scan of the four possible $\Delta\Phi$ angles. It has been observed in the experiment that the most pronounced effect of RMP on CDR, similarly to [54], is associated with the

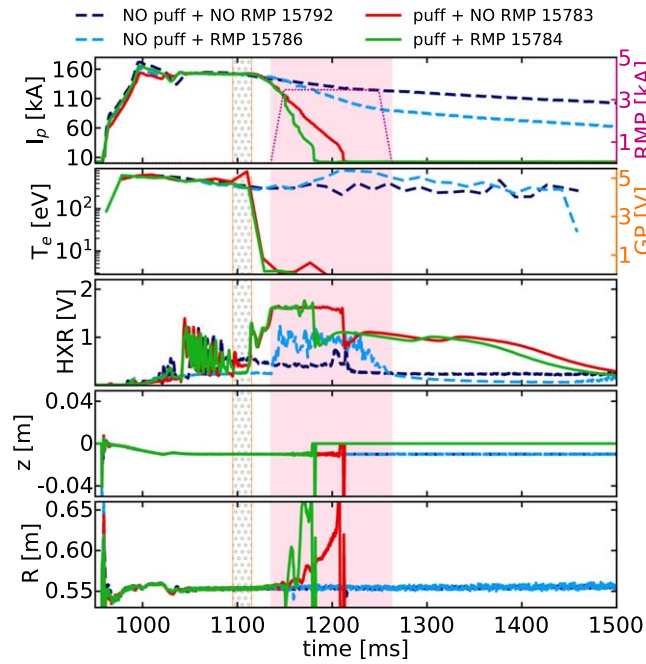


Figure 6. Termination of the RE dominated discharge with zero U_{loop} , showing consequences of argon puff at 5×10^{18} particles, and/or the $n = 1$ RMP field.

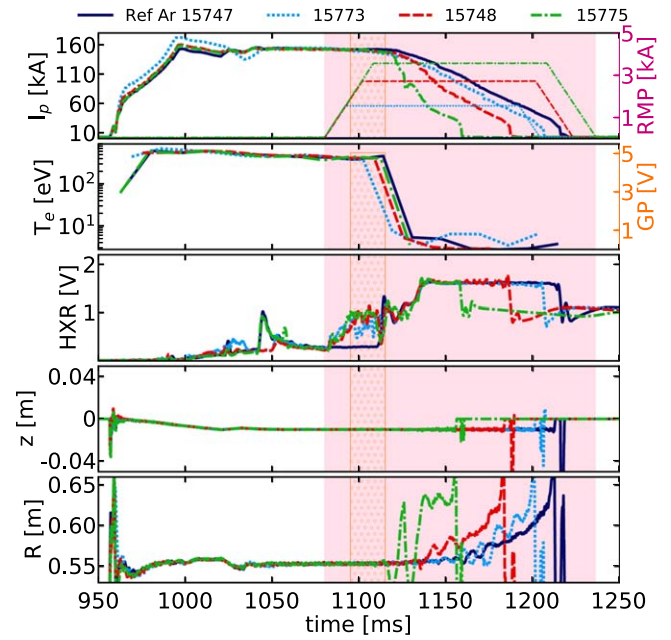


Figure 8. Observed increase of CDR with increase of the RMP amplitude. The scan was performed for the argon puff at 5×10^{18} particles, the partly resonant phase $\Delta\Phi = 270^\circ$ and zero U_{loop} .

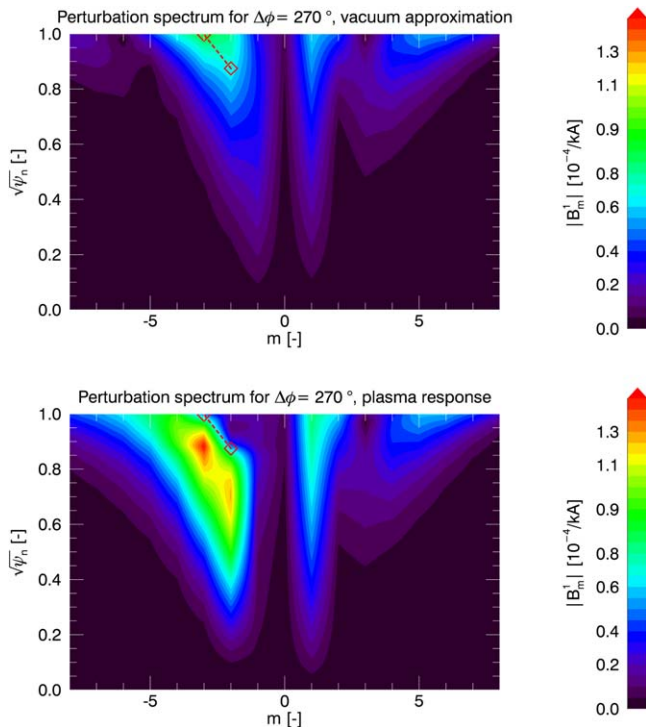


Figure 7. Fourier decomposition of dimensionless perturbation field magnitude $|\mathbf{B}'| = \left| \frac{\mathbf{B}_{pert} \cdot \nabla \Psi}{\mathbf{B}_{equi} \cdot \nabla \Phi} \frac{q}{R^2 B_0} \right|$ into poloidal modes as a function of radius ($\sqrt{\Psi_n} \approx r/a$). The magnitude is normalised to I_{coil} of perturbation coils at $\Delta\Phi = 270^\circ$. Positions of equilibrium rational surfaces are shown in diamond symbols. Top plot—vacuum approximation, bottom plot—plasma screening included.

strongest coupling of screened RMP to the equilibrium rational surfaces. Furthermore, comparison of vacuum perturbation spectrum to the one including plasma response in figure 7 reveals that under these conditions a strong kink mode amplification due to plasma screening appears, as it is indicated by amplification of components at $|m|$ higher than those of rational surfaces (shown by red symbols). This is also in agreement with observations in [54].

Next, experiments scanning the amplitude of the RMP were performed. The highest RMP amplitude in the most resonant (from screened RMP-equilibrium coupling point of view) $\Delta\Phi = 0^\circ$ phase resulted in a fast disruption with sudden current quench and no RE dominated discharge for RMP amplitude >1.1 kA in the case of argon and 1.7 kA in the case of neon. Therefore, the second most resonant phase $\Delta\Phi = 270^\circ$ and the argon puff at 5×10^{18} particles was used in the published amplitude scan, see figure 8. Additionally, in this set of experiments the RMP coils were switched on well before the gas puff to investigate influence of the perturbed field on the current plateau. The figure shows that with increasing amplitude of current in the RMP coils the CDR increased as expected, and that increased RE losses due to the RMP field occurred even before the thermal quench, as can be seen from the HXR signal. These data demonstrate presence of well-confined RE in the current plateau phase, i.e. before the thermal quench, which acts as the RE seed in the RE dominated discharge. The seed can be partly lost due to the RMP field.

The overview statistics of the RE experiments in all four phases of the $n = 1$ RMP fields and either argon or neon induced thermal quench at COMPASS is presented in figure 9. The figure shows CDR as a function of average early level in

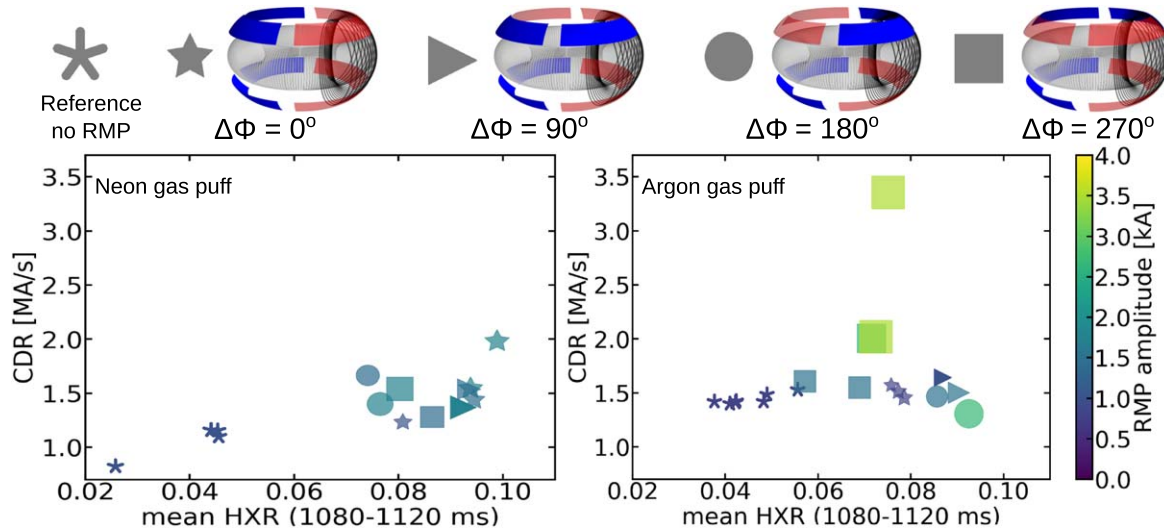


Figure 9. Overview of results obtained with application of $n = 1$ RMP field. Current decay rate for the four different RMP phases is shown as a function of the early HXR radiation level.

the HXR data (from 1080 to 1120 ms, avoiding signal saturation). No RMP field was applied in the reference discharges. The strong correlation between the early HXR intensity and the CDR is apparent in particular in the neon case: the more intense the HXR radiation, the faster the CDR. It is also apparent that the fastest decay was achieved for $\Delta\Phi = 0^\circ$ for neon and $\Delta\Phi = 270^\circ$ for argon. In the case of argon, the CDR seems to be almost independent of the early HXR level except for the highest RMP current amplitudes in the $\Delta\Phi = 270^\circ$ phase, where the CDR was substantially faster.

Systematic experimental studies were also performed for $n = 2$ RMP with two different phases: the even phase with $\Delta\Phi = 0^\circ$, and the odd phase with $\Delta\Phi = \pm 90^\circ$. Higher losses of RE (linked to more intense HXR radiation and higher CDR) were observed in the odd phase, which was correlated with onset of a rotating MHD mode (detected by an in-vessel local poloidal magnetic field probe) and the fluctuations of HXR signal observed upon powering the RMP coils. However, a still stronger effect is expected at $\Delta\Phi = 45^\circ$. As in the $n = 1$ case the RMP amplitudes >3.25 kA led to immediate current quench with no surviving RE in the case of the argon gas puff, while in the case of the neon gas puff the RE beam survived even the highest RMP amplitude.

It should be pointed out that due to the specific proximity of RMP coils to plasma at COMPASS, and their relatively high coil currents, it is possible to exert a strong perturbation (not necessarily resonant) to plasma equilibrium, in comparison to other devices. As it is shown in figure 8, this is responsible for the increase in the CDR. Although RMP is not foreseen as a RE mitigation scheme due to minor effect on RE at large facilities, the above presented results are relevant for validation of models which shall improve understanding of interaction of RE with perturbed magnetic field.

2.3. Complementary research programme

The complementary research programme in support of RE experiments is fostered at COMPASS in order to build up the

basis for further progress. The programme consists of development of modelling tools, development and integration of dedicated novel diagnostics and implementation of new control methods into the discharge scenario.

The present modelling of the RE dynamics at COMPASS [46] relies on fast transport code METIS [57], which has been recently coupled to the 1D2V relativistic bounce-averaged kinetic Fokker–Planck solver LUKE [45, 58]. As a result, radial electric field and estimate of the fraction of current carried by RE can be calculated self-consistently as well as dynamics and distribution function of the RE. Modelling of effects of impurity seeding, transport and radiation losses on the RE current decay and future benchmarking with experiments started within a broad international collaboration. As another example, contributions to coupling of dynamics of energetic particles and MHD modes modelling in tokamaks have been developed. The coupling is based on simulations of transport of REs in the presence of MHD perturbation with the Hybrid Gyrokinetic Code [59]. Fundamental theory works with respect to RE distribution function and radiation have been also fostered in the team since 2018. In the longer term, the new COMPASS Upgrade project presents an important challenge to the team due to preparation of the prospective programme, with an exciting potential [60].

The RE related work also contributes to development and exploitation of new dedicated diagnostics. Three channel Cherenkov detector, under development in the Polish NCBJ institute [61, 62] makes a regular part of the RE campaigns with a particular advantage of sensitivity to lower energy RE seed. A new method of observation of the confined RE electrons at 50–140 keV using vertical ECE measurements on the 3rd harmonics proved to provide new valuable insights into the RE dynamics and its interaction with the core plasma [43]. Next, a 2D soft x-ray matrix detector MediPix is under detailed tests at COMPASS as it would provide invaluable information on spatial distribution of the RE interaction with the first wall [63]. The same detector shall be used in the

planned solid pellet injector experiments. Last but not least, exploitation of the RE Infrared Spectroscopy detector REIS on loan is foreseen [64].

In the field of implementation of the new control methods, the aim is to develop a reliable active control of the position and current in RE dominated discharge and/or for pure RE beam in tokamaks, with the motivation to minimise the RE interaction with the first wall. At COMPASS, with support of expertise of foreign collaborators, the MARTE real-time framework was installed and current quench detector was implemented as well as the radial position and plasma current reference policies [19]. With the present encouraging results, the development of the RE control is bound to continue.

3. Conclusions

Research into foreseeable methods of the RE mitigation presents a high priority task in support of ITER. The COMPASS tokamak has contributed extensively to this research recently, in particular in the field of experiments focused on RE interaction with injected gas and with magnetic perturbation. The shared expertise with other facilities, including the possibility to participate in the JET, ASDEX Upgrade and TCV RE studies were instrumental.

Role of filamentation due to the field line helicity and role of toroidal magnetic field intensity were studied in the MGI triggered post-disruption RE beam experiments in the current ramp-up phase. Majority of the RE research results presented in this contribution was achieved with gas puff into low density current plateau phase of the discharge, which reliably resulted in a rapid thermal quench of the plasma followed by a slow current decay of the RE dominated discharge. Better understanding of the RE mitigation in these experiments was achieved due to introduction of the zero U_{loop} via an active control of the constant current in the Central Solenoid of COMPASS. Differences between application of argon and neon were identified in evolution of the RE dominated discharges and attributed to their different ionisation potential. Studies of the role of the ionisation potential with respect to the discharge conditions were complemented by deuterium fuelling of the RE dominated discharge. It was concluded that the additional fuelling results in cooling of the background plasma, which effectively improves the RE confinement.

A large number of experiments with RMP was performed in the same scenario. In all the experiments the RMP field led to increased losses of RE. The undertaken scans in the RMP phase agreed well with predictions of the MARS-F interpretative MHD model, showing that most important RE losses (and, subsequently, the fastest current decays in the RE dominated discharges) were associated with the coupling between the plasma-screened RMP and the magnetic equilibrium rational surfaces. The RMP coils were powered both before and after the impurity gas puff, demonstrating that the RE deconfinement due to perturbation appears in the RE dominated disruption independently of the same effect on the

hot plasma. In the case of large RMP amplitudes, the perturbation followed by gas puff often led to immediate current quench without any surviving RE beam. With this exception, the scan on RMP amplitudes demonstrated that the higher the RMP amplitude, the higher the CDR in the RE dominated discharges.

Interpretation of the RE experiments is challenging partly due to inadequate features of common tokamak diagnostic systems for the RE research as well as due to multiple complexities in theory and modelling of fast particles in magnetically confined plasmas. Therefrom, research and development of RE relevant diagnostics and computer models make an integral part of the RE studies at COMPASS. Scenario development based on novel position and current controllers presents another opportunity for the COMPASS RE research complementing the experimental studies. Indeed, the RE control seems feasible with the tokamak field actuators, while it may prove to have an important potential for the required RE mitigation schemes.

Acknowledgments

The work has been supported by the grants GA18-02482S and GA16-24724S of the Czech Science Foundation (GACR), the MEYS projects LM2015045, CZ.02.1.01/0.0/0.0/16_019/0000768 and carried out within the framework of the EUROfusion Consortium. It has also received funding from the Euratom research and training programme 2014-2018 under grant agreement No 633053 with the Co-fund by MEYS project number 8D15001. The views and opinions expressed herein do not necessarily reflect those of the European Commission.

ORCID iDs

J Mlynar  <https://orcid.org/0000-0003-4718-4321>
 O Ficker  <https://orcid.org/0000-0001-6418-9517>
 E Macusova  <https://orcid.org/0000-0002-0381-9244>
 T Markovic  <https://orcid.org/0000-0003-4607-3881>
 D Naydenkova  <https://orcid.org/0000-0003-0307-2301>
 G Papp  <https://orcid.org/0000-0003-0694-5446>
 J Urban  <https://orcid.org/0000-0002-1796-3597>
 V Weinzettl  <https://orcid.org/0000-0001-8936-7578>
 D Carnevale  <https://orcid.org/0000-0001-6214-7938>
 A Casolari  <https://orcid.org/0000-0002-5074-402X>
 M Farnik  <https://orcid.org/0000-0002-7106-0719>
 M Gobbin  <https://orcid.org/0000-0001-5261-3683>
 M Gospodarczyk  <https://orcid.org/0000-0002-9299-6495>
 P Kulhanek  <https://orcid.org/0000-0003-1364-2486>
 M Imrisek  <https://orcid.org/0000-0003-0967-7758>
 M Marcisovsky  <https://orcid.org/0000-0003-0860-7897>
 R Panec  <https://orcid.org/0000-0002-6106-3422>
 V V Plyusnin  <https://orcid.org/0000-0003-1277-820X>
 M Rabinski  <https://orcid.org/0000-0002-9875-370X>
 P Svihra  <https://orcid.org/0000-0002-7811-2147>
 J Varju  <https://orcid.org/0000-0002-6888-6077>

References

- [1] Connor J W and Hastie R J 1975 *Nucl. Fusion* **15** 415
- [2] Dreicer H 1959 *Phys. Rev.* **115** 238
- [3] Granetz R S et al 2014 *Phys. Plasmas* **21** 072506
- [4] Gurevich A V, Milikh G M and Roussel-Dupre R 1992 *Phys. Lett. A* **165** 463
- [5] Rosenbluth M N and Putvinski S V 1997 *Nucl. Fusion* **37** 1355
- [6] Embreus O et al 2018 *J. Plasma Phys.* **84** 905840102
- [7] Knoepfel H and Spong D A 1979 *Nucl. Fusion* **19** 785
- [8] Popovich Z et al 2016 *Phys. Plasmas* **23** 122501
- [9] Paz-Soldan C et al 2014 *Phys. Plasmas* **21** 022514
- [10] Smith H M and Verwichte E 2008 *Phys. Plasmas* **15** 072502
- [11] Papp G et al 2013 *Nucl. Fusion* **53** 12301
- [12] Hollmann E M et al 2015 *Phys. Plasmas* **22** 021802
- [13] Boozer A H 2017 *Nucl. Fusion* **57** 056018
- [14] Feher T et al 2011 *Plasma Phys. Control. Fusion* **53** 035014
- [15] Mlynar J et al 2015 *Proc. 42th EPS Conf. Plasma Phys.* vol 39E (Lisbon) (ECA) P4.102
- [16] Lehnen M et al 2015 *J. Nucl. Mater.* **463** 39
- [17] Riccardo V et al 2010 *Plasma Phys. Control. Fusion* **52** 124018
- [18] Hender T C 2007 *Nucl. Fusion* **47** S128–202
- [19] Carnevale D et al 2018 *Plasma Phys. Control. Fusion* (<https://doi.org/10.1088/1361-6587/aef53>)
- [20] Paz-Soldan C et al 2017 *Phys. Rev. Lett.* **118** 255002
- [21] Tinguely A R et al 2018 *Nucl. Fusion* **58** 076019
- [22] Hoppe M et al 2018 *Nucl. Fusion* **58** 082001
- [23] Hoppe M et al 2018 *Nucl. Fusion* **58** 026032
- [24] Boozer A H 2015 *Phys. Plasmas* **22** 032504
- [25] Stahl A et al 2016 *Nucl. Fusion* **56** 112009
- [26] Reux C et al 2015 *Nucl. Fusion* **55** 093013
- [27] Papp G et al 2016 *Preprint: 2016 IAEA FEC (Kyoto, Japan)* (IAEA) CN 234 EX/9-4
- [28] Pautasso G et al 2017 *Plasma Phys. Control. Fusion* **59** 014046
- [29] Decker J et al 2018 *Plasma Phys. Control. Fusion* submitted
- [30] Coda S et al 2017 *Nucl. Fusion* **57** 102011
- [31] Esposito B et al 2016 *Proc. 26th IAEA FEC (Kyoto, Japan)* (IAEA) CN 234 EX/P8-27
- [32] Vlainic M et al 2015 *J. Plasma Phys.* **81** 475810506
- [33] Ficker O et al 2017 *Nucl. Fusion* **57** 076002P
- [34] Plyusnin V V et al 2018 *Nucl. Fusion* **58** 016014
- [35] Panek R et al 2016 *Plasma Phys. Control. Fusion* **58** 014015
- [36] Weinzettl V et al 2011 *Fusion Eng. Des.* **86** 1227
- [37] Bilkova P et al 2018 *J. Instrum.* **13** C01024
- [38] Mlynar J et al 2012 *Rev. Sci. Instrum.* **83** 10E531
- [39] Hesslow L et al 2017 *Phys. Rev. Lett.* **118** 255001
- [40] Stahl A et al 2015 *Phys. Rev. Lett.* **114** 115002
- [41] Vlainic M et al 2015 *Proc. 42th EPS Conf. Plasma Phys.* vol 39E (Lisbon) (ECA) P4.108
- [42] Ficker O et al 2017 *Proc. 44th EPS Conf. Plasma Phys.* vol 41F (Belfast) (ECA) P5.126
- [43] Farnik M et al 2018 *Proc. 45th EPS Conf. Plasma Phys.* vol 42A (Prague) (ECA) P1.1010
- [44] Zeng L et al 2013 *Phys. Rev. Lett.* **110** 235003
- [45] Nilsson E et al 2015 *Plasma Phys. Control. Fusion* **57** 095006
- [46] Macusova E et al 2017 *Proc. 44th EPS Conf. Plasma Phys.* vol 41F (Belfast) (ECA) P4.141
- [47] Odstrcil M et al 2012 *Nucl. Instrum. Methods Phys. Res. A* **686** 156
- [48] Plyusnin V V et al 2006 *Nucl. Fusion* **46** 277
- [49] Landreman M et al 2014 *Comput. Phys. Commun.* **185** 847–55
- [50] Stahl A et al 2016 *Nucl. Fusion* **56** 112009
- [51] Hesslow L et al 2018 *Plasma Phys. Control. Fusion* **60** 074010
- [52] Cahyna P et al 2009 *Nucl. Fusion* **49** 055024
- [53] Markovic T et al 2016 *Nucl. Fusion* **56** 092010
- [54] Gobbin M et al 2018 *Plasma Phys. Control. Fusion* **60** 014036
- [55] Denner P et al 2014 *Nucl. Fusion* **54** 064003
- [56] Liu Y Q and Bondeson A 2000 *Phys. Plasmas* **7** 3681
- [57] Artaud J F et al 2010 *Nucl. Fusion* **50** 043001
- [58] Decker J et al 2016 *Plasma Phys. Control. Fusion* **58** 025016
- [59] Briguglio S et al 1995 *Phys. Plasmas* **2** 3711
- [60] Panek R et al 2017 *Fusion Eng. Des.* **123** 11
- [61] Rabinski M et al 2017 *J. Instrum.* **12** C10014
- [62] Cerovsky J et al 2018 *Proc. 45th EPS Conf. Plasma Phys.* vol 42A (Prague) (ECA) P2.1006
- [63] Neue G et al 2015 *J. Instrum.* **10** C04013
- [64] Esposito B et al 2017 *Plasma Phys. Control. Fusion* **59** 014044

Demonstration of Safe Termination of Megaampere Relativistic Electron Beams in Tokamaks

Cédric Reux^{*}

CEA-IRFM, F-13108 Saint-Paul-les-Durance, France

Carlos Paz-Soldan[†]

*General Atomics, P.O. Box 85608 San Diego, California 92186-5608, USA
and Department of Applied Physics and Applied Mathematics, Columbia University, New York, New York 10027, USA*

Pavel Aleynikov

Max-Planck-Institut für Plasmaphysik, Greifswald, Germany

Vinodh Bandaru[‡]

Max-Planck-Institut für Plasmaphysik, Garching, Germany

Ondrej Ficker[§]

Institute of Plasma Physics of the CAS, Za Slovankou 1782/3, 182 00 Praha 8, Czech Republic

Scott Silburn[¶]

CCFE, Culham Science Centre, Abingdon, Oxon OX14 3DB, United Kingdom

Matthias Hoelzl^{||}

Max-Planck-Institut für Plasmaphysik, Garching, Germany

Stefan Jachmich

ITER Organization, Route de Vinon sur Verdon, 13115 St. Paul Lez Durance, France

Nicholas Eidietis^{||}

General Atomics, P.O. Box 85608 San Diego, California 92186-5608, USA

Michael Lehnen^{||}

ITER Organization, Route de Vinon sur Verdon, 13115 St. Paul Lez Durance, France

Sundaresan Sridhar^{||}

CEA-IRFM, F-13108 Saint-Paul-les-Durance, France

JET contributors[†]



(Received 19 September 2020; revised 19 February 2021; accepted 16 March 2021; published 30 April 2021)

For the first time it is experimentally demonstrated on the JET tokamak that a combination of a low impurity concentration bulk plasma and large magnetohydrodynamic instabilities is able to suppress relativistic electron beams without measurable heat loads onto the plasma facing components. Magnetohydrodynamic simulations of the instability and modeling of the postinstability plasma confirm the prompt loss of runaways and the absence of regeneration during the final current collapse. These surprising findings motivate a new approach to dissipate runaway electrons generated during tokamak plasma disruptions.

DOI: [10.1103/PhysRevLett.126.175001](https://doi.org/10.1103/PhysRevLett.126.175001)

Published by the American Physical Society under the terms of the Creative Commons Attribution 4.0 International license. Further distribution of this work must maintain attribution to the author(s) and the published article's title, journal citation, and DOI.

Introduction.—Runaway electrons (REs) are created in thunderstorm clouds [1,2], solar flares [3,4], as well as during disruptions of tokamak plasmas [5]. The latter two situations share a close link to magnetic reconnection events [6], an ability to convert magnetic energy into

kinetic energy and similar ranges of densities and electric fields [7–9]. In tokamak disruptions, REs reach energies up to 10s of MeV in multi-mega-ampere beams [10–12] and lead to significant localized damage on plasma facing components (PFC) upon termination [13,14]. The kinetic and magnetic energy stored by a RE beam in future tokamaks will reach 10s of megajoules [15,16]. A mitigation strategy is therefore mandatory [17].

Shattered pellet injection (SPI) [18] is presently the baseline RE mitigation actuator planned for the ITER tokamak. Its goal is to avoid generating REs by suppressing primary RE generation mechanisms (Dreicer [19], hot tail [20]) and reduce the avalanche [21]. However, state-of-the-art models when applied to ITER 15 MA plasma conditions find finite RE primary populations are created [15,22] and avalanched [21,23]. A second line of defense is therefore needed to mitigate a mature RE beam. SPI was first tested for RE mitigation on DIII-D [24] and was shown to successfully dissipate RE beam energy with high-Z noble gases, building on earlier experiments with massive gas injection [25–27]. Yet, high-Z mitigation was found to be ineffective in some JET experiments [10]. There is also evidence from theoretical models [15,22,28] that high-Z mitigation will not be sufficient for larger RE currents.

This Letter reports on the use of deuterium injections to mitigate a RE beam. For the first time, RE beams with currents up to 1.27 MA were mitigated at JET with no measurable energy deposition to the plasma facing components. This level of RE current is well in excess of levels previously found to lead to significant damage to the first wall in JET [29]. This result is achieved through a combination of the excitation of a large magnetohydrodynamic (MHD) instability followed by the absence of regeneration of REs. Qualitatively similar RE terminations were observed at DIII-D [30]. However, owing to incomplete thermography of the PFCs the DIII-D experiments were unable to assess the implications for first-wall integrity. The present work builds on those experimental findings and shows that this deconfinement method is benign for the wall despite large currents at RE termination. Although the avalanche amplification $\gamma_{RE} t \approx I_p / [I_{\text{Alfvén}} \ln(\Lambda)]$ [21] is predicted to be larger for ITER than for JET, this mitigation scenario opens a new approach to dissipate REs generated during tokamak plasma disruptions.

Experimental background and runaway impact on the wall.—In this study, RE beams are created in the JET tokamak using argon injections in a limiter configuration. A standard RE scenario is shown on Fig. 1, blue curves. 2.38×10^{21} atoms of argon are used to trigger the disruption (twice the deuterium inventory of the predisruption plasma) exciting a 750 kA runaway beam. The companion plasma coexisting with the RE beam is mainly composed of argon from the disruption-triggering injection [31]. The impact at beam termination is characterized by infrared

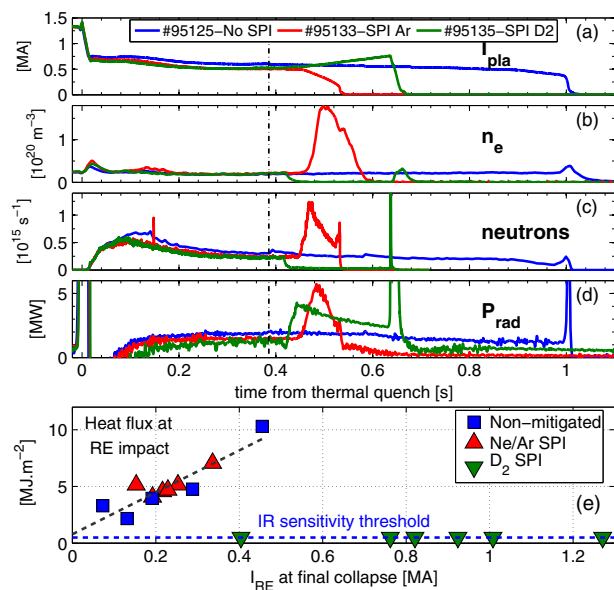


FIG. 1. Overview of three different RE beam termination scenarios. (a) Total current. (b) Average electron density. (c) Total neutron rate. (d) Total radiated power. (e) Heat flux on the wall following RE impact. Vertical dashed line is the SPI trigger time.

thermography. JET camera systems monitor the vast majority of the plasma facing components, thus ruling out the possibility of missing localized RE impacts. Heat loads are computed using a 1D finite difference heat diffusion method similar to Ref. [29], where the energy flux and the deposition depth are used to fit the measured surface temperature decay following the impact. The energy deposition duration and footprint are determined by the camera images. Injecting high-Z material into the beam leads to a faster RE current decay (red curves on Fig. 1) and a final collapse producing significant heat loads on the wall [10].

Using deuterium SPI leads to completely different dynamics. On JET pulse #95135, a shattered pellet containing 1.46×10^{23} deuterium atoms is fired onto the RE beam. Instead of decreasing as with high-Z injections (Fig. 1, red curves), the RE current rises [Fig. 1(a), green curve]. Free electron density drops to nonmeasurable values [$< 10^{18} \text{ m}^{-3}$, Fig. 1(b)]. The neutron rate drops by a factor 10 [Fig. 1(c)]. The effect of D_2 is qualitatively similar to that reported in DIII-D [24], AUG [32], and COMPASS [33], with the exception of a marked rise in the radiated power [up to 4.3 MW, Fig. 1(d)], a feature seen only on JET. The current increase is attributed to a decrease of the effective resistivity of the RE + companion plasma system. The decrease of argon line radiation and the appearance of deuterium lines are consistent with the argon being expelled from the plasma [34]. The low free electron density indicates that the plasma has recombined.

A large neutron spike occurs 220 ms after the shattered pellet arrival, with $I_{\text{RE}} \approx 760 \text{ kA}$. The infrared synchrotron

emission disappears in less than 3 ms, indicating significant loss of REs. A large magnetic perturbation is measured and a current quench similar to a conventional disruption occurs thereafter similarly to Ref. [30].

Full-view thermography of this event available at JET reveals the striking absence of any localized impact on the first wall, with heat loads below the infrared (IR) camera measurement threshold (0.5 MJ m^{-2}). This safe termination is unique to deuterium-background RE beams as shown in Fig. 1(e) and reported here for the first time. Owing to incomplete IR camera coverage on DIII-D, only a postmortem analysis of the event reported in Ref. [30] was performed. This inspection could only conclude that no visible damage occurred to the DIII-D carbon tiles. The heat flux needed to ablate $30 \mu\text{m}$ of material from a carbon tile following a $100 \mu\text{s}$ pulse [30] is around 30 MJ m^{-2} from simulations [35]. It can be considered as the minimum heat loads inferable from a postmortem analysis. This value is much larger than the 0.5 MJ m^{-2} sensitivity of the measurements reported here and too large for making reliable predictions of RE terminations in future tokamaks. The observation reported in the present Letter is therefore the first time a conclusive demonstration of the absence of heat loads can be obtained in mega-ampere scale RE beam terminations. In contrast, REs mitigated by high-Z material produce significant heat loads despite lower currents at termination as shown in Fig. 1(e). The benign termination is explained by the combination of two mechanisms which will now be elaborated in turn: (1) a violent MHD instability stochastizing the plasma and (2) the absence of regeneration of REs during the subsequent current quench resulting from the expulsion of the high-Z impurities.

Development of the MHD instability.—The deuterium SPI leads to an increase of the RE current and therefore a decrease of the edge safety factor q_{edge} . The MHD instability triggering the final RE collapse happens when q_{edge} is between 2 and 5 [high-Z fraction below 0.3 on Fig. 2(a)]. The large dispersion of q_{edge} at MHD onset suggests that it is not exclusively a simple current-limiting instability as proposed in Ref. [30]. Simulations of pulse #95135 using the SOFT code [36] have been performed to reconstruct the infrared synchrotron camera images. A spatially uniform RE energy and pitch angle distribution was assumed. The best match between the simulation and the IR images is obtained when the pitch angle is between (0.1–0.3), the energy less than 15 MeV, and the RE density profile is hollow (peak density around mid-radius), as shown on Figs. 3(a) and 3(b). Using a peaked RE density profile, no energy and pitch angle distribution that explains the observed pattern on the camera image could be identified. The RE current profile therefore likely presents some degree of flatness.

Magnetic islands visible in the infrared images show that a $m = 4$ surface lies at a third of the radius shortly before

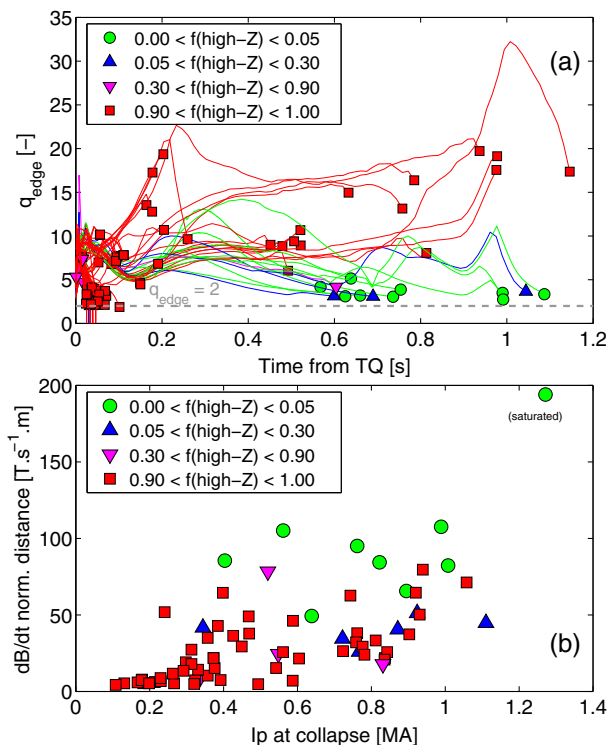


FIG. 2. Development of the collapse-inducing instability. (a) Edge safety factor of RE beams for various fractions of high-Z species in mitigation material. (b) MHD perturbation amplitude normalized to the distance to the sensor versus RE current at termination.

the collapse [37]. The final instability develops without a precursor, and reaches its peak dB/dt in $10\text{--}20 \mu\text{s}$ as shown on Fig. 4(b). The toroidal mode number $n = 1$ determined by a Mirnov coil array is the most probable, consistent with a $q = 4$ instability. q_{edge} is about 5.1 at this stage and the visible $q = 4$ surface is close to the core ($r/a \approx 0.3$); this is therefore further evidence for a non-monotonic q profile. Magnetohydrodynamic simulations of this RE beam using the JOREK code [38,39] have been made [37] using the RE fluid model from Ref. [40] and the current profile estimated above. The dynamics are dominated by tearing mode formation at the two $q = 4$ surfaces

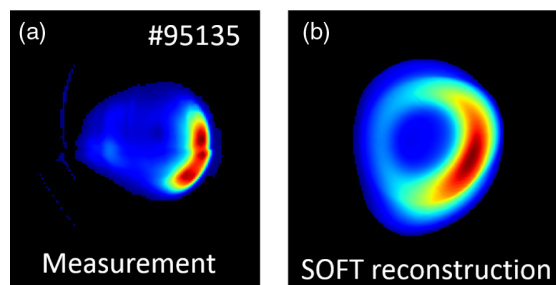


FIG. 3. (a) Measured infrared ($\lambda = 3\text{--}3.5 \mu\text{m}$) synchrotron radiation image. (b) Reconstructed synchrotron radiation using SOFT.

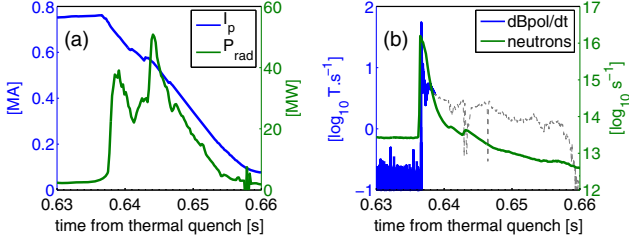


FIG. 4. Collapse of a D_2 -mitigated RE beam. (a) Total current (blue) and radiated power (green). (b) Measured magnetic perturbation amplitude (blue) and neutron rate (green). The dashed part of the curve is the $n = 0$ perturbation due to I_p decay.

leading to a stochastization of the magnetic field first around the outer $q = 4$ surface, followed by the shrinking of the core and the destruction of the entire confinement in about $100 \mu s$ (Fig. 5) on a timescale consistent with the experimental measurements of magnetic fluctuations. During the burst of MHD activity, more than 95% of the REs are lost in the simulation and the current is converted into thermal current while a small current spike appears. The current profile is strongly flattened by fast magnetic reconnection during the MHD event. The simulated RE loss area near the contact point is widened by the edge stochastization.

The normalized growth rate dB_{pol}/dt of the instability measured experimentally is compared between cases where a significant energy is deposited by REs (natural and high- Z injections) and cases with no measurable impacts on Fig. 2(b). The growth rate of the perturbation is larger for D_2 -mitigated than high- Z -mitigated beams, but with overlap. The magnitude $\delta B_{pol}/B_{pol}$ of the instability is even less correlated with wall heat loads. The short timescale of the instability in D_2 cases is therefore a key ingredient of the large RE loss, but not sufficient to explain the absence of heat loads.

Regeneration of runaway electrons.—The prompt loss of REs is followed by a current quench. The current carriers

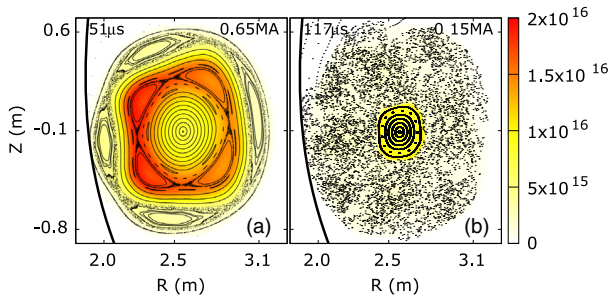


FIG. 5. Poincaré plots at different times in the JOREK simulation showing double tearing mode formation and stochastization starting from the edge. REs are largely lost during the MHD event. (a) $t = 51 \mu s$, (b) $t = 117 \mu s$. Early nonlinear phase is taken as reference time $t = 0$. Background color scale represents n_r .

shift from REs to bulk plasma, thus leading to plasma reionization and a 50 MW radiated power spike [Fig. 4(a)]. Line radiation of weakly ionized argon dominates the current quench, indicating that the argon is not completely purged. For higher argon concentrations some REs are regenerated: a few milliseconds after the initial termination, a small RE beam reappears as evidenced by synchrotron emission (Fig. 6). The current quench rate and the maximum radiated power normalized to the initial magnetic energy are correlated with the ratio of the amount of argon (used to trigger the disruption) to deuterium (in the SPI) as shown in Fig. 7(a). This behavior can be investigated through the following model. In the absence of impurities, the Ohmic reheating of cold plasma is faster than Dreicer and avalanche mechanisms of RE production [41]. If enough impurities remain in the plasma, reheating is hindered by line radiation and the persistent electric field facilitates the RE avalanche. The system of equations governing energy balance, vessel current I_v , total plasma current I , and RE current I_{RE} is solved numerically to analyze the plasma temperature and current evolution self-consistently with the RE generation [42,43]:

$$\begin{aligned} \frac{3}{2} \frac{\partial}{\partial t} n_f T_e &= \frac{(I - I_{RE})^2}{\sigma S^2} - n_f n_Z L(T_e) \\ \frac{d}{dt} (LI + L_v I_v) &= -2\pi R E \\ \frac{d}{dt} (L_v I + L_v I_v) &= -I_v R_v \\ \frac{1}{I_{RE}} \frac{\partial I_{RE}}{\partial t} &\approx \frac{n_f + n_b}{n_f \ln \Lambda_f(p_c) + n_b \ln \Lambda_b(p_c)} \dots \\ &\dots \frac{1}{\sqrt{Z_{RE}(p_c) + 5}} \frac{e(E - E_{crit})}{m_e c} \end{aligned}$$

where the free electron density $n_f = n_D + n_Z Z(T_e)$, n_D and n_Z are deuterium and impurity densities, $Z(T_e)$ and $L(T_e)$ are the mean impurity ionization level and radiation efficiency [44], σ the Spitzer conductivity, S the poloidal cross section area, and R the major radius. The mutual plasma-vessel inductance is taken equal to the vessel

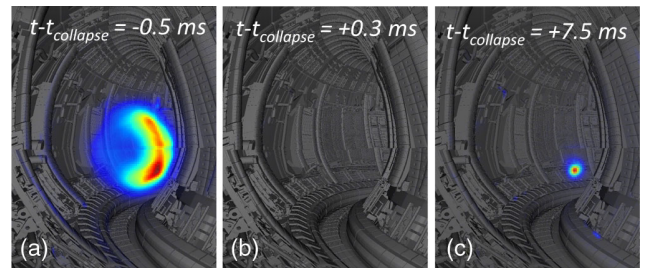


FIG. 6. IR synchrotron emission images (a) just before the RE dissipation (b) just after the RE dissipation, (c) during the final collapse, showing regenerated REs.

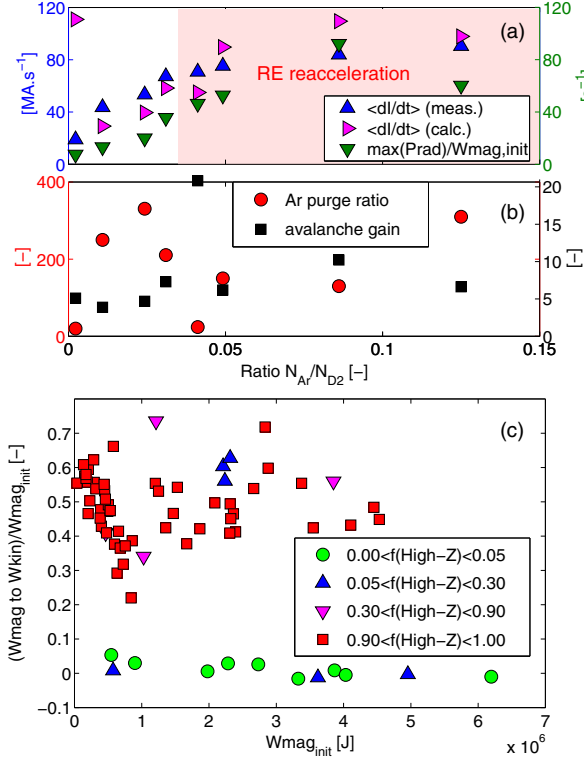


FIG. 7. Effect of the high-Z impurity content on the RE collapse. (a) Current decay rate (measured and calculated by the model), maximum radiated power of the final collapse versus Ar/D₂ ratio from injection material. (b) Calculated argon purge ratio needed to match the radiated power and avalanche gain. (c) Fraction of RE magnetic energy converted into RE kinetic energy during the final collapse versus precollapse magnetic energy for various fractions of high-Z impurities from injection material.

inductance L_v , while the plasma inductance $L \approx L_i + L_v$ (with $L_i \approx 0.5 \mu_0 R l_i$ being the internal plasma inductance). The Rosenbluth-Putvinski avalanche formula [21] is modified to include the effect of partially ionized impurities [28,45], i.e., only a fraction of bound electrons contributes to the friction of fast particles. This fraction is given by the ratio of Coulomb logarithms for free [$\ln \Lambda_f(p_c)$] and bound [$\ln \Lambda_b(p_c)$] electron collisions. In the simulations the quantities $\ln \Lambda_b(p_c)$, $\ln \Lambda_f(p_c)$, and $Z_{\text{RE}}(p_c)$ are taken from Eqs. (27), (29), and (40) of Ref. [41], respectively. The critical momentum $p_c(E)$ is obtained from the acceleration-friction force balance equation. Deuterium density is estimated from the injection amount, while the residual argon density n_Z is chosen such that the maximum radiated power matches the experiment. With the vacuum vessel resistive time $\tau_v = L_v/R_v \approx 5$ ms [46] and its inductance $L_v \approx 2 \mu\text{H}$, the trend in current quench rates obtained from the calculations agrees qualitatively with the experimental measurements [Fig. 7(a)]. Figure 7(b) shows that the argon purge rate $N_{\text{Ar,initial}}/N_{\text{Ar,final}}$ is between 50 and 300. The

calculated avalanche gain is too low to regenerate a full RE beam in these cases but the small increasing trend with Ar/D₂ ratio in Fig. 7(b) highlights the role of residual impurities in the RE regeneration. The cases of pure high-Z SPI can thus be seen as limit cases in which regeneration occurs continuously during the collapse. Note that an ITER full current case would require a larger purge ratio due to the higher RE avalanche amplification.

Continuous RE regeneration during collapse plays a decisive role in the process of conversion of magnetic energy (current carried by REs) into kinetic energy deposited on the wall. For the case presented in Figs. 4(a) and 4(b), the magnetic energy $W_{\text{mag}} \approx 2.2$ MJ is larger than the kinetic energy $W_{\text{kin}} \approx 0.4$ MJ. Therefore damage may arise if a large fraction of W_{mag} is converted into W_{kin} [15,16]. The conversion rate calculated using the method proposed in Ref. [16] adding radiated power as a loss term is shown in Fig. 7(c). The conversion rate is close to zero for cases where the companion plasma contains less than 30% of high-Z impurities. Low-Z and high-Z cases are clearly distinguished showing that benign terminations due to deuterium SPI rely on the weak conversion of W_{mag} to W_{kin} .

Discussion.—A scenario leading to a safe termination of large RE beams is found to be efficient and reproducible on JET. Further experiments are planned to explore the minimum level of companion plasma purity needed to achieve the safe termination scenario and to investigate the conditions in which the MHD instability develops. The applicability of such scenarios to larger tokamaks is an open question: larger avalanche gains are predicted for ITER, therefore simulations are required to assess the accessibility of a regime with a large enough MHD instability and purge ratio. The role of magnetic reconnection will also be investigated further: MHD reconnection is known to lead to such energy conversion in solar plasmas [47], but its role in tokamak plasmas is more ambiguous: it can lead to conversion [48] or the absence of it as reported in the present Letter. Nonetheless, even if some runaway regeneration occurs during the final MHD collapse, only a fraction of the precollapse current will be converted back to REs via the avalanche. It is therefore conceivable that a sequence of harmless RE beam quenches could ensure a safe termination of an arbitrarily large RE beam by multiple deuterium SPIs leading to a stepwise reduction of RE current below the damage threshold. The deuterium RE mitigation scenario reported in the present Letter could therefore potentially solve one of the major issues of future reactors based on the tokamak concept.

This work has been carried out within the framework of the EUROfusion Consortium and has received funding from the Euratom research and training programme 2014-2018 and 2019-2020 under Grant Agreement No. 633053. The views and opinions expressed herein do not necessarily

reflect those of the European Commission. Some of the simulations presented in this article were performed using the Marconi-Fusion supercomputer. This work was supported by the EUROfusion—Theory and Advanced Simulation Coordination (E-TASC). This material is based upon work supported by the U.S. Department of Energy, Office of Science, Office of Fusion Energy Sciences, under Award No. DE-SC0020299.

*Corresponding author.

cedric.reux@cea.fr

†See the author list of “Overview of JET results for optimising ITER operation” by J. Mailloux et al. to be published in Nucl. Fus. Special issue: Overview and Summary Papers from the 28th Fusion Energy Conference (Nice, France, 10–15 May 2021).

- [1] C. T. R. Wilson, The acceleration of β -particles in strong electric fields such as those of thunderclouds, *Math. Proc. Cambridge Philos. Soc.* **22**, 534 (1925).
- [2] A. Gurevich, G. Milikh, and R. Roussel-Dupre, Runaway electron mechanism of air breakdown and preconditioning during a thunderstorm, *Phys. Lett. A* **165**, 463 (1992).
- [3] G. Haerendel, Evidence for field-parallel electron acceleration in solar flares, *Astrophys. J.* **847**, 113 (2017).
- [4] G. D. Holman, Acceleration of runaway electrons and joule heating in solar flares, in *Unstable Current Systems and Plasma Instabilities in Astrophysics*, edited by M. R. Kundu and G. D. Holman (Springer, Dordrecht, Netherlands, 1985), pp. 191–196.
- [5] E. P. Gorbunov and K. A. Razumova, Effect of a strong magnetic field on the magnetohydrodynamic stability of a plasma and the confinement of charged particles in the tokamak machine, *J. Nucl. Energy, Part C* **6**, 515 (1964).
- [6] D. Spicer, An unstable arch model of a solar flare, *Sol. Phys.* **53**, 305 (1977).
- [7] J. Guo, A. G. Emslie, and M. Piana, The specific acceleration rate in loop-structured solar flares—Implications for electron acceleration models, *Astrophys. J.* **766**, 28 (2013).
- [8] L.-G. Eriksson, P. Helander, F. Andersson, D. Anderson, and M. Lisak, Current Dynamics During Disruptions in Large Tokamaks, *Phys. Rev. Lett.* **92**, 205004 (2004).
- [9] R. Gill, B. Alper, A. Edwards, L. Ingesson, M. Johnson, and D. Ward, Direct observations of runaway electrons during disruptions in the JET tokamak, *Nucl. Fusion* **40**, 163 (2000).
- [10] C. Reux *et al.*, Runaway electron beam generation and mitigation during disruptions at JET-ILW, *Nucl. Fusion* **55**, 093013 (2015).
- [11] E. Hollmann *et al.*, Study of argon assimilation into the post-disruption runaway electron plateau in DIII-D and comparison with a 1d diffusion model, *Nucl. Fusion* **59**, 106014 (2019).
- [12] F. Saint-Laurent, G. Martin, T. Alarcon, A. Le Luyer, P. Parks, P. Pastor, S. Putvinski, C. Reux, J. Bucalossi, S. Brémond, and P. Moreau, Overview of runaway electron control and mitigation experiments on Tore Supra and lessons learned in view of iter, *Fusion Sci. Technol.* **64**, 711 (2013).
- [13] R. Nygren, T. Lutz, D. Walsh, G. Martin, M. Chatelier, T. Loarer, and D. Guilhem, Runaway electron damage to the Tore Supra phase III outboard pump limiter, *J. Nucl. Mater.* **241–243**, 522 (1997).
- [14] G. F. Matthews, B. Bazylev, A. Baron-Wiechec, J. Coenen, K. Heinola, V. Kiptily, H. Maier, C. Reux, V. Riccardo, F. Rimini, G. Sergienko, V. Thompson, and A. W. and, Melt damage to the JET ITER-like wall and divertor, *Phys. Scr.* **T167**, 014070 (2016).
- [15] J. Martín-Solís, A. Loarte, and M. Lehnen, Formation and termination of runaway beams in ITER disruptions, *Nucl. Fusion* **57**, 066025 (2017).
- [16] A. Loarte, V. Riccardo, J. Martín-Solís, J. Paley, A. Huber, and M. L. and, Magnetic energy flows during the current quench and termination of disruptions with runaway current plateau formation in JET and implications for ITER, *Nucl. Fusion* **51**, 073004 (2011).
- [17] M. Lehnen *et al.*, Disruptions in ITER and strategies for their control and mitigation, *J. Nucl. Mater.* **463**, 39 (2015).
- [18] L. Baylor, S. Meitner, T. Gebhart, J. Caughman, J. Herfindal, D. Shiraki, and D. Youchison, Shattered pellet injection technology design and characterization for disruption mitigation experiments, *Nucl. Fusion* **59**, 066008 (2019).
- [19] H. Dreicer, Electron and ion runaway in a fully ionized gas. I, *Phys. Rev.* **115**, 238 (1959).
- [20] H. M. Smith and E. Verwichte, Hot tail runaway electron generation in tokamak disruptions, *Phys. Plasmas* **15**, 072502 (2008).
- [21] M. Rosenbluth and S. Putvinski, Theory for avalanche of runaway electrons in tokamaks, *Nucl. Fusion* **37**, 1355 (1997).
- [22] O. Vallhagen, O. Embréus, I. Pusztai, L. Hesslow, and T. Fülöp, Runaway dynamics in ITER-like disruptions in the presence of massive material injection, *J. Plasma Phys.* **86**, 475860401 (2020).
- [23] T. Fülöp, O. Embréus, A. Stahl, S. Newton, I. Pusztai, and G. Wilkie, Kinetic modelling of runaways in fusion plasmas, in *26th IAEA Fusion Energy Conference* (International Atomic Energy Agency (IAEA), 2016), p. 066008.
- [24] D. Shiraki, N. Commaux, L. Baylor, C. Cooper, N. Eidietis, E. Hollmann, C. Paz-Soldan, S. Combs, and S. Meitner, Dissipation of post-disruption runaway electron plateaus by shattered pellet injection in DIII-D, *Nucl. Fusion* **58**, 056006 (2018).
- [25] D. G. Whyte, T. C. Jernigan, D. A. Humphreys, A. W. Hyatt, C. J. Lasnier, P. B. Parks, T. E. Evans, M. N. Rosenbluth, P. L. Taylor, A. G. Kellman, D. S. Gray, E. M. Hollmann, and S. K. Combs, Mitigation of Tokamak Disruptions Using High-Pressure Gas Injection, *Phys. Rev. Lett.* **89**, 055001 (2002).
- [26] E. Hollmann *et al.*, Control and dissipation of runaway electron beams created during rapid shutdown experiments in DIII-D, *Nucl. Fusion* **53**, 083004 (2013).
- [27] F. Saint-Laurent, C. Reux, J. Bucalossi, A. Loarte, S. Brémond, C. Gil, P. Moreau, and J.-L. Segui, Control of runaway electron beams on Tore Supra, *36th EPS Conference on Plasma Phys. Sofia* (European Physical Society, 2009), p. 4.205.
- [28] L. Hesslow, O. Embréus, O. Vallhagen, and T. Fülöp, Influence of massive material injection on avalanche

- runaway generation during tokamak disruptions, *Nucl. Fusion* **59**, 084004 (2019).
- [29] C. Reux *et al.*, Runaway beam studies during disruptions at JET-ILW, *J. Nucl. Mater.* **463**, 143 (2015).
- [30] C. Paz-Soldan, N. W. Eidietis, Y. Q. Liu, D. Shiraki, A. H. Boozer, E. M. Hollmann, C. C. Kim, and A. Lvovskiy, Kink instabilities of the post-disruption runaway electron beam at low safety factor, *Plasma Phys. Controlled Fusion* **61**, 054001 (2019).
- [31] S. Sridhar, C. Reux, P. Beyer, M. Lehnen, I. Coffey, R. Guirlet, and N. Fedorczak (JET contributors), Characterization of cold background plasma during the runaway electron beam mitigation experiments in the JET tokamak, *Nucl. Fusion* **60**, 096010 (2020).
- [32] G. Pautasso, M. Dibon, M. Dunne, R. Dux, E. Fable, P. Lang, O. Linder, A. Mlynek, G. Papp, M. Bernert, A. Gude, M. Lehnen, P. McCarthy, and J. Stober, Generation and dissipation of runaway electrons in ASDEX upgrade experiments, *Nucl. Fusion* **60**, 086011 (2020).
- [33] J. Mlynar *et al.*, Runaway electron experiments at COMPASS in support of the EUROfusion ITER physics research, *Plasma Phys. Controlled Fusion* **61**, 014010 (2019).
- [34] E. M. Hollmann, I. Bykov, N. W. Eidietis, J. L. Herfindal, A. Lvovskiy, R. A. Moyer, P. B. Parks, C. Paz-Soldan, A. Y. Pigarov, D. L. Rudakov, D. Shiraki, and J. Watkins, Study of argon expulsion from the post-disruption runaway electron plateau following low- z massive gas injection in DIII-D, *Phys. Plasmas* **27**, 042515 (2020).
- [35] H. Pacher, I. Smid, G. Federici, Y. Igitkhanov, G. Janeschitz, R. Raffray, and G. Vieider, Erosion lifetime of ITER divertor plates, *J. Nucl. Mater.* **241–243**, 255 (1997).
- [36] M. Hoppe, O. Embréus, R. Tinguely, R. Granetz, A. Stahl, and T. Fülöp, SOFT: A synthetic synchrotron diagnostic for runaway electrons, *Nucl. Fusion* **58**, 026032 (2018).
- [37] V. Bandaru, M. Hoelzl, C. Reux, O. Ficker, S. Silburn, M. Lehnen, N. Eidietis, and J. Team, Magnetohydrodynamic simulations of runaway electron beam termination in JET, *Plasma Phys. Controlled Fusion* **63**, 035024 (2021).
- [38] G. Huysmans and O. Czarny, MHD stability in x-point geometry: Simulation of ELMs, *Nucl. Fusion* **47**, 659 (2007).
- [39] M. Hoelzl *et al.*, The JOREK non-linear extended MHD code and applications to large-scale instabilities and their control in magnetically confined fusion plasmas, [arXiv: 2011.09120](https://arxiv.org/abs/2011.09120) [*Nucl. Fusion* (to be published)].
- [40] V. Bandaru, M. Hoelzl, F. J. Artola, G. Papp, and G. T. A. Huijsmans, Simulating the nonlinear interaction of relativistic electrons and tokamak plasma instabilities: Implementation and validation of a fluid model, *Phys. Rev. E* **99**, 063317 (2019).
- [41] B. N. Breizman, P. Aleynikov, E. M. Hollmann, and M. Lehnen, Physics of runaway electrons in tokamaks, *Nucl. Fusion* **59**, 083001 (2019).
- [42] J. R. Martín-Solis, A. Loarte, and M. Lehnen, On the avalanche generation of runaway electrons during tokamak disruptions, *Phys. Plasmas* **22**, 082503 (2015).
- [43] P. Aleynikov and B. N. Breizman, Generation of runaway electrons during the thermal quench in tokamaks, *Nucl. Fusion* **57**, 046009 (2017).
- [44] H. Summers, M. O’Mullane, A. Whiteford, N. Badnell, and S. Loch, ADAS: Atomic data, modelling and analysis for fusion, *Ame. Inst. Phys.* **901**, 239 (2007).
- [45] J. R. Martín-Solis, A. Loarte, and M. Lehnen, Runaway electron dynamics in tokamak plasmas with high impurity content, *Phys. Plasmas* **22**, 092512 (2015).
- [46] R. Albanese, M. Mattei, and F. Villone, Prediction of the growth rates of VDEs in JET, *Nucl. Fusion* **44**, 999 (2004).
- [47] V. V. Zharkova, A. O. Arzner, K. Benz, P. Browning, C. Dauphin, A. G. Emslie, L. Fletcher, E. P. Kontar, G. Mann, M. Onofri, V. Petrosian, R. Turkmani, N. Vilmer, and L. Vlahos, Recent advances in understanding particle acceleration processes in solar flares, *Space Sci. Rev.* **159**, 357 (2011).
- [48] S. J. Freethy, K. G. McClements, S. C. Chapman, R. O. Dendy, W. N. Lai, S. J. P. Pamela, V. F. Shevchenko, and R. G. L. Vann, Electron Kinetics Inferred from Observations of Microwave Bursts During Edge Localized Modes in the Mega-amp Spherical Tokamak, *Phys. Rev. Lett.* **114**, 125004 (2015).

RE beam generation in MGI disruptions on COMPASS

O. Ficker^{1,2,#}, J. Mlynar¹, E. Macusova¹, M. Vlainic⁴, V. Weinzettl¹, J. Urban¹,
J. Cerovsky^{1,2}, M. Farnik^{1,2}, T. Markovic^{1,3}, R. Paprok^{1,3}, P. Vondracek^{1,3},
M. Imrisek^{1,3}, M. Tomes^{1,3}, J. Havlicek¹, J. Varju¹, M. Varavin¹,
O. Bogar^{1,5}, A. Havranek^{1,6}, M. Gospodarczyk⁷, M. Rabinski⁸, M. Jakubowski⁸,
K. Malinowski⁸, J. Zebrowski⁸, V. Plyusnin⁹, G. Papp¹⁰, R. Panek¹, M. Hron¹,
the COMPASS team¹ & the EUROfusion MST1 Team*

¹Institute of Plasma Physics of the CAS, Prague, Czech Republic, ²FNSPE, Czech Technical University in Prague, Prague, Czech Republic, ³Faculty of Mathematics and Physics, Charles University, Prague, Czech Republic, ⁴Department of Applied Physics, Ghent University, Gent, Belgium, ⁵ Faculty of Mathematics, Physics and Informatics, Comenius University, Bratislava, Slovakia, ⁶FEE, Czech Technical University in Prague, Prague, Czech Republic, ⁷ University of Rome Tor Vergata, Rome, Italy, ⁸ National Centre for Nuclear Research (NCBJ), Otwock-Swierk, Poland, ⁹ IST - IPFN, Lisbon, Portugal, ¹⁰IPP, Garching, Germany, #ficker@ipp.cas.cz

* See the author list of "Meyer et al, Overview of progress in European Medium Sized Tokamaks towards an integrated plasma-edge/wall solution, accepted for publication in Nuclear Fusion"

Introduction. Despite extensive experimental and modelling work in the last several decades that was intensified in the last couple of years, it is yet unsure whether a generation of runaway electron (RE) beam in ITER during the mitigated disruption may be prevented. And if not, whether we have an efficient tool to safely terminate and mitigate the beam itself [1]. High Z impurity massive gas injection (MGI) or pelet triggered disruptions in medium size and large machines are currently the major tool of experimental investigation of this phenomena, while modelling focuses on solutions of the individual problems in the field where many key questions still remain open and the effort to model the disruption with RE beam generation in its full complexity is at the very beginning. The COMPASS tokamak[2] is a small device with an ITER-like shaped plasmas operated by the Institute of Plasma Physics of the Czech Academy of Sciences. Major radius of the machine spans $R_0 = 0.56$ m and minor radius $a = 0.23$ m. The typical toroidal field is $B_T = 1.15$ T and plasma current in the flat-top phase may be in the range $I_p = 80 - 400$ kA. The divertor D-shaped configuration allows routine H-mode operation, either Ohmic or NBI assisted (2x300 kW, 40 keV), while the limiter circular configuration is useful, among others, for the studies of runaway electrons (RE). The COMPASS tokamak has been contributing to the RE-related research since 2014. The COMPASS experiments are normally deuterium fuelled and the typical pulse length is about 0.4 s, although the low current

circular discharge with high fraction of RE can last up to one second. COMPASS RE team contributes to both the runaway studies in the flattop of low density discharges and disruptive scenarios with Ar or Ne MGI. Interesting effects of shaping [3] and relation of RE losses and various magnetic oscillations [4] have been observed in the flattop. The continuing effort in the terms of understading of MGI generated RE beams has been reported namely in [5].

Diagnostics. COMPASS is equipped by a large set of diagnostics coils [6], e.g. $3 \times 3 \times 24$ Mirnov coils and 16 calibrated internal partial Rogowski coils, that allow for a detailed study of MHD perturbations during the disruption. The diagnostics of lost RE is based namely on two HXR NaI(Tl) scintillation detectors and one Pb-shielded composite scintillator sensitive to photoneutrons and high flux of HXR. These detectors

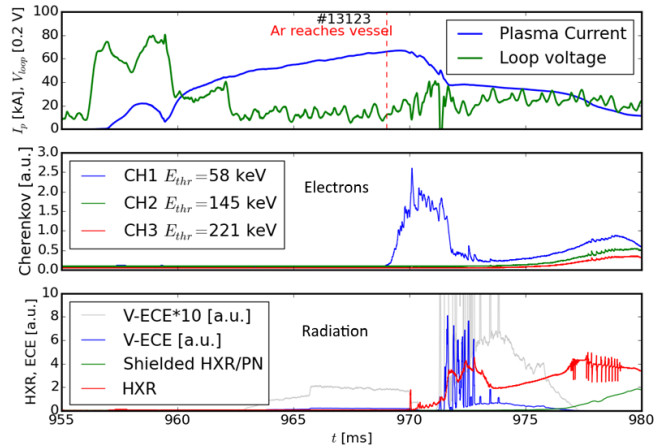


Figure 1: Ramp-up MGI RE scenario

are typically measuring the interaction with the outer midplane protection limiter or central column limiters. Moreover, the lost runaway electrons may be detected earlier by the state-of-the-art Cherenkov detector (developed by NCBJ). This detector is located at a radially movable manipulator on the outer midplane of COMPASS. The detector measures directly electrons with a 3-channel energy resolution ($E_{thr1,2,3} = 58, 157, 211$ keV) thanks to the different thickness of the Mo coating layer of the CVD diamond crystal. Another rather special diagnostics is a 16-channel radiometer (76-90 GHz) measuring the suprathermal component of electron population via the 3rd and the higher harmonics of the electron cyclotron emission (ECE). As the line of sight of the detector is vertical (VECE), there is no influence of $B_T(r)$ and the measured radiation is a function of parallel and perpendicular components of electron velocity only. This detector should be sensitive to electrons namely in the range of 50-100 keV. The evolution of the MGI disruption has been also observed by the fast visible range camera Photron Mini UX-100 with a standard frame rate of 8 kfps.

Scenario. The typical disruption with RE beam generation is achieved in the current ramp-up phase, 10-25 ms after the plasma breakdown with a pre-disruptive current $I_p = 60 - 100$ kA. With B_T constant in time, this gives rather high $q_{95} = 5 - 6$. The disruption is triggered by an Ar MGI (solenoid valve placed outside the reach of large magnetic fields) in the pressure range $p_{MGI} = 0.8 - 3$ bar. This corresponds to number of injected Ar atoms $N_{Ar} = 1 - 5 \cdot 10^{20}$. In

Fig. 1, time traces of the relevant signals are displayed - in the top graph (displaying plasma current I_p and loop voltage U_{loop}) the phases of the disruption may be identified - after the Ar injection, thermal quench (TQ) occurs (slightly visible in ECE, Thomson scattering signal not displayed here), followed by the current quench easily noticeable in the I_p signal. The current does not reach zero like in a normal disruption but stabilises at the value of several tens of kA - it enters the RE beam plateau phase, which later terminates due to position instability or decay of the beam. In the center graph of Fig. 1, the signals from the three channels of the Cherenkov detector are displayed. Interestingly, the first channel shows a strong signal immediately after the Ar injection, while the other two experience continuous increase of signal in the beam plateau phase. The VECE displayed in the third graph shows very interesting spiky signal already in the beam plateau phase, which is analysed in further text, while the HXR unshielded detector shows spikes during the current steps in the CQ and rather continuous signal later. Given the energy range of the different detectors, it can be perhaps concluded that 50-100 keV runaway electrons dominate the disruption phase.

MHD perturbation during current quench. The relation between the magnetic perturbation level in the CQ and the resulting RE current in MGI disruptions was considered important and analysed on various machines, e.g. TEXTOR[7]. However it seems that different components of the frequency spectrum may be important. Moreover, COMPASS MGI disruptions with RE generation seem not to follow the claim that the RE beam generation should not be possible in $B_T < 2\text{ T}$ [4]. In Fig. 2, the effect of perturbations from the high frequency part of the spectrum ($f > 10\text{ kHz}$) on the runaway beam generation (achieved runaway current) for COMPASS ramp-up MGI discharges is displayed. The whole set of 16 Mirnov coil encircling the plasma poloidally is used for the analysis and thus the effect of position instability is partially compensated. However, toroidal asymmetries (MGI vs coil ring position) and different vessel conditions may still affect the observations. It seems that for higher mean square amplitude of magnetic perturbation, the generation of the beam is less probable, although it is difficult to obtain a clear threshold. Similarly, a linear decreasing trend may be observed in Fig. 2 but the points are rather clusterised. The relative perturbation is in the order of 10^{-3} which is expected to be the critical value to allow the generation of the beam.

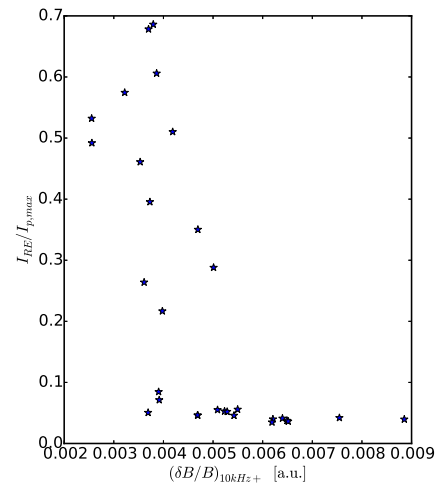


Figure 2: High frequency magnetic perturbation during CQ vs runaway current

Beam plateau stage - filaments. The most interesting and unique feature observed in the MGI experiments on COMPASS are the highlighted filaments in the early beam plateau phase (see Fig. 3, center frame) that appear to be accompanied by the spikes of the vertical ECE, small Mirnov coil bursts and followed by an increase of Cherenkov CH1 signal and later also HXR signal. The FWHM of the spikes in the ECE signal seems to be $20\mu\text{s}$. This value compared, to the frame rate of the fast camera (8 kfps), may explain why the filaments are caught always just in one frame. As the exposure time is smaller than the inverse value of the framerate, some filaments might be missed. To prove that the spikes in the ECE data and filaments in the camera correspond to the same phenomena it is necessary to correlate the time stamps of the events. The result is positive, almost each large peak coincides with a filament in the studied discharges.

Conclusions. MGI disruptions using argon in the ramp-up phase of the COMPASS discharge may lead to generation of the runaway electron beam. It seems that lower global levels of magnetic perturbations are more beneficial for the beam generation and larger beam current. Surprisingly, low toroidal field of COMPASS is still sufficient for the beam generation. The current quench is accompanied by prompt losses of low energy RE, detected by the Cherenkov detector. Furthermore, small bursts of magnetic perturbation, spikes of fast-particle-related signal on the VECE and loss increases measured by HXR or Cherenkov detector in the early beam plateau phase are correlated with filaments observed in the camera images. This indicates that the phenomena might be related to a MHD-like decay of the beam at the early stage.

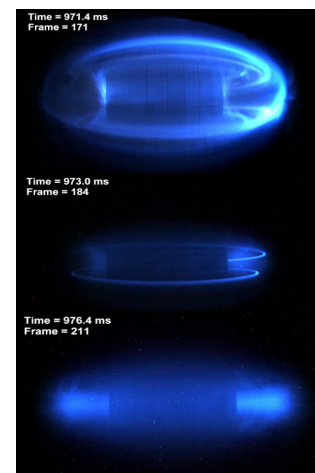


Figure 3: Camera images of CQ and RE beam phase

Acknowledgement. This work has been supported by MEYS projects LG14002 and LM2015045 and carried out within the framework of the EUROfusion Consortium. It has also received funding from the Euratom research and training programme 2014-2018 under grant agreement No 633053 with the Co-fund by MEYS project number 8D15001. The views and opinions expressed herein do not necessarily reflect those of the European Commission.

References

- [1] Reux C. *et al.* 2015 *Nucl. Fusion* **55** 129501
- [2] Panek R. *et al.* 2016 *Plas. Phys. Contr. Fusion* **58** 014015
- [3] Mlynar J. *et al.*, 2015 *42nd EPS Conf. on Plasma Physics (Lisbon, Portugal)* P4.102
- [4] Ficker O. *et al.* 2017 *Nuclear Fusion* **57** 076002
- [5] Vlainic M. *et al.* 2015 *J. Plasma Phys.* **81** 475810506
- [6] Weinzettl, V. *et al.*, 2017, Progress in diagnostics of the COMPASS tokamak. *Submitted to J. Inst.*
- [7] Zeng L. *et al.* 2013 *Phys. Rev. Lett.* **110** 235003
- [8] Macusova E. *et al.* 2017 *44th EPS Conf. on Plasma Physics (Belfast, UK)* P4.141

Analysis of MGI disruptions and runaway electron beams at COMPASS using tomography and fast camera data

O. Ficker^{1,2}, M. Imrisek^{1,3}, J. Mlynar¹, E. Macusova¹, J. Svoboda², V. Weinzettl¹, J. Urban¹,
A. Havranek¹, J. Cerovsky^{1,2}, M. Farnik^{1,2}, O. Grover^{1,2}, M. Hron¹, R. Panek¹, V. Plyusnin⁵,
M. Vlainic⁴, the COMPASS team¹ & the EUROfusion MST1 Team*

¹*Institute of Plasma Physics of the CAS, Prague, Czech Republic (ficker@ipp.cas.cz)*

²*FNSPE, Czech Technical University in Prague, Prague, Czech Republic*

³*Faculty of Mathematics and Physics, Charles University, Prague, Czech Republic*

⁴*Institute of Physics, University of Belgrade, Belgrade, Serbia*

⁵*IST - IPFN, Lisbon, Portugal*

* See the author list "H. Meyer et al 2017 Nucl. Fusion 57 102014"

Introduction. The phenomenon of runaway electron (RE) beam generated during a tokamak disruption is a continuous challenge for modelling. Moreover, experiments on smaller devices can only partly mimic the expected parameters of ITER disruptions and the scaling of these complex transient processes is far from being clear. Despite this, smaller machines are one of the key ingredients in the strategy to find a reliable RE mitigation method as they can help to analytically clarify the open questions related to this issue using a relatively large number of discharges and higher flexibility in the diagnostics and feedback set-up. The COMPASS tokamak[1] is a small device with an ITER-like shaped plasmas operated at the IPP of the Czech Academy of Sciences. Major radius of the machine spans $R_0 = 0.56\text{m}$ and minor radius $a = 0.23\text{m}$. It is operated with magnetic field $B_T = 0.9 - 1.5\text{T}$ and plasma current in the flat-top phase in the range $I_p = 80 - 400\text{kA}$. Despite the main scope of the machine being the edge plasma physics and plasma-wall interaction including studies of H-mode nad L-H transition, the COMPASS RE team contributes to both the runaway studies in the flattop of low density discharges and disruptive scenarios with Ar or Ne MGI [2]. A significant attention is also given to the studies of the effect of perturbed magnetic field on RE [3], lately including the resonant magnetic field (RMP) system, as presented at this conference [4].

Tomography and AXUV detectors. The reconstruction of 2D profiles of radiation from plasma cross-section using data from multi-LOS systems is a well known and often utilised data analysis process at tokamaks. However, disruption and RE beam phase requires an especially careful check of the raw data and special border conditions so automated routines can be rarely used. The AXUV system of COMPASS consists of 6 20-LOS pinhole cameras with semiconductor chips. Unfortunately, during the disruptions with runaway electron beam gener-

ation or injection to RE dominant discharges, most of these cameras cannot be used as they are affected by HXR radiation from walls (direct or through X-ray fluorescence in surrounding metals), do not have enough signal (before injection) or are affected by strong noise. The only fully reliable camera is the AXUV "F" detector with increased slit size and location safe from high HXR fluxes (HFS bottom) which still allows to resolve radial profile. The tomographic software used at COMPASS, but also e.g. at JET, is based on Tikhonov regularisation with minimising of Fisher information (MFI) with optimal solution discriminated using the expected detector errors and preferential smoothing along magnetic flux contours. This technique can be used even with a single camera and allows to get spatially reliable reconstructions (in radial coordinate) if optimal border shape is selected. Using smooth border of a big circular plasma shape 1, slightly separated from limiters, allows to suppress apparent artefacts at the bottom of the machine and discriminate the wall radiation. On the other hand, if we are interested in RE beam or plasma-wall interaction, a layer around the chamber wall can be used as the reconstruction area. If the reconstruction can be considered reliable, useful information can be obtained: spatial and time propagation of gas during MGI ($v_{diff,AXUV}$), total radiated power (P_{rad} in the AXUV sensitivity region - comparison, time evolution), position and profile of the beam gas interaction, etc.

RE diagnostics and cameras.

The full COMPASS diagnostics is listed in the overview paper [5]. The diagnostics of lost RE at COMPASS is based namely on shielded and unshielded HXR detectors and Cherenkov detector, while low energy RE in the plasma can be detected also by vertical ECE system. The evolution of the MGI disruption and RE beam phase has been observed by the two fast visible

range color cameras Photron Mini UX-100 with a standard frame rate 5 kfps (4 or 8 kfps or 40 kfps in dedicated discharges with reduced field of view). For selected discharges also the state-of-the-art Photron SA-X2 has been used (up to 100 kfps as an overview camera or focused on a small area within the beam). The camera data can contribute to the studies of these scenarios in many ways: time, spatial and color (gas ion species) evolution of radiation (gas penetration,

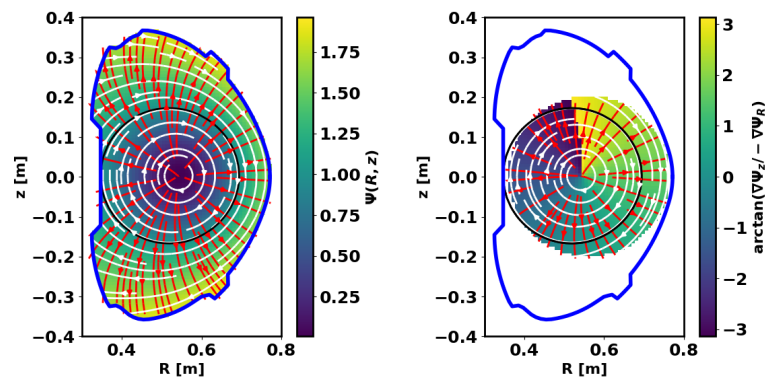


Figure 1: *Left: Normalised poloidal magnetic flux, its gradient and contours used in the MFI tomographic reconstruction. Right: Arcus tangents of the gradient ratio that is used in the smoothing matrix of MFI, limited to the optimised reconstruction area.*

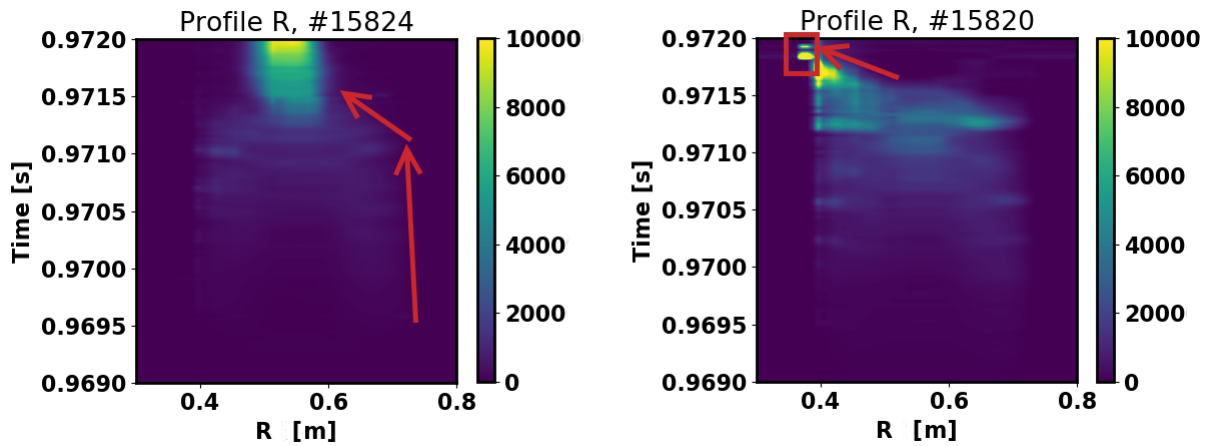


Figure 2: Radial profile of AXUV radiation during the massive gas injection. Left: successful beam generation. Right: No beam generated, just current quench - HFS termination

ionisation, 2 gas species interaction, beam-gas interaction position and 'profile', ...), additional broad range HXR detector (number of saturated pixels/dots), analysis of instabilities, etc. Based on the spectral sensitivity range of the cameras, in case of Ne, namely Ne I lines (orange region) and in case of Ar, the Ar II lines (blue region) are detected.

Ramp-up MGI, AXUV and camera evolution. As described in the invited talk [4], the first scenario used at COMPASS for RE beam generation relies on injection of roughly 10^{20} Ar atoms to the current ramp-up stage of a low density discharge, this often leads to a classical disruption with generation of a radially unstable RE beam that carries tens of percent of the pre-disruptive current or a "full conversion" with a smooth decay of the beam. AXUV data may help to clarify the variety of possible results. A comparison of radial profiles of tomographic reconstructions for the successful beam generation and no beam disruption, which apparently ends by the HFS termination in the critical phase of RE beam generation, can be seen in 2. This kind of termination occurred for the low B_t cases in the toroidal field scan. However, the exact reason why the lower B_t discharges are unstable in the beam generation phase is still a question. Furthermore, in the case of beam generation the radiation peaks on magnetic axis almost 1 ms earlier than on the camera, which corresponds to the different energies of measured radiation and seems to be linked to the generation of the supra-thermal particles in the core. It seems that the radiation front propagation speed increases as the gas is approaching the core.

Flattop scenario - radiated power, comparison of MGI and gas puff discharges The other scenario used at COMPASS, mostly for the beam decay experiments, was also presented during the invited talk. In this case, $< 10^{19}$ (gas puff) or $\sim 10^{20}$ (MGI) Ar or Ne atoms are injected to a flattop of low density discharge with a sufficient RE seed causing a 'thermal quench' and

no immediate current quench. The RE beam then decays with a rate proportional to the gas amount. Consistently with this, also the radiated power based on AXUV tomography seems to be in a linear relation with the current decay rate, slightly larger for Ne for given $\frac{dI}{dt}$.

Conclusions. The MGI triggered disruptions with occasional RE beam generation were investigated using the AXUV tomographic reconstruction. Despite only one fully reliable camera being available during this scenario, the reconstructions provided very

interesting information that radiation propagates to the core with increasing speed and that it peaks on axis (AXUV) well before Ar II radiation (camera). Also, the unsuccessful cases with no beam apparently ended with radial position instability during the beam creation phase. The AXUV radiation and cameras were also used in the study of beam decay phase under controlled conditions (flattop, no external loop voltage during beam decay). It appears that total radiated power is increasing linearly with the order of magnitude of the injected gas amount and with the current decay rate. The color camera allows to track the Ne I (neutral, orange) and Ar II (charged, blue) gas species/radiation.

Acknowledgement. The work has been supported by the grant GA18-02482S of the Czech Science Foundation. This work has been supported by MEYS projects LG14002 and LM2015045 and carried out within the framework of the EUROfusion Consortium. It has also received funding from the Euratom research and training programme 2014-2018 under grant agreement No 633053 with the Co-fund by MEYS project number 8D15001. The views and opinions expressed herein do not necessarily reflect those of the European Commission. This work was supported by the Grant Agency of the Czech Technical University in Prague, grant No. SGS17/138/OHK4/2T/14.

References

- [1] Panek R. *et al.* 2016 *Plas. Phys. Contr. Fusion* **58** 014015
- [2] Vlaine M. *et al.* 2015 *J. Plasma Phys.* **81** 475810506
- [3] Ficker O. *et al.* 2017 *Nuclear Fusion* **57** 076002 (10pp)
- [4] Mlynar J. *et al.* 2018 *45th EPS Conf. on Plasma Physics (Prague, Czech Republic)* I1.002
- [5] Weinzettl, V. *et al.* 2017 *Journal of Instrumentation* **12** C12015

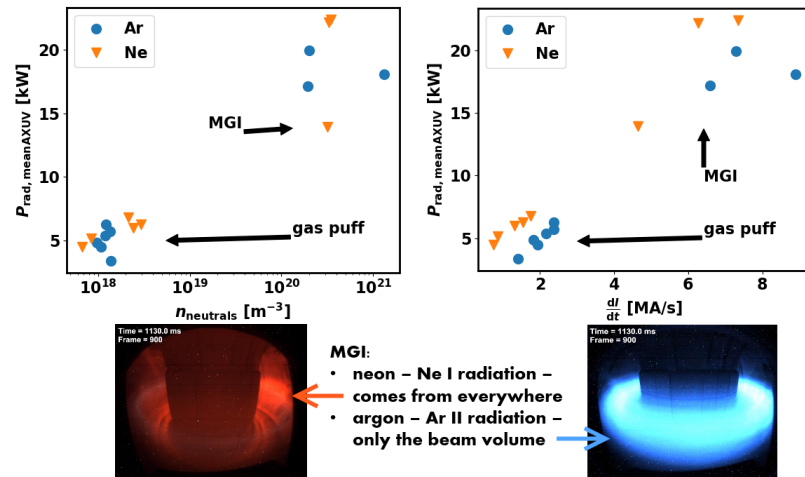


Figure 3: Top right: Relation of the density of neutrals in the vessel after the puff and the mean radiated power. Top left: Mean current decay rate of RE beam versus the mean radiated power. Bottom: Comparison of camera images from the beam decay phase in Ar and Ne after the MGI.

Analysis of RE beams in COMPASS and JET using betatron equilibrium and radiation diagnostics

O. Ficker^{1,2,#}, E. Macusova¹, J. Cerovsky^{1,2}, L. Kripner^{1,3}, A. Dal Molin⁴, S. Silburn⁵,
C. Reux⁶, M. Hoppe⁷, C. Sommariva⁸, E. Joffrin⁶, G. Ghillardi⁹, R. A. Tinguely¹⁰,
J. Mlynar^{1,2}, E. Panontin⁴, M. Nocente⁴, M. Tardocchi¹¹, S. Jachmich¹², C. Paz-Soldan¹³,
P. Vondracek¹, A. Casolari¹, M. Farnik^{1,2}, J. Caloud^{1,2}, V. Weinzettl¹, J. Cavalier¹,
J. Havlicek¹, A. Havranek¹, M. Imrisek^{1,3}, J. Svoboda^{1,2},
M. Hron¹, the COMPASS team^a & JET Contributors^b

[#]ficker@ipp.cas.cz ¹IPP CAS, Prague, Czech Republic; ²FNSPE, CTU in Prague, Prague, Czech Republic; ³FMP, Charles university, Prague, Czech Republic; ⁴Universita degli Studi di Milano-Bicocca, Milan, Italy; ⁵JET, CCFE, Culham, UK; ⁶IRFM, CEA, Saint-Paul-lez-Durance, France; ⁷Chalmers University of Technology, Gothenburg, Sweden; ⁸Ecole Polytechnique Fédérale de Lausanne (EPFL), Swiss Plasma Center (SPC), CH-1015 Lausanne, Switzerland ⁹ENEA, Frascati, Italy; ¹⁰PSFC, MIT, Cambridge, USA ¹¹ISTP-CNR, Milan, Italy; ¹²ITER I.O., Saint-Paul-lez-Durance, France; ¹³Columbia University, NY, USA; ^aAuthor list of "M. Hron et al. 2021 'Overview of the COMPASS results' submitted to Nucl. Fusion"; ^bSee the author list of 'Overview of JET results for optimising ITER operation' by J. Mailloux et al. to be published in Nuclear Fusion Special issue: Overview and Summary Papers from the 28th Fusion Energy Conference (Nice, France, 10-15 May 2021)"

Introduction

Runaway electrons (RE) still present a serious for the tokamak operation. Furthermore, the physics phenomenon itself is complicated and extrapolation to the large devices is difficult. In order to understand the RE phenomenon, it is necessary to optimise the diagnostics of the runaway electrons. Some of the properties of RE can be measured using the standard tokamak diagnostics directly (e.g. plasma or runaway current measurement by magnetic diagnostics). In some cases, it is necessary to improve the understanding of the effect of the RE on the diagnostics (e.g. electron cyclotron emission measurement by radiometer) by modelling and analytical approximations. However, often it is necessary to introduce a completely new diagnostics, that can be used specifically for RE (e.g. local loss measurement using a Cerenkov detector). In this contribution a new application of magnetic measurements for estimation of the RE energy is discussed for two European machines with extensive RE experimental program. The COMPASS tokamak [1] is a device with ITER-like plasma shape operated at the IPP of the Czech Academy of Sciences. Major radius of the machine spans $R_0 = 0.56$ m and minor radius $a = 0.21$ m. It is operated with magnetic field $B_T = 0.9 - 1.5$ T and the current in the runaway electron beam phase $I_p < 150$ kA. The overview of the latest RE experiments is presented at this Conference [2]. The JET tokamak is the largest tokamak device currently in full operation with $R_0 = 3$ m and with ITER-like plasma facing component materials (Be/W). The RE experiments are typically conducted in $B_t = 3 - 3.5$ T and with runaway electron beam currents up to 1.2 MA. In the latest RE experiments using the Shattered pellet injector (SPI) [3], very interesting results were achieved with D2 secondary injection causing increase of the RE beam current, most probably decrease of the kinetic energy and a benign termination of the RE beam triggered by the non-monotonic current profile [4].

Runaway electron equilibrium

The equilibrium of the high current RE beams was studied in high current plasma assisted modified (with toroidal field B_t added) betatrons. Later, it was also theoretically and numerically studied in the tokamak geometry by Yoshida [5]. Based on the application in the betatron physics, the main change with respect to the tokamak equilibrium based on the poloidal mag-

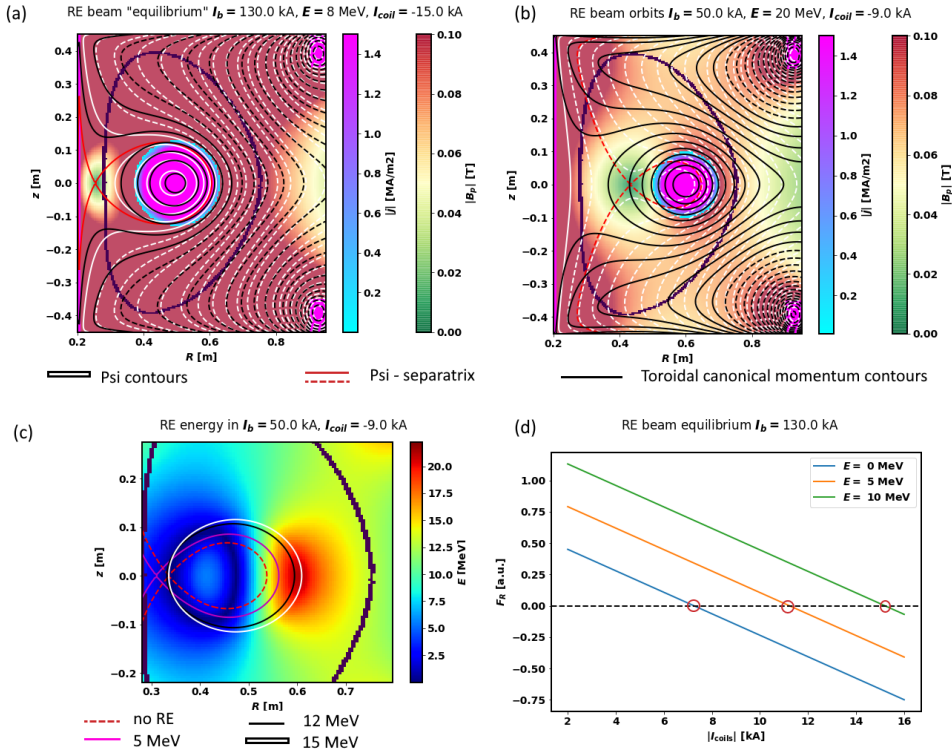


Figure 1: *COMPASS* geometry: (a) Runaway electron beam with current 130 kA and energy 8 MeV in equilibrium with the magnetic field; (b) high energy fraction in the low current RE beam being limited at the LFS; (c) Map of stable energies in the R, z plane and separatrix for different energies; (d) Radial force acting on the mono-energetic RE beam

netic flux Ψ , the equilibrium parameters in the RE beam are functions of toroidal canonical momentum (P_ϕ), the surfaces of constant P_ϕ are also called drift surfaces and

$$P_\phi(R, z) = \gamma m_e R c - e \psi(R, z), \quad (1)$$

with γ being the relativistic factor, R the radius coordinate and m_e , c and e known constants. A modified version of Grad-Shafranov equation can be introduced to analyse this equilibrium, however for a quick estimate of energy with higher order effects neglected, it is possible to use 2D cyclic symmetry Biot-Savart solver in real coil geometry to simulate the equilibrium of the RE beam and the external PF coils. At *COMPASS* this task is relatively easy as winding that is dedicated to securing the radial equilibrium of the plasma is not connected to the winding with other purposes. The equilibrium field power supply (EFPS) and fast B_v power supplies (position stability) are actuating the radial position. The strong RE outward pressure is contributing to feedback request and may cause β_N values up to 40% when standard EFIT reconstruction is used. The effect is so strong that standard position control feedback scheme was not able to sustain the required position in case of decreasing current and increasing energy. This was solved by weakening the dependence of the control algorithm on the current, this special setup is appropriate only for the RE beam phase. In figure 1 some properties of quasi-equilibria of some combinations of RE beam current, currents in the coils and RE beam energy are shown together with a (R, z) map of optimal energies that would be sustained in given vertical magnetic field in case of no poloidal motion (external + from beam current) and Ψ or P_ϕ "separatrix", which contains a HFS X-point in the vessel for low energy components and the companion plasma. The last plot shows the total radial force acting on the RE beam of given current and energy

with different equilibrium coil currents.

Estimate of energy in COMPASS experiments

The experimental estimates of energy in a small device can be based on two methods using the magnetic configuration data: Method 1 - using the EFIT β_N that gives a pressure related to I_p , B_t and a : $E_\beta[\text{MeV}] = 3.75\beta_N a B_t$; Method 2 - Simple inversion of radial control equation [6] $E_{FB}[\text{MeV}] = RcB_v^{an}/10^6$, where B_v^{an} is the vertical magnetic field that is needed for radial stability on top of the value necessary for sustaining the plasma of the given current. The first method gives an estimate of the energy for which the beam is in equilibrium with the external vertical field, while the second gives a more dynamically evolving estimate that corresponds to the maximum energy that can be confined by the B_v^{an} only. Comparison of the two methods is given in figure 2. The RE beam in #21286 was triggered by Ne gas puf and further accelerated by fixed Ohmic current drive. The envelope as well as log-average of the HXR-derived energy spectra is rising in agreement with the derived quantities. In the Ar injection triggered discharge #21107, the synchrotron radiation power in the near IR region also follows the derived energy quantities. In figure 3 the comparison of energy estimate evolution in different gases is shown, the most important conclusion is that the D2 injection can stop the rise of energy, while the decay of current still continues though it is slowed down.

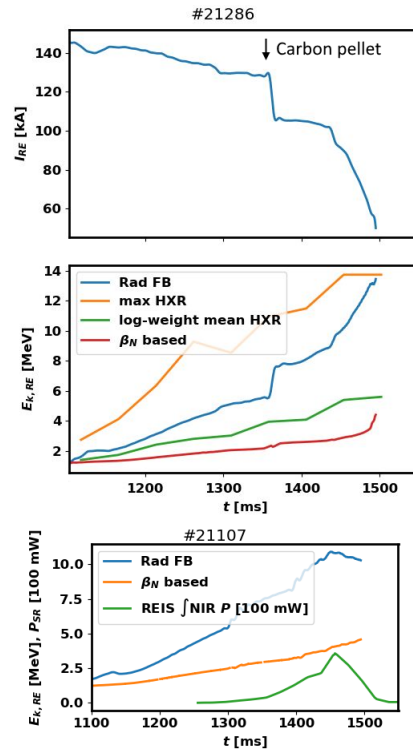


Figure 2: COMPASS: Comparison of evolution of quantities related to RE beam energy for the discharges with additional acceleration #21286 (Ne + C pellet) and #21107 (Ar)

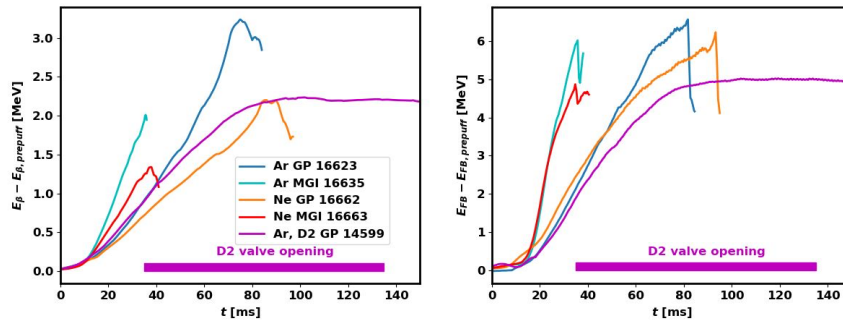


Figure 3: COMPASS data; Left: Evolution of energy based on the EFIT β_N for two MGI triggered RE beams, two beams created by the low impurity injection amount and one with secondary deuterium injection, right estimate based on radial position feedback for the same discharges.

Estimates of energy for JET

Method 1 was used applied to JET, which is characterised by larger minor and major radius of the beams as well as larger B_t and I_{beam} . The energy evolution derived from magnetic diagnostics can be compared with the inversion of HXR data [11] that gives an estimate of the runaway electron distribution function. The JET RE experiments with SPI mitigation have brought interesting results [3], [10]. Three different cases are studied in figure 4. These are based on Ar

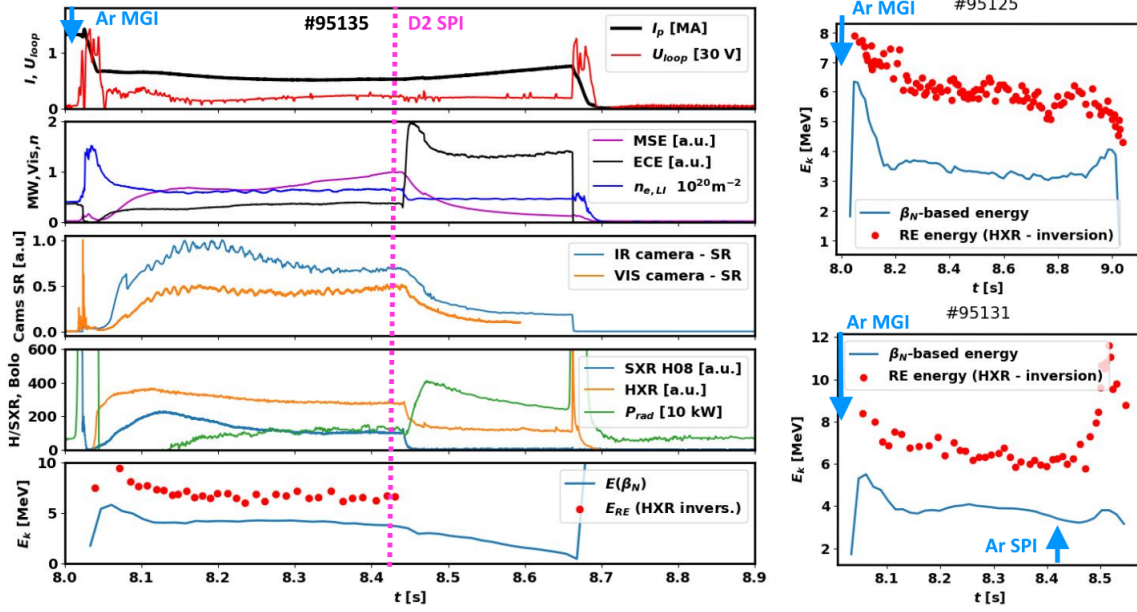


Figure 4: JET: Comparison of average kinetic energy derived from β_N and HXR inversion, top - RE beam triggered by Ar MGI, bottom similar pulse with secondary Ar SPI.

massive gas injection RE scenario: Ohmic plasma $I_p = 1.5\text{MA}$, $B_t = 3.0\text{T}$, $n_{e,li} = 4 \cdot 10^{19}\text{m}^{-2}$. In all of them the energy based on the HXRs seems to be the highest just after disruption and decreasing afterwards. In the discharge #95135 secondary D₂ (effect also further studied in [10]) SPI caused a significant changes in most of the signals: the I_p rises, HXR counts are no longer sufficient for application of the inversion method, the cameras observing the synchrotron radiation show a significant decrease of the intensity and the estimate of energy based on the β_N also gradually drops. On the other hand, injection of the secondary SPI into the RE beam causes a significant increase of energy based on the HXR emission and a small bump in the time evolution of the β_N estimate as well. It can be concluded, that low Z injection is definitely promising mitigation scenario and deserves further study.

Conclusions

An average RE energy estimate based on the equilibrium of the RE beam with the external field can be a quick and useful alternative to the more complicated methods based on the measurement of the HXR or synchrotron radiation and subsequent inversion problem solution or forward fitting of a complicated multi-parameter problem. A first comparison of the results of the method with estimates based on HXR and evolution of the synchrotron radiation intensity was done for COMPASS and JET and agreement of the main trends was confirmed. The method can support the evaluation of the different RE beam mitigation methods together with all other available diagnostics.

Acknowledgement. This work has been supported by MEYS project LM2018117 and carried out within the framework of the EUROfusion Consortium. It has also received funding from the Euratom research and training programme 2014-2018 and 2019-2020 under grant agreement No 633053 with the Co-fund by MEYS project number 8D15001. The views and opinions expressed herein do not necessarily reflect those of the European Commission. This work was supported by the Grant Agency of the Czech Technical University in Prague, grant No. SGS19/180/OHK4/3T/14.

References

- [1] Panek R. *et al.* 2016 *Plas. Phys. Contr. Fusion* **58** 014015
- [2] Macusova, E. *et al.* 2021 *EPS Conf. Plas. Phys.* **12.106**
- [3] Reux, C. *et al.* 2021 *EPS Conf. Plas. Phys.* **13.103**
- [4] Reux, C. *et al.* 2021 *Phys. Rev. Lett.* **126**, 175001
- [5] Yoshida, Z., 1990 *Nucl. Fusion* **30** 317
- [6] Ficker, O. *et al.* 2019 *Nucl. Fusion* **59** (9) 096036
- [7] Cerovsky, J. *et al.* 2021 *to be submitted to JINST*
- [8] Hoppe, M. *et al.* 2018 *Nucl. Fusion* **58**, 026032
- [9] Causa, F. *et al.* 2019 *Rev. Sci. Inst.* **90** 073501
- [10] Sommariva, C. *et al.* 2021 *EPS Conf. Plas. Phys.* **P1.1041**
- [11] Nocente, M. *et al.* 2017 *Nucl. Fusion* **57** 076016